Self-Assembly and Superlubricity of 2D Material Auto-Kirigami Ribbons

Pierce Sinnott

A thesis submitted for the degree of

Doctor of Philosophy in Physics

School of Physics

Trinity College Dublin

2025

Declaration

I declare that this thesis has not been submitted as an exercise for a degree at this or any other university and it is entirely my own work.

I agree to deposit this thesis in the University's open access institutional repository or allow the Library to do so on my behalf, subject to Irish Copyright Legislation and Trinity College Library conditions of use and acknowledgement.

I consent to the examiner retaining a copy of the thesis beyond the examining period, should they so wish (EU GDPR May 2018).

Pierce Sinnott

31-01-2025

Acknowledgements

I would like to sincerely thank my supervisor Prof. Graham Cross for his continuous guidance, from his first encouragement to pursue a PhD during my undergraduate capstone project throughout the entire experience. This PhD would undoubtedly have been impossible without his direction, generosity of time and of knowledge, and good nature.

I would also like to thank my fellow members, past and present, of the nanomechanics research group: Majid, Zahra, Aaron, Ahmed and Daragh. I can only hope that I have in some small way repaid the advice and support that you all have provided.

My thanks as well to various friends from my undergraduate years, those who as recklessly as I decided that another four years in Trinity was wisest, and those just as wise who moved to pastures new. Similarly, my thanks to the many Hist hacks from my years in the society who simply keep popping up both on- and off-campus; we truly can never escape the Hist.

Last but by no means least, my deepest gratitude to Laura for her endless supply of cute animal pictures, confectionery and patience which have fuelled this thesis; to my siblings Catherine, Margaret and John for always listening to rants about my research regardless of how much or how little sense it made either to them or to me and finally to my parents who have supported me throughout these past eight years in Trinity and who instilled in me such commitment to curiosity from an early age.

Abstract

Auto-kirigami describes a novel self-assembly process in graphene involving thermodynamically driven tearing, substrate peeling and sliding of graphene, all occurring spontaneously in ambient conditions. Following rupture of mechanically exfoliated graphene sheets by small amplitude sheared nanoindentation, this process results in formation of folded graphene auto-kirigami ribbons with micrometre scale lengths. This growth is enabled by the low sliding friction of structural superlubricity between graphene ribbons and their host graphene sheets in incommensurate contact.

In this work, auto-kirigami ribbons are studied and characterised by atomic force microscopy (AFM), particularly using the high resolution PeakForce Quantitative Nanomechanical Mapping Mode. Using this mode, ordered stripe hydrocarbon adsorbates of atmospheric origin are observed ubiquitously on graphene surfaces, which strongly modify the friction of these surfaces. Time resolved formation and dynamics of stripe friction domains are studied. Crucially, we further demonstrate that these adsorbates are also present in the graphene-graphene interface of ribbons, in buried graphene-graphene interfaces within graphitic flakes and at graphene-substrate interfaces, with significant implications for the cleanliness of van der Waals structures. Despite this, we show that superlubricity can persist in stripe-contaminated ribbon interfaces.

Rupture of graphene sheets as a necessary precursor to auto-kirigami is studied by small amplitude sheared indentation nucleation using a 2D indentation contact system, with the contributing effects of graphene layer number, shear oscillation frequency and strain rate on rupture depth examined.

We also develop a novel method of nucleating auto-kirigami ribbons which can be performed using only a standard AFM. This facile, high yield method does not require an applied small amplitude shearing oscillation, which massively extends the applicability of auto-kirigami nucleation and growth.

Successful auto-kirigami is also demonstrated on graphene produced by chemical vapour deposition using both nucleation methods, facilitating large scale application of auto-kirigami without the area and yield limitations of micromechanical exfoliation of graphene. While auto-kirigami is inhibited by the presence of residual PMMA contaminants on CVD materials, we review and perform thermal annealing, catalytic cleaning, and mechanical micro-cleaning by AFM on these contaminants.

Finally, towards developing auto-kirigami ribbons as nanoelectromechanical devices, we induce reversible growth of ribbons by mechanical manipulation with an AFM and explore methods towards electrical control of graphene auto-kirigami ribbons.

Publications associated with this research

P. Sinnott, M. Jadidi, D. Sánchez, L. Yuan, R. Carpick, and G. Cross, 'Superlubric Sliding of Graphene Auto-Kirigami with Interfaces Containing Self-Assembled Stripe-Pattern Adsorbates', Small, **2024**, 10.1002/smll.202401979.

M. Jadidi, P. Sinnott, G. Tribello, R. Carpick, and G. Cross, 'Auto-Kirigami: Self-Assembling, Superlubricious Molecular Machines in 2D Materials', in preparation.

P. Sinnott, M. Jadidi, L. Yuan, R. Carpick and G. Cross, 'Graphene Auto-Kirigami Nucleation by AFM Hard Tapping', in preparation.

P. Sinnott, A. Uluca, M. Jadidi and G. Cross, 'Strain and Rupture of Graphene Sheets during Shear-assisted Indentation', in preparation.

Table of contents

Declaration ..... **i**

Acknowledgements ..... **ii**

Abstract ..... **iii**

Publications associated with this research ..... **v**

Table of contents ..... **vi**

List of figures ..... **viii**

Chapter 1: Introduction **1**

1.1 Introduction and outline 1

1.2 Graphene 1

1.2.1 Superlubricity 4

1.3 Graphene synthesis 7

1.3.1 Mechanical exfoliation 8

1.3.2 Chemical Vapour Deposition 10

1.4 Atomic Force Microscopy 11

1.4.1 Contact mechanics 18

1.5 Nanoindentation 21

1.5.1 2-Dimensional Indentation 26

1.5.2 AFM based indentation 29

1.6 Graphene self-assembly/auto-kirigami 31

1.7 Conclusions 41

Chapter 2: Stripe adsorbates **43**

2.1 Introduction 43

2.2 Stripes on graphene surfaces 44

2.3 Stripe dynamics and formation 52

2.4 Effect on superlubric friction 59
2.4.1 Effect of stripes on superlubricity 65
2.5 Interactions of surface features and stripe friction domains 70
2.6 Stripes between surfaces 77
2.7 Conclusions 87
Chapter 3: Nucleation of 2D material auto-kirigami 88
3.1 Introduction 88
3.2 AFM nucleation 88
3.2.1 Ribbon nucleation on non-graphene 2D materials 102
3.2.2 Crystallography of the torn edges of auto-kirigami ribbons 106
3.3 Graphene Rupture during 2D Nanoindentation 110
3.4 Conclusions 125
Chapter 4: AK formation in CVD 2D materials 127
4.1 Introduction 127
4.2 Nucleation in CVD 2D materials 128
4.3 Cleaning of CVD samples 138
4.4 Conclusions 149
Chapter 5: Mechanical and electrical control of gr-AK ribbons 151
5.1 Introduction 151
5.2 Mechanical control 151
5.3 Electrical control 157
5.4 Conclusions 162
Chapter 6: Conclusions and future work 163
6.1 Conclusions 163
6.2 Future work 165
References 170

List of figures

Fig. 1.1: Overview of graphene lattice structure, stacking and orbitals 2

Fig. 1.2: Armchair and zigzag edges of a mechanically exfoliated graphene flake 4

Fig. 1.3: Friction of commensurate and incommensurate graphite contacts 5

Fig. 1.4: Layer number dependence of graphene friction 6

Fig. 1.5: Overview of graphene mechanical exfoliation 8

Fig. 1.6: Sketch of AFM schematic in operation 11

Fig. 1.7: Sketch depicting the variation in z position, force, and cantilever deflection with time over a single peak-force tapping cycle 14

Fig. 1.8: Derivation of mechanical properties from PFQNM 16

Fig. 1.9: Sketch of contact mechanics models 19

Fig. 1.10: Indentation load-displacement curves and impressions in different materials 22

Fig. 1.11: Schematic of continuous stiffness method (CSM) applied to indentation 24

Fig. 1.12: Sideview (a), plan view (b) and 3D isometric view (c) of Berkovich tip 25

Fig. 1.13: Schematic of Gemini nanoindenter 28

Fig. 1.14: AFM and sketch of representative graphene auto-kirigami ribbon 32

Fig. 1.15: Geometric determination of graphene twist angle 37

Fig. 1.16: MD simulation of auto-kirigami ribbon tearing and folding 39

Fig. 2.1: PFQNM imaging of stripes on graphene terraces 45

Fig. 2.2: Graphene with adsorbate stripes and stripe friction domains 48

Fig. 2.3: AFM and STM images of stripes and their inner structure 51

Fig. 2.4: Development and evolution of stripe friction domains with time after initial exposure of pristine graphene monolayer to atmosphere 53

Fig. 2.5: Direct imaging of stripes development and evolution 55

Fig. 2.6: Selection of a series of consecutive TFM images of stripe friction domains taken in 17-minute intervals 56

Fig. 2.7: Direct observation of stripe orientation change in PFQNM 57

Fig. 2.8: Rotation of ribbons to reveal stripes at former interface areas 62

Fig. 2.9: Alignment of alkane chains on graphite lattice 71

Fig. 2.10: Effect of wrinkles and step edges on stripe domains 72

Fig. 2.11: Effect of indentation on "established" domains of stripes 73

Fig. 2.12: Effect of indentation on "fresh" domains 74

Fig. 2.13: Correlation of mechanical properties to PFQNM channels 76

Fig. 2.14: Stripes on folded ribbons and between substrates 78

Fig. 2.15: Stripes on newly formed ribbons produced by AFM indentation and AFM-assisted nucleation 81

Fig. 2.16: Stripes on all steps of a thick ribbon peeled from graphite 82

Fig. 3.1: Ribbon nucleation by AFM cutting 89

Fig. 3.2: Effect of scanner tube motion during AFM indentation 94

Fig. 3.3: Ribbon nucleation by AFM indentation and "hard tapping" 96

Fig. 3.4: Ribbon nucleation and growth assisted by AFM hard tapping 98

Fig. 3.5: Ribbon growth ceases in absence of hard tapping 99

Fig. 3.6: Auto-kirigami ribbon nucleation within thick graphite without the involvement of substrate adhesion 101

Fig. 3.7: "Stone wall" model of self-retracting motion in HOPG graphite mesas 102

Fig. 3.8: Ribbon nucleation by AFM indentation and hard tapping on single-layer MoS_2 105

Fig. 3.9: Assessment of ribbon edge crystallography from stripe direction. 107

Fig. 3.10: Crystallography of ribbon edges by AFM-based indentation and by SASIN 109

Fig. 3.11: Indentation via a 2D nanoindenter of 300 nm SiO_2/Si substrate with and without mechanically exfoliated single layer graphene on SiO_2/Si substrate 111

Fig. 3.12: Variation of rupture depth with graphene layer number 112

Fig. 3.13: Lateral contact stiffness and lateral displacement signals immediately before and after rupture point 115

Fig. 3.14: Rupture depths in thicker graphene 117

Fig. 3.15: Variation of rupture depth with lateral oscillation frequency and strain rate 118

Fig. 3.16: Folding at the ribbon head 120

Fig. 3.17: Effect of tip shape and indent crater shape on nucleated ribbons 121

Fig. 3.18: Ribbon nucleation with no applied oscillations 123

Fig. 4.1: Sample survey of AFM-based indentation by PFQNM 129

Fig. 4.2: Nucleation success rates in different CVD materials and with different nucleation methods 130

Fig. 4.3: PMMA contamination on CVD graphene samples 132

Fig. 4.4: Effect of wrinkles and surface contamination on ribbon growth in CVD materials 133

Fig. 4.5: Contaminants on samples exposed to ambient lab conditions for 1+ years 135

Fig. 4.6: AFM survey of many indents to assess nucleation success rates 137

Fig. 4.7: Effect of thermal anneals on PMMA residue 140

Fig. 4.8: Platinum-metal catalysed cleaning of PMMA residues 142

Fig. 4.9: Outline of scanned area, showing PMMA swept to each side of the scan area 144

Fig. 4.10: Variance in rupture depth of CVD graphene 148

Fig. 5.1: Methods to demonstrate ribbon reversal using AFM 152

Fig. 5.2: Ribbon healing and reversal during "hard tapping" imaging 154

Fig. 5.3: Height discrepancies of "healed" ribbons relative to surrounding graphene sheet 155

Fig. 5.4: Sketch demonstrating concept of capacitive ribbon control 158

Fig. 5.5: Erosion of graphene flakes from edges with 100 V, 50 kHz sinusoidal waveform 159

Fig. 5.6: Frequency dependence of rate of graphene erosion 161

Fig. 6.1: "Grouping" of rupture points in monolayer mechanically exfoliated graphene 165

Fig. 6.2: Rare, anomalous ribbon growth in graphene 167

Fig. 6.3: Schematic of experiment testing intercalation of stripe adsorbates 169

Chapter 1: Introduction

1.1 Introduction and outline

In this chapter, we will introduce a number of foundational topics to this work: firstly, we will discuss the two-dimensional material upon which a majority of this research is performed, graphene, its frictional properties which are central to auto-kirigami, and methods to produce graphene, primarily mechanical exfoliation and chemical vapour deposition (CVD).

We will then review the main experimental techniques applied in this work, namely atomic force microscopy (AFM) and nanoindentation. On AFM, we will discuss the fundamentals of this technique and further operational details on the primary AFM modes used, contact mode and PeakForce Quantitative Nanomechanical Mapping (PFQNM). In nanoindentation, we will review both one- and two-dimensional indentation and specifically how the latter has been used to produce graphene auto-kirigami ribbons through small amplitude sheared indentation nucleation. A fracture mechanics model describing the growth of auto-kirigami ribbons, self-assembled structures incorporating thermodynamically self-driven tearing, sliding and folding of graphene, is also presented.

1.2 Graphene

Graphene is a carbon allotrope consisting of a monolayer of carbon atoms arranged in a hexagonal lattice with 120° C-C-C bond angles as in Fig. 1.1 (a). Each atom is bonded to its 3 nearest (in plane) neighbours with bond lengths of 0.142 nm through σ-bonding of sp^2-hybridised orbitals and one delocalised π orbital perpendicular to the plane as in (c) and (d).

Layers are stacked with an interplanar spacing of 0.335 nm to form the graphite allotrope. Bernal stacking, or AB stacking, as depicted in (b) refers to bilayer graphene where half of the atoms in one layer are positioned over an atom of the other layer, while the other half are located over the center of the hexagon of the opposite layer. Graphene stacked out of registry as in (e) has also been studied extensively with regards to superconducting "magic angle" twisted bilayer graphene for example[1], as well as being of interest for its frictional properties (see section 1.2.1).

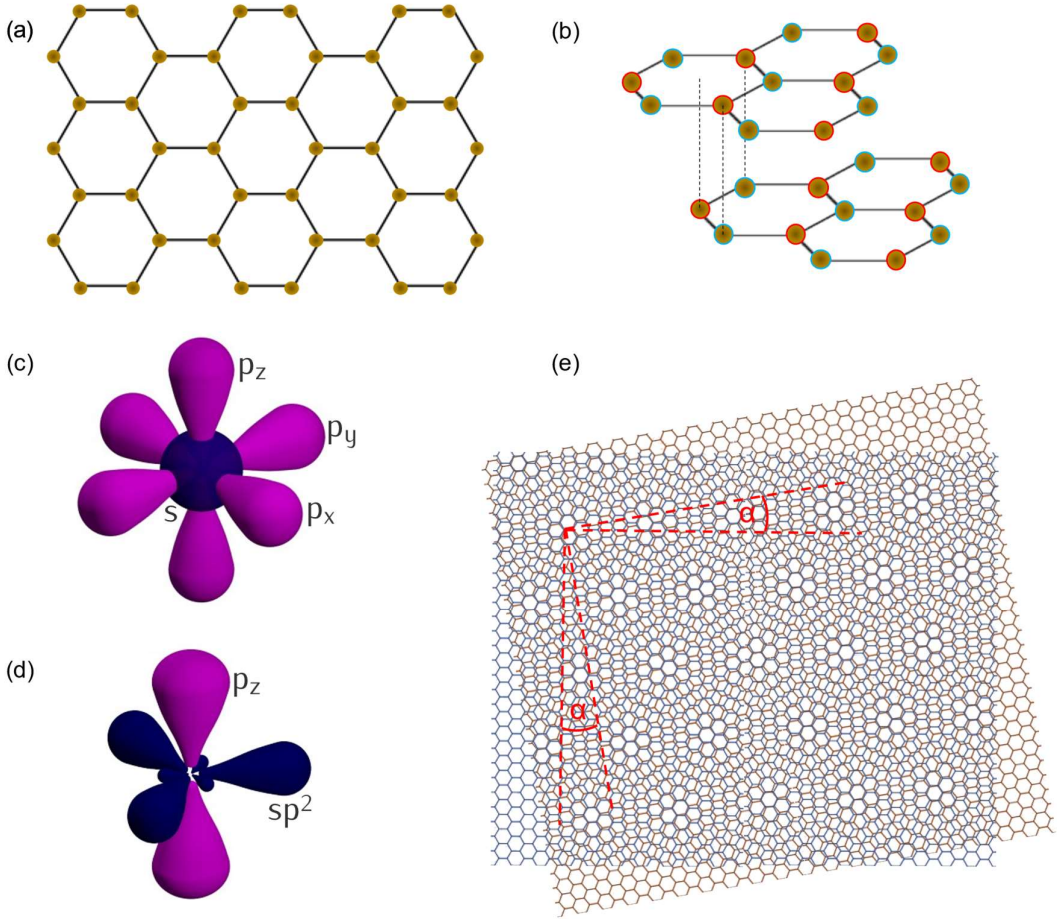

Fig. 1.1: Overview of graphene lattice structure, stacking and orbitals. (a) Hexagonal honeycomb lattice of graphene, with bonds indicated by black lines and atoms by gold circles. Though terminology and usage may vary, "graphene", per ISO standards, is taken to mean strictly monolayer, while bilayer graphene (BLG), as in (b) is used for two layers, here in Bernal (AB) stacking whereby half of the carbon atoms in each layer are positioned above/below the centre of the hexagons defined by the neighbouring layers. The carbon 2s and $2p_x$ and $2p_y$ orbitals (c) form graphene's hybrid sp^2 orbitals in plane (d), with one remaining electron per atom in the p_z π orbital oriented out-of-plane. (e) A twist angle (α) may be present between graphene layers giving rise to twisted bilayer graphene in this case. (c) and (d) reproduced from Wikimedia Commons.

It had previously been thought that graphene, or indeed any 2D crystal, could not exist at any finite temperature due to thermal fluctuations[2,3] unless of very limited size or containing many crystal defects, supported by experimental observations whereby sufficiently thin layers would decompose or segregate unless stabilised by being grown on a bulk crystal with a matching lattice or embedded in a 3D matrix[4,5]. However, nearly perfect rather than perfect 2D films could exist, as demonstrated by Meyer et al. for example[6]. Intrinsic microscale roughening could allow single layer graphene to exist suspended even without a substrate, where rather than being perfectly flat, the sheet may exhibit out-of-plane deformations of up to 1 nm on suspended graphene, three times the interplanar distance. These corrugations arising from bending of the sheet out of plane give rise to reproducible roughness, increasing elastic energy but supressing thermal vibrations with the net effect of minimising free energy. This "crumpling" allows for the known thermodynamic stability and is most pronounced in thinner samples. Atomistic Monte Carlo simulations also indicate that ripples can spontaneously appear as a result of thermal fluctuations with a typical size of 80 Å. Such ripples are expected to be subdued where the graphene is on a substrate rather than suspended due to strong conformation of the sheet to the substrate.

Experimentally, graphene was first isolated by Novoselov and Geim in 2004[7] by micromechanical cleavage of bulk graphite (also referred to as the Scotch tape method, described in full in section 1.3.1). This material has remained a focus of research since then[8] due to a number of its characteristics: both monolayer and bilayer graphene are zero-gap semiconductors/zero-overlap semimetals, and high crystallinity allows its high mobility charge carriers (massless Dirac fermions) to travel with little scattering[9]. Similarly, graphene has numerous superlative properties, such as its ultimate tensile strength, Young's modulus[10], high in-plane thermal conductivity[11], and low friction coefficient[12] for example.

Graphene features two main crystallographic directions: armchair and zigzag as indicated in Fig. 1.2 (b). Neubeck et al. reported that the edges of graphene flakes produced by mechanical exfoliation typically follow one of these two orientations[13], such that edges of mechanically exfoliated graphene flakes are typically arranged at (n × 30°) intervals as depicted in Fig. 1.2 (a) (for natural number n). Arrangement of edge atoms has a strong influence on structural, mechanical and electronic properties of graphene[14].

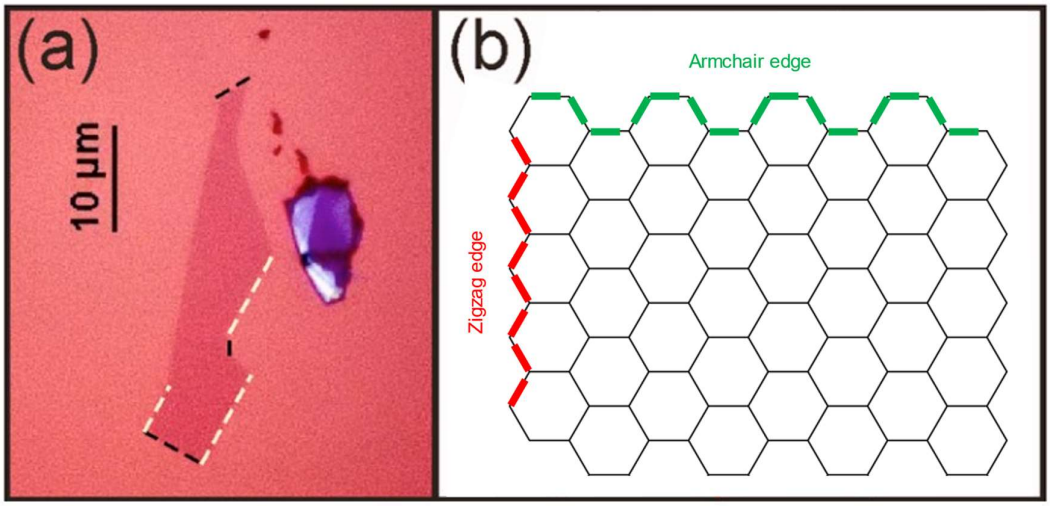

Fig. 1.2: Armchair and zigzag edges of a mechanically exfoliated graphene flake. (a) Terminating edges of the graphene flake (highlighted by white and black dashes) are often straight lines which are observed to vary by 30° intervals over micrometre lengths. (b) Sketch of graphene honeycomb lattice (black) with armchair and zigzag edges indicated by green and red dashed lines respectively. Further armchair and zigzag directions are present at 60° intervals from the previous armchair/zigzag respectively. (a) reproduced from 13.

1.2.1 Superlubricity

Friction, the force resisting relative motion of bodies/layers, has been studied since antiquity, including by Leonardo da Vinci from 1493 for example[15]. In the classical case, the force of sliding (kinetic) friction $F_{friction}$ can be simply described by Amonton's Law, or $F_{friction} = \mu \cdot F_{normal}$, with dimensionless coefficient of friction µ and normal force F_{normal}, with $F_{friction}$ being independent of apparent contact area and sliding speed. This is broadly true for macroscopic bodies, where the real contact area is actually much smaller than the apparent contact area as the surfaces interact between asperities on

each surface rather than the entire surfaces[16], but this relationship breaks down in the microscale and smaller. Atomic scale stick-slip friction can be well described by the Prandtl-Tomlinson model[17,18], which considers frictional sliding in 1D as a point-like tip coupled to a mass M with a spring constant k, interacting with a periodic surface potential $V(x_t)$ and moving with velocity v_m, described by

$$m_x \ddot{x}_t = c_x(x_M - x_t) - \frac{\partial V(x_t)}{\partial x_t} - \gamma_x \dot{x}_t \quad (1)$$

for effective mass m_x, equilibrium position of the tip at time t x_M, and damping constant γ_x. The friction force $F_{friction}$ is then the averaged lateral force $\langle F_x \rangle$ where $F_x = c_x (x_M - x_t)$. Frenkel and Kontorova's later model instead considering chains of elastically coupled atoms subject to a periodic potential can also be applied[19].

Structural superlubricity, as proposed by Hirano and Shinjo[20] in 1990, is a phenomenon whereby friction between sliding bodies becomes negligibly small and minimal wear occurs. Per the conventional Coulomb definition of dry friction, we can define this as requiring a friction coefficient μ of less than 0.01. As proposed, this however necessitated very stringent requirements of the interface, such as to be composed of atomically flat, molecularly clean, weakly interacting and structurally incommensurate surfaces[21]. This would then result in a sub-linear relation of friction with contact area[22].

This was experimentally demonstrated in graphite by Dienwiebel et al. in 2004[23]. By measuring the lateral forces between a graphite substrate and a graphite flake attached to a tungsten tip with varying sample rotation, ultra-low friction was measured for the majority of the 100° angular range studied, with sharp, narrow peaks of friction

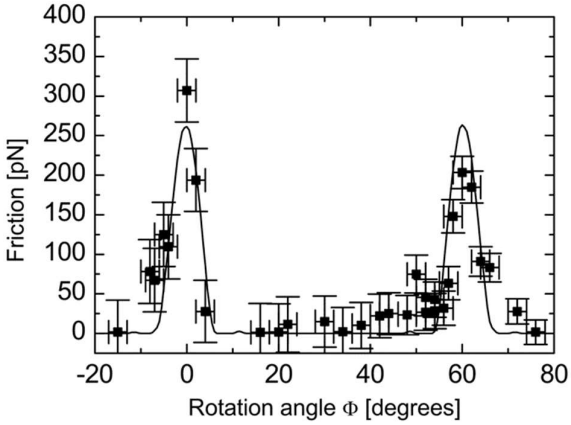

Fig. 1.3: Friction of commensurate and incommensurate graphite contacts. Average friction as a function of rotation angle between HOPG substrate and graphite flake. Reproduced from 23.

observed at 60° intervals, corresponding to the 60° symmetry of the graphite lattice per Fig. 1.3. These friction peaks are attributed to where the substrate and flake graphite are in commensurate contact. While this and other early experimental validations of structural superlubricity required UHV conditions[24], it has also been demonstrated in limited instances in ambient conditions as well[25–27,21].

The definition of superlubricity as requiring a friction coefficient μ of less than 0.01 per Coulomb friction cannot always readily be applied, however. This is the case where a normal force cannot easily be defined for example. We can instead describe a shear stress (per unit area friction) between the sliding bodies[28]. From Liu et al.'s research in microscale superlubricity in between graphite surfaces, superlubricity then corresponds to shear stress up to 10s of kPa[29].

Graphite is widely applied as a lubricant, and graphene also acts as a lubricant, with low friction observed on graphene on silicon substrates for example. Lee et al. reported a monotonic decrease in friction with increasing number of graphene layers on silicon substrates from 1 to 5 layers by AFM (a decrease of 50-60%), with no further change for 5+ layers[30], as indicated in Fig. 1.4. Similar results were observed for graphene freely suspended over a well[30]. This was attributed to deformation of the graphene due to AFM tip motion, whereby the sheet experiences an out-of-plane deformation (puckering) in front of the tip (in the direction in which the tip travels), arising from the tip-graphene adhesion and high out-of-plane flexibility of graphene[31].

This puckering increases contact area between the tip and sheet and therefore

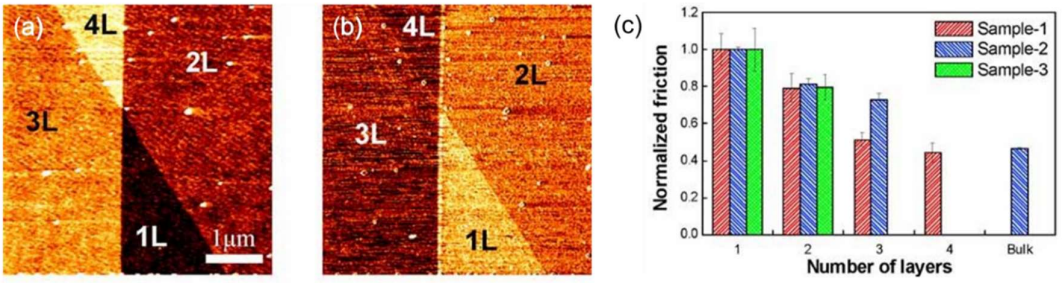

Fig. 1.4: Layer number dependence of graphene friction. (a) AFM topography image with neighbouring areas of 1-4 layers thickness (indicated as 1L-4L). (b) Simultaneous friction force imaging of same areas as (a), with highest friction in 1-layer graphene and monotonically decreasing friction up to 4-layers. This trend is reproduced across different samples (c), with friction of 5-layers graphene indistinguishable from friction on bulk. Reproduced from 30.

increases friction. With more layers, the bending stiffness of the graphene increases, with bending stiffness proportional to the cube of the layer number (assuming no interlayer sliding[32]), corresponding to decreased susceptibility of thicker sheets to out-of-plane deformation[33]. Puckering is therefore suppressed for thicker sheets, hence the friction decreases with layer number. This trend was not observed for graphene on mica substrates however, on which the friction of graphene and bulk graphite is indistinguishable. This is attributed to the much stronger adhesion of mica to graphene, reducing any rippling of the sheet that could experience puckering.

Later atomistic simulations by Li et al. demonstrate that this layer dependence of friction on few-layer graphene sheets arises not only from evolution of the quantity of tip-sheet contact (i.e. contact area increasing with enhanced puckering) but also from the quality of this contact (i.e. stronger local pinning by individual atoms and an increase in the number of such atoms)[34].

1.3 Graphene synthesis

A number of techniques exist for production of graphene including chemical methods such as liquid phase exfoliation (LPE)[35], electrochemical methods[36], epitaxial growth[37], mechanical exfoliation[7] and chemical vapour deposition (CVD)[38] for example. The methods of mechanical exfoliation and CVD will be the focus of this work. Mechanical exfoliation provides the highest quality of few layer graphene, albeit in limited size scales and with low yield. This method is therefore appropriate for laboratory scale exploratory research only. In contrast, CVD allows for large scale, high yield growth of graphene suitable for scaling to applications but is of lower mechanical quality, with residual PMMA contamination, tears, wrinkles and other defects ubiquitous. In LPE, bulk graphite is ultrasonicated to overcome interlayer attraction in a solvent with surface tension similar to graphene surface energy to stabilise the resulting sheets. However, these sheets can show a dispersion in layer number even after centrifuging and individual flakes are typically no larger than 3 μm, which prevents their use in this work[35]. In electrochemical exfoliation, an applied voltage causes ionic species from an

electrolyte to intercalate into a graphite electrode, increasing the interlayer separation and exfoliating the electrode graphite[39], though this method similarly results in graphene flakes of lower lateral sizes and typically of at least few nanometre thicknesses[40]. An example of epitaxial growth is thermal decomposition of silicon carbide at high temperature and low pressure over larger areas (up to cm scale) at high purity but with small grains of varying thicknesses and at very small scale[41].

1.3.1 Mechanical exfoliation

Micromechanical exfoliation, or the Scotch tape method, was the first technique

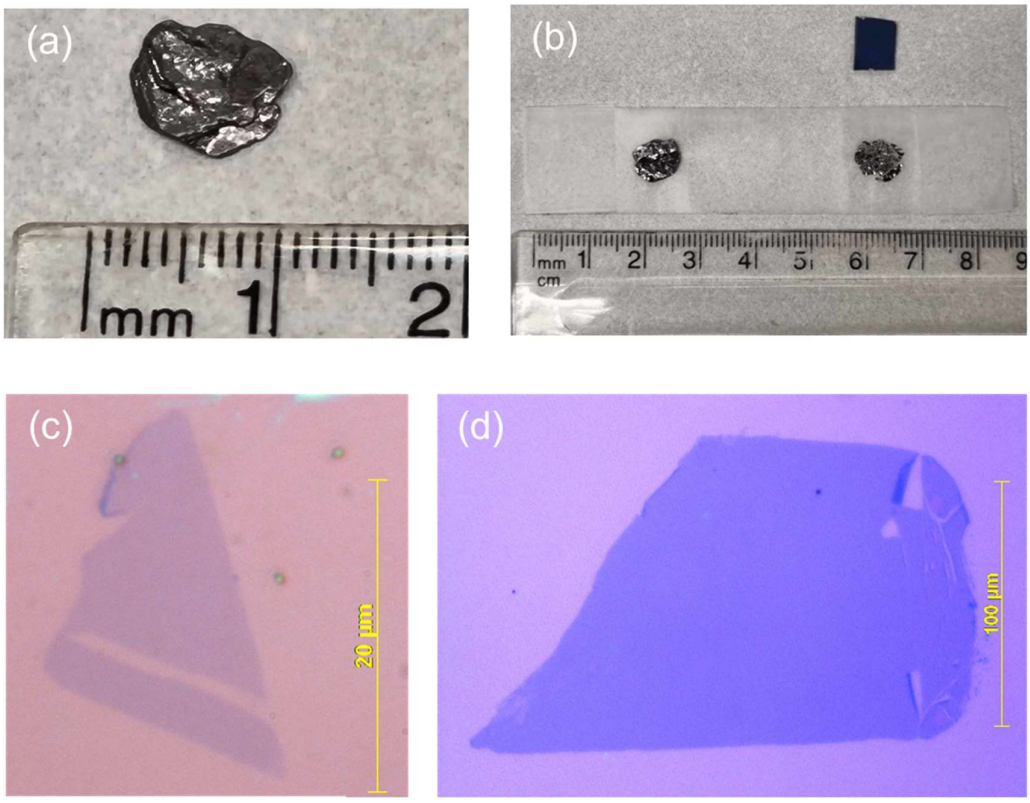

Fig. 1.5: Overview of graphene mechanical exfoliation. (a) Natural graphite (graphenium) flakes (NGS Naturgraphit) up to 1 cm lateral dimensions were exfoliated by the Scotch tape method (b), using 3M Magic tape. Representative few layer graphene flakes (bilayer in (c) and trilayer in (d)) using Kish graphite and no chemical or plasma pre-cleaning in (c) and with graphenium flakes, chemical and plasma pre-cleaning of substrate in (d), resulting in areas up to 60 times larger.

designed to produce single layer graphene. Few layer flakes typically range from only tens to ≈100 μm in size laterally, making detection of exfoliated flakes by optical microscopy difficult as the optical absorbance of graphene per layer is only 2.3 ± 0.1% with negligible reflectance[42]. However, selecting 300 nm SiO_2/Si as the substrate (or less commonly 100 nm SiO_2/Si) provides much greater optical contrast due to interference, allowing the exfoliated flake to be readily identified by optical microscopy[43], albeit with uncertainty in determining the number of layers by this method alone.

The method used here follows that of Huang et al.[44], which represents a refined albeit qualitatively similar method to that originally used by Novoselov et al. The target SiO_2 substrate is ultrasonically cleaned sequentially in acetone, isopropanol and DI water, followed by drying by compressed air and heating to 110 °C for several minutes. The substrate is then cleaned by oxygen plasma to remove any remaining organic adsorbates. Graphenium flakes produced from flake graphite ore deposits (NGS Naturgraphit) (Fig. 1.5 (a)) with lateral dimensions of up to 10 mm are brought into contact with the synthetic acrylic tape (3M Scotch Magic Invisible tape) as indicated in Fig. 1.5 (b). The tape/graphenium is pressed against another piece of tape typically 3-5 times, with the final tape/thinned graphenium pressed onto the cleaned substrate immediately after plasma cleaning. The substrate/flake/tape is then heated at ≈110 °C on a standard laboratory hotplate for 2-5 minutes before cooling to room temperature and peeling the tape from the substrate to transfer few-layer graphene to the substrate, as in Fig. 1.5 (c) and (d). While intuition might suggest that the tape should be separated a greater number of times (assuming each separation halves the number of layers from the approximately 3×10^6 in a 1 mm thick bulk graphenium flake, then 21-22 exfoliations would be required to reduce the bulk flake to single layer), the adhesion between the tape and graphenium is typically greater than the adhesion between graphene layers and substrate. Few layer graphene flakes seen transferred to substrates by this method are the outermost layers exfoliated from the comparatively thick crystals remaining on the tape rather than directly from the tape itself. Increasing the number of separations then may only reduce the thickness of the areas exfoliated (with thicknesses greater than 50 nm) and cause the flakes to split, resulting in smaller sizes of exfoliated flakes. The annealing of the substrate/graphite/tape is proposed as the key step in increasing

yield of total area of exfoliation by 20-60 fold: heating increases the pressure of gases trapped in the graphite/SiO_2 interface which can then escape through the exfoliated flake edges (as graphene is impermeable to all gases[45]), which then increases the strength of the van der Waals forces between flake and substrate, therefore preventing gases from entering during and after cooling.

In this work, it was found that flakes with dimensions approaching or greater than 100 µm typically also featured a number of fractures or tears within the flake as in Fig. 1.5 (d), limiting the useful size. This was attributed to non-uniform strain in the exfoliated flakes exacerbated by increased pressure during the annealing step resulting in rupture of the flake.

1.3.2 Chemical Vapour Deposition

Chemical vapour deposition (CVD) is a vacuum deposition technique that allows for growth of graphene films on centimetre size scales[46]. While various combinations of temperature, pressure, substrate etc may be used, for illustrative purposes the method of Ruoff et al. will be described here[46]. Polycrystalline copper foils which act as the substrate are annealed in a hot wall furnace at high temperatures (typically ≈1,000 °C) in a low-pressure hydrogen atmosphere. A hydrogen/methane mixture is introduced into the system and the methane, catalysed by the copper foil, decomposes into carbon radicals and forms graphene on the copper foil substrate. The graphene film is over 95% monolayer as the graphene growth surface reaction is self-limiting, since the catalytic copper becomes covered in graphene and is no longer exposed, with the remainder primarily bilayer or few-layer. The graphene-coated face of the substrate is coated with a thin layer of a polymer such as poly-methyl methacrylate (PMMA) and baked to remove the solvent. The copper can then be dissolved in an iron nitrate solution leaving only the PMMA-graphene film which is later cleaned by DI water. This can then be transferred onto an appropriate substrate such as SiO_2 with relatively little damage to the film and the now top-facing PMMA layer is removed by acetone.

While large areas are readily available with this method, the continuous CVD graphene

films formed are polycrystalline with small grain sizes (often only a few microns) and this polycrystallinity can reduce mechanical strength by an order of magnitude for example[47]. It is also challenging to ensure that CVD films are free from contamination, especially of the polymer used in the transfer process[48], with a broad range of cleaning methods presented to attempt to remove this contamination spanning thermal annealing, plasma, mechanical and light-based methods[49].

1.4 Atomic Force Microscopy

Atomic Force Microscopy (AFM) was developed by Binnig, Quate and Gerber in the 1980s[50]. Capable of angstrom vertical resolution and nanometer lateral resolution even

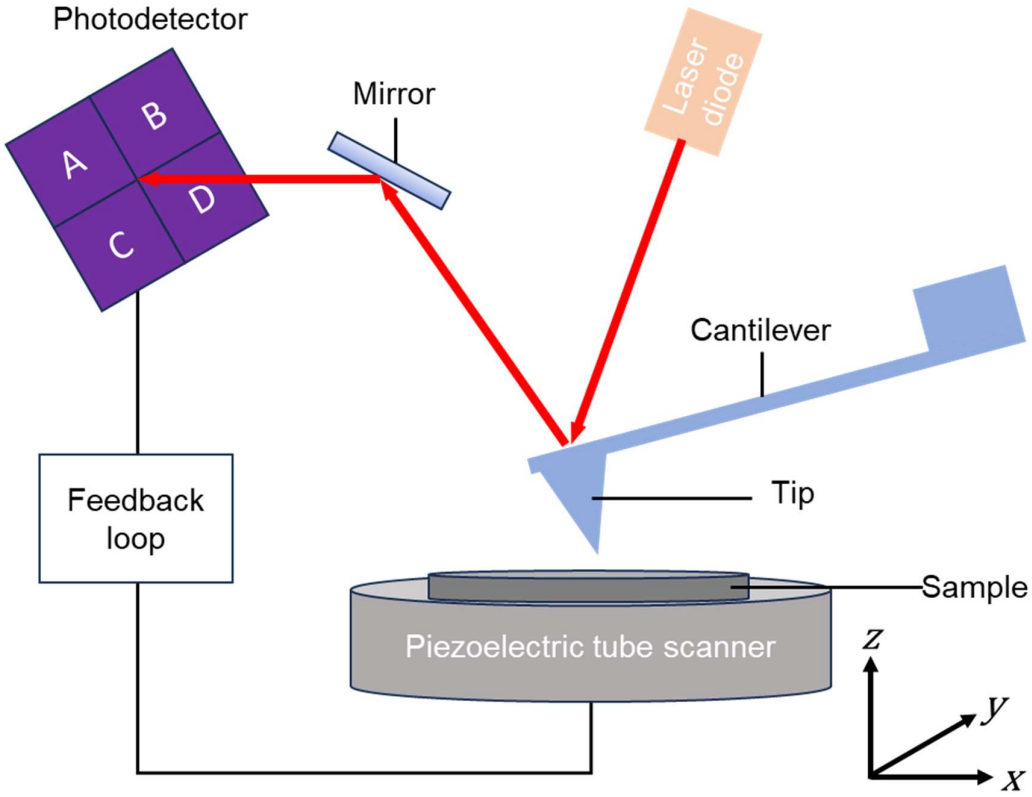

Fig. 1.6: Sketch of AFM schematic in operation. The cantilever is brought into contact with the sample surface with a force setpoint and is deflected by the surface topography. The laser is reflected from the backside of the cantilever to the mirror and hence to the position sensitive four-quadrant photodetector, where variation of the laser position is monitored by the feedback loop and used to control the piezoelectric tube scanner to maintain the force setpoint through z position and to move the sample relative to the tip (x and y positions).

in ambient conditions (and even atomic resolution under more specialised conditions), the capacities and functioning of the AFM have evolved significantly from its original conception as a combination of the pre-existing scanning tunnelling microscope (STM) and stylus profilometer into a broad class of scanning probe microscope. AFM can be used on samples ranging from delicate bacteria or biological cells[51] to even the hardest of materials, in ambient, vacuum and fluid conditions, on conducting and non-conducting samples. Qualitatively similar to the STM, the AFM images by means of a sharp tip (with tip end radii generally ranging from 2 – 50 nm) at the end of a micromachined cantilever probe attached to a larger chip (with standard dimensions of 3.4 mm x 1.6 mm) for handling. Tips are generally manufactured from silicon or silicon nitride, with specialised designs such as doped diamond available for electric applications for example. In the optical deflection/ "beam bounce" technique depicted in Fig. 1.6, a laser is shone incident on/near the free end of the cantilever. A reflective metal coating such as aluminium is typically present on the cantilever to ensure maximum reflectivity of this laser signal and to minimise interference from any laser signal reflecting from the sample rather than the cantilever. The laser is reflected from the cantilever to a position sensitive 4-quadrant photodetector. The tip is rastered over the sample surface at a constant force setpoint, resulting in deflection of the cantilever by the surface topography and therefore a variation in the laser intensity across the photodetector. A feedback loop maintains this force setpoint by monitoring the error signal (the difference between the defined and measured imaging force for example derived from laser intensity across the photodetector), with the controller then varying the z position to minimise that error signal in constant force-controlled systems while monitoring the real-time height deviation. This feedback loop must be sufficiently fast for the piezo to respond to the sample topography but not so fast as to introduce oscillations in the system[52]. This mechanism is represented schematically in Fig. 1.6.

In contact AFM (C-AFM) imaging, the tip is brought sufficiently close to the sample that repulsive van der Waals forces arising from the electron clouds of tip and sample atoms repelling one another dominate the interactions. Other interactions include an attractive capillary force where a contaminant layer is present on the sample and that the cantilever itself will exert a shear force on the sample. The tip is then held in

continuous contact and “dragged” over the sample both forward and backwards in every scan line (with forward and backward described as the trace and retrace directions).

While constant force and constant height setpoints are available for feedback control in C-AFM, constant height where the z position is not varied is much less common due to the risk of damage if the tip encounters steps on the surface during imaging. During C-AFM scanning in the much more widely used constant force mode, the cantilever deflection is the feedback parameter. This is monitored through the photodetector signal, with the tip height adjusted by the piezoelectric tube to constantly correct the deflection to the specified value, therefore keeping both force and height at the predefined value. This contact mode imaging enables not just capturing topographic data but also frictional data (described alternatively in the literature as lateral force microscopy or friction force microscopy (FFM), the latter of which will be used throughout here). The fast scan axis is set up perpendicular to the main axis of the cantilever such that the cantilever experiences torsion and twists. The magnitude of this twisting is directly proportional to the friction between tip and sample during scanning, which is recorded as a difference in laser signal between left and right quadrants of the photodetector. This provides a qualitative measurement of friction, while calibration of the torsional spring constant can allow quantitative friction measurements[53]. As the twisting of the cantilever and hence friction signal is also affected by topography of the sample surface in equal but opposite degrees, the friction is recorded in both trace and retrace directions, and then averaged as ((trace-retrace)/2).

While C-AFM represents a robust and fast method of imaging, while also allowing up to atomic resolution in the correct conditions, the requirement for constant contact between tip and sample can result in contamination, wear and damage to both. These problems are overcome in tapping mode AFM imaging (T-AFM). The cantilever is instead oscillated by the piezoelectric actuator at or near the resonant frequency of the cantilever. In free air, this results in oscillations with amplitudes of ≈20-100 nm. The tip is then brought close to the sample surface such that it contacts the surface only during the lowest position of the oscillation. Energy loss due to the contact, while accounting for only a small fraction of the oscillation cycle in time, results in change of the

oscillation amplitude with decreased amplitude while scanning over higher sample features and increased while passing over lower sample features. This change is recorded by the system to generate a topography signal as a function of the tip's lateral position (i.e. the final image), as well as to generate the error signal for the actuator to adjust tip-sample separation to maintain the pre-defined oscillation amplitude. This results in typical applied forces between tip and sample of only few to tens of nN. However, a number of issues persist: for example, measured changes in amplitude are averages of multiple interactions rather than single interactions, limiting attribution of results to specific sample properties, and cantilever dynamics are more complex at resonance making control more demanding and resulting in greater risk of tip damage[52]. Many of these limitations are removed in a related AFM mode, PeakForce Tapping (PFT).

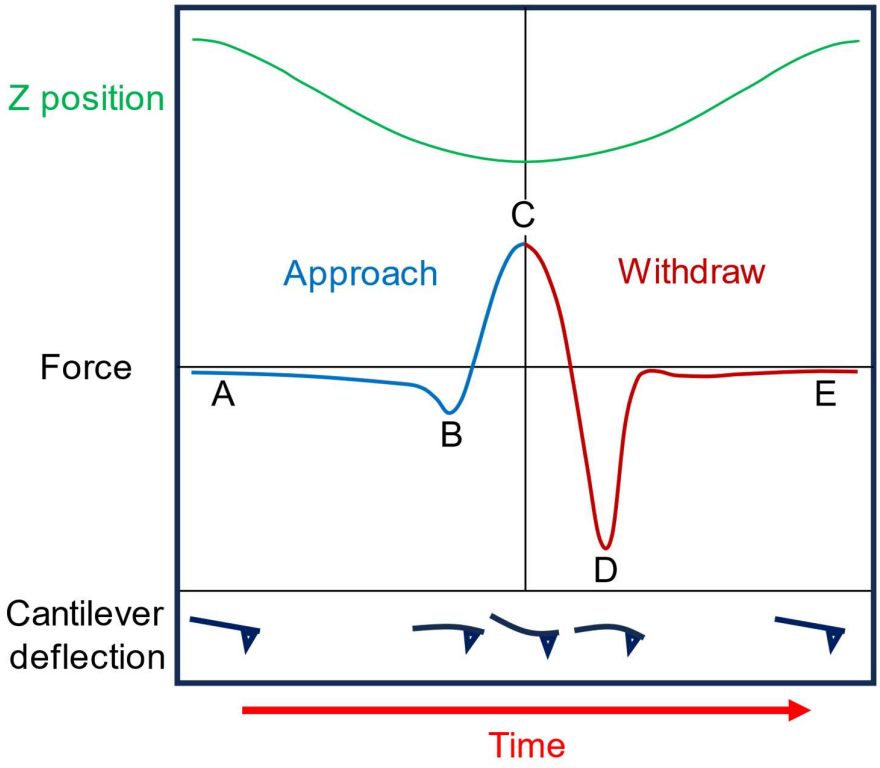

Fig. 1.7: Sketch depicting the variation in z position, force, and cantilever deflection with time over a single peak-force tapping cycle. Z position is lowered into contact (A-C) during approach and withdrawn after the setpoint is reached (C-E). Negligible force is experienced by the cantilever while far from the surface (A) before the tip snaps into adhesive contact (B) and the force is further ramped to the repulsive contact due to short-range forces at the force setpoint (C). The tip withdraws and force decreases to a minimum at D, the pull-off point before forces again go to zero away from the surface at E.

PFT is a proprietary AFM mode developed by Bruker in 2010[54,55], with a primary difference being that the cantilever is sinusoidally oscillated at a set frequency much lower than the resonant frequency of the cantilever (typically in the range of 0.5 – 4 kHz) regardless of the cantilever resonant frequency, with amplitudes typically of 100-150 nm. A force-distance curve is captured at every pixel of the image as in Fig. 1.7, whereby initially the tip is sufficiently far enough away from the sample that forces between tip and sample are negligible (labelled A in Fig. 1.7), with attractive vdW, electrostatic or capillary forces increasing as this separation decreases until dF/dx becomes greater than the cantilever spring constant and the tip snaps into contact with the sample for less than 100 μs in each cycle (B). In contact, short-range repulsive forces dominate until the peak force is reached (C), at which point the cantilever retracts with the tip still held in contact by adhesive forces (D) until snapping out of contact and withdrawing to E.

Imaging in this mode is unaffected by the Q-factor of the cantilever and removes the requirement for cantilever tuning prior to imaging. This allows direct force control and the capturing of the force-distance curve at every pixel of the image, from which a number of mechanical properties can be simultaneously derived, such as modulus, adhesion, deformation and dissipation[54,56] (with this mode referred to as PeakForce Quantitative Nanomechanical Mapping (PFQNM)) as illustrated in Fig. 1.8. This is possible in PFQNM as instantaneous forces on the tip are measured rather than only a time-average of force or dissipation, requiring a high bandwidth force sensor relative to the frequency of the tip interactions. This analysis is performed for every cycle in real-time, with the same resolution as the topography image. The Derjaguin-Muller-Toporov (DMT) model, described in more detail in section 1.4.1, is often used to derive the sample's reduced elastic E_r. Adhesion is calculated by the difference in the baseline force (≈0 nN) and the minimum force recorded at position D per Fig. 1.7. Deformation is determined as the distance from the peak force position to the deformation force level, which is the z position at 15% of the peak force to minimise error from baseline noise. This results in deformation being a slight underestimate of the total deformation. Dissipation shows the hysteresis between the load and unload curves, or the integrated area between the trace and retrace curves i.e. the energy loss per cycle. The titular peak

force in PFQNM can be as low as 10 pN, helping to minimise damage or wear to tip and sample, or as high as micronewtons with a sufficiently stiff cantilever.

Assuming that the damping is primarily air damping, the cantilever can be described by a sinusoidal damped harmonic oscillator as

$$F_0 = m^* \frac{d^2 z}{d\,t^2} + b \frac{d\,z}{d\,t} + k_z \qquad (2)$$

with driving force F_0, (where $F_0 = k\ A_0$), effective mass of the *cantilever* m^*, lever displacement z, damping coefficient b and spring constant k. With the natural frequency $\omega_0 = \sqrt{\frac{k}{m^*}}$ and relaxation time $\tau_0 = \frac{m^*}{b}$, the lever's amplitude can be expressed as

$$A(\omega_e) = \frac{\mathrm{A}_0}{\sqrt{\left[1 - \left(\frac{\omega_d}{\omega_0}\right)^2\right] + \frac{1}{(\omega_0\,\tau)^2}\left(\frac{\omega_d}{\omega_0}\right)^2}} \qquad (3)$$

Here, we can define the quality factor, Q, of a system as the ratio of the initial energy stored in the system divided by the energy loss per radian during each cycle, $Q = \omega \cdot \tau$ and the maximum amplitude at resonance $A_r = A_0 \cdot Q$ [57].

As the laser deflection signal is output in volts, the system must be calibrated to convert

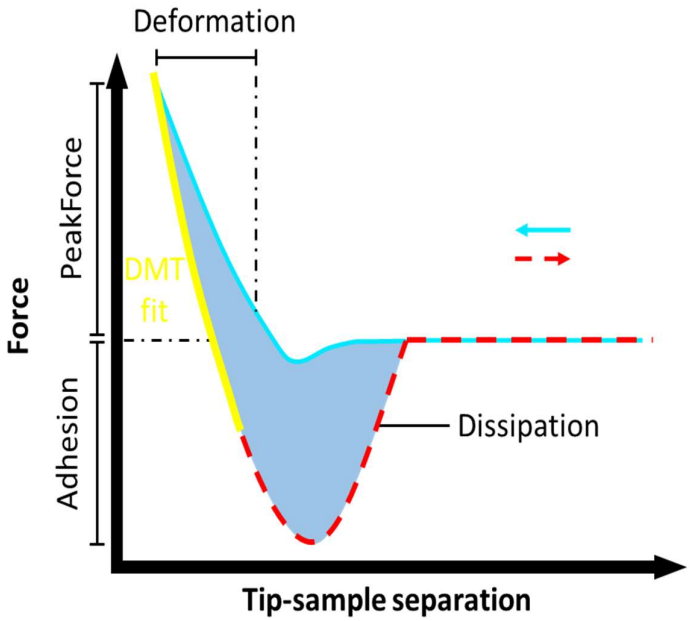

Fig. 1.8: Derivation of mechanical properties from PFQNM. Approach and withdraw indicated by blue and dashed red lines respectively. Sample modulus is derived from fit of yellow region of retract curve to DMT model per eqn. (15). PFQNM also allows derivation of peak force, adhesion, dissipation per tapping cycle and sample deformation when indenting to force setpoint. As PFQNM is force-defined, PeakForce shows the user setpoint plus error signal.

this to force, with the primary calibrations here being for the deflection sensitivity and cantilever spring constant. The deflection sensitivity (nm/V) relates the photodetector signal to real displacement of the cantilever, and is calibrated by ramping the cantilever on an appropriately hard sample relative to the cantilever, with the inverse of the slope of the linear contact region (when plotted as Volts vs displacement) yielding this value. While a number of methods exist for determining the spring constant (N/m), the most widely used is the Sader thermal method[58], whereby a fit of the thermal noise power spectra of the cantilever to a simple harmonic oscillator response with white noise floor

$$A_{white} + \frac{A_0 \ \omega^4}{(\omega^2 - \omega_r^2)^2 + \frac{\omega^2 \omega_r^2}{Q^2}} \quad (4)$$

with cantilever free amplitude A_0, frequency ω, cantilever resonant frequency ω_r and quality factor Q yields both the quality factor Q and resonant frequency ω_r.

For a rectangular cantilever, the spring constant is described by

$$k = M_e \rho_c b \ h \ L \omega_{vac}^2 \quad (5)$$

for normalised effective cantilever mass M_e, cantilever density ρ_c, cantilever thickness, width and length h, b and L respectively and fundamental radial resonant frequency in vacuum ω_{vac}. Application of this equation proves highly challenging however: cantilever density proves difficult to determine due to the deposition of (typically uncharacterised thicknesses of) thin metal films on cantilevers to promote reflectivity of the laser from the cantilever backside; operation of AFM in air rather than vacuum can modulate the resonant frequency from the value measured in vacuum; and cantilever thickness h proves much more difficult to determine than the width and length which are readily measured by optical microscopy.

However, where the quality factor $Q_f >> 1$, as it typically is for a cantilever in air, we can relate ω_{vac} to the resonant frequency in fluid ω_f by

$$\omega_{vac} = \omega_f \left(1 + \frac{\pi \rho_f b}{4 \rho_c h} \Gamma_r(\omega_f)\right)^{1/2} \quad (6)$$

with areal mass density $\rho_c h$ defined as

$$\rho_c h = \frac{\pi \rho_f b}{4} \left[Q_f \Gamma_i(\omega_f) - \Gamma_r(\omega_r)\right] \quad (7)$$

for fluid density ρ_f, and real and imaginary components of the hydrodynamic function Γ. The analytical form of the hydrodynamic function (not provided here for simplicity) is defined by Sader in equations 20-22 of Ref. ([59]).

Substitution of eqns. (6) and (7) into (5) yields

$$k_z = 0.1906\, \rho\, b^2\, L\, Q_f\, \omega_f^2\, \Gamma_i^f\left(\omega_f\right) \quad (8)$$

which then allows the spring constant k_z to readily be derived. Sader et al. later extended this method from rectangular cantilevers only to cantilevers of arbitrary shape[60].

1.4.1 Contact mechanics

Hertz theory can describe the contact between a smooth elastic sphere and a rigid flat sample surface as represented in Fig. 1.9 (a), albeit not accounting for any surface forces or adhesion i.e. assuming $F_{ad} = 0$ [61]. From the geometry of Fig. 1.9, assuming maximum deformation in the contact zone (defined by a contact radius a), we observe

$$(R - \delta)^2 + a^2 = R^2 \quad (9)$$

Assuming that the deformation is much smaller than the contact zone ($\delta \ll a$), we can write

$$\delta = \frac{a^2}{2R} \quad or \quad \frac{\delta}{a} = \frac{a}{2R} \tag{10}$$

where $\frac{a}{R}$ describes deformation of the elastic body. Per Johnson[62], deformation will depend on the stress (described here by average contact pressure $\overline{\mathrm{P}}$) and material stiffness E^* as in

$$\frac{a}{R} \propto \frac{\bar{P}}{E^*} \tag{11}$$

For a spherical indenter,

$$F = \pi a^2 \bar{P} \tag{12}$$

so combining eqns. (11) and (12) yields

$$F \propto \pi E^* \frac{a^3}{R} \tag{13}$$

Using the relation in eqn. (10) and expressing in terms of deformation (readily measured by the indenter system) rather than contact radius, we obtain

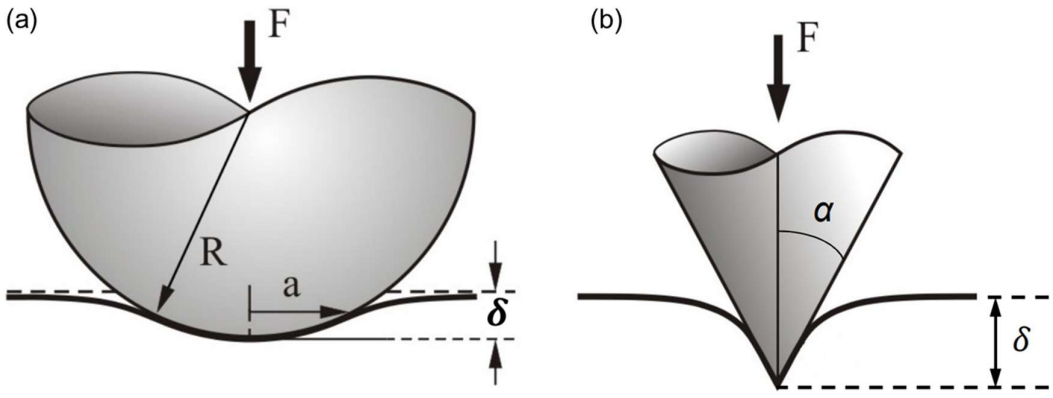

Fig. 1.9: Sketch of contact mechanics models. (a) The Hertzian model can describe contact of a smooth, rigid sphere and a half-plane while the Sneddon model (b) can be used for large-sample indentation with a sharper tip shape. Reproduced from 70.

$$F \propto \pi E^* \sqrt{R \delta^3} \tag{14}$$

While this simple method does not provide the constant of proportionality, it does yield the correct relationship of force with tip radius *R* and deformation δ. A full derivation of the Hertz contact force requiring the solution of Boussinesq's problem[63] (not addressed directly here for simplicity), yields

$$F = \frac{4}{3} E^* \sqrt{R \delta^3} \tag{15}$$

However, this can only describe AFM contacts where the load is sufficiently high or surface forces low[64]. As the AFM tip is typically stiffer than the sample material and sample deformation is not negligible, Sneddon analysis must also be applied as represented in Fig. 1.9 (b)[65]. This describes the force *F* as

$$F^{\frac{1}{2}} = \left(\frac{2}{\pi} \frac{E}{(1 - v^2)} \tan(\alpha)\right)^{\frac{1}{2}} \delta \tag{16}$$

where α is the indenter half-angle used to describe the profile of the indenter.

Combining Hertz and Sneddon deformations can describe the deformation during AFM if surface forces are negligible; otherwise, these surface forces can be considered by Derjaguin-Müller-Toporov (DMT) theory and Johnson-Kendall-Roberts (JKR) theory. DMT considers deformation of the elastic sphere as per Hertz theory, but also accounts for forces acting between the bodies outside of the contact region. The adhesive force F_{ad} is given by

$$F_{ad} = 2 \pi R W \tag{17}$$

with work of adhesion *W*. This can be applied for small tip radii in low adhesion systems with high stiffness[66].

JKR does not consider long range forces outside of the contact area, and accounts only for short-range forces inside the contact area. Here, the adhesive force is given by

$$F_{ad} = \frac{3}{2} \pi R W \quad (18)$$

such that JKR is most applicable for larger tip radii and highly adhesive systems with low stiffnesses[67].

1.5 Nanoindentation

Nanoindentation, developed in the 1970s, allows the measurement of mechanical properties of materials in small volumes[68]. A hard tip, often diamond, is brought into contact with and penetrates a sample to a defined load, with the displacement of the tip and associated load as the most fundamental parameters to be measured. This peak load may be maintained to reduce creep and relaxation effects in the unload, where the tip is brought out of contact at a defined rate.

Sneddon derived a general equation relating load and displacement of

$$P = \alpha h^m \quad (19)$$

For indenter load P and constants α and m, with m defined by the geometry of the indenter[69].

The load-displacement curves captured during indentation, surface deformation and indentation impressions vary depending on the elasticity and/or plasticity of the sample material, as shown in Fig. 1.10 (a). In elastic solids, all deformation of the sample is recovered during unloading with no resulting impression on the sample. In rigid-perfectly plastic solids, plastic flow occurs after the yield stress is reached with no recovery such that the indenter impression is unchanged from the point of peak load even after unloading. In elastic-plastic solids, the material conforms exactly to the tip shape with elastic and plastic deformation during loading, with elastic recovery during unloading then altering the final indent crater shape from the tip shape[70,71].

This is illustrated in Fig. 1.10 (b). Contact depth h_c is the indenter depth as the tip, under load, is in contact with the sample. This is not the same as the measured indentation depth, h, which must also include depression of the sample around the indent caused by elastic displacements, h_s, as per $h_s = h - h_c$. During unloading, elastic deformation is recovered with a final depth h_f observed upon fully withdrawing the tip. These depths are also represented in a sample load-displacement curve on an elastic-plastic material in Fig. 1.10 (c).

In conventional microindentation testing, hardness H (a measure of the material's resistance to local plastic deformation) can be measured by

$$H = \frac{P_{max}}{A_c} \qquad (20)$$

where P_{max} is the maximum load and A_c is the residual indentation contact area. This would also require A_c to be measured by another technique such as AFM, introducing errors for smaller indents.

From load-displacement data (P vs h), stiffness can be derived from the slope of the tangent to the unloading curve

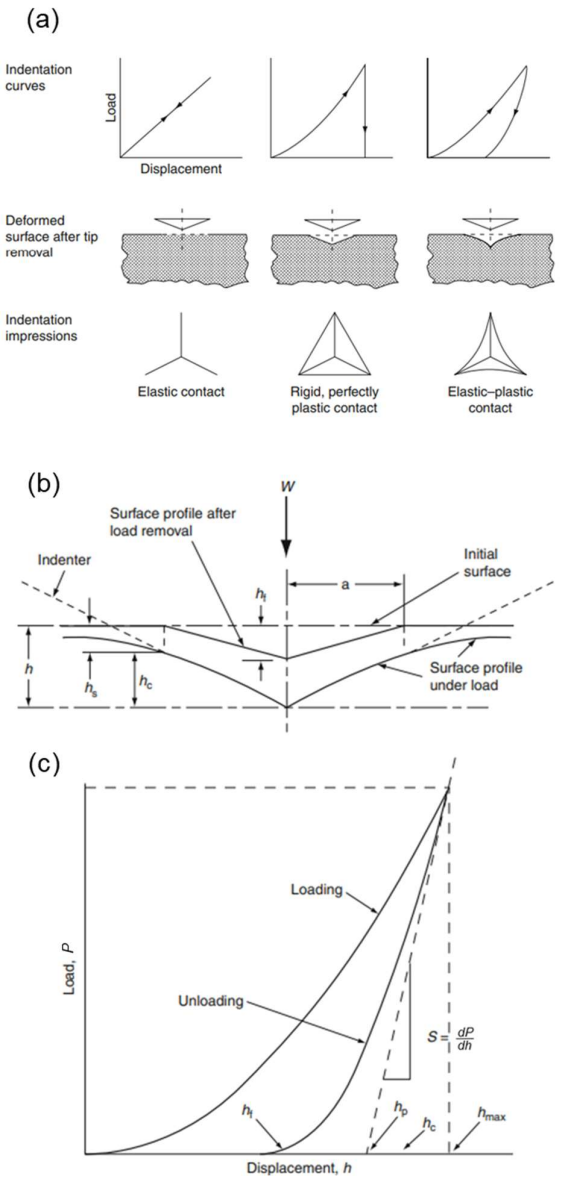

Fig. 1.10: Indentation load-displacement curves and impressions in different materials. (a) Load-displacement, sketch of sample surface deformation and impression after indentation in perfectly elastic, rigid-perfect plastic and elastic-plastic materials respectively from left to right. (b) Schematic of initial surface profile, surface profile during loading and after removing load. (c) Representative load-displacement curve for an elastic-plastic material, with maximum depth h_{max}, contact depth h_c, projected depth h_p and final depth h_f. (a) and (c) reproduced from 70, (b) reproduced from 77.

at the maximum load as in Fig. 1.10 (c) per the Doerner and Nix method[72] introduced in 1986, such that

$$S = \frac{dP}{dh} \qquad (21)$$

A major limitation of nanoindentation as a technique was that a single indent could provide only a single value for hardness and Young's modulus, although these parameters may be depth-dependent, requiring multiple indents at discrete depths on a single sample. This was overcome by the continuous stiffness measurement (CSM) method developed by Oliver and Pethica in 1989[73], depicted in Fig. 1.11. In CSM, a small, fast oscillation is added by applying a dynamic load in addition to the nominally increasing load *P* (as in inset of (a), often with RMS oscillation amplitude of a few nm and frequency between 50-100 Hz[74]). A lock-in amplifier measures the displacement at the excitation frequency and phase angle. This can be considered as applying many indents to few nm depths (orange signal in Fig. 1.11) during the single "main" indent (black signal in Fig. 1.11).[75]

From this, stiffness is measured and hence Young's modulus and hardness can be calculated quasi-continuously during loading at any given indentation depth rather than only a single value from the unload after peak load is attained. CSM also allows for accurate determination of the surface location, where the excitation frequency is selected slightly larger than the natural frequency, such that a strong phase angle response is observed upon the tip contacting the sample[76].

The analysis of Oliver and Pharr from 1992 also revolutionised the capacity of nanoindentation as an experimental technique[77]. At the maximum applied load P_{max}, a maximum depth into the sample of h_{max} is reached, where the permanent residual depth after the load is removed is h_f (the plastic unrecoverable depth), and $(h\text{-}h_f)$ is the elastic recoverable depth, such that the unload curve can be described by

$$P = \alpha(h - h_f)^m \qquad (22)$$

This better describes the unload curve than the linear fit suggested by Doerner and Nix. The contact depth h_c can be obtained by

$$h_c = h_{max} - h_s \tag{23}$$

for elastic surface displacement (or amount of sink-in) h_s, which assuming negligible pile-up is given by

$$h_s = \epsilon \frac{P_{max}}{S} \tag{24}$$

for constant ϵ determined by indenter geometry and stiffness S, in turn yielding

$$h_c = h_{max} - \epsilon \frac{P_{max}}{S} \tag{25}$$

From load-displacement data (P vs h), stiffness can then be derived as per

$$S = \frac{dP}{dh} = \beta \frac{2}{\sqrt{\pi}} E_r \sqrt{A_c} \tag{26}$$

where A_c is the cross-sectional contact area and β is a factor correcting for the nonaxisymmetric shape of the probe, with the *dP/dh* taken from the upper portion of

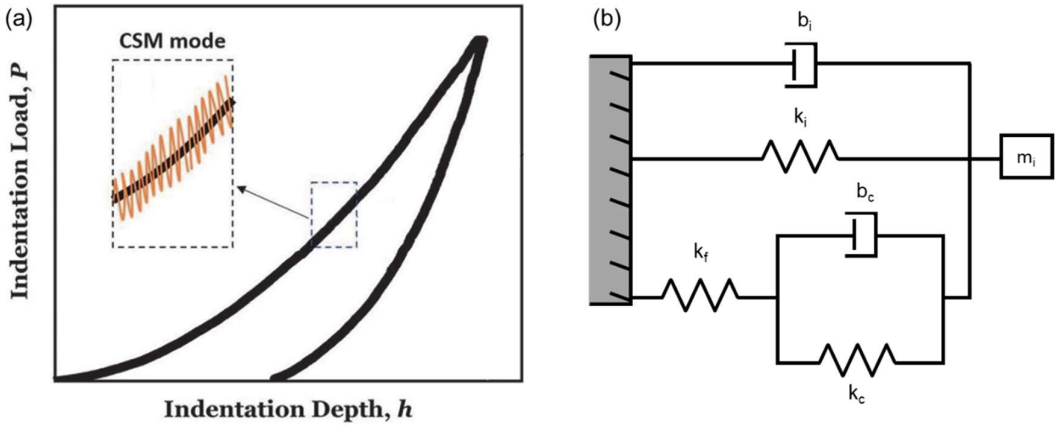

Fig. 1.11: Schematic of continuous stiffness method (CSM) applied to indentation. (a) Rather than evaluating properties such as Young's modulus and hardness only from a single point at unload, these properties can instead be measured quasi-continuously during loading per inset. (b) Schematic of 1D damped harmonic resonator in contact with the sample used in CSM model, with indenter damping and contact damping b_i and b_c, indenter mass m_i, force from electromagnets F, and support, contact and frame spring stiffnesses k_s, k_c, and k_f. (a) reproduced from 75.

the unloading curve and having defined a reduced modulus, E_r by

$$\frac{1}{E_r} = \frac{(1-\nu^2)}{E} + \frac{(1-\nu_i^2)}{E_i} \tag{27}$$

where E and E_i are the Young's modulus for the sample and indenter respectively, and similarly ν and ν_i are the Poisson's ratio for sample and indenter respectively. Hardness can then be determined as per eqn. (20).

The above is valid for any axisymmetric indenter and for both elastic and elastic-plastic contact, with the β factor introduced above ranging from 1.0226 to 1.085 for a Berkovich tip[74]. The Berkovich tip is a self-similar three-sided pyramid with 65.27° half angle and included angle of 142.3° shown in Fig. 1.12. It is widely used in nanoindentation as it can be readily manufactured to a sharp point, induces plasticity at very small loads and its well-defined geometry allows for determination of cross-sectional contact area from indentation depth h_c per

$$A(h_c) = C_0\, h_c^2 + C_1\, h_c^1 + C_2\, h_c^{1/2} + C_3\, h_c^{1/4} + \ldots + C_8\, h_c^{1/128} \tag{28}$$

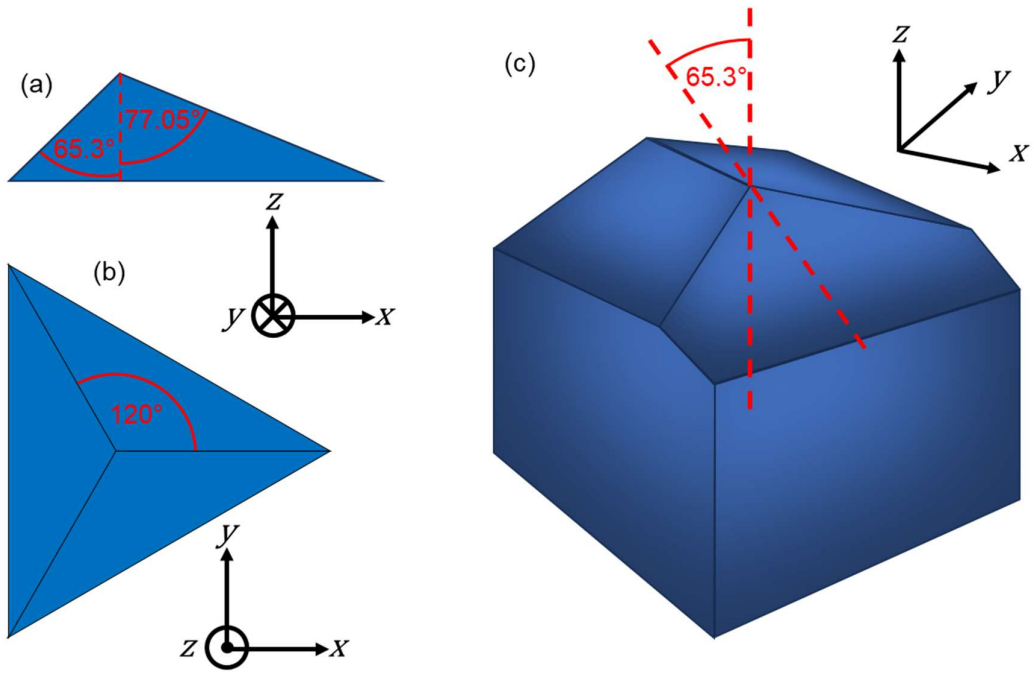

Fig. 1.12: Sideview (a), plan view (b) and 3D isometric view (c) of Berkovich tip, with ideal semi-angle α of 65.3° and total included angle of 142.3° indicated. Some degree of rounding at the end of the tip is likely, diverging from the ideal contact area geometry.

with leading coefficient C_0 of 24.56, where the subsequent terms account for deviations in the real geometry, such as rounding of the tip from grinding during manufacturing or wear during use, with experimentally determined calibration constants C_n.

Contact compliance C_c can be defined by

$$C_c = \frac{dh}{dP} = \frac{\sqrt{\pi}}{2\,E_r\,\sqrt{A}} \tag{29}$$

However, elastic displacements of the system load frame must also be accounted for by machine compliance C_m, where total compliance C_{total} is given by

$$C_{total} = C_m + C_c = C_m + \frac{\sqrt{\pi}}{2\,E_r\,\sqrt{A}} \tag{30}$$

A plot of C_{total} against $A^{-1/2}$ at varying depths then yields the machine compliance C_m as the y-intercept and contact compliance C_c as the difference in measured C_{total} and determined C_c. This is also used to determine the area function coefficients from eqn. (28) by indenting on a reference sample with well-known values for the elastic modulus and Poisson ratio, such as aluminium, by successive fitting of the area function until convergence of the value of C_m is achieved[78].

1.5.1 2-Dimensional Indentation

Indentation is performed with two devices in this work: a Bruker Multimode 8 AFM and KLA's Gemini dual-axis nanoindenter (Nanomechanics Inc., Oak Ridge, TN). In contrast to conventional 1D nanoindenters which represent almost all research in this field, the Gemini features two independent indenter heads, each with an actuator (i-Micro) mounted along the x and z axes as indicated in Fig. 1.13 (b), with schematic of a single actuator in Fig. 1.13 (a)[79]. Both vertical and lateral heads are mounted on an aluminium frame as in (b) and are independent of one another. The vertical and lateral actuators

can apply forces simultaneously of up to 50 mN in z and x direction respectively. Forces are applied by the electromagnets in the actuator heads and displacements are measured by a three plate capacitance gauge within the actuator. As the shaft moves under the force of the electromagnet coil, the plate attached to the indenter shaft (blue in Fig. 1.13 (a)) experiences an identical displacement indicated by the red arrows in (a). This results in varying capacitance between the moving indenter shaft plate (blue) and the fixed upper and lower capacitor plates (green in Fig. 1.13 (a)), from which displacement can be directly measured. Load resolution in nN ranges and displacement in pm ranges can be acquired, though this requires thermal stability as well as vibration and noise isolation. This isolation is provided in the Gemini system by mounting in a self-contained cabinet mounted on an air table, which in turn is mounted on a concrete plinth (≈ 1 m × 1 m × 1.5 m). The support springs/leaf springs ensure high resistance to torsional motion and to linear motion in axes other than the x axis for the x actuator and z axis for z actuator.

Both actuators are securely fixed into stable position in the indenter frame, with vertical frame stiffness of this system of $\approx 10^6$ N/m and lateral stiffness of $\approx 10^5$ N/m[80]. The indenter heads are connected to the tip mounting block by glass coupling plates, with dimensions of 1.5 cm × 0.5 cm × 0.1 cm per Fig. 1.13 (b). The glass coupling plates meet at the tip mounting block where the indenter tip, mounted on the head of a screw, is locked into place in the block. Sites on the sample to be indented are surveyed by digital camera/optical microscope. Calibration of the distance travelled by the stage from microscope to indenter position is performed with reference to an array of test indents to ensure that the chosen locations are indented.

2-dimensional indentation, with actuators in both x and z axes, crucially allows for measuring of friction and application of a lateral oscillation during normal indentation. An independent phase lock-in amplifier for each actuator allows for both vertical and lateral contact stiffnesses to be continuously measured by the CSM method described above[77].

The lateral and vertical components of the indenter are modelled as independent, damped simple harmonic oscillators. The stiffness can then be measured continuously

and independently in both axes.

The total spring stiffness K_{tot} is given by

$$K_{tot} = \left[\frac{1}{K_f} + \frac{1}{K_c}\right]^{-1} + K_i \tag{31}$$

with frame stiffness K_f, contact stiffness K_c and indenter support spring stiffness K_i. Contact stiffness is therefore provided by

$$K_c = \frac{K_f\ (K_{tot} - K_i)}{K_f - (K_{tot} - K_i)} \tag{32}$$

Load on the sample in the lateral (x) direction P_x is described by

$$P_x = F_x - k_x\ (d_x - d_0) \tag{33}$$

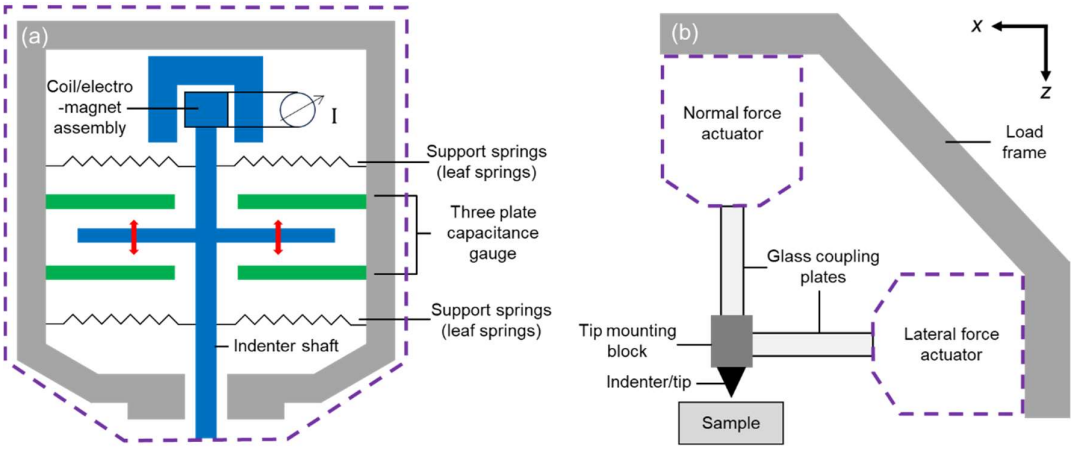

Fig. 1.13: Schematic of Gemini nanoindenter. (a) Schematic of the actuator heads (identical for normal and lateral force actuators) arranged as indicated in (b), where the electromagnetic assembly applies forces on the indenter shaft and displacement of the shaft is measured by three-plate capacitance gauge. Leaf springs act as support. Two actuators, as indicated in schematic in purple dash outline in (a), are arranged perpendicular in x and z axes in the 2D Gemini system in (b). Actuators are connected to tip mounting block by glass coupling plates, with tip attached to mounting block. (c) Labelled image of Gemini system.

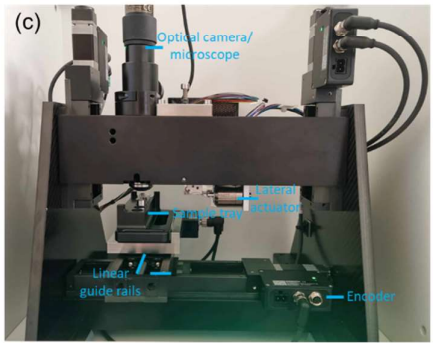

with lateral force applied by the x-axis actuator F_x, stiffness of the indenter shaft k_x, normal position of the tip as measured by the three-plate capacitance gauge d_x and position prior to application of force by the actuator d_0.

In the InQuest controller used, the force and oscillating force are separately defined by the PC, submitted to two separate digital-to-analog converters (DAC1 and DAC2 respectively), with these signals then combined before being fed to the actuator, which in turn outputs the combined displacement and oscillating displacement to the analog-to-digital converter which resolves the separated displacement and oscillating displacement. A photograph of the system (excluding controllers and lock-in amplifiers) is provided in Fig. 1.13 (c).

During indentation, while existing standards and practice indicate that a minimum spacing of 20 times the depth of the indent should be maintained between indents[81], this has recently been demonstrated to be unnecessarily large. Instead, a spacing of only 10 times the indent depth or greater is sufficient to avoid interactions between neighbouring indents for a Berkovich geometry[82], and strict separation of the plastic zones is not required, which will inform indent spacing in this work. With indentation in our samples typically ranging from normal loads of 0.1 mN to 45 mN, corresponding to depths of ≈20 nm - ≈300 nm in SiO_2 substrates, indent spacing is typically maintained at 3 – 10 μm between indents as we must also consider interactions between the auto-kirigami ribbons nucleated during indentation in our work (described in section 1.6).

1.5.2 AFM based indentation

Nanoindentation can also be performed by AFM systems, albeit with a number of limitations such as that AFM-based indentation data is often qualitative rather than quantitative due to complex spring/mass combinations and degrees of freedom of motion, hindering precise calibration of the forces applied[83]. An especially stiff cantilever is used, often of metal foil such as stainless steel or single crystal diamond

rather than the silicon or silicon nitride used in most AFM cantilevers, with a high spring constant of up to 500 N/m and diamond tip. These cantilevers are also thicker, longer and wider than standard AFM imaging cantilevers (13 × 350 × 100 µm for the DNISP probe used for this purpose in this research). This allows normal loads of ≈1-1000 µN to be applied. The cantilever deflection measured by the photodetector (V) and piezo scanner displacement (*z*) are recorded. Cantilever deflection voltage can be converted to deflection as a distance (δ)(nm) by the deflection sensitivity (nm/V) measured by the in-contact repulsion of the cantilever on a sufficiently hard sample (such as sapphire). The AFM tip displacement *h* is then determined by

$$h = z - \delta \tag{34}$$

which can hence be converted to load by the calibrated cantilever spring constant (N/m)[84,85].

The surface contact point is determined by variation of the oscillation amplitude of the cantilever beyond a defined setpoint after an initial fast approach to the defined lift height from the surface. The loads attainable by AFM are 2 orders of magnitude lower than the loads achievable in both axes using the KLA Gemini system, and 3 orders of magnitude lower than in purely 1D indentation in the same system using an alternative indenter head. AFM tips used in nanoindentation must be carefully oriented on the cantilever to compensate the few degree (typically 12°) angle of the cantilever beam relative to the horizontal after mounting in the AFM, with AFM tips typically oriented perpendicular to the cantilever. To correct for this and to prevent ploughing of the surface by the tip in the direction of the main tip axis (+X direction) or the tip pitching forward, the piezo scanner tube moves the sample in the opposite direction during indentation. This ploughing can arise from cantilever bending during indentation or movement in the +X direction arising from X-Y coupling of the piezo scanner. Pitching of the cantilever can also move the laser spot such that the laser beam experiences less deflection at the photodetector than it should at a specific force, resulting in deeper indentation. This will be considered in greater detail in section 3.2.

1.6 Graphene self-assembly/auto-kirigami

Nanomaterial synthesis can broadly be grouped into two classes: top-down and bottom-up. In top-down synthesis, the final product is obtained by removal from the bulk by exfoliation or fragmentation for example, while in bottom-up synthesis nanoscale chemical or physical forces assemble the final structure through methods such as aggregation or self-assembly.

A novel example of such graphene self-assembly was reported by Annett et al. in 2016, there referred to as graphene ribbons. A sample graphene ribbon imaged by AFM is shown in Fig. 1.14 (a), with schematic in (b) and sideview sketch in (c). To avoid confusion with graphene nanoribbons, we here apply the terminology "auto-kirigami" to refer to the self-assembly and growth process and auto-kirigami ribbon (also AK-ribbon or ribbon for simplicity in this text) to an individual resulting self-assembled structure. Here, "auto" refers to the spontaneous, self-assembling nature of this process, while "kirigami" is a variation of the practice of origami, whereby complex three-dimensional designs can be produced only by folding a two-dimensional sheet, though kirigami specifically also allows cutting of the sheet (*kiri* meaning "to cut" and gami derived from *kami*, meaning paper.

In their work, Annett et al. performed nanoindentation on few-layer mechanically exfoliated graphene sheets on 300 nm SiO_2/Si substrates with an applied small amplitude (≈1 nm) lateral oscillation at high frequency in ambient conditions. We will refer to this method as small amplitude sheared indentation nucleation (SASIN) throughout. This resulted in the spontaneous growth of self-folded ribbons to micrometre-scale lengths with high yield (>70%), with the lateral oscillation specifically judged to be crucial to the nucleation as no ribbons were observed in its absence. These ribbons typically featured straight edges with a constant inward taper angle as in Fig. 1.14 (a), and a final width characteristic of the number of graphene layers (from ≈290 nm for single layer to ≈490 nm for three layer).

Annett et al. proposed that the growth mechanism arose from a thermodynamic exchange of graphene-substrate area with graphene-graphene area, sufficient to

overcome the tearing resistance of the graphene sheet, sliding resistance between ribbon and underlying sheet as well as the strain energy of the resulting fold. Using Griffith-style elastic fracture analysis[86], the internal energy was described by

$$U = U_{fold} + 2\lambda c + \Delta W_{2D-s}\,(A_{sheet} - A_{ribbon}) - \Delta W_{2D-2D}\,(A_{ribbon}) \quad (35)$$

where U_{fold} is the fold strain energy, λ is the rupture energy per unit length of the torn graphene sheet (assumed isotropic with respect to crystallography), c is the tear path length assumed identical for both tears, A_{sheet} and A_{ribbon} are the areas of the sheet and ribbon respectively, and $\Delta W_{2D\text{-}s}$ and $\Delta W_{2D\text{-}2D}$ are the adhesion energies of the sheet to the substrate and of the sheet to itself respectively.

Neglecting friction, the fracture energy release rate per increase in tear path length δc for each tear can be derived as

$$\frac{\partial U}{\partial c} = \frac{\partial U_{fold}}{\partial w}\frac{\partial w}{\partial c} - (\Delta W_{2D-2D} - \Delta W_{2D-s})\, w \frac{\partial l}{\partial c} + 2\lambda \quad (36)$$

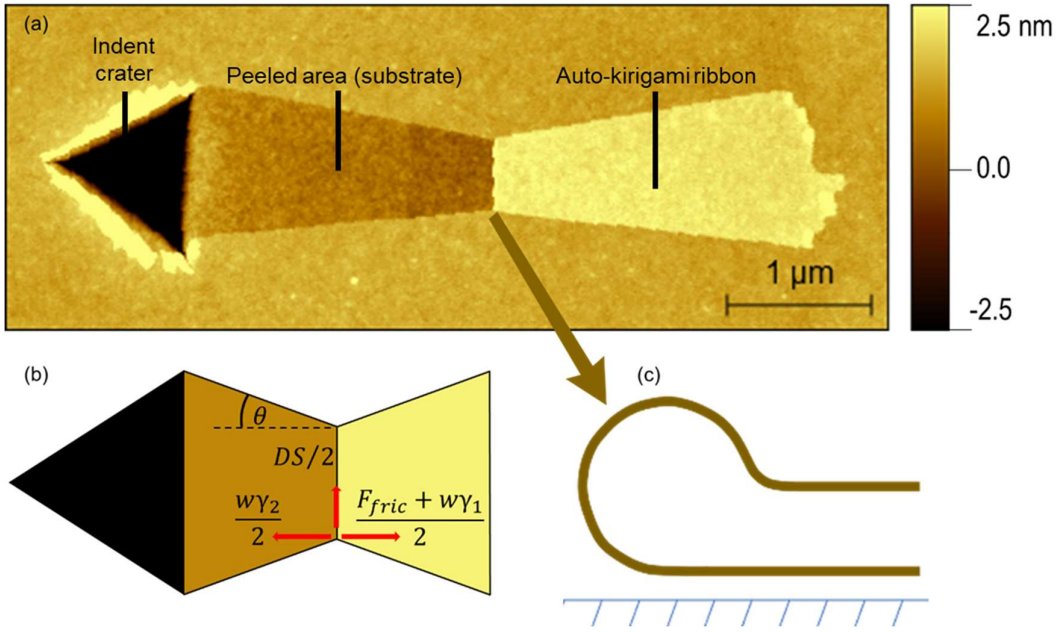

Fig. 1.14: AFM and sketch of representative graphene auto-kirigami ribbon. (a) AFM topography of a ribbon in bilayer graphene with indent (black), peeled area of exposed substrate (brown) and folded ribbon (yellow). (b) Sketch of the forces described in eqn. (37) indicating driving, resisting and inward tapering forces. (c) Sideview sketch of the fold.

where the length and shape of graphene unadhered in the fold becomes constant such that $U_{fold} = U_{fold}(w)$ only. Under quasi-static, end-of-growth conditions, the energy release rate must be 0. From the geometry of the system as defined in Fig. 1.14 (b), we note that $(\delta l/\delta c) = cos\,\theta$, $(\delta w/\delta c) = -2sin\,\theta$ and by requiring the sum of the forces to be identical at each crack tip we can write that

$$F_{advance} = \frac{\Delta W_{2D-2D} \cdot w\, cos\theta}{2} + D\, S\, sin\theta = \frac{\Delta W_{2D-s} w \cdot cos\theta}{2} + \lambda = F_{resist} \quad (37)$$

or that at each crack tip in the direction of ribbon growth

$$\frac{(\Delta W_{2D-2D} - \Delta W_{2D-s})w}{2} = \lambda cos\theta \quad (38)$$

The tear is expected to take the path of minimum force by maximising the energy release rate[86], so taking the derivative of eqn. (37) with respect to θ yields

$$\tan\theta = \frac{F_{fold}}{F_{int}} = \frac{2DS}{(\Delta W_{2D-2D} - \Delta W_{2D-s})\, w} \quad (39)$$

where θ is the taper half-angle.

With all terms on the right-hand side of eqn. (39) constants, this indicates that the taper half-angle should also be a constant, which is indeed observed experimentally. However, this analysis specifically neglected to include friction, implying that any friction term that would act to impede growth which would be represented in the denominator must be negligible. This contribution by friction will be examined further in Chapter 2. This analysis can also provide further insight into the growth dynamics of the ribbon: although a positive driving force is obtained by the exchange of graphene-substrate contact area for graphene-graphene contact area, ribbons near universally narrow to a terminal width rather than widening. This can be attributed to the tendency to reduce the fold strain energy, described by

$$DS = \lambda\, sin\,\theta \quad (40)$$

along the fold direction, which manifests as the constant inward taper angle observed. This reduction in fold width in turn limits the driving interfacial force as smaller areas of contact are exchanged per unit δl of ribbon growth. This is also consistent with the final widths being characteristic of the layer number, where tearing resistance increases with layer number. We note here that the description of the energy release rate from eqn. (36) did not account for friction, but that the constant taper angle in the derived eqn. (39) nonetheless agrees well with our experimental observations. As wear is not observed of the flake or ribbon during sliding, this resistive force could be specifically interfacial friction[87], arising purely from the shear resistance at the interface, which is directly proportional to the interfacial contact area A as $F_{fric} = \tau \cdot A$ for interfacial shear strength τ [88]. However, as the contact area increases with growth of the ribbon, F_{fric} would then increase resulting in an evolving taper half-angle θ, which is not experimentally observed, implying that friction here is negligible i.e. $F_{int} \gg F_{fric}$. Incommensurate stacking of ribbons was also confirmed by Annett et al. by Raman spectroscopy[89], consistent with structural superlubricity. These ribbons therefore represent several square micron areas of twisted graphene (or ≈1 femtogram mass of graphene) in superlubric contact, albeit tethered to the underlying flake by the fold.

This description is also purely isotropic and does not account for the anisotropy of graphene due to crystallography for example which is expected to impact the tearing resistance along different crystallographic directions. This anisotropy can be described by

$$\lambda(\alpha) \;=\; 2\,\lambda_{AC}\,sin(\alpha) \;+\; 2\,\lambda_{ZZ}\,sin(30 - \alpha) \qquad (41)$$

for angle from the nearest zigzag direction α, and rupture energies per unit length along armchair and zigzag directions λ_{AC} and λ_{ZZ} respectively.

While we occasionally observe double-folding at the end of a ribbon (especially if the growing ribbon head encounters an obstacle such as a flake edge or step), we have not observed scrolling behaviour resulting from SASIN.

Júnior et al. carried out LAMMPS molecular dynamics simulations of graphene sheets (without substrates) showing that even with initial parameters of an armchair edge

folded graphene sheet scrolled to 2π radian twist angle (i.e. a full folded "circle" at the edge), that the scroll will unfurl to form a simple folded bilayer instead[90]. This is attributed to the interlayer van der Waals interactions in the flake being too weak to overcome the bending rigidity of the single layer graphene sheet. Twist angles of 3π and greater of the armchair edge folded graphene were necessary to observe further scrolling of the sheet to produce graphene nanoscrolls.

Initiating a simple 2π radian twist angle scroll structure would result in increased bending energy required to form this structure while decreasing graphene-substrate adhesion with no direct graphene-graphene adhesion achieved. However, as in Júnior et al.'s simulations, a nanoscroll with a greater degree of folding (≥3π) may benefit from the minimal frictional losses of graphene-graphene contact and enhanced graphene-graphene contact areas (of both sides of the sheet of interior folds and the inner side of the outermost sheet compared to only the lower and upper of the upper and lower sheet respectively in a simple folded structure). The requirement for a ≥3π radian twist angle appears unlikely to be spontaneously formed by SASIN, where the effect of the oscillating indenter tip on the torn graphene edge during indentation and unloading is difficult to characterise.

Experimentally, scrolling of graphene edges has been achieved for example by ultrasonication of graphite in dimethylformamide[91], freeze-casting of reduced graphene oxide[92] and by intercalation of various species, including IPA[93] and KC_8[94]. In MD simulations, Zhang et al. demonstrated spontaneous formation of carbon nanoscrolls initiated by a separate carbon nanotube placed on the edge of a supported graphene monolayer[95], further indicating that the initial configuration of the folded graphene sheet necessary for scrolling to occur spontaneously is highly significant.

Despite the potential of large-area superlubric contacts, with applications as sensors or actuators as a novel class of nanoelectromechanical systems (NEMS), few simulations and fewer experimental studies have been reported on these auto-kirigami ribbons in the intervening near decade since original publication of these results. We can ascribe two broad reasons for this lack of experimental results. Firstly, the strict requirement of lateral oscillation during indentation for successful ribbon growth (over 70% yield with oscillation and 0% without) motivates use of two- or three- dimensional indentation.

For example, the nanoindentation system used to nucleate the ribbons in the original publication is a wholly novel three-dimensional nanoindenter, of which no other commercial or indeed custom-built equivalents are known to us. While two-dimensional nanoindenters such as KLA's Gemini described above are commercially available, we have observed exceedingly few publications using this device (indeed only in one other research group). While the necessary lateral oscillations could instead be introduced by the use of an appropriate shear piezoelectric chip, the Gemini system retains the considerable advantage of also monitoring lateral signals such as stiffnesses for example which may provide further useful information on the nucleation mechanism as we will discuss in section 3.3. This also motivates the exploration of alternative methods of ribbon nucleation not requiring such highly specialised devices, as will be covered in 3.2.

Secondly, study of these ribbons is uniquely hampered by statistics. The original publication reported over 100 ribbons nucleated, all in few-layer mechanically exfoliated graphene. With ribbons lengths readily achieving several microns and typical graphene flake dimensions in the study rarely exceeding 20-30 microns, the number of ribbons achievable on a single flake could be as few as ≈20 even with optimal placement of indents on the flake. This strongly motivates application of auto-kirigami in CVD 2D materials, as reported in Chapter 4.

While broader studies can be considered with ensembles of ribbons nucleated across multiple flakes, whether on the same substrate chip or separate, it is difficult to control or even to directly measure variation that could exist between such samples. Indents are placed without consideration of the anisotropy of graphene, such that the direction of ribbon growth (which is typically broadly perpendicular to the side edge of triangular indent crater), and associated tears (which can be estimated to be at equal, few degree offsets from this direction tapering inwards) cannot readily be chosen by the operator except by rotation by hand of the sample. Even where crystallography could be determined prior, as indent positions must be selected purely from optical imaging, errors of several degrees would be likely if using a flake edge for example as a reference. While this would be equivalent for many indents on a single flake with defined crystallography, this could not be controlled across different flakes. Also, the interfacial

force which drives ribbon growth arises from a difference in adhesion energies ($\Delta W_{2D-2D} - \Delta W_{2D-s}$); a variation in these adhesions could arise from contamination of the substrate surface prior to or during exfoliation, or contamination on the graphene surface, which would then be expected to strongly influence ribbon growth. This could arise from exposure time of substrate to the atmosphere prior to exfoliation for example or varied cleaning methods which have been observed to influence the water contact angle (WCA). WCA in turn allows calculation of the surface free energy which determines adhesion[96]. This may also arise from the presence of unclassified airborne hydrocarbon contaminants, where strong variation in WCA is observed with time from exfoliation attributed to these contaminants and even from different materials of storage containers[97,98]. These parameters also prove difficult to directly measure on individual mechanically exfoliated flakes.

Qualitatively similar folded structures have been studied by Rode et al. Twisted bilayer graphene (TBG) samples are obtained by chance in small numbers following exfoliation, as well as by cutting with an AFM tip applying µN forces to produce trenches, which may induce folding and nucleate ribbons from their torn edges. This growth mechanism is attributed to the same interfacial force described above following "flip-over" of the edge graphene by the AFM tip[99]. Following from the observation that straight edges of graphene flakes are often armchair or zigzag, interlayer rotation angle (or twist angle) θ can be calculated as $\theta = 2 \cdot \phi$, where ϕ is the angle between the folded and reference straight edge. This is depicted as applied to a graphene flake image by AFM and schematically in Fig. 1.15 (a) and (b) respectively. Among other results, they reported a variance in interlayer distance with twist angle in TBG, where rather than well-

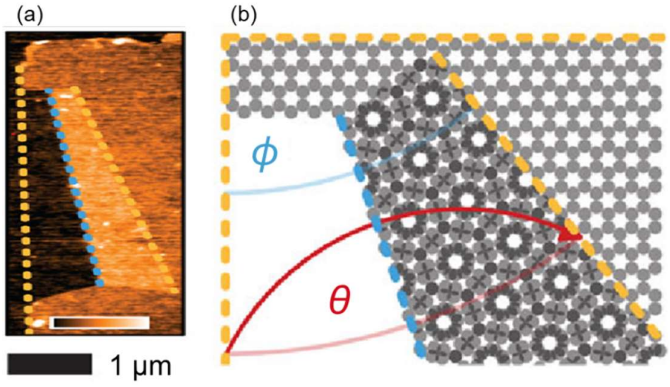

Fig. 1.15: Geometric determination of graphene twist angle. Angles are measured of the initial sample edge and new edge of folded area (yellow dashed lines), as well as of fold direction (blue dashed line) as shown on AFM topography image in (a) and schematically in (b) with defined angles θ and ϕ. Reproduced from 99.

established invariant interlayer distance of 0.34 nm, the distance may be as high as 0.63 nm at select twist angles. We note however that this arises from a sample size of only 16 folds over the 30° angle range and that such variations in height have not elsewhere been observed to our knowledge, although deviations of a few angstroms have been attributed to AFM tip morphology or even up to ≈1 nm to AFM scan parameters in tapping mode which may not adequately penetrate a capillary water layer for example[100]. While AFM cutting is higher yield than random folding from exfoliation, both methods prove to have very low throughput with sample sizes per publication comparable to the number of ribbons that can be produced by the oscillatory shear nanoindentation method in as little as a few hours. They also obtained Moiré pattern resolution on TBG by lateral force imaging using an AFM scanner restricted to 1 μm scan sizes[99]. From this Moiré pattern, twist angle θ can be determined from the observed moiré superlattice wavelength λ_M by[101]

$$\lambda_M = \frac{(1+\delta)\,\alpha}{\sqrt{2\,(1+\delta)(1-cos\,\theta)+\delta^2}} \tag{42}$$

for the general case assuming a heterostructure with lattice mismatch δ, graphene lattice constant α (with α = 0.246 nm). In TBG with no lattice mismatch, this simplifies to

$$\lambda_M = \frac{\alpha}{2sin\left(\frac{\theta}{2}\right)} \tag{43}$$

Rode et al. also reported that, unlike the established trend of monotonically decreasing friction for increasing layer number of graphene from 1 to 5 layers, friction on TBG is in fact greater than that of both AB stacked bilayer graphene and single layer graphene, with significant variation from ≈1 to ≈1.5 times the normalised friction on single layer measured on these TBG samples[102]. This variation is attributed to frictional anisotropy due to the hexagonal superlattice moiré pattern, which they explain by local Moiré corrugations increasing surface area, local detachment of the upper layer in response to the tip and increased ductility of the TBG compared to Bernal, all contributing to

interlayer superlubricity in fact enhancing friction at the TBG surface. We note that these TBG frictions were determined relative to an adjoining monolayer graphene area and as such that crystallography of the sample was not accounted for in these reported values and that relative angle of AFM fast scan axis and crystallographic direction was not controlled for. They further report an exponential dependence of fold radius with length of the fold, which from Annett's model would alter the fold strain energy, with lengths studied (up to 2 µm) covering a majority of the range of widths possible in ribbons nucleated by nanoindentation (typically from a lower limit of ≈0.2 µm at end of ribbon growth to ≈3 µm defined by length of the Berkovich tip crater side at maximum normal load of 50 mN). The smallest fold radii of ≈2 Å (such that the diameter is near indistinguishable from interlayer spacing of 3.4 Å) corresponding to fold lengths of ≈0.25 µm is not replicated in our studies where a "bump" of the fold is always observed, as with Chen et al. as well[32]. Sample sets in a publication include 16 ribbons on 7 different flakes on 6 different substrates[103], which may introduce considerable variance in adhesion energies for example as all experiments are performed under ambient conditions.

The model of ribbon growth driven by exchange of adhesion has been supported and reproduced by a number of molecular dynamics simulations. Tearing and folding behaviour has been studied using the adaptive intermolecular reactive empirical bond order (AIREBO) potential in large-scale atomic/molecular massively parallel simulator (LAMMPS) to describe the carbon atom interactions[104–106], and folding of entire graphene sheets in fully-atomistic MD simulations using the ReaxFF[107] potential in LAMMPS[108]. Fonseca et al. specifically set an initial crack edge within the flake as either zigzag or armchair as in Fig. 1.16. We note in experimental cases that the crystallography

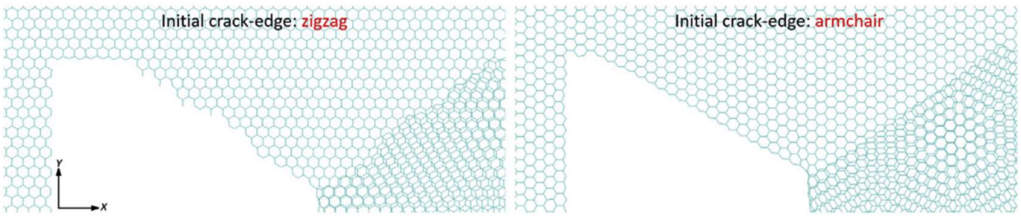

Fig. 1.16: MD simulation of auto-kirigami ribbon tearing and folding. Tearing occurs along different crystallographic directions with differently chosen initial crack edge direction. Reproduced from 105.

of the crack edge is not controlled, so these restricted initial edges may limit results substantially. With a simulation box is 100 × 200 × 10 nm and a crack edge length of 80 nm (less than half of a typical indent edge length) though this proves sufficient to reproduce graphene tearing and ribbon folding at 300K[105]. This simulated tearing is not symmetric as it appears experimentally however, and extends for no more than 5 nm over several nanosecond timescales. Thermal fluctuations were found to either favour or inhibit the folding depending on their magnitude[106]. Increasing temperature from 300 to 600 K increased the rate of bond breaking and ribbon propagation velocity, comparable with increased ribbon growth shown by Annett et al., though even higher temperatures of 1000K resulted in carbon-carbon bond formation between layers, preventing growth.

He et al.[104] incorporated a substrate, with the fold created by establishing two initial parallel cracks in the graphene sheet, lifting the flap edge in the *z* direction, displacing the flap in the *x* direction and then allowing the system to relax, resulting in self-folded graphene, with initial widths up to 256 nm. He et al. also studied the effect of varying by graphene-substrate adhesion energy by 3 orders of magnitude from 0.004 to 5 J/m^2. Increased graphene-substrate adhesion resulted in larger taper angles, and tear edges are not straight or mirror symmetric in the bilayer case. A scaling law for tapering angle in monolayer samples is derived as

$$sin\theta \approx \left(\frac{\Delta W_{2D-s}}{\Delta W_{2D-2D}}\right)^{0.1} \quad (44)$$

and for bilayer samples

$$sin\theta \approx \left(\frac{\Delta W_{2D-s}}{\Delta W_{2D-2D}}\right)^{0.5} \quad (45)$$

From their study, they concluded that self-assembly could be controlled by substrate adhesion, temperature and number of layers, facilitating origami- or kirigami-like folding.

We note that none of the above studies introduce gaseous species that would be present during tearing, although these species would likely bond with the carbon atoms now available after the carbon-carbon bond breaking. Huang et al. demonstrated that chemomechanical conditions can regulate the fracture path in tearing monolayer graphene, where a graphene nanoribbon produced by tearing in vacuum or in hydrogen environment displays armchair edges, whereas the sheet fractures along a zigzag direction in oxygen environment[109].

1.7 Conclusions

In this chapter, we have reviewed the materials (primarily graphene), concepts (superlubricity, self-assembly and auto-kirigami), and experimental techniques (mechanical exfoliation, chemical vapour deposition, atomic force microscopy and nanoindentation) fundamental to this study on 2D material self-assembly.

In Chapter 2 we will consider a crucial complication to the picture of graphene as presented above: a self-assembled stripe adsorbate of environmental origin that is present ubiquitously on graphene surfaces. We also reveal that this adsorbate is present not only on graphene surfaces, but also within graphene-substrate interfaces and graphene-graphene interfaces, with significant implications for superlubricity in auto-kirigami ribbons.

Currently, reliable auto-kirigami nucleation is available only by SASIN, requiring a highly specialised indentation system of which only two are known in the world. In Chapter 3 we will examine methods of auto-kirigami nucleation, including existing 2D indentation methods such as SASIN and a novel AFM-based method of nucleation developed in this work which significantly extends the capacity and ease of production of auto-kirigami. We will also consider auto-kirigami nucleation in other 2D materials and the process of graphene rupture during indentation.

Scaling up of the area of 2D materials on which auto-kirigami ribbons can be manufactured is necessary to development of ribbons for application outside of

laboratory settings and to obtaining greater statistical strength. Therefore, in Chapter 4 we will perform indentation on CVD-produced 2D materials, with successful albeit limited auto-kirigami nucleation in these materials.

In Chapter 5 we will discuss methods to control and reverse ribbon growth towards development of ribbons as nanoelectromechanical devices, as well as a novel frequency dependent, electrically induced erosion of graphene sheets.

Finally in Chapter 6 we will summarise these findings within the context of this entire body of research, as well as highlighting miscellaneous phenomena discovered in this work requiring further investigation and the next anticipated experimental work inspired by these findings.

Chapter 2: Stripe adsorbates

2.1 Introduction

Many of the superlative properties of graphene can be modified by the presence of ambient environmental contaminants[110]. However, this has received relatively little attention in the overall field of 2D materials despite its wide-reaching implications for any devices prepared or operated outside of ultrahigh vacuum conditions, such as auto-kirigami ribbons for example.

In this chapter, we will firstly use AFM to detect and observe a recently discovered self-assembled stripe adsorbate ubiquitously present on graphene surfaces exposed to ambient conditions. This adsorbate is shown to modify the measured friction of graphene and is further revealed to be present at the graphene-graphene interface of auto-kirigami ribbons. However, auto-kirigami ribbon growth occurs successfully despite the presence of this adsorbate, from which we will derive an upper bound of frictional shear force, indicating that superlubricity can nonetheless exist in the presence of this adsorbate.

Furthermore, ribbons represent a unique method to access and to investigate graphene interfaces as these interfaces can become revealed with folding. We will exploit this to reveal that stripe adsorbates are present at graphene-substrate interfaces and buried graphene-graphene interfaces as well, with significant implications on the cleanliness and operation of van der Waals heterostructure devices. We also provide insight into stripe formation and dynamics by demonstrating how stripes can interact with surface features and with themselves.

2.2 Stripes on graphene surfaces

It has long been understood in the field of surface science that any surface exposed to atmosphere will rapidly become covered in contaminants[111,112]. The incident molecular flux onto a surface can be described by the Hertz-Knudsen equation as

$$\mathrm{F} = \frac{\alpha P}{\sqrt{2 \pi m k_B T}} \tag{46}$$

for flux *F (molecules m^{-2} s^{-1})*, anomalous evaporation coefficient α *($0 \leq \alpha \leq 1$)*, gas pressure at the surface *P (Pa)*, molecule mass *m (kg)* and temperature *T (K)*. Assuming a sticking coefficient of unity, at standard temperature and "rough" pressures of 1×10^{-4} – of 1×10^{-6} mbar, this would result in monolayer coverage of a surface by a typical gas-phase adsorbate within millisecond timescales, or in few minute timescales even at high vacuum pressures of 10^{-8} mbar. For graphene and other 2D materials however, while the effect of ambient species on the electronic properties such as the local carrier concentration (with resolution corresponding to even a single molecule[113,114]) has been reported previously, this often appears to be overlooked in mechanics-focused research, which is generally performed in ambient conditions. All previously reported auto-kirigami (AK) ribbon nucleation and growth has occurred in ambient conditions, which will include the results presented in this work. The adsorbates which may be present on graphene surfaces are also typically unclassified, described only in general terms as atmospheric contaminants or attributed to water vapour. This is probably due to the ubiquity of these species and perhaps a sense that the effects of such contamination can be removed by thermal treatment (e.g. annealing to ≈150° C[115]) or mechanical shearing. The structure of such contaminants is also typically not considered.

In the last decade AFM-based imaging has advanced understanding of atmospheric contaminants on graphene surfaces however, revealing self-assembled hydrocarbon structures referred to throughout this thesis as stripes. In 2012, Lu et al.[116] first reported row-like structures at graphite-water interfaces. These rows were attributed to nitrogen accumulating at the hydrophobic-water interface as the rows developed most rapidly

with the injection of N_2 into an environmental chamber in which their experiments were performed compared to other gas species such as O_2, Ar or CO_2, though the stripes were also observed across various independent laboratories, using different AFM systems as well as different sources and containers for the water, leading to the assumption that the rows arise from dissolved gas in the water. However, the spacing of the observed rows of 4.2 ± 0.3 nm, height of ≈0.45 nm and presence of 3 different row orientations with three-fold symmetry, with 60° intervals between each within distinct domains, is more consistent with alternative descriptions of stripes proposed later. Wastl et al. reported similar structures on epitaxial graphene in ambient conditions[117,118], described as a solid-gas monolayer at the solid-liquid interface, though the liquid here refers only to a presumed ultrathin water layer on the surface that was not directly identified or observed. An example of our imaging of these stripes is shown in Fig. 2.1, with stripes of different orientations on two graphene terraces. A periodicity of 6 nm is observed here with a peak-to-trough height of ≈0.2 nm. Stripes within a particular domain are not perfectly parallel, with some waviness observed as in lower right of Fig. 2.1 (a) for example.

An apparently unrelated description of micrometre rather than nanoscale ripples with an effect on friction was observed by Choi et al.[119–121], with the common feature of three-fold symmetry on graphene. Friction force microscopy revealed an anisotropic

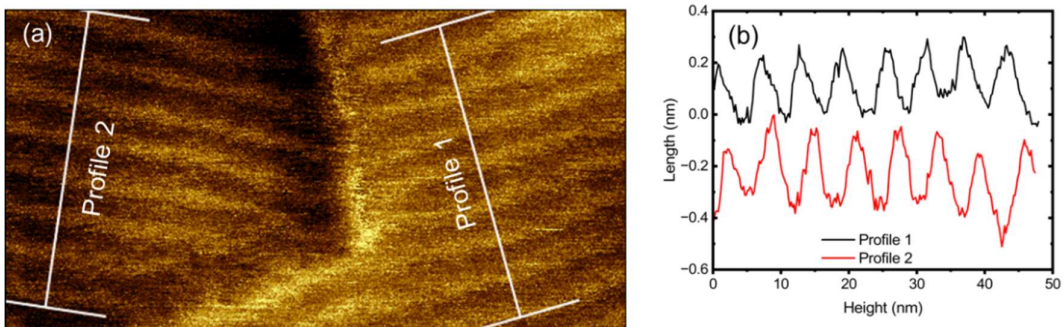

Fig. 2.1: PFQNM imaging of stripes on graphene terraces. (a) Two graphene terraces with stripe domains of different orientations, showing periodicity of stripe pattern, with pitch of 6 nm. (b) Height profiles along lines indicated on topography image in (a). Total linear z scale in (a) of 1.5 nm.

friction signal on exfoliated monolayer graphene with angle dependence across three distinct friction domains, with no correlating features observed in topographic imaging, optical microscopy or micro-Raman. This was attributed to the formation of micrometre-scale ripples caused by stress-induced deformations arising from inhomogeneous graphene-substrate interactions. The ripples were assumed to form along a stiff direction of the lattice (either armchair or zigzag), giving rise to the domains with 60° separation. A modified version of friction force microscopy (FFM) (described in the literature variously as cantilever torsion microscopy, transverse shear microscopy and transverse force microscopy (TFM), with the last used throughout this work) was found to image these friction domains with significantly greater reliability and contrast. In FFM, the fast scan axis is perpendicular to the main axis of the cantilever and the signal recorded is the cantilever torsion as a result of varying friction of the sample in that perpendicular direction. In contrast, in TFM the cantilever torsion is recorded with the fast scan axis parallel to the cantilever's main axis. Crucially however, these proposed ripples were never directly observed by Choi et al., as their proposed aspect ratio (<1/10) could not be resolved by AFM.

In 2016, Gallagher et al. unified the above observations with a number of observations on these stripes. They observed stripes of 4-6 nm pitch and peak-to-trough height of ≈0.1 nm on graphene (see Fig. 2.1 (a) and (b)), and on another 2D material, hexagonal boron nitride (hBN). Stripes were also directly imaged by Gallagher et al. on graphene/hBN heterostructures, on which Moiré patterns arising from the graphene-hBN lattice mismatch were also observed. Analysis of the Moiré pattern period allows for inference of the crystallography of the graphene[122], which in conjunction with stripe imaging demonstrated that stripes align along the armchair axis of graphene and hBN. Direct correlation was observed between the three-fold symmetric friction domains imaged in TFM and stripe direction, where the magnitude of the TFM friction signal is proportional to the cosine of the angle defined by the fast scan axis and stripe direction. The surface anisotropy defines a local "easy" axis which the tip is pushed toward, resulting in the torsion measured. Gallagher et al. also demonstrated a controllable method by contact mode scanning of erasing or swapping the orientation of stripes within a particular region. That this method could have very

strong or weak responses on different SLG samples suggests that the stability of domains may be determined by a local strain field in the flake. An example of stripes and stripe friction domains from our research is seen in Fig. 2.2. A bilayer graphene flake is imaged in PFQNM, with the flake edge and substrate seen in the lower left of Fig. 2.2 (a). No notable features are observed in topography beyond the expected roughness of the sample. However a TFM image of the same location shows three distinct regions with varying TFM friction signal in Fig. 2.2 (b). The boundary of these regions is highlighted with yellow dashed lines. A 500 nm scan at the intersection of these three domains (Fig. 2.2 (c), the same area highlighted in red in Fig. 2.2 (b)) reveals the stripes directly and the characteristic 60° angle between stripe domains. Green, orange, and blue dashed lines act as a guide to the eye to indicate the stripe directions in Fig. 2.2 (c). Stripes typically are not perfectly straight and some waviness can be present. Therefore, angles and stripe pitch are derived from a 2D Fast Fourier Transform, with the modulus, showing the absolute value of the complex Fourier coefficient proportional to the square root of the power spectrum density function, displayed as an inset highlighted in white in Fig. 2.2 (c).

This provides an averaging of these values over an entire domain in question. We emphasise here that stripes are only seen directly in high-resolution AFM topography imaging in scan sizes of 500 nm and below, whereas friction domains are seen occasionally in FFM and consistently in TFM over any scan size available. That TFM can be readily applied to scan sizes of tens of microns makes this a more achievable method of examining stripes over whole-flake dimensions, though the typical tip radius of ≥ 10 nm used in contact mode imaging (and blunting that would likely occur in contact mode of a sufficiently sharp tip) precludes simultaneous direct stripe imaging with friction domain imaging.

We also note that on some rare occasions, a stripe structure is apparently observed with a period of 20-30 nm instead of the expected 4-6 nm on scan sizes of a few microns, over which the lateral dimensions of a single pixel of the image would in fact correspond to the ≈4-6 nm instead. Upon decreasing the scan size in such areas, the expected stripe structure of 4-6 nm is revealed. We therefore attribute this to a rare digital aliasing effect of the AFM.

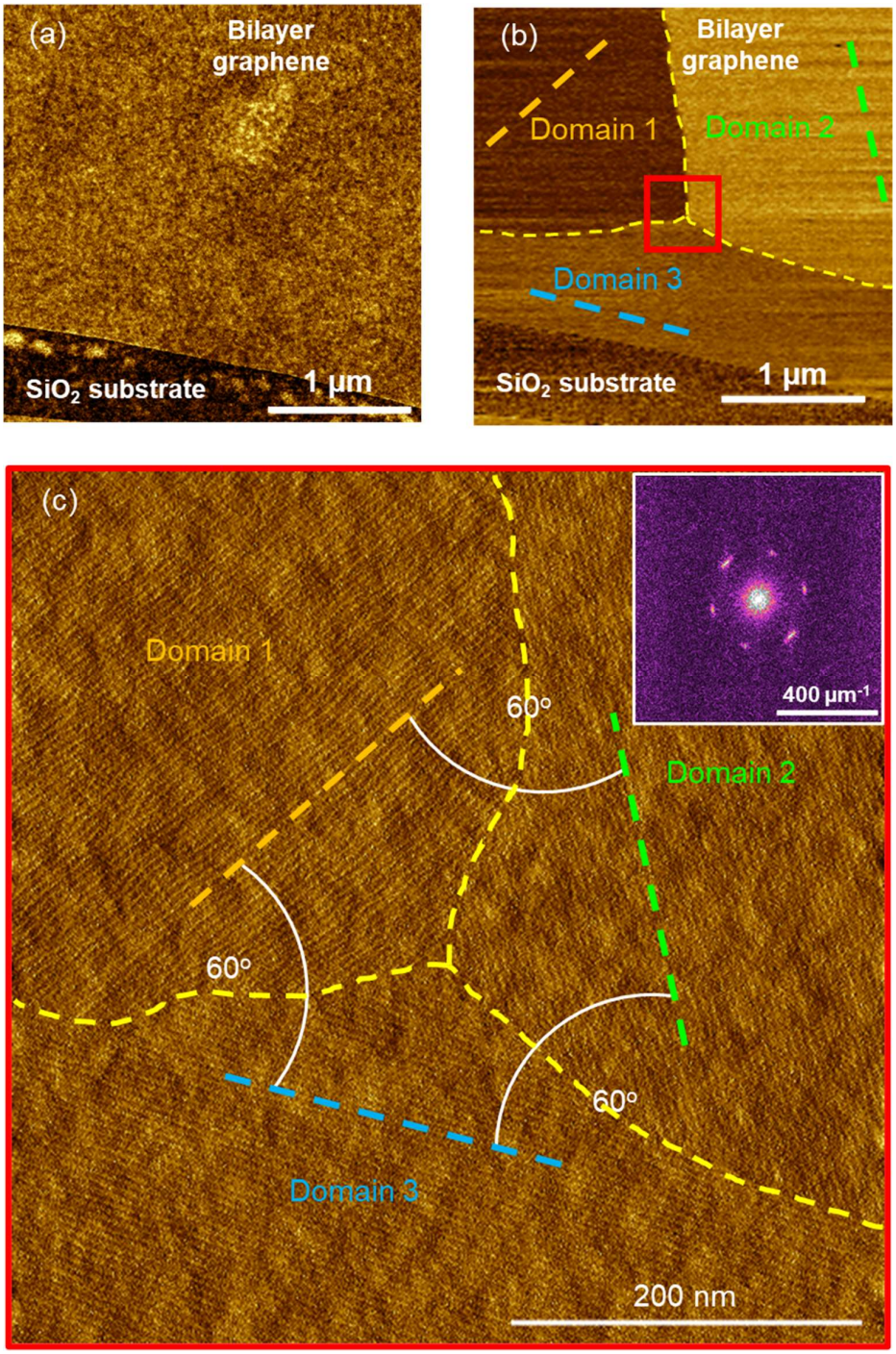

Fig. 2.2: Graphene with adsorbate stripes and stripe friction domains. (a) AFM PFQNM topography image of a bilayer graphene area bordered by SiO_2 substrate, with no notable figures on the graphene area. (b) TFM imaging of the same area reveals three distinct friction domains separated by yellow dashes, with thicker dashes within each labelled domain corresponding to stripe directions directly observed in (c), high-resolution PFQNM topography image of the area at the boundary of 3 domains highlighted in red in (b). 60° separation of stripes is observed. Height image in (c) is 2D FFT filtered to minimise background noise and enhance visibility of stripes.

Later work by Gallagher et al. in 2018 using polarization-contrast microscopy further demonstrated that friction domains arose from adsorbate stripes, such as a self-assembly of chainlike organic molecules, rather than intrinsic ripples[123]. Stripes or their associated friction domains had then been observed on graphene[124], hBN[125], graphite[126,127], and MoS_2[128]. The consistency of the stripe height and pitch especially across all of these materials with different bending stiffnesses and stress responses[129] strongly suggests that the phenomena cannot be as a result of an intrinsic property of the 2D material and instead may be an adsorbate structure common to all of these materials. As a result, Gallagher et al. suggested that the stripes may be comprised instead of adsorbed airborne hydrocarbons which would be sufficiently ubiquitous to produce this result in labs around the world. Temiryazev et al. in 2019 observed stripes on HOPG, mechanically exfoliated graphene and "graphite plates" (50 -200 nm thick flakes of graphite), also demonstrating the ability to rewrite domain stripe directions to a specific direction within and around the AFM tip scan area, though with no ability to control or predict the exact area which may extend well beyond the scan area, and whether this defined domain would relax to the previous direction or even grow in area[130].

In 2020, Seibert et al. reported stripes at a water-graphite interface, in a similar manner to Lu et al. in 2012. Seibert noted that stripes were observed in 80% of over 100 experiments where the ultrapure water was added by a hydrocarbon based plastic syringe, but never in seven further experiments using a glass syringe. Exchanging water initially added by a glass syringe with a plastic syringe also soon resulted in stripe formation. Siebert et al. therefore claimed that earlier assessments of stripes as nitrogen should be reconsidered as species originating from polypropylene or polyethylene plastics in the syringe or surfactants commonly used in cleaning agents. Seibert et al. also performed high-resolution AFM fluid imaging, which resolved an inner structure of the stripes of broadly parallel lines with a period of 0.5 nm, oriented perpendicular to the direction of stripes[131]. However, at this point we note that specific chemical characterisation had not been performed on any of the above reported stripes, which may indeed have different origins in different cases discussed above.

Stripes also had not been observed in STM even where atomic resolution had been achieved.

Significant clarity was brough to the topic by Pálinkás et al. in 2022, who determined the chemical composition of the stripes common to various vdW materials including graphene, graphite, MoS_2 and hBN[132]. Stripes on HOPG were observed directly by AFM and STM topography as in Fig. 2.3 (a) and (b) respectively. Infrared spectroscopy was used to characterise the stripes as self-assembled structures composed of 20-26 carbon atom alkane chains, which they propose selectively displace other surface contaminant species and may dominate surface interactions with the environment. Alkanes in this range are present in the environment from biological sources[133] as well as in lubricants, mineral oils and combustion engine exhausts[134], accounting for their ubiquity and relative abundance. Low temperature STM imaging of the stripes (Fig. 2.3 (c)) was also achieved by applying a large tunnelling resistance (>10 GΩ) to avoid the tip perturbing the adlayer. A similar inner structure to that reported by Siebert et al. was observed, with the parallel lines being individual alkane chains, which was also consistent with DFT calculations performed in their report. This is also presented in their schematic reproduced in Fig. 2.3 (d).

From AFM and ellipsometry analysis, Pálinkás et al. propose that an unordered contamination layer consisting of water and various hydrocarbons builds up within 40-60 minutes of initial exposure of a pristine surface to the atmosphere, while these are selectively replaced and interchanged with alkane chains. Friction domains were observed and studied from 4 days following exposure of the pristine flakes, with a steady state achieved after 10-14 days. The increasing adsorption energy per carbon atom with chain length but decreasing atmospheric abundance and vapour pressure of longer alkane chains results in the observed 20-26 carbon atom alkanes as the eventual dominant surface contaminant species. The distribution of these lengths of alkane chains in Fig. 2.3 (e) also shows the close agreement of stripe width with the length of the C_{26} alkane. This adlayer can also be desorbed by heating to 200°C for 1 hour.

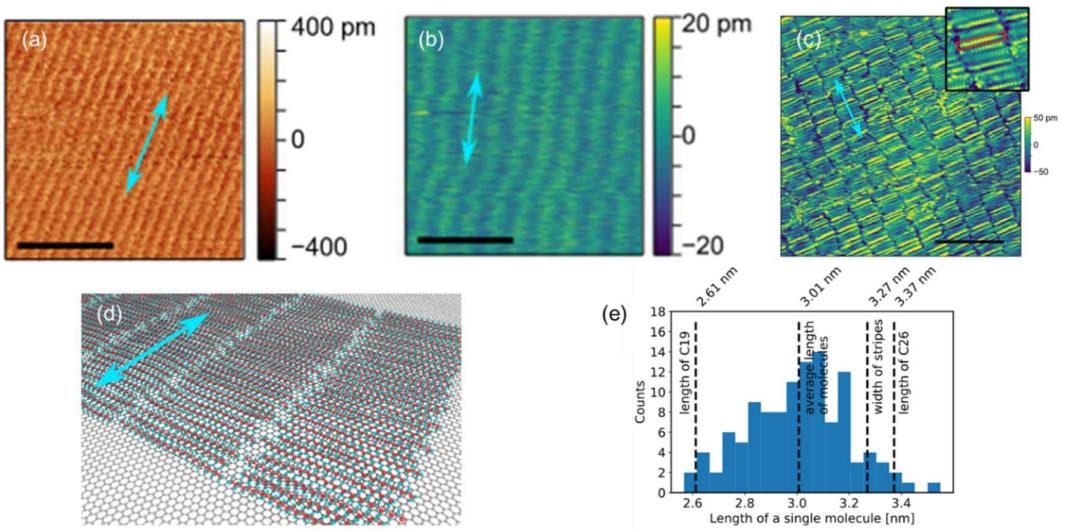

Fig. 2.3: AFM and STM images of stripes and their inner structure. (a) PFQNM topography on bulk HOPG surface showing parallel stripes. (b) Room-temperature STM topography of the monolayer's smectic phase. (c) Low temperature (9K) STM topography showing stripe inner structure and alkane chain building blocks, with inset (6 nm x 6 nm) showing atomic scale structure of a single stripe highlighted in red. (d) Schematic of alkane molecules on graphene surface. (e) Distribution of lengths of individual molecules in stripe layer. Blue arrows aligned with stripe direction in each. Scale bars: 30 nm, 20 nm and 10 nm in (a), (b) and (c) respectively. (a)-(e) reproduced from 132.

A method to rewrite the stripe orientation on a more deterministic and permanent basis than had been achieved before was also presented, specifically by scanning with the fast-scan axis parallel to the zigzag direction, resulting in reorientations which were stable for periods of several months, unlike less controlled methods to swap or rewrite stripe direction discussed above.

Following this review of existing literature on stripes, we note a number of topics which remain unexplored, which we will consider here. These are primarily the influence of stripes on mechanical properties beyond friction; the presence, or lack thereof, of stripes not only on surfaces but also within interfaces and between layers of graphene; stripe dynamics and motion separate from their deliberate manipulation and control; and the interactions of stripes with surface features. Observations are also provided on the evolution of stripes from a pristine surface. While some of these topics must be treated phenomenologically through observation rather than deterministically, these observations nonetheless provide further insight into these novel adsorbates.

2.3 Stripe dynamics and formation

Questions remain unanswered on how stripes form, in terms of surface interactions between graphene and hydrocarbons which comprise the stripes as well as any other atmospheric contaminants such as shorter chain alkanes and water. Following Pálinkás et al.'s report, these unclassified other contaminants should be present in the first few days after exfoliation and initial exposure but are selectively removed by the preferential adsorption of the 20-26 carbon atom alkane chains. In this section we describe efforts to understand the development and evolution of stripes over their critical formation time period.

Experiments were performed using both TFM and PFQNM on a graphene monolayer freshly exfoliated onto 300 nm SiO_2/Si substrate, with Bruker SNL probes. The sample was stored in a sealed (albeit not airtight) non-vented polystyrene petri dish in standard laboratory conditions when not under scanning. TFM imaging was carried out at 10 nN setpoint to minimise any effect of scanning on the domains and PFQNM at PFT setpoints of less than 1 nN. In Fig. 2.4 (a), captured 380 minutes after exfoliation, a uniform TFM friction is observed across the entire graphene sheet (with small exceptions being wrinkles in the sheet seen as lines of higher or lower friction in bottom and top left respectively for example). Nascent domains are observed 54 hours after exfoliation in Fig. 2.4 (b), labelled here I-III from lowest to highest TFM friction signal. However, rather than the typical image of three distinctly defined domains with near straight or low curvature boundaries, a fourth region of intermediate friction relative to domains I and II is observed. Distinct boundaries are observed in Fig. 2.4 (c) and (d) 102 and 169 hours after initial exfoliation however, with three domains corresponding to stripes oriented along the sheet's armchair directions and only minor changes in domain areas in this period. A swap of stripe orientation has also occurred between the entirety of regions I and II, indicated by II now being the lowest friction and I intermediate, despite the boundaries remaining largely similar. We therefore attribute the blurring in Fig. 2.4 (b) to the coexistence of these two neighbouring stripe domains, direct evidence of which is presented in Fig. 2.7. This coexistence may occur as a precursor to the swap in friction domains between Fig. 2.4 (b) and (c). We can confirm the origin of these domains as

stripe orientation by PFQNM at the boundary of these three domains, area highlighted in red in Fig. 2.4 (d), as seen in Fig. 2.4 (e) with periodicity illustrated by 2D FFT of this area in Fig. 2.4 (f). Dashed colour lines aligned with stripe directions are provided as a guide to the eye.

Whereas TFM can image stripe friction domains over scan sizes of 10s of microns with ease, as in Fig. 2.4, direct stripe imaging proves to be more experimentally demanding. This requires scan sizes of 500 nm or less to readily resolve the ≈4 nm pitch of the stripes, alongside tip sharpness of 2 nm and adequate vibration and noise isolation to maintain precision to angstrom scale displacements. As is performed throughout this work, this resolution was achieved wholly in ambient conditions, even considering the presence of a commuter rail line within as little as 15 m laterally (albeit several metres underground), which often can be audibly heard from the laboratory in question. Vibration isolation was achieved by mounting the AFM system on an air table, which in turn was mounted on an ≈1 m^3 concrete plinth, providing additional mass damping.

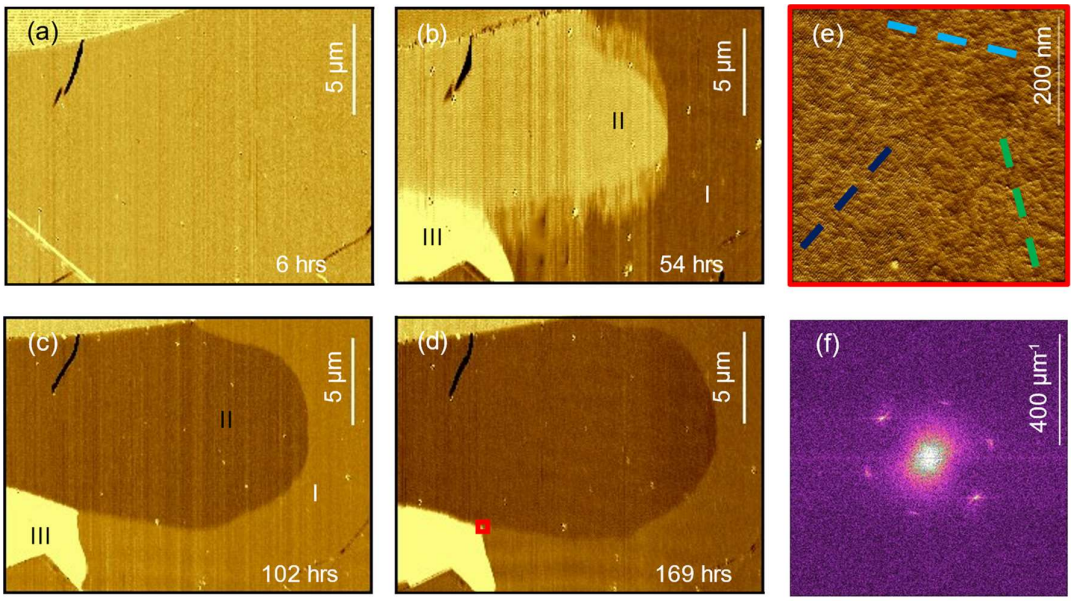

Fig. 2.4: Development and evolution of stripe friction domains with time after initial exposure of pristine graphene monolayer to atmosphere. (a)-(d): TFM images of same area of SLG bordering SiO_2 substrate (top left corner of each) at t = 380 minutes, 54 hours, 102 hours, and 169 hours respectively after mechanical exfoliation. Total linear z-range of 0.1 V for (a)-(d) from -0.05V – 0.05 V. (e) Zoom in to area highlighted in red in (d) at boundary of three stripe domains, and (f) associated 2D FFT of (e) demonstrating the regular 60° spacing and stripe pitch.

Stripe development following exfoliation was also studied concurrently by PFQNM in a nearby location on the same sample, using fresh Bruker SNL AFM tips with a nominal tip radius of 2 nm to ensure sufficient sharpness. This was confirmed by imaging using the same tip on a reference graphene sample (which had been exposed to ambient lab conditions for over a year and upon which stripes had been reliably imaged previously) both before to check tip sharpness and afterwards to ensure that blunting had not occurred during imaging that may have impaired resolution. Before and after imaging on the reference sample is shown in insets outlined in red in the upper right and lower right respectively of Fig. 2.5 (a) – (d). Stripes are not directly observed within a few hours as in Fig. 2.4 (a), though unlike for stripe friction domains, they also cannot be observed directly in Fig. 2.5 (b) despite the presence of their characteristic friction domains. Stripes are faintly but distinctly observable in Fig. 2.5 (c) and more apparent in Fig. 2.5 (d). Given the comparable visibility of stripes on a reference sample across all instances, we attribute this to a temporal build-up of hydrocarbon adsorbate material rather than simply a product of imaging quality.

However, we observe that despite stripes not being directly visible by eye in Fig. 2.5 (b), a very faint signal is observed in the 2D FFT that corresponds exactly with the stripe period and orientation angle seen more clearly 2 days later in Fig. 2.5 (c). A slight angular misalignment of the FFT peaks between the two exactly corresponds to a small change in the angle at which the sample is mounted by hand in the AFM as determined by comparing flake edges. That a signal is observed even at only 2 days after exfoliation decreases the window for stripe formation from atmosphere from 4-5 days previously reported[132]. This also demonstrates the high sensitivity of TFM to stripe friction domains where they cannot be observed even with z resolution of ≈1 Å and lateral resolution of 1-2 nm in PFQNM and the complementarity of these imaging modes.

While the ability of C-AFM to erase or rewrite has been demonstrated[130,132], this has only been reported to occur at elevated setpoints (30 nN for Gallagher et al. for example[125]), while from our own experience a setpoint of 20 nN or higher can often erase domains, albeit depending on the angle between scan axis and orientation of the stripes in the particular domain being erased.

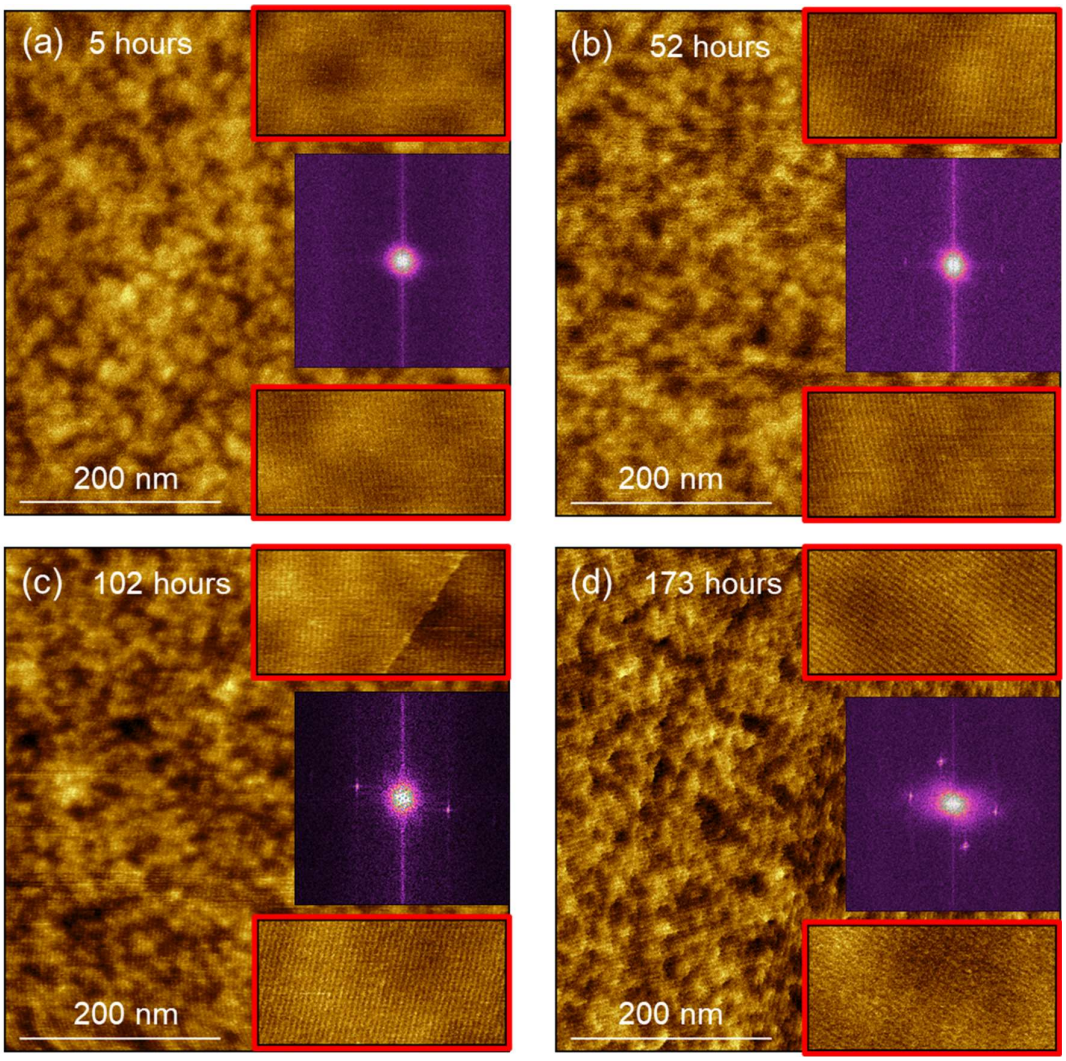

Fig. 2.5: Direct imaging of stripes development and evolution concurrent with Fig. 2.4. (a)-(d) main: PFQNM imaging of same sample imaged in Fig. 2.4 5 hours, 52 hours, 102 hours, and 173 hours after mechanical exfoliation respectively. Red highlighted insets of each demonstrates sufficient tip sharpness to resolve stripes on a reference sample immediately before (top right of each) and after (bottom right of each) imaging of main. Inset mid-right of each is 2D FFT of main of each. Total linear z range of 1.5 nm for all height images.

To monitor how domains may evolve with negligible influence of the scanning itself on an aged sample, we performed a series of consecutive TFM images on a 4-layer graphene area (Fig. 2.6). The sample used was mechanically exfoliated from Kish graphite one year previously, and had been stored in a sealed (not airtight) Gel-Pak container in ambient laboratory conditions in the intervening time. This imaging was performed using an especially low stiffness cantilever (qp-SCONT, nominal spring constant= 0.01 N/m, tip radius ≈10 nm) designed for soft contact, with a normal setpoint of 1-2 nN maintained throughout. This variation in normal setpoint arose from

drift of the laser signal over the ≈15.5 hours of continuous scanning, with thermal expansion also likely contributing as the experiment was performed overnight. While domains over the majority of the area remained stable, some variation was observed in locations indicated by markers I and II in Fig. 2.6 (a), with timelapse of these areas shown in green and blue highlighted areas respectively in (a) shown as series in (b)-(d) and (e)-(g) respectively.

The change in stripe area per image varies from ≈3.9 μm^2, or ≈0.2 μm^2/minute in some of the earliest images in the sequence to ≈0 μm^2 in later images, compared to the total flake area of ≈220 μm^2, representing a maximum change in stripe orientation of ≈1.8% of the total graphene area per image. Therefore, although Pálinkás et al. describe a steady state of build-up of the contaminant layer achieved within 10-14 days (over a 2 month run of ellipsometry measurements), this cannot be taken to imply that no further development of stripes occur and that surface properties which may be modulated by their orientation can be assumed to reach a steady state as well.

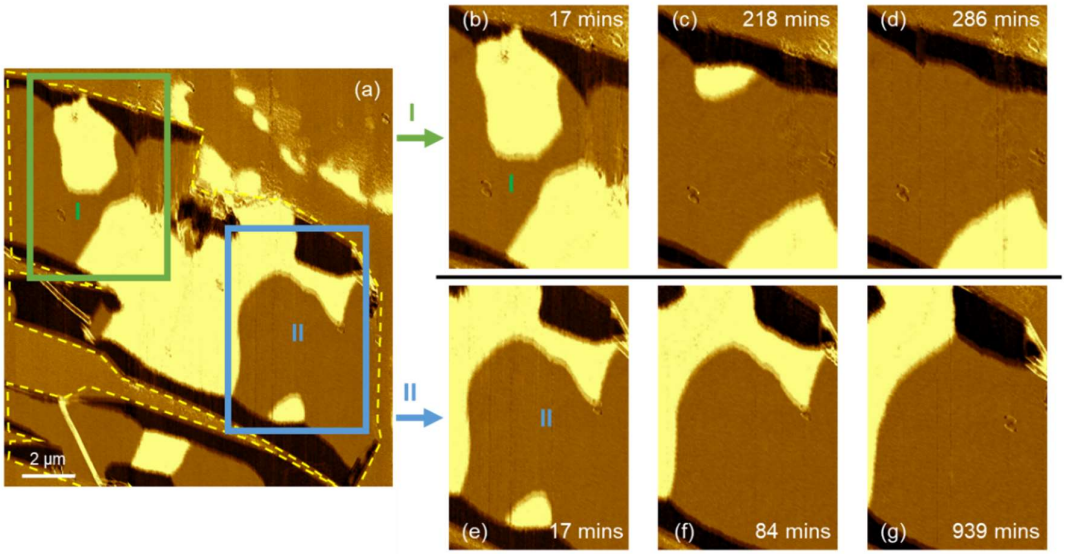

Fig. 2.6: Selection of a series of consecutive TFM images of stripe friction domains taken in 17-minute intervals. (a) Stripe friction domains after first image (t = 17 mins). Yellow dash outlines indicate edges of graphene flake. Zoom-in to areas I and II highlighted in green and blue respectively in (b) and (e), sequences in areas I and II in (b)-(d) and (e)-(g) respectively. In (b) – (d), upper yellow domain reduces in area and later disappears, and lower yellow area also reduces in area. Similarly in (e) – (g), rapid disappearance of lower yellow domain is seen in (f) with similar change in area of upper yellow domain in (g) over longer timescale. After (g), no further developments were observed across the entire flake in the following ≈7.5 hours of the ≈15.5 hour sequence. Total Δz range of 1.0 V (-0.5 V – 0.5 V) for all images.

Even using deliberately low setpoints in TFM, it can be difficult to claim with complete confidence that tip interactions are not influencing the stripe domains however while imaging in contact. It is therefore significant that stripe evolution has also been observed decisively using PFQNM, which operates at much lower average force setpoints and without the inherent directionality of the cantilever and tip on the surface which appears to be central to the capability of C-AFM to rewrite or erase domains. This was performed in Fig. 2.7 using Fluid ScanAsyst+ probes with nominal stiffness of 0.7 N/m and tip sharpness of 2 nm, sufficient to resolve stripes. While a distinct boundary is observed in Fig. 2.7 (a), an image in the same area taken within 1 hour shows an intrusion of the upper domain into the lower (Fig. 2.7 (b)). This advances in Fig. 2.7 (c), imaged consecutive to Fig. 2.7 (b). Note that both (b) and (c) are taken with capture direction down (i.e. the slow scan axis from top to bottom of the image), such that growth of the domain in corresponding areas between images occurs exactly 9 minutes

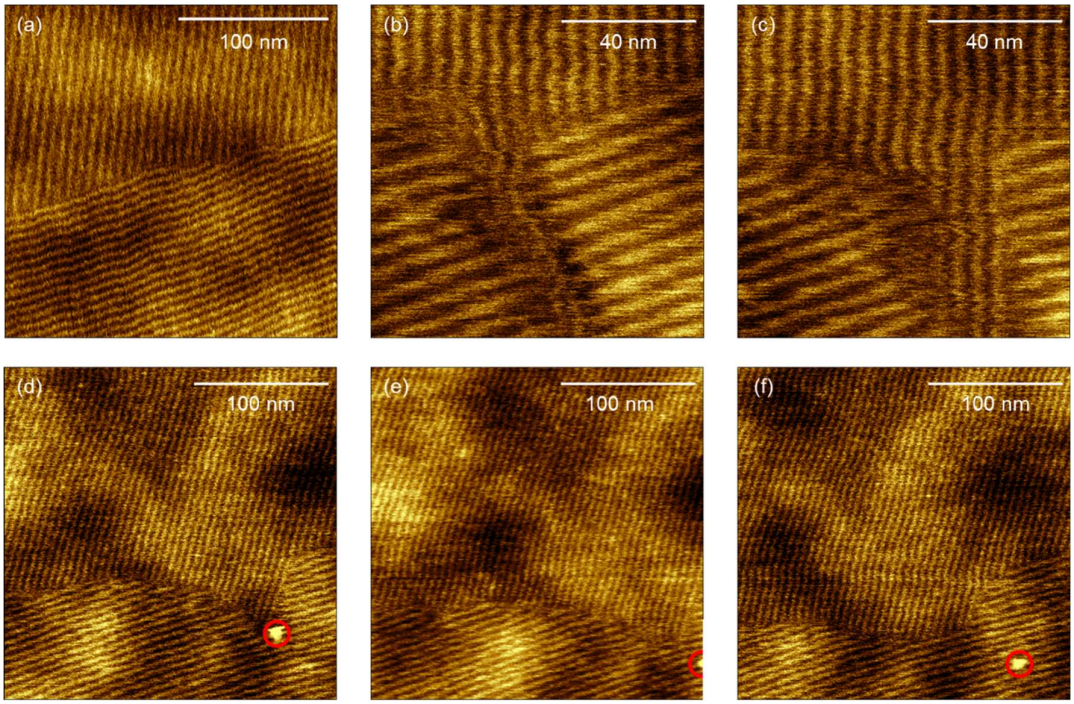

Fig. 2.7: Direct observation of stripe orientation change in PFQNM. (a) Two stripe domains with clear boundary at which stripes of each orientation terminate. (b) and (c): Consecutive images (scan completed 9 minutes apart), where the vertical upper domain begins to extend into a lower domain. A single stripe is seen extending across this boundary in (b) and 3 in (c). (d)-(f): A feature highlighted by a red circle is used as a reference point to indicate the changing domain areas (18 minutes between scans (d) and (e), 81 minutes between (e) and (f)). The feature initially at the boundary of two domains eventually is contained wholly within the lower domain. Total linear z-range of 0.5 nm for all images, PFQNM topography channel.

apart rather than a total difference of 0 minutes at beginning of the latter image and 18 minutes at the end as would occur for a varying capture direction. A bright spot on the surface (highlighted by red circles in Fig. 2.7 (d) – (f)) is used as a reference point in these images taken of the same area to show how the domains interchange over the course of 120 minutes. Within 20 minutes of (d) the lower domain around the reference point has grown to the left by as little as 21 nm, or at a rate of as little as 1 nm/minute. This value in fact represents a relatively higher rate observed, with a change of as little as a single stripe can be resolved between Fig. 2.7 (f) and an otherwise near identical image (not here pictured for redundancy) captured 30 minutes later, corresponding to ≈0.1 nm/minute rate of growth.

Considering a shared area of 55,000 nm^2 (determined by overlapping and considering only the common area imaged in both (d) and (f) using the reference marker indicated to gauge this area), an area of only 1,960 nm^2 changes orientation in the intervening 120 minutes of continuous AFM imaging of this region, albeit with some minor AFM drift causing the reference feature to "move" between images, or 17 nm^2/minute. Assuming no preferential direction of growth, this corresponds to an averaged ≈2 nm/minute growth in any direction. We emphasise that the PeakForce setpoint maintained throughout this imaging was less than 1 nN. With a PeakForce tapping amplitude of 150 nm, a total contact time of the tapping cycle performed at each pixel of the scan is typically as low as 125 μs in contrast to previous contact imaging, resulting in an average force over time per cycle on single pN scales. This is as many as 4-5 orders of magnitude lower than that required to rewrite or erase domains by C-AFM. Furthermore, we emphasise that we directly observed stripe orientation change (as in Fig. 2.7) on only two instances over hundreds of PFQNM images taken over an approximately 2 year time span, with stripe resolution on comparable samples with the same or similar tip and at similar PeakForce setpoints. As such, we contend that this cannot be a tip-induced phenomenon and instead represents a rarely observed self-driven mechanism for the motion of adsorbed species. This in fact supports our earlier supposition of a blurred "fourth" domain observed shortly after mechanical exfoliation being a region where different stripe directions could coexist with one intruding into the other as in Fig. 2.7 (b) and (c). Such a mechanism likely describes how

domain switching seen in larger areas such as in Fig. 2.6 occurs as well. The rarity of these observations agrees well with the domain area changes seen in Fig. 2.6: taking the maximum area change observed between 2 successive images as an upper bound, the chance of a scan randomly landing on an area on which stripe direction is changing therefore has an upper bound probability of 0.9 % per scan. This value, derived purely from Fig. 2.6, is broadly consistent with our experimental observations as discussed in relation to Fig. 2.7.

2.4 Effect on superlubric friction

As discussed in section 1.2.1, superlubricity is a phenomenon whereby friction between sliding bodies becomes vanishingly small. This was observed between bulk HOPG and a graphite nanoflake in incommensurate contact under UHV conditions by Dienwiebel et al. in 2004[23]. In 2012, superlubricity was also observed between microscale contact areas of up to 10 × 10 μm^2 under ambient conditions in graphite mesas by Liu et al.[29] (graphite mesas discussed in further detail below). Following Liu et al.'s example, we will consider superlubricity to be present where interlayer shear stresses of 10s of kPa or below or present as a normal force cannot readily be defined here to meet the criteria of a friction coefficient μ of less than 0.01 per the Coulomb definition of friction.

From the initial discovery of auto-kirigami ribbons by Annett et al. in 2016[89], it was concluded from that friction must be negligible. Otherwise, a friction force resisting growth scaling with the increasing area of the propagating ribbon would result in a non-constant taper angle of the ribbons over micron lengths; in contrast, constant taper angles are almost always observed, suggesting superlubric contact between host flake and folded ribbon. The discovery of the presence of stripes ubiquitously on graphene samples not realised in the original publication would seem to complicate a simple picture of incommensurate graphene sliding if, as is typical, the nucleating indentation is performed on a graphene sheet with sufficient time after mechanical exfoliation that stripes must be present: will the stripes be carried forward to become sandwiched in

the folded area between the ribbon and host sample, or will shear forces during sliding result in displacement and removal of the stripe material leaving a clean interface?

To resolve this question, a bilayer graphene sheet was mechanically exfoliated from bulk natural graphite (NGS Naturgraphit) onto 300 nm SiO_2/Si substrate. Nanoindentation was performed on this sheet with a Bruker Multimode 8 AFM using a diamond cube corner (Bruker DNISP) probe one month later such that stripes were then present and readily visible on the surface. The two ribbons shown in Fig. 2.8 were nucleated from these indents by a novel AFM-based method described in further detail in section 3.2 as "hard tapping". Contact mode imaging was performed using an Adama Innovations diamond apex probe (AD-2.8-SS) with a normal spring constant of 1.9 N/m calibrated by thermal tune. Ribbon 1 was rotated by scanning the ribbon and surrounding 25 μm^2 area at 25 nN setpoint until rotation occurred, with rotation in the direction of retrace of the horizontal fast scan axis direction (Fig. 2.8 (a) and (b)) chosen perpendicular to the direction of ribbon growth. While this method was unsuccessful in inducing rotation in ribbon 2, scanning over a single scan line at an elevated setpoint of 250 nN was successful as per similar before and after in (d) and (e) respectively. This scan line was selected such that it was set approximately perpendicular to the main direction of ribbon growth, near the end of the ribbon to increase the moment of rotation and covering both the ribbon and adjacent host sheet, though this also caused minor damage to the ribbon as seen in a notch in the left ribbon edge and localised tearing of nearby graphene seen in Fig. 2.8 (f). Both rotations are associated with minor extensional growth of the ribbon along one torn edge (right torn edge in ribbon 1 and left in ribbon 2). Simply increasing contact setpoint during imaging of a ribbon often proves to be unsuccessful in manipulating the ribbon (by rotation or by attempting to push/pull the ribbon along the direction of growth) resulting only in tearing of the host graphene sheet or ribbon. These rotations therefore represent a rare instance of successful manipulation, which to our knowledge has not elsewhere been demonstrated. It should be noted that this limitation inhibited our testing of a greater number of ribbons in the present work.

Crucially, these rotations were successful in revealing an area of the host flake graphene that had previously been sandwiched within the sheet-ribbon interface, with ribbon 1

rotated 22° counterclockwise while ribbon 2 was rotated 33° clockwise. Follow-up imaging using the same tip at lower setpoint in contact mode did not cause any further rotation or ribbon growth.

High-resolution PFQNM imaging was performed on the areas of the host flake previously sandwiched in the interface and now exposed, with imaging occurring within 110 minutes of rotation for Ribbon 1 and within 40 minutes of rotation for Ribbon 2. As concluded from previous discussion in section 2.3, these time periods would be insufficient to allow stripes to form by adsorption from the atmosphere if no stripe material were already present in the stable interface. In both cases, stripes are readily observed at the former interface areas (host flake areas included within the green outline in (b)/(c) and (e)/(f) for ribbons 1 and 2 respectively). These stripes are entirely continuous with stripes in neighbouring areas, with no variation in stripe height, pitch, angle or other properties observed across the former ribbon edge. Inferring the graphene lattice armchair orientation from the stripe directions on host graphene and on the rotated ribbons, both ribbons appear to have rotated into commensurate contact with the host sheet. Similar lock-in has been reported previously in simulations of micromanipulated graphite stacks[135], ambient environment experiments[29,136] and thermally relaxing nanoflakes in vacuum[137], attributed solely to commensuration of the atomic lattices. This increased friction contact is predicted to preclude any further ribbon growth or rotation, and likely accounts for the final positions observed here as the final locations were not specifically defined by the contact imaging. However, this also gives rise to the question of how atomic commensuration can still occur with the mediation of stripes, or whether this commensuration still exists between only the exposed regions of the lattice between the stripes or a contribution to commensuration associated with alignment of the stripes themselves.

We can expand here on the related configuration of graphite contacts in the form of microscale graphite mesas as described by Lu et al.[138], whereby an approximately 100 nm thick SiO_2 film is deposited on top of a layer of highly oriented pyrolytic graphite (HOPG) as a cap. The HOPG/SiO_2 is then carved into square islands of 0.5-5 μm width and ≈200 nm height by electron beam lithography using a negative photoresist etched under an oxygen plasma. These mesas are used to study graphene-graphene sliding and

friction as they exhibit self-retracting motion[139]. A micromanipulator probe laterally pushes the stack resulting in lateral displacement of upper layers relative to the base layers at a naturally occurring incommensurate interface. Upon withdrawal of the probe, the suspended portions immediately, fully and automatically retract under superlubricious sliding to their initial stacked location.

Wang et al. report interlayer shear stresses of commensurate and incommensurate graphite contact in these mesas, both where contacts are presumed to be perfectly clean and where ambient, uncharacterised contaminants are introduced to the

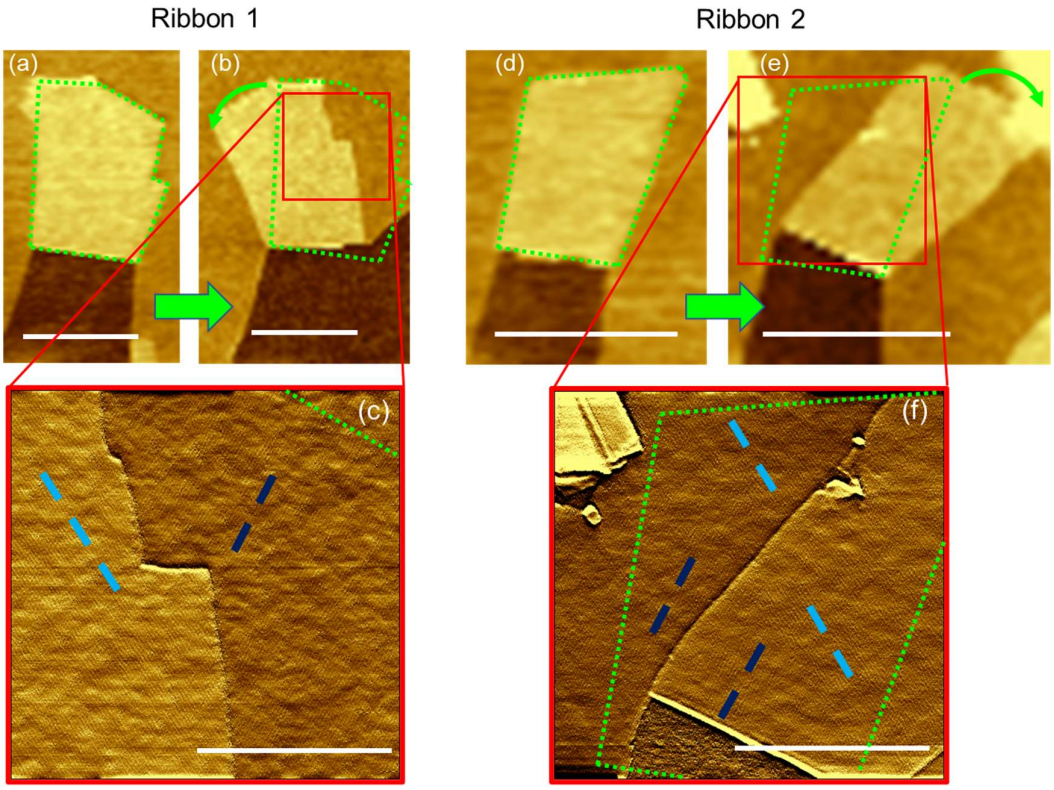

Fig. 2.8: Rotation of ribbons to reveal stripes at former interface areas. (a) Ribbon 1 position and shape before (a) and after (b) rotation by contact mode imaging of the ribbon and surrounding area. Ribbon initial position and direction of rotation indicated by green dash outline and arrow respectively. (c) Zoom-in to area highlighted in red in (b), formerly at the ribbon-host sheet interface. Stripes are observed over all areas, including former interface area with previous edge in top right corner of (c) as per green dashed line. Similarly for ribbon 2, ribbon before (d) and after (e) rotation by contact imaging. Stripes are similarly present over former interface area, with previous ribbon position indicated by green dashed outline in (f). Light and dark blue lines present to serve as a guide to the eye for stripe directions. 1D horizontal FFT filtering applied to (c) and (f) to maximise stripe visibility. Scale bars: 500 nm for (a), (b), (d) and (e), 250 nm for (c) and (f). Total linear z range of 6 nm for (a) - (f).

interface by sliding[28]. They find that interlayer shear stress of clean commensurate contacts are four orders of magnitude greater than that of clean incommensurate contacts, while the introduction of ambient contaminants over a duration of 1,000 minutes increases friction of the incommensurate contact five-fold but decreases friction of the commensurate contact by two orders of magnitude. Assuming for comparison that these values would be valid for our system, we transition from unclean incommensurate to commensurate, or a twenty-fold increase in interlayer shear stress, significantly less than the four orders of magnitude for the same transition in the case of clean interfaces. This demonstrates that while the presence of third bodies can significantly modulate interactions between the surfaces, some lattice-scale locking nonetheless occurs. However, we cannot here state with certainty the extent to which the orientation of the stripes themselves may have on interlayer shear stress, or whether acting as a barrier between the graphene surfaces is its sole effect.

Overall, these results indicate that the stripes are sufficiently robust that they are not displaced by the sliding motion of the ribbon during growth, or by the attractive vdW forces between ribbon and host sheet graphene even after three days from nucleation to rotation and imaging. This is in contradiction to a claim in a very highly cited perspective that trapped contamination can "clean itself off the interfaces", or else these heterostructures would be "layer cakes" rather than neat crystals[140]. This self-cleaning effect was attributed to the attractive vdW forces between layers squeezing out contaminants or trapping contaminants into micrometre scale bubbles, such that there is minimal effect on devices on the scale of tens of microns which could be considered clean with atomically sharp interfaces. As our observation is starkly contradictory to this claim, the results that lead to this conclusion are detailed and considered here.

Haigh et al. studied mono- and bilayer graphene interlaid within hBN crystals, using focused ion beam milling to examine a cross-sectional slice of this interface by STEM[141]. The graphene and hBN crystals were prepared in ambient conditions, and hence some adsorbates were expected to be present at these surfaces/interfaces. They observed that adsorbates would diffuse over micron distances to form individual islands of few-micron lateral dimensions and ≈20 nm maximum height of the trapped material,

identified as hydrocarbons by energy dispersive x-ray (EDX) spectroscopy and electron energy loss spectroscopy (EELS). This diffusion left clean, flat areas of micron widths to act as the fabricated devices, with this diffusion aided by heating to 300°C. They also measured the interlayer distances between these layers, which varied from the basal plane separation by only ≈0.07 nm, suggesting that no adsorbates could be present in sub-monolayer thicknesses. In this observation specifically, it appears likely that adsorbates indeed are not present as stripes are known to desorb from graphene surfaces with heating to 200°C [119,132].

Georgiou et al. fabricated graphene/tungsten disulfide/graphene heterostructures[142], with high-angle annular dark-field (HAADF) STEM imaging of cross-sections of these heterostructures showing no visible trapped adsorbates (though this is not specifically explored in their report). No specific reference is made to the presence or lack thereof of contamination except a brief remark that the zero-bias resistivity of graphene-WS_2 transistor prepared as described above may be limited by unspecified remaining wafer contamination.

Lui et al. describe ultra-flat graphene[143] produced by mechanical exfoliation of kish graphite onto mica substrates (in an atmosphere with concentrations of less than 1 ppm of water to minimise adsorption onto the highly hydrophilic mica) as well as onto bulk SiO_2 substrates in ambient conditions cleaned by sonication in methanol with no thermal processing. Graphene on mica is seen to be five times smoother than that on SiO_2, with height variation of less than 25 pm over micron scan sizes. The claim that adsorbates are not present appears to arise from the observation that any such height variations present are much less than an atomic diameter, though these height variations refer to the difference in minimum and maximum heights in an area rather than with respect to expected interlayer distances which may be modulated by the presence of adsorbates. Lui et al. only report that their graphene samples are extremely smooth, which would not be contradicted by the presence of an adsorbate layer of uniform height as the stripes appear to be.

As such, we conclude that although contaminants or trapped adsorbates may in some instances be removed by a self-cleaning phenomenon or specifically removed by annealing for example, this should by no means be assumed to be a universal

phenomenon of vdW structures. This presents serious implications for stacked structures such as vdW heterostructures more generally and for superlubricity specifically, where this challenge appears to have become increasingly acknowledged in the past decade[144–146] despite the stated previous assumption that adsorbates would be removed. Mayorov et al. observed that ballistic transport of charge carriers in vdW heterostructures is entirely inhibited by the presence of trapped adsorbates at the interface between the graphene and hBN layers for example[147]. Similarly, Frisenda et al. report decreased mobility in regions where interlayer contaminants are present in vdW heterostructure-based transistors[148].

A number of techniques have been proposed to limit the presence of contaminants or to remove contaminants present, such as assembly in a pure argon or nitrogen environment[149], encapsulation[150], thermal processing[141] and nano-"squeegee" cleaning by AFM tip. In general, these cleaning methods are slow, cumbersome and risk damaging the device. Furthermore, if such devices are to be used in applications outside of precisely controlled research environments alone, knowledge of the effects of ambient conditions such as we consider here will be highly relevant.

2.4.1 Effect of stripes on superlubricity

It has broadly been thought that superlubricity could only exist in exceptionally clean circumstances. This was supported for example by Peyrard and Aubry's requirement for cancellation of lateral forces[151] and following He et al.'s demonstration that "third bodies" such as small hydrocarbon molecules can adsorb onto crystalline surfaces to lock these contacting surfaces together for example[152]. Indeed, most experiments studying superlubricity have been performed specifically in UHV conditions[24,137,153,154] or on interfaces with applied mechanical cleaning as a result of oscillation of the surfaces for example[25,26,29,155]. As such, the presence of these stripe adsorbates introduces complications for the existing model of ribbon growth motivated by the continuum energy balance described in section 1.6, which concludes that very low

friction must be present at the ribbon sliding interface. As a reminder, this described the internal energy *U* of the symmetric, tapered ribbon as

$$U = U_{fold} + 2\lambda c + \Delta W_{2D-s}(A_{sheet} - A_{pleat}) - \Delta W_{2D-2D}(A_{pleat}) \quad (47)$$

Here, we can determine the fracture energy release rate by taking the derivative of eqn. (47) with respect to increase in tear path length δc. Equating advancing and resisting forces at each crack tip under end-of-growth conditions, we find

$$F_{advance} = \frac{\Delta W_{2D-2D} \cdot w\, cos\theta}{2} + D\, S\, sin\theta = \frac{\Delta W_{2D-s} w \cdot cos\theta}{2} + \lambda = F_{resist} \quad (48)$$

While this model was devised with a picture of a clean graphene sheet, it may still broadly capture modifications that might arise from the presence of further species or contamination. The presence of an intermediate contaminant species in the interface is expected to increase flake-ribbon separation relative to expected graphene-graphene separation of 0.335 nm, reducing interlayer coupling and decreasing adhesion between the flake and ribbon, $\Delta W_{2D\text{-}2D}$. As the stripes align along the armchair axis of the graphene but at most one torn edges of the ribbon can also lie in this direction, the alkane chains comprising the stripes must also be displaced, which is expected to increase the rupture energy of graphene λ. As such, the presence of stripes modulates nearly every component of the above continuum energy description. As the presence of stripes may introduce a non-negligible sliding friction, to iterate on eqn. (39) in section 1.6, we introduce a friction term by hand here in the denominator i.e. resisting growth as in the lefthand side of eqn. (49) below. Now explicitly accounting for a possible resistive frictional term F_{fric} introduced by the stripes, fracture mechanics determines that the tear will take the path of minimum force[86]. This is obtained by maximising the energy release rate of the system i.e. differentiating eqn. (37) with respect to θ, yielding

$$tan\theta \;=\; \frac{F_{fold}}{F_{int} + F_{fric}} \;=\; \frac{2DS}{(\Delta W_{2D-2D} - \Delta W_{2D-s})\, w + F_{fric}} \qquad (49)$$

We note however that taper half-angle θ appears constant even over ribbons of micrometre lengths, suggesting only a very small contribution by this possible resistive friction term F_{fric}.

This allows us to obtain an estimate for the upper bound of graphene/stripe - stripe/graphene sliding friction. Annett et al. estimated an interfacial energy $\Delta W_{total} = (\Delta W_{2D\text{-}2D} - \Delta W_{2D\text{-}s}) \approx 0.02$ eV nm^{-2} for a ribbon with constant taper angle and final width of 350 nm from analysis of the speed of ribbon growth in terminal conditions before growth stopped/became sufficiently slow to no longer be observable in AFM imaging timescales[89]. This suggests a frictional force $F_{fric} \ll \Delta W_{total} \cdot w \approx 1$ nN. Alternatively, given the observed ≈2 μm^2 area of the ribbon used in the above analysis, this yields a frictional shear stress $\sigma_{fric} \ll 1$ kPa. Considering the ribbons used in the above experiment, this provides a more conservative estimate of the upper bound of friction of ≈10 kPa, obtained by noting the constant taper angles and final ribbon area of ≈0.1 μm^2.

This calculation can be compared to estimates in the literature of superlubric shear stress of incommensurate graphene-graphene interfaces in ambient conditions, where contaminants are also expected to be present even if not specifically addressed by the authors. Using the graphite mesas described in section 2.4, Wang et al. adhered the upper graphite flake of a mesa to a micromanipulator tip to fully lift it away, then left the newly formed interface exposed to ambient laboratory conditions for varying times from 5 to 1000 minutes. While contaminants are not characterised here, for each length of exposure time, friction measured immediately upon replacing the upper flake is ≈2-4 times higher than friction before exposure and reduces following a running-in process with reciprocating motion between the flakes, initially very quickly in the first 10-100 sliding cycles[27], though only to ≈1.5 times the initial friction even after hundreds of sliding cycles and never returns to the pristine value. Wang et al. estimates an interlayer shear stress of 50 kPa for such a contaminated incommensurate contact, while Deng et al. report an interlayer shear stress of 7 kPa from similar experiments in ambient

conditions (albeit not quantifying exposure time to contaminants)[27]. Liu et al. report a comparable interlayer shear strength of 15 kPa derived from strain evolution between layers. These values are found to be generally consistent with the upper bound of ≈10 kPa that we have derived. The formation of an AK ribbon by folding and sliding can be considered as a half-sliding cycle from the perspective of self-retracting motion cycles, such that the cleaning effect, which cannot perfectly restore a graphite mesa interface even upon hundreds of cycles, should not be expected to remove a significant amount of adsorbate species.

We can also check for consistency with reported values of line energy of torn graphene. Considering only forces along the direction of ribbon growth in Annett et al.'s continuum model[89], we obtain

$$\Delta W_{2D-s} w + 2n\lambda \cos\theta = \Delta W_{2D-2D} w \quad (50)$$

for *n*-layer graphene. Given a small, constant taper angle θ such that cos (θ) ≈1, we note Annett et al.'s observation that a plot of w_{final} versus *n* yields a slope of (2 λ / ΔW_{total}) ≈150 nm. Rusanov et al. calculated a line energy of 1.67 × 10^{-9} J m^{-1} (10.4 eV nm^{-1}) for torn graphene[156], from which we can calculate ΔW_{total} = 0.14 eV nm^{-2} (22.4 mJ m^{-2}). This is consistent with the values for ΔW_{2D-s} and ΔW_{2D-2D} from Li et al.[157], from which an interfacial force of ($\Delta W_{2D-2D} - \Delta W_{2D-s}$) ≈0.23 eV nm^{-2} (37 mJ m^{-2}) is obtained. This provides a friction shear stress upper limit of ≈10 kPa for ribbons with final widths of 300-400 nm and few square micrometre area, consistent with our previous derivation.

These reports of ambient superlubricity, as well as our own, nonetheless appear to contradict the established understanding of superlubricity. However, we note that He et al.'s indeed specified that contaminants leading to loss of superlubricity should be sufficiently mobile along the interface to achieve a local energy minimum without deformation of the contacting bodies. While stripe motion and mobility has been demonstrated, this occurs over longer timescales of minutes-hours, or upon the application of high force setpoints and hence high local pressures in C-AFM, and does not appear to occur within ribbon interfaces where stripes remain relatively stable, potentially owing to their high adsorption energies to graphene. The strict alignment of

stripes with the host graphene sheet's armchair direction suggests that lattice mismatch induced superlubricity may have an analogue in stripe orientation mismatch friction dependence, as a graphene-graphene interface in incommensurate atomic matching will as a consequence also feature stripe incommensuration. Furthermore, the stripe motion and mobility demonstrated through TFM and PFQNM in Fig. 2.6 and Fig. 2.7 respectively are not expected to represent sufficient mobility to satisfy He et al.'s requirements, and avoid creating pinning sites due to their stability against rotation when sheared. Stripes are sufficiently stable that the adhesive pressure present in a ribbon interface cannot displace them for example, domain changes occur over only relatively small proportions of surface areas relative to entire flakes, with the majority of the area of domains appearing stable. However, in our systems, superlubricity is of primary importance specifically in ribbon growth after nucleation through sliding and folding, a process which occurs very quickly. Annett et al. estimate that this self-assembly can occur within a fraction of a second even at room temperature[89], similar to self-retracting motion of superlubricious graphite mesas at mm/s speeds at room temperature[158], and definitively occurs over a timescale less than that of AFM imaging of several minutes. This is also supported by observations in this research, whereby ribbon growth is not observed during AFM imaging following nanoindentation using another system (with a resulting minimum time of at least 30-60 minutes between indentation and imaging), implying that almost all, if not all, self-driven ribbon growth occurs in smaller timescales. Where ribbons are nucleated by AFM indentation alone, allowing a reduction in the timescale between indentation and imaging to as little as 10 minutes, growth is still not observed. Furthermore, where growth occurs as a result of AFM cutting for example where the nucleating event and imaging can occur simultaneously, growth still appears to occur within as little as a single fast axis scan line, or 1 second at typical scan rates as will be discussed in further detail in section 3.2. Overall, we anticipate that the timescale on which ribbon growth occurs is small enough relative to any stripe motion or realignment to allow us to consider these stripes as insufficiently mobile to destroy the structural superlubricity between the underlying graphene sheet and the growing ribbon.

2.5 Interactions of surface features and stripe friction domains

As discussed above, a key aspect of the stripe structures is that they align along the armchair axis, giving rise to the characteristic three-fold symmetry of the friction domains with respect to angle and allowing a relatively simpler method of inferring crystallography of graphene sheets in AFM without the much more challenging requirement of direct atomic resolution[159].

A further consideration then is, of the three equivalent directions available on a graphene surface, how does the hydrocarbon adsorbate material "choose" which of these to follow? There currently does not appear to be a convincing answer to this. Gallagher et al, using a combination of "brushing" and erasing of domains in TFM, wrote an identical stripe domain pattern across different locations on a graphene flake[125]. This pattern developed differently depending on location, with the newly defined domains of the pattern in some places growing or in others diminishing, with the rate of growth or shrinkage also dependent on location. On other flakes however this patterning may occur much less effectively. They therefore conclude, in the absence of symmetry-breaking mechanisms, that the relative stability of domains is determined by local strain induced by the substrate in the graphene sheet (e.g. during mechanical exfoliation to the surface), and hence the particular armchair direction of three possibilities that is chosen. Firstly, it is instructive to examine why stripes align along this direction rather than along the zigzag for example or without respect to crystallography whatsoever.

McGonigal et al. in 1990 studied *n*-alkanes (specifically *n*-$C_{32}H_{66}$) applied directly on graphite samples[160]. Their STM imaging shows an arrangement of stripes on the graphite surface in a manner near identical to that of the relatively shorter alkanes believed to comprise stripes studied here. They firstly surmise that this adlayer is commensurate with the graphite lattice, as aliasing due to mismatching periods of the substrate and adlayer were not observed. Where the alkane chains are oriented along the zigzag direction, the alkane C-C-C zigzag length is 0.251 nm, which deviates from the spacing of the hollows of the graphite hexagonal structure of 0.246 nm by only 2%. This

matching gives rise to both the commensurate structure of the adsorbate and the adsorbate's affinity to graphite[161]. As these alkane chains which form the inner structure of the stripes align perpendicular to the stripe lines observed in AFM, the stripes then appear along the armchair direction. This is illustrated in Fig. 2.9. A sample of our PFQNM imaging of stripes on graphene is indicated for reference in Fig. 2.9 (a), with the blue arrow indicating the stripe direction as observed by AFM and inferred crystallographic directions per Gallagher et al.'s observations[125]. This arrow also indicates the direction of stripes relative to the orientation of the individual alkane chains (horizontal series of dots) which comprise these stripes in Fig. 2.9 (b). This matching may also account for the stripe direction chosen in a particular area of graphene. We therefore consider surface features on graphene sheets, detectable by PFQNM, which may be suspected to influence strain in a graphene sheet such as local effects of indents and other surface features which appear to directly influence friction domains, namely step edges, wrinkles and nucleated ribbons.

We observe a number of common features of stripe domains which can help to further this understanding. Stripe domains may be continuous over wrinkles with heights of

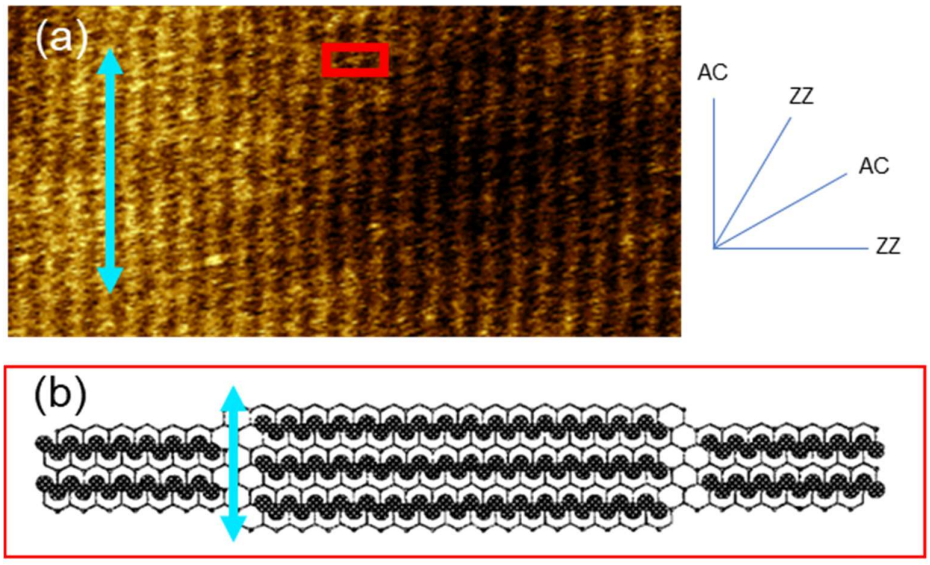

Fig. 2.9: Alignment of alkane chains on graphite lattice. (a) Stripes align along armchair direction of graphene lattice. (b) Schematic representative of zoom-in to area highlighted in red in (a). Alkane chains align along zigzag direction, with alkane chains perpendicular to stripe direction indicated by blue arrow. (b) reproduced from 160.

only a few nanometres for example, as in Fig. 2.10 (a) and (b), or wrinkles of similar widths but even lower aspect ratios can appear as strict edges, as in Fig. 2.10 (c) and (d). Often different orientations are observed around step edges, even where the upper and lower step are of the same crystallinity.

We can produce steps through ribbon nucleation (albeit incommensurate with the underlying sheet), and may expect local strain to be influenced by indentation of the graphene sheet[162], which provides further avenues to explore how these features may affect domain formation and shape. We therefore selected two graphene sheets which were mechanically exfoliated on the same day, with indentation and ribbon nucleation occurring on one 39 days later (Fig. 2.11), and on the same day on the other (Fig. 2.12).

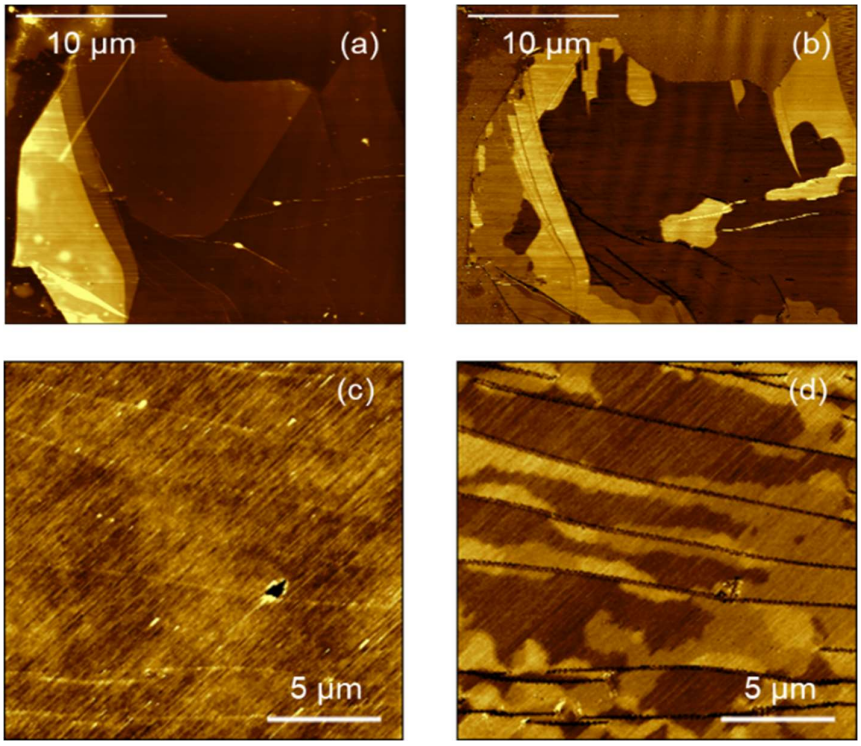

Fig. 2.10: Effect of wrinkles and step edges on stripe domains. Effect of steps edges on simultaneous topography (a) and transverse force microscopy (TFM) signal (b) of a graphene sample with complex stacking and wrinkles (height of 2-6 nm and 0.2 µm width) throughout. On this sample, domains appear invariant to stripes, and do not change orientation at one 4.5 nm step but do change at a neighbouring 5.5 nm step. Simultaneous topography (c) and transverse force signal (d) of a graphene bilayer with wrinkles of 0.1 – 0.3 nm height and 0.2 µm width which are faintly visible in topography, and which appear as black lines in TFM image. Unlike in (a) and (b), domains in this area are generally not continuous over these lower aspect ratio wrinkles. Total linear z range in (a) of 20 nm and in (c) of 1.0 nm.

Fig. 2.11 (a) and (b) show the topography and simultaneous TFM respectively immediately before indentation. An array of 10 × 10 indents was performed on this three-layer flake by AFM using cube corner diamond tip to a load of 0.5 mN, corresponding to depths of 45 nm. No alteration of the stripe domains is observed due to the indentation nor is any evolution of the domain pattern seen 30 days after indentation (Fig. 2.11 (d) – (e)). This suggests that the effect of e.g. induced strain in the sheet may be negligible, or perhaps that these domains are sufficiently stable due to the existing strain in the sheet.

However, this is not the case in another sheet depicted in Fig. 2.12, on which AFM indentation with the same parameters was performed within 140 minutes of exfoliation rather than after 39 days. Domains of course cannot be imaged prior to indentation and nucleation in this instance as it is performed too soon (within 140 minutes) after exfoliation for the adsorbates to build up. 3 arrays of indents are performed on this sheet, with 75 indents in each array. The majority of the indents in each array lie solely within the single stripe domain dominant in that region of the sample. However, when the lateral force friction domains are imaged on this sample seven days later, a strong relationship is observed between the indentation-induced surface features and the domain shapes and boundaries. Firstly, ribbons in Fig. 2.12 are readily identified even in TFM by their strong local contrast to the underlying domain, suggestive of a twist angle between the host flake and ribbon as expected for superlubric growth.

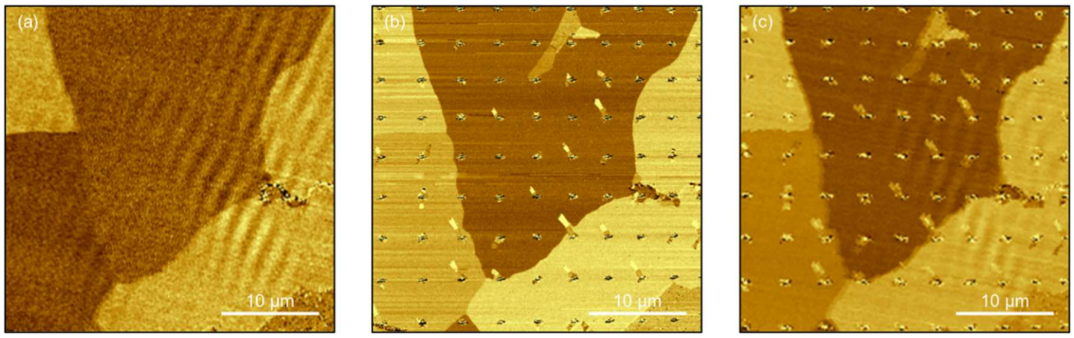

Fig. 2.11: Effect of indentation on "established" domains of stripes. (a) TFM of a three-layer graphene flake taken 41 days after exfoliation to the surface with distinct friction domains observed immediately prior to AFM indentation. Subsequent AFM indentation was successful in nucleating multiple ribbons, as shown in TFM imaging (b) performed 85 minutes after indentation. (c) Follow-up TFM taken 30 days later shows that these domains have remained stable over the intervening time.

From our experience, domain shapes as illustrated in Fig. 2.6 and Fig. 2.11 for example are typical, with blob-like domain shapes and low curvature domain edges. By contrast, the domain boundaries in Fig. 2.12 (a) are strongly defined by indentation craters and self-assembled ribbons features. In Fig. 2.12 (b) and (c), the edges of the sheet torn during a ribbon self-assembly define the stripe domains in a manner reminiscent of a child's "dot-to-dot" drawing. Despite this, there does not appear to be a uniform response of the sample to each indent as derived from the resulting domains around each indent, even though many domains in Fig. 2.12 can be approximated well by the "dot-to-dot" drawing. In many instances, two different domains are observed at opposite sides of a single ribbon, with domain boundaries in Fig. 2.12 (a) defined almost exclusively by the position of the heads of the ribbon that have grown into place before stripe formation.

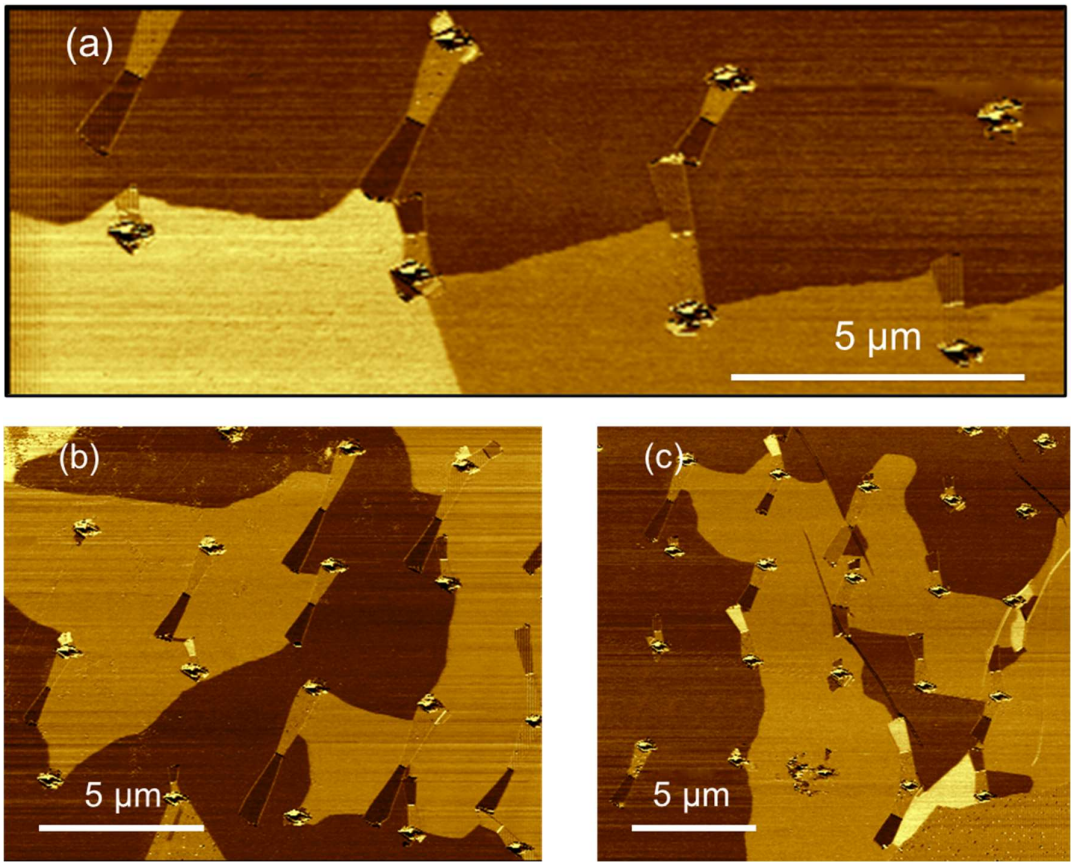

Fig. 2.12: Effect of indentation on "fresh" domains. (a)-(c): Sample areas of a bilayer flake with three 15 × 5 arrays of indents performed within 140 minutes of mechanical exfoliation, and imaging performed 7 days later when domains are readily visible in TFM. Domain shapes and boundaries appear to be defined by surface features such as ribbons and indents, suggesting the presence of a symmetry-breaking mechanism.

Initially, it may appear this common feature of ribbon heads being located at domain boundaries arises from a subtle difference in sliding friction. This may be speculated to originate in a form of stripe-stripe incommensuration between the stripes at the underside of the ribbon and the host flake, whereby friction between the growing ribbon would vary with the varying stripe orientation in the domains into which it grows. This could result in termination of ribbon growth at this boundary where stripe-stripe friction apparently increases. However, we emphasise that stripes are not expected to be present while this particular ribbon growth occurs as indentation is performed shortly after exfoliation. Instead, it appears that the domains form around surface features, or perhaps local strain induced by the applied indents specifically.

This first possibility appears that it should be discounted in this instance as domains are not expected to be present during this ribbon growth. However, comparison of ribbon growth within 140 minutes of indentation and during TFM imaging 7 days later reveals a number of ribbons which had not visibly nucleated from their respective indents in the early imaging but had grown in the meantime, as well as ribbons which underwent further extensional growth in that interval, in accordance with Annett et al.'s observations on ribbon growth[89]. Considering that ribbon growth continues for up to 14 days after nucleation, that stripe domains could form on the surface within as few as two days, and that stripes may even be present at the new or growing ribbon interfaces by intercalation, this possibility that a form of stripe incommensuration which affects sliding friction and results in ribbon growth ending as the growing ribbon head reaches a domain boundary appears plausible.

This also suggests the possibility of domain engineering, analogous and possibly related to strain engineering of graphene by non-rupturing AFM indentation[162]. While this could allow control of the proposed stripe incommensuration friction, it also can have a clear effect on mechanical properties as measured by PFQNM.

As stripe orientation can have subtle effects on measured mechanical properties of graphene, this could present a method of tailoring such properties to a limited degree. While domains being affected by indentation sites also provides further support to the claim of domains being defined by sheet strain, this cannot wholly explain why the

edges of ribbons, which should not affect strain on the underlying sheet, in fact appear to influence domain boundaries strongly.

Although not universal, we have on multiple occasions observed a clear contrast in mechanical properties of exfoliated graphene sheets correlated exactly to stripe domains, as in Fig. 2.13. No contrast is observed in adhesion or dissipation channels, suggesting that this contrast does not arise from a change in surface energies or chemistry between these areas. However, both deformation and Young's modulus (log scale) show a distinct contrast here, with differences of 20 pm and 0.25 respectively, corresponding to a difference of 5 GPa. Mechanical properties measured by PFQNM are derived from fits of a force-distance curve at every point, which in this instance with a relatively hard substrate and soft cantilever corresponds to a very small total deformation, the response of which may be dominated by stripe interactions rather than the graphene sheet or bulk substrate.

Fig. 2.13 also highlights a feature noted by other researchers in imaging stripes by PFQNM[132,163]: that while stripes may be poorly visible in one channel, such as the lower

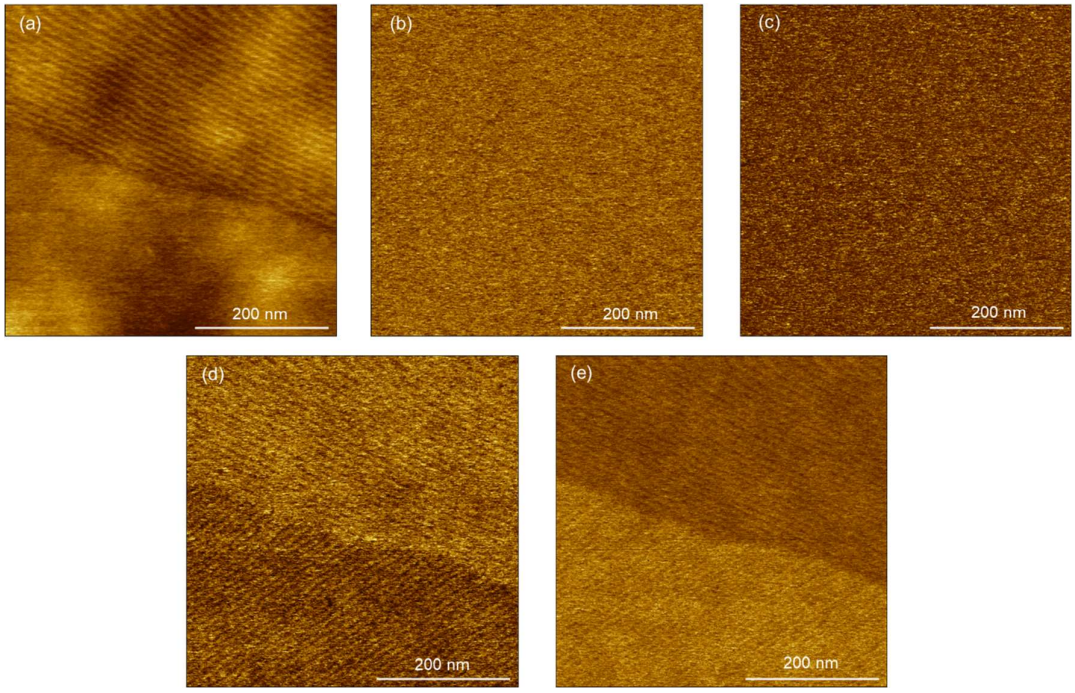

Fig. 2.13: Correlation of mechanical properties to PFQNM channels. (a) Height, (b) adhesion (c) dissipation, (d) deformation and (e) modulus (logarithm). Linear z scales: (a) 1.0 nm, (b) 100 eV, (c) 0.3 nN, (d) 0.2 nm and (e) 2.

domain in height in Fig. 2.13 (a), they may be readily observed in other channels, such as deformation and Young's modulus here (Fig. 2.13 (d) and (e)).

2.6 Stripes between surfaces

In section 2.4, we established that stripes are not necessarily cleaned from, or "squeezed out" from graphene-graphene interfaces by attractive vdW forces between the host sheet and the folded ribbon by examination of the underlying sheet graphene after rotation of the entire ribbon associated with some additional extensional growth of the ribbon. In Fig. 2.14 (a), a ribbon formed by gr-AK self-assembly was then imaged by C-AFM at a 30 nN setpoint to undergo tip-induced additional folding. This is seen in a kind of intermediate form in the intermediate Fig. 2.14 (b), where the AFM tip is dynamically inducing folding while also imaging this folding. With the slow scan direction from right to left of the image (indicated by yellow arrow) and fast scan axis vertical in Fig. 2.14 (b), some minor extensional growth appears to have occurred immediately upon the tip reaching the upper edge of the fold, with a sudden jump seen soon after within a single scan line. Then switching to PFQNM, an image taken 160 minutes after this manipulation (Fig. 2.14 (c)) reveals the final, full, induced folding of a segment of the ribbon including stripe structures around the axis indicated by the red line in Fig. 2.14 (c) in the direction indicated by red curved arrow. This manipulation resulted in the exposure of the areas of the graphene sheets previously within the ribbon interface (highlighted by green dashed lines in Fig. 2.14 (c). We denote the area of the now exposed ribbon underside as I and the corresponding area of the host sheet as II, left and right of the red axis of rotation within green dashed lines respectively. Similarly, the area of graphene previously in contact with the SiO_2 substrate is also exposed (marked III, highlighted by blue dashed lines in Fig. 2.14 (c). III represents a region of the host sheet underside now folded over and IV the substrate surface that this graphene was in contact with, left and right of the red axis of rotation respectively.

This ribbon was nucleated and remained stably present on the sample for over 3 months, with the host graphene sheet having been mechanically exfoliated over 2

months prior to that. A number of conclusions can be derived from this observation alone. Firstly, the stripes contained within this green highlighted area in Fig. 2.14 (c) (both on the ribbon underside I and on the host sheet II) were also not removed by sliding of the ribbon over the host sheet. In the earlier Fig. 2.8, it may be claimed that removal of stripes by attractive vdW forces failed due to the limited time, as the ribbon rotation which revealed these stripes occurred only 3 days after ribbon nucleation and creation of this interface. In Fig. 2.14 (c), a former ribbon-sheet interface is seen mirrored around the red line within the green highlighted area (I and II). Here, we observe that stripes remained present at this interface for 3 months following ribbon nucleation and that the proposed universal self-cleaning effect in vdW interfaces has evidently not occurred here. Although no timescale over which this proposed self-

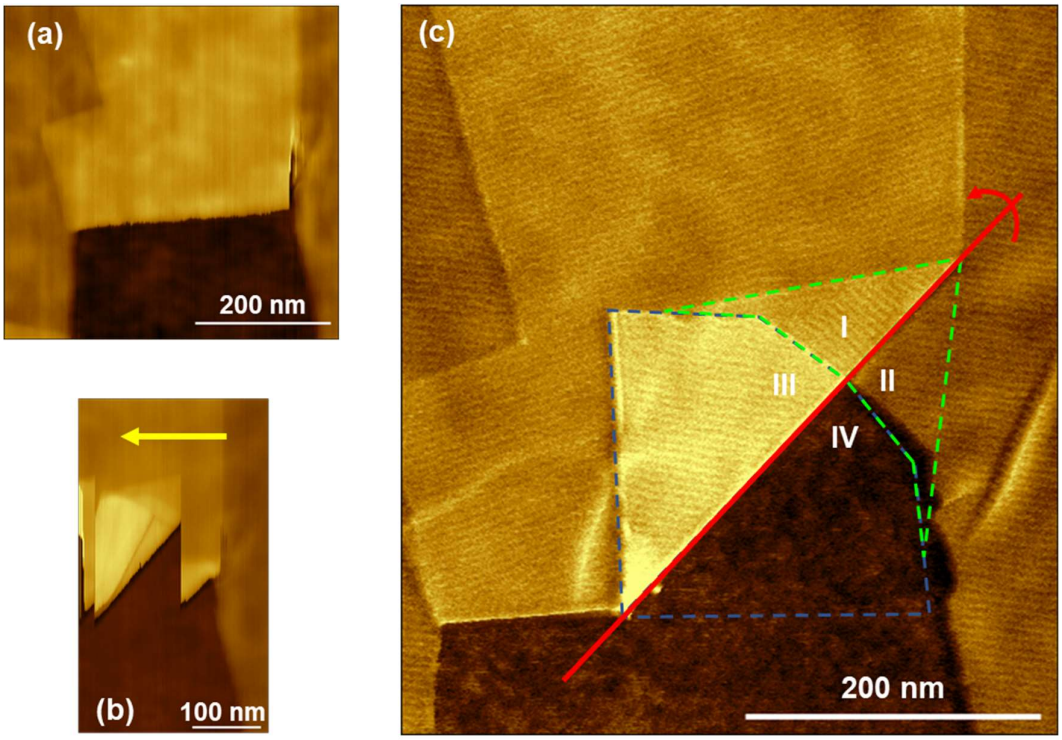

Fig. 2.14: Stripes on folded ribbons and between substrates. (a) Self-assembled ribbon in C-AFM (topography channel). (b) The AFM tip is used to manipulate the fold to induce further folding, C-AFM topography. Yellow arrow indicates slow scan direction. (c) PFQNM imaging of the newly induced fold shortly after folding around the rotational axis (red) in direction of arrow, with resulting mirror symmetry of shapes defined by dashed green and blue lines (former host graphene sheet-ribbon and former host graphene sheet-substrate interfaces respectively). This folding reveals stripes present on all graphene surfaces, including at sheet-substrate interface area never exposed to the surface previously. Folding Total linear z range of 5 nm, 10 nm and 6 nm for (a), (b) and (c) respectively.

cleaning may act was provided, we suggest that its absence over 3 months indicates that it is not applicable to this interface.

Of further significance, stripes are observed on the area of graphene which, only 160 minutes prior to this imaging, was directly in contact with the silica substrate since the time of exfoliation (region III, graphene within blue dashed lines in Fig. 2.14 (c)). This graphene was not exposed to the atmosphere long enough for stripe material to adsorb. These stripes have the same hight, pitch and orientation as the original surrounding flake material, albeit on the opposite side of the sheet. Considering the impermeability of graphene to atoms/molecules as minute as helium and hydrogen[45], it appears unfeasible that the alkane chains which comprise stripes could directly penetrate the sheet to form on the underside of the graphene sheet at the sheet-substrate interface, and neither could stripes form on these areas in this timescale from previous arguments. This also could not have built up before or during the process of mechanical exfoliation, as prior to exfoliation this graphene sheet would be stacked relatively centrally within as many as 3 million layers of graphene and would have been exposed to the atmosphere for a few minutes at most during repeated exfoliations from tape to tape before pressing onto the prepared, cleaned SiO_2 substrate. From this, we contend that stripe-forming hydrocarbons may intercalate into the graphene-substrate interface over sufficiently long timescales and there form stripes as well.

We therefore set out to examine this phenomenon of stripes being present not only within ribbons, which are novel as they are both twisted and folded graphene interfaces, but also at graphene-substrate interfaces. These interfaces are typically not directly visible, being observed only by cross-sectional imaging techniques by Geim et al. for example[140]. However, ribbon nucleation and folding readily exposes large areas of such substrates for us to examine.

Indentation with a diamond cube corner tip using an AFM was performed on the three-layer graphene flake in Fig. 2.15. This sheet was mechanically exfoliated 4 months prior to this indentation, with stripes readily visible on the surface as expected immediately before indentation. However, following only AFM-based indentation (Fig. 2.15 (a)), nucleation and growth of ribbons rarely occurs, attributed to the absence of lateral oscillations during indentation. Ribbon growth can proceed in high yields

however with the application of AFM “hard tapping”, as will be described further in Chapter 3. In Fig. 2.15 (b), taken following application of hard tapping on (a) for 11 minutes, a small degree of ribbon growth has occurred. After a further 11 minutes of hard tapping in (c), significant extensional growth has occurred of the ribbons first observed in (b) as well as nucleation and growth from additional indents.

Further detailed study by PFQNM of the regions indicated in Fig. 2.15 (c) as green and red boxes appear in Fig. 2.15 (d) and (e). These show that stripes are readily visible on both ribbons within only 29 and 42 minutes respectively after their growth. The upper side of the folded graphene that we observe in Fig. 2.15 (c) – (e) as the ribbon surface was previously the underside of the graphene sheet at the sheet-substrate interface. An additional feature of interest in (d) is observed when considering the graphene armchair axes inferred from the stripe directions, following the assumption that the stripe directions follow the armchair axes. The stripe direction (and inferred armchair axes) of the ribbon and of the host flake are indicated by yellow and red dashed lines respectively in (d) and (e). By mirroring the armchair axes of the ribbon (yellow dashed lines) around the axis of the fold (red line with curved arrow indicating mirror axis), we can infer the armchair axis of the now-folded graphene as it lay on the now-peeled area prior to folding. This direction is indicated by gold dashed lines, with rotation around the axis of 98° and 77° in (d) and (e) respectively. The stripe direction (and hence inferred armchair axis) on the host graphene is indicated by cyan dashed lines in both.

In (d), mirrored ribbon armchair axis and host sheet armchair axes differ by 39° rather than the expected (n × 60)°. The expected (n × 60)° interval is observed between armchair axes of ribbon and host sheet in (e) however. Furthermore, the stripe pitch is measured as 4.5 nm on the ribbon in (d) but 5.5 nm on the host sheet in (d) and on both ribbon and sheet in (e) ((d) and (e) being on the same graphene flake as indicated in (a)-(c)).

With this being an exceptional observation, we tentatively attribute this to a rearrangement of the stripes upon exposure to the surface. Nonetheless, we can follow the same argument made for the previous sample in Fig. 2.14 above: with the underside of the flake exposed to air for minutes at most during exfoliation and to air after exfoliation for less than an hour, stripes are nonetheless visible at these exposed areas

of graphene. We conclude that the hydrocarbons comprising the stripes can intercalate between the substrate and graphene sheet. This is therefore not an isolated event but an repeatedly observed phenomenon.

This is a somewhat surprising result given that graphene is expected to primarily follow the morphology of the underlying substrate, limited only by its low out-of-plane bending stiffness which prevents complete conformation[164]. Referring back to eqn. (47), as we have now provided evidence that the stripe contaminant can also develop within the graphene-substrate interface, we expect that this may also modulate the value of the graphene-substrate adhesion energy $\Delta W_{2D\text{-}s}$, further demonstrating the influence that these stripes can have on every aspect of ribbon energetics. However, inspired by

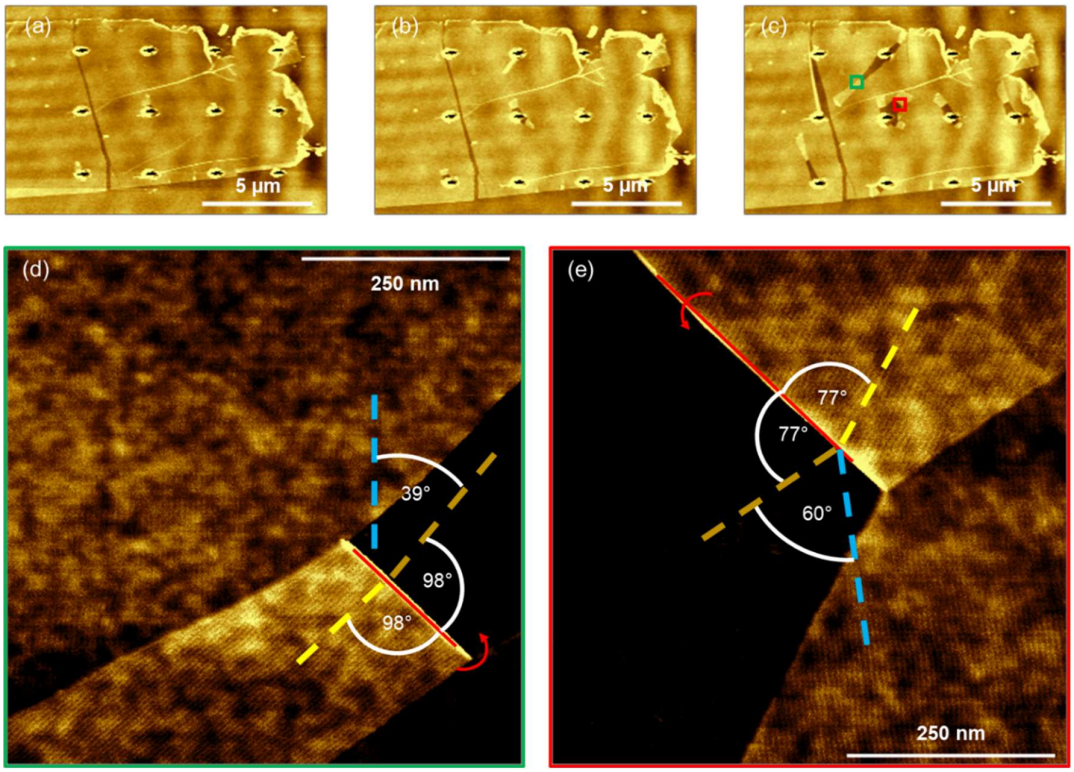

Fig. 2.15: Stripes on newly formed ribbons produced by AFM indentation and AFM-assisted nucleation. (a) Three-layer graphene sheet with AFM cube-corner indentations at 4 µm spacing in x and y. In this method described further in section 1.6, nucleation does not occur alongside indentation and instead must often be produced by AFM "hard tapping" method. Ribbon growth is observed as a result between (a) and (c) over the course of 22 minutes, with minimal nucleation observed in the 120 minutes prior to this application in (a). Two ribbons are selected in (d) and (e) from green and red highlighted areas in (c) respectively, with well-developed stripes observed on both. PFQNM topography total linear z range of 4 nm for (a) – (e).

this discovery, we can still examine one further location in which stripes may be present- between graphene layers.

As a final example, we consider gr-AK growth in a very thick layer of graphene – a sample closer to a graphitic flake. We have found a novel result that ribbon growth can also occur in any thickness of graphene/graphite with the application of what we term a hard tapping method. This method provides an alternative, external driver to spontaneous ribbon growth by replacing the thermodynamic energy minimization effect of exchange of graphene-substrate adhesion for graphene-graphene adhesion with small amplitude oscillatory mechanical excitation from the AFM tip.

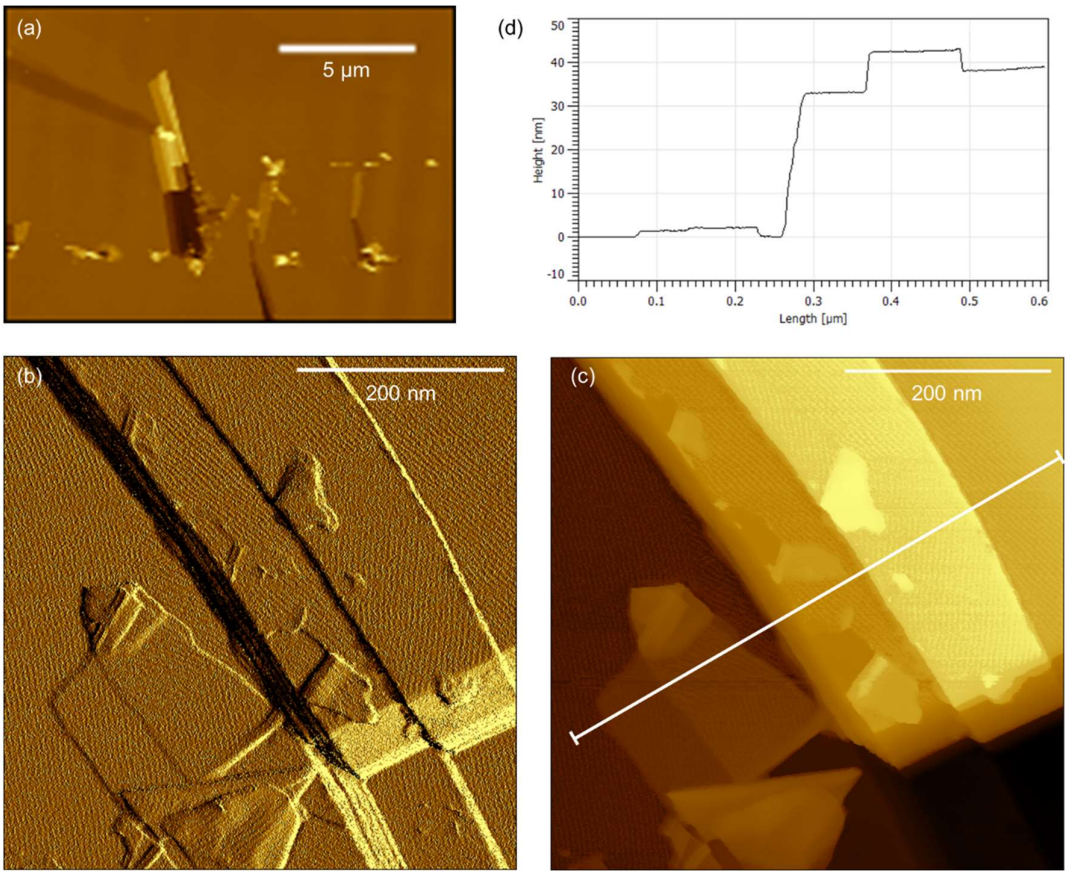

Fig. 2.16: Stripes on all steps of a thick ribbon peeled from graphite. (a) Overview of the complex ribbons which can result from application of "hard tapping" on very thick samples (>100 nm), total z range of 70 nm. (b) Stripes on all steps of surface, as depicted in PeakForce Error channel to allow visibility of presence of stripes on all surfaces regardless of height. (c) Adaptive nonlinear colour mapping of topography image showing stripes directly, total z range of 88.9 nm. (d) Height profile along line in (c) (from left to right) indicating size of steps on thick graphitic ribbon.

We begin with a graphite sample of 58 nm thickness on a silicon substrate shown in Fig. 2.16. The graphite flake was mechanically exfoliated over 3 months prior to AFM indentation, while nucleation by hard tapping was performed within 1 hour of indentation and imaging in Fig. 2.16 (b) and (c) within a further 103 minutes after nucleation. As a result of AFM indentation and hard tapping on this 58 nm thick sample, we observe the production of a single ribbon with unusual features: it has a variable thickness across its width of 33-43 nm and the exposed peeled area consists of 15-25 nm thick graphite rather than SiO_2 substrate. An example of such is seen in Fig. 2.16.

As per previous arguments, stripes could not form from ambient in this timescale. Nonetheless, stripes are observed on every graphene step and surface in Fig. 2.16. We emphasise that less than 3 hours prior to this observation in Fig. 2.16 (b) and (c), all of these surfaces of the ribbon were buried 33-43 nm deep while other areas of lesser thicknesses exposed by the damage associated with the hard tapping technique with depths as little as 4 and 6 layers (bottom left of Fig. 2.16 (b) and (c)) similarly show stripes consistent with extrapolation of the armchair axis in other locations.

We can contrast this method of revealing buried interfaces in graphite by ribbon nucleation in our 100+ layer graphite flakes with cleavage of graphite mesas as performed by, among others, Liu et al.[29] and Wang et al.[28] as discussed above.

While the graphite mesa setup can allow examination of interfaces by shearing a portion of the mesa, there is no direct control of where in the stack this cleavage may occur. In the graphite mesas, cleavage occurs at pre-existing naturally incommensurate interfaces in the mesa among the ≈4,000 layers present in a typical HOPG mesa[138]. These incommensurate interfaces can arise from a grain boundary at an arbitrary depth in the mesa for example[29]. Lower shear resistance is present at such grain boundaries, facilitating the superlubric self-retraction phenomenon. Similarly, in a ribbon nucleated from 100+ layer graphite, we cannot control which layer-layer interfaces of the graphite become revealed i.e. the number of layers in the ribbon or the number of layers remaining in the peeled area. Shearing of a graphite mesa reveals only a single layer-layer interface. In contrast, ribbon nucleation and the additional tearing induced by "hard tapping" in graphite flakes reveals at least 10 different step heights in Fig. 2.16. Each step height corresponds to graphene layers previously at buried interfaces of

varying depths equal to that step height across the flake. As in Fig. 2.16 (b) and (c), stripes are present at every one of these steps, and therefore at each of these buried interfaces at different depths in the graphite flake. We can therefore exclude a hypothesis that stripes being observed on these ribbons implies only that stripe hydrocarbons may be able to intercalate into rare "weak" interfaces which may have less intimate contact between neighbouring layers. While we cannot here establish a length of permeation by diffusion of stripe material, we note that stripes have been observed on all ribbons on the same flake as in Fig. 2.16, with ribbons located up to 50 μm from flake edges. We present a method for experimentally determining a rate of intercalation and potential diffusion limit in section 6.2.

This observation presents another pressing query: if stripe hydrocarbons can intercalate between apparently any number of layers even when embedded deep within relatively thick graphite, then how are any graphene surfaces ever observed to be clean of stripes? We have demonstrated that graphene layers freshly exposed by exfoliation do not feature stripes within less than 2 days, in accordance with other experimental observations[131,132,96] so those layers should be pristine upon exfoliation. Here, we hypothesise that this distinction may arise from the different size scales of graphite that we consider pre and post mechanical exfoliation. The natural graphite graphenium flakes used for mechanical exfoliation here are of ≈0.5 cm to 1.0 cm widths and ≈0.1 cm thicknesses (or Kish graphite flakes of 1-2 mm widths and ≈0.2 mm thicknesses). The size of graphite flakes that are commonly found on the SiO_2 substrate after exfoliation, such as that indented in Fig. 2.16 are 100 – 500 μm in width and 50-200 nm in height. This difference in lateral scale of 100-fold could suggest that the intercalation process is self-limiting with distance from the flake edge, so can occur to provide the stripes in Fig. 2.16 but would not be expected to be observed on these smaller graphite flakes remaining after exfoliation, which should be randomly distributed across the sample relative to the position of the original graphenium flake. As the exfoliation results in tearing, often along crystallographic directions, these newly formed edges are expected to experience less passivation than the previous edges[165], and may not act as barriers to stripe hydrocarbons as effectively. In their modified method of mechanical exfoliation with 20-60 times greater yield, higher quality flakes and up to 50 times

greater areas of individual flakes compared to conventional mechanical exfoliation, Huang et al. crucially apply a heat treatment to the substrate-graphene-tape sandwich[44]. They speculate that heating to 100°C increases the pressure of any gas molecules trapped between the flake and substrate, which encourages the transfer of gas from the interface via the edges, which they claim act as a one-way valve. However, the specification of a one-way valve is not experimentally supported in the text, so we suggest that these edges may in fact be significantly more accessible to specific species than previously thought.

We should also consider the peak-to-trough height of the stripes which are apparently trapped at every graphene-graphene interface in Fig. 2.16. Although reported and indeed our own values of this amplitude vary somewhat (typically 0.1 ± 0.05 nm, this value being at the limit of AFM z resolution which may account for this variance), this is an appreciable value in comparison to the interlayer separation of graphene of 0.34 nm[166], which is approximately the van der Waals thickness of a carbon atom monolayer[167]. We note that this value of 0.34 nm is derived from XRD of graphite. In AFM, it has been long established that the measured height of graphene layers can vary significantly. In 2008, Nemes-Incze et al. observed a variation in thickness measurements of single graphene layers on SiO_2 substrates from 0.35 nm to 1 nm[100], following reports from other researchers of similarly inconsistent thicknesses[168–170]. This was primarily attributed to inconsistencies in AFM measurements, both in tapping-mode and contact mode AFM. In tapping-mode, Nemes-Incze et al. report that poorly chosen free amplitudes of the AFM cantilever result in such variations. While it can be tempting to image at the lowest setpoints possible to minimise damage to the sample and to extend tip lifetime, it must be ensured that imaging occurs with setpoints sufficient to bring the tip into repulsive contact with the surface with cantilever damping arising primarily from surface topography rather than capillary forces for example. Even in contact-mode AFM, different lateral forces across different materials being imaged within the same scan (such as a graphene sheet and substrate) can introduce errors to the thickness measurements of up to 0.2 nm for example. While this satisfactorily explains large thickness variations, we speculate that such variations may

not arise wholly from instrumentation but could reflect the presence of interlayer species as observed here.

Water adlayers between graphene and the substrate have been observed previously which can introduce variation in height profiles for example, and which also indicate the possibility of another intercalated species[171]. Recently, Tallon et al. studied how exfoliated graphene can protect Si(111)-7×7 surfaces from oxidation in ambient conditions[172]. However, even areas of Si(111)-7×7 upon which graphene has been exfoliated in vacuum become oxidized within only 2 days of exposure to ambient conditions, with the authors suggesting that adsorbates could migrate under graphene flakes from flakes edges under these conditions.

Shearer et al. report that graphene heights may be accurately measured if imaged at sufficiently high forces or if no buffer layers are present[173]. However, even in this case where imaging is performed with a small diameter tip (a single wall carbon nanotube to apply sufficient pressure to displace any possible underlying buffer layers) and at an optimal force set point, Shearer et al. nonetheless report an error of 0.1 - 0.3 nm for the first layer alone. However, they did not study samples of two or more layers, upon which it was speculated that the pressure would quickly become dissipated and would no longer act upon any underlying buffer layers. Yao et al. developed a histogram method to determine graphene thickness, with measured thicknesses for single layer graphene of 0.41 ± 0.29 nm[174]. Sidorov et al. reported an initial thickness measurement of ≈0.35 nm that relaxes to 0.8 nm after 45 days, which they partially attribute to moisture creeping into the sheet-substrate interface[175]. From this review, we can see that graphene interlayer thickness is rarely measured by AFM as the expected value of 0.34 nm, and instead is always greater than rather than being distributed around this value. While inconsistent contact of the AFM tip and surface has been proposed to explain this discrepancy, we hypothesise that the additional component of intercalated stripes for example could also clarify why the value of 0.34 nm can so rarely be achieved.

2.7 Conclusions

In this chapter, we have firstly reviewed the current understanding of stripe adsorbates available in the literature, albeit representing only a handful of papers focused on this topic in the previous decade since their discovery. Key parameters such as their characteristic pitch of 4-6 nm, peak-to-trough height of ≈0.1-0.2 nm and three-fold symmetry resulting in distinct friction domains were established and demonstrated on our graphene samples by PFQNM. Stripe dynamics were explored, with the timescale over which stripes form on pristine surfaces established, stripe friction domains observed dynamically evolving in shape with time as well as stripes observed changing direction directly. Stripe friction domains also appeared to be influenced by surface features such as wrinkles, ribbons and indents. As we demonstrated that stripes can influence graphene material properties such as friction and subtly affect measured adhesion and deformation for example, we highlight the need to account for stripes in studies of graphene.

By manipulation of folded graphene ribbons with an AFM tip, we exposed the graphene-graphene interface, within which stripes were stably present, in contradiction to widespread claims that van der Waals forces can remove hydrocarbon contaminants from these interfaces. We also derived an upper bound of friction shear stress in a typical ribbon consistent with superlubric sliding, in agreement with Annett et al.'s previous description of ribbon formation, even in the presence of these stripe adsorbates. We attribute this persistence of superlubricity to the relative lack of mobility of these stripes and lack of pinning sites generated.

As auto-kirigami ribbons can reveal graphene interfaces, we further demonstrated that stripes are present not only on graphene surfaces, but also at graphene-substrate and buried graphene-graphene interfaces in graphite. We proposed that stripe adsorbate material can intercalate into these interfaces as stripes could not form in these locations within the relevant timescales after exposure. This presents serious implications to the cleanliness of van der Waals interfaces more generally, which we propose can no longer be simply assumed to be clean.

Chapter 3: Nucleation of 2D material auto-kirigami

3.1 Introduction

As discussed in Chapter 1, prior to this work two methods for ribbon nucleation have been proposed. These are via indentation on mechanically exfoliated graphene with applied lateral oscillations as discovered by Annett et al.[89], and by AFM cutting as demonstrated by Rode et al. for example[102].

Nucleation by indentation has thus far only been applied on few-layer mechanically exfoliated graphene samples. Here, we extend this to mechanically exfoliated MoS_2 and graphite, and later in Chapter 4 we will discuss indentation on a number of CVD 2D materials as well. We also present a novel method for nucleation of graphene auto-kirigami ribbons by AFM indentation with no requirement for applied oscillation. This extends the production of AK-ribbons from the oscillatory shear technique implemented by 2D nanoindenter systems[89,176], of which only a very small number exist, to the workhorse AFM system present near universally in laboratories worldwide.

Rupture of graphene is also examined as a necessary precursor to ribbon formation, with insights into ribbon formation obtained.

3.2 AFM nucleation

Firstly, we review and extend the application of AFM cutting for ribbon nucleation as demonstrated by Rode et al.[99,102,103]. Secondly, we demonstrate a novel method for nucleation of ribbons using AFM-based indentation and tapping-mode imaging. We also note that self-folded areas of graphene and even ribbon structures may also be observed in rare instances on graphene immediately following mechanical exfoliation. This is attributed to complex shear forces present during mechanical exfoliation, and as such is not a reliable method for studying folded graphene.

Cutting is performed in AFM using an Adama super-sharp diamond probe (AD-2.8-SS, tip radius less than 5 nm, 2.8 N/m spring constant, 65 kHz resonant frequency). Different methods of cutting were applied as highlighted by sketches in Fig. 3.1 (a) – (c) with varying levels of success. The most promising method found was cutting a line scratch through a graphene sheet, with ribbons nucleated from this torn edge (Fig. 3.1 (a)) similar to the method of Rode et al. While ribbons may be observed immediately upon imaging the newly formed scratch line, contact mode imaging around the scratch at setpoints of few tens of nNs (sufficiently low to avoid causing further damage or tearing) can also induce further folding from the scratch line. From exploratory testing, this method proved relatively consistent in inducing folding of areas of graphene but the resulting folded graphene could vary significantly. In some instances, a ribbon may grow perpendicularly or approximately perpendicular to the scratch line as above the scratch line in Fig. 3.1 (a) and as imaged by AFM in (d). In others, a ribbon may form around only one tear as below scratch line in (a). This may instead result in folding of edges of the

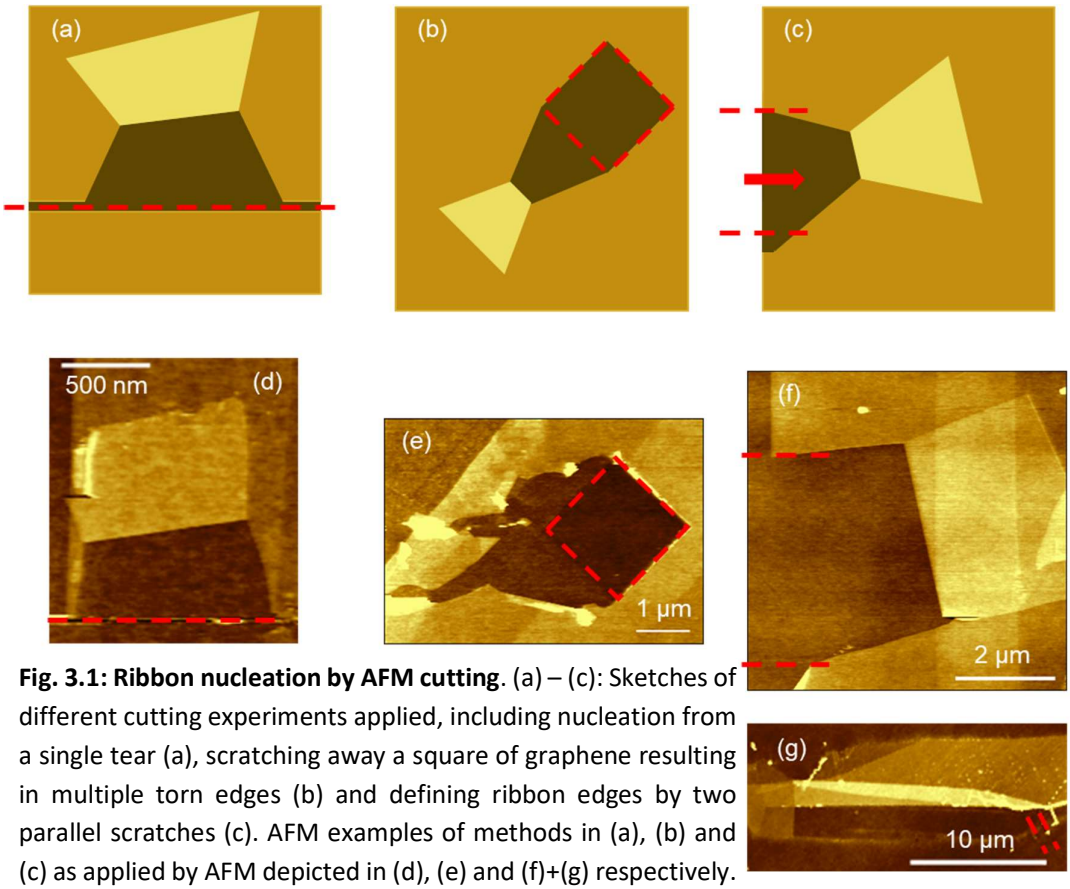

Fig. 3.1: Ribbon nucleation by AFM cutting. (a) – (c): Sketches of different cutting experiments applied, including nucleation from a single tear (a), scratching away a square of graphene resulting in multiple torn edges (b) and defining ribbon edges by two parallel scratches (c). AFM examples of methods in (a), (b) and (c) as applied by AFM depicted in (d), (e) and (f)+(g) respectively. Total linear z scale of 4 nm for (d) - (f), 6 nm for (g).

flake to lengths of 1-2 μm but widths of 10-20 μm. While reliable in producing folding, the lack of control over and consistency in the resulting folds makes this method less appealing.

Mechanically etching away a square using AFM contact mode imaging as in (b) was intended to incorporate both the scratching effect of (a) with a repeated back-and-forth motion of the tip along the trace-retrace direction which may encourage formation of initial folded tabs at the newly torn edges defined by square scan area. As such, this method can be viewed as a crude analog to SASIN as discussed in section 1.5. While Annett et al. applied a high frequency, small amplitude (≈1 nm) lateral shearing oscillation during indentation to reliably induce nucleation[89], we can here attempt to mimic lateral oscillation with the trace-retrace motion of the AFM tip. With typical scan rates per line of 0.5 – 2 Hz in AFM scanning, this would represent a lower frequency than the 10s Hz typically applied in SASIN.

However, tearing caused by this method was poorly controlled, rarely being limited to the scan area and ribbon peeling. While crude ribbon-like folds can be seen in Fig. 3.1 (e), these were also judged to be too irregularly shaped to allow categorisation or to readily be studied. This method also required additional time compared to scratching only a single line as in (a).

A third method depicted in (c) sought to nucleate ribbons of arbitrary, controllable initial widths. With SASIN, the maximum initial ribbon width is typically limited by the side length of the triangular indent crater of the Berkovich tip. While 1D indentation can be performed with loads of up to ≈1 N in standard nanoindentation instruments, there is a limit of ≈50 mN maximum load available in 2D nanoindentation systems which are based on the highest precision actuator heads. This in turn limits the maximum indent crater side length to ≈3 μm. Assuming a typical final width of 300 nm of an inward tapering ribbon with half angle of ≈6°, this would place a limit on maximum ribbon length of 12.9 μm.

Our study of graphene AK ribbons has thus been limited to ribbons with initial widths from ≈0.2 μm to ≈3 μm, and Annett et al.'s interfacial force growth mechanism has not been tested at higher widths.

From Annett et al.'s model, a minimum final fold width is observed where the interfacial force can no longer overcome tearing resistance of the graphene sheet[89]. The interfacial force, proportional to the growing ribbon area δA decreases during growth in ribbon length $\delta l = \delta c \cos \theta$ (for tear length δc and taper angle θ) due to the inward tapering of the ribbon which acts to minimise the strain energy of the fold. However, the tearing resistance of both tears $2\lambda\, \delta c$ then depends only on incremental length δl. Therefore, for increasingly larger initial fold widths, the ratio of tearing resistance 2λ to interfacial driving force $w \cdot \Delta\gamma$ becomes increasingly smaller. Nucleating ribbons of arbitrarily large widths is therefore of interest to examine if the fold itself would remain perfectly straight over increasing fold widths. This may modulate fold bending stiffness, previously assumed by Annett et al. to be a linear function of width if the unadhered length and shape of graphene in the fold does not vary with ribbon growth.

We here assume negligible frictional resistance per earlier conclusions in Chapter 2. However, Qu et al.'s report that the total friction force of incommensurate graphite contacts under ambient conditions is dominated by friction of edge atoms rather than inner atoms for contacts up to 10 μm in lateral size, with an average contribution to friction of inner atoms as no more than 10^{-4} that of edge atoms[177].

The increasing contribution of inner atoms is presumed to follow a power law[177,178,24,136,26,179] with $F_{fric} = f_1 A^{\eta}$ for $0 < \eta < 0.5$. With the driving interfacial force scaling linearly with area, although a minimum fold width is observed, there appears to be in principle no maximum fold width. However, ribbon growth is often terminated where the growing ribbon head encounters a flake edge, neighbouring ribbon or peeled area or sufficiently large contaminant body, which becomes increasingly more likely for larger ribbons. A potential bending of the fold itself over sufficiently large fold widths may also set a ribbon width upper bound, causing a change in taper angle with fold width.

As sketched in Fig. 3.1 (c) and demonstrated in (f), two short scratches are made (as marked by red dashed lines) approximately perpendicular to a flake edge to define the edges of a ribbon. Contact mode imaging is then performed with top and bottom edges of the scan also defined by the red dashed lines in interleave mode. This ensures that contact scanning occurs only in the trace direction with the tip retracting during the

retrace (or vice versa), here with the effect of the tip "pushing" only from left to right during scanning along the flake edge between the two scratched lines similar to Chen et al.'s method of producing folded graphene[32]. This may then result in folding of the graphene to form a ribbon with chosen initial width as per (f). Here, the scratches were made 5 µm apart, which could allow a ribbon length of up to 22.5 µm, though in this instance the ribbon growth stops as the fold encounters a step, increasing tearing resistance such that self-assembly is no longer favourable. While this method could be applied, it also proved difficult to control. In Fig. 3.1 (g), two parallel scratches were made ≈1 µm apart at the edge of a 3-layer mechanically exfoliated graphene sheet. Rather than tearing the sheet, each scratch resulted in local folding of the sheet to a folded length of ≈0.7 µm following the first scratch and ≈1.2 µm following the second. Despite applying only that scratching and no further high setpoint contact mode, neighbouring graphene with a different edge direction folded to a length of ≈2.5 µm over a width of ≈17.5 µm. The majority of this folding is 3-layers folded onto 3-layers, but in a small area shown in far left of (g) only 2-layers fold onto adjacent 3-layers, leaving 1-layer in the "peeled" area. Graphene sheet thicknesses were obtained by comparison of the height of these folded areas compared to neighbouring graphene areas where no tearing or folding occurred, as obtained by subsequent PFQNM imaging.

We also note here that the fold appears predominantly straight over this width of ≈17.5 µm, suggesting that, over short ribbon lengths at least, Annett et al.'s model remains valid with constant taper angle and straight fold and ribbon edge observed in this instance. However, we note that the resulting folded structure produced in (g) is starkly different to the anticipated ribbon shape per schematic in (c), and that such large ribbon widths could not be reliably reproduced.

Furthermore, applying two parallel scratches could instead result in nucleation separately from each scratch line as per (a) rather than as intended in (c), and contact mode scanning often resulted in tearing and destruction of the sheet rather folding.

Nonetheless, these methods represent various approaches that can be applied to nucleate ribbons in the absence of SASIN. This can facilitate more widespread study of auto-kirigami ribbons for fundamental research, though currently lacks the control and scale of indentation-based methods. Publications featuring similar methods of AFM-

based folding of graphene applied by Rode and Chen feature a total of 30 and 21 successful folds respectively[32,102], indicating the similar struggles of yield faced by other researchers.

As AFM cutting cannot provide the desired yields and consistency of AK-ribbons, we tested AFM based indentation methods using a Bruker Multimode 8 AFM. A DNISP cantilever is used, consisting of a stainless-steel cantilever with reflective gold coating on the backside of the cantilever and a hand-crafted natural diamond tip with cube corner geometry. This probe was pre-calibrated by the supplier with a spring constant of 297.32 N/m, deflection sensitivity of 131.1 nm/V and frequency of 56.4 kHz. This is performed specifically using a nanoindentation software module which is not provided as default for many AFM systems. However, the primary advantages of this software are to correct cantilever tilt in order to minimise ploughing (which we deliberately misalign such that ploughing occurs regardless), and to generate arrays of indents with controllable indentation rate, location and number. This software also facilitates imaging of the indent and surrounding area pre- and post-indentation in tapping mode with the very stiff indenting probe rather than in contact mode to minimise sample damage. However, it is entirely possible to reproduce indentation in this manner without this module using only a standard ramp procedure to produce force-distance curves in contact mode, as is routinely applied in calibrating cantilever deflection sensitivity. A maximum load of ≈0.5 mN can be applied (to a depth of ≈110 nm) with individual indents completed within as little as ≈10 s.

This 1-dimensional indentation produces strains largely in the normal direction, and as such is not predicted to nucleate ribbons per Annett et al.'s observations that nucleation by indentation occurs only when a small, high frequency lateral oscillation is applied. Nonetheless small, folded tabs of graphene are often seen at the edges of the indents. Per Annett et al.'s model, these tabs are precursors to ribbon growth, indicating further promise of this method.

Unfortunately, the low loads accessible by AFM indentation result in indent side lengths of only ≈0.2 µm. A ribbon with an initial fold width (w_0) this low is below the typical threshold width required to generate an interfacial force of sufficient magnitude to drive self-assembly; as described in section 1.6, this interfacial force arises from the

difference in adhesion energies between the graphene ribbon/host flake ($\Delta W_{2D\text{-}2D}$) and the host graphene flake/substrate ($\Delta W_{2D\text{-}s}$), with the interfacial force at beginning of growth $F_{int,0} = w_0 \cdot (\Delta W_{2D\text{-}2D} - \Delta W_{2D\text{-}s})$. With such low values of w_0 the exchanged adhesion energy per unit length of ribbon growth is too low to overcome the bond rupture energies required to tear the sheet and any other impediments to self-assembly that may be present. It is therefore necessary to increase this torn length.

AFM cantilevers are typically oriented with a ≈12° deflection of the cantilever from the horizontal, with a corresponding tilt of the tip itself. To correct for this misalignment and to prevent ploughing of the surface due to the tip pitching forward during indentation, the piezo scanner is moved in an opposite direction to the cantilever during indentation. The effect of this correction is seen in Fig. 3.2. The expected triangular shape of the indent crater is seen in Fig. 3.2 (b) with an appropriate correction. Under-correction (Fig. 3.2 (a)) results in increased pile-up at lower and right indent edges, and pitching of the cantilever such that the laser spot moves opposite to the direction of normal deflection. This counter-effect results in deeper indents with higher forces despite equal or less cantilever deflection. Alternatively, over-correcting results in smaller indents at the same deflection setpoint as in Fig. 3.2 (c).

Instead of indenting with a correctly aligned cube corner we deliberately misalign the cantilever by altering the piezo scanner correction. As AFM indentation curves are almost always qualitative rather than quantitative as described in section 1.5.2, and

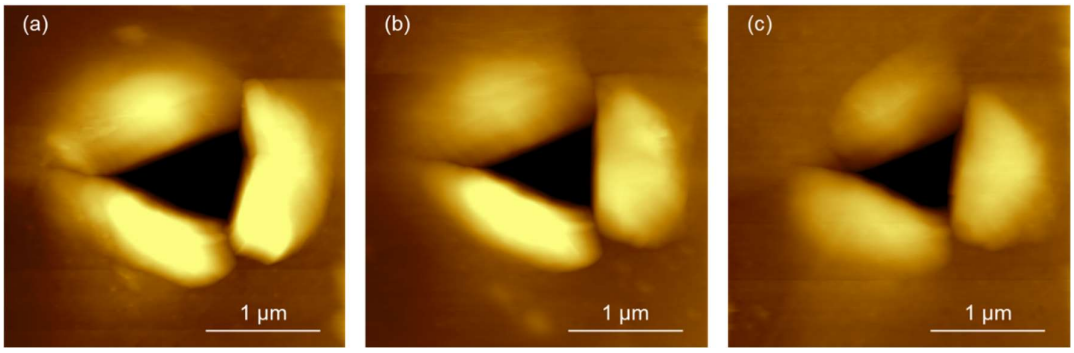

Fig. 3.2: Effect of scanner tube motion during AFM indentation. Lateral motion of the scanner tube during indentation to correct for cantilever ploughing of the surface due to cantilever vending or coupled motion in Z axis. This motion is contained within "x rotate" parameter measured in degrees in software. (a) – (c): Indents to the same nominal setpoint of 0.35 mN with varying x rotate parameter of 0, 12 and 20° respectively on aluminium.

since the applied force is poorly known in these AFM indentation experiments especially since we deliberately misalign the cantilever resulting in incorrectly defined deflection setpoints and hence inaccurate forces, we do not include AFM load-displacement curves here. This misalignment creates elongated indents rather than equilateral triangle indents, which increases the torn length of graphene from each indent. Instead of ≈0.2 μm, indent side lengths of 0.3 – 0.5 μm are obtainable, which potentially provides a long enough initial tear length such that the exchange of adhesion energy of the total area of graphene that would be folded can overcome tearing, sliding and strain energy of the fold. However, this alone is typically not observed to be sufficient to nucleate ribbons. We therefore also incorporate aspects of AFM cutting experiments, whereby contact mode imaging at elevated setpoints is applied around newly cut graphene. While this can also prove effective in nucleating ribbons from graphene cut by AFM indentation, the elevated setpoints in contact mode typically result in damage to any newly formed ribbons and to the host graphene sheet, making contact mode unreliable in this purpose. Instead, we apply tapping mode.

A major advantage of tapping mode over contact mode imaging is that contact is intermittent rather than continuous and that setpoints can be as low as 0.1 nN. This absence of dragging shear differentiates this from experiments producing graphene nanoribbons by tearing[180] and simple pushing by AFM tip during contact scanning[181].

These factors can minimise damage and wear of both the tip and sample. Here, a setpoint of 0.5 – 5 μN is instead applied, which we dub “hard tapping” as setpoints are 2-3 orders of magnitude higher than typical of this imaging mode. Hard tapping is applied using a monolithic silicon Nanoworld NCL AFM probe (spring constant of 48 N/m, resonant frequency of 190 kHz). This cantilever was chosen from requirements for a higher spring constant to allow higher tapping setpoints and a tip radius of < 8 nm to allow sufficient resolution for imaging both during and after hard tapping even if tip blunting occurs during hard tapping as a result of the high peak forces applied.

An elongated indent by this method on mechanically exfoliated graphene/SiO_2 is shown in Fig. 3.3 (a), while the inset shows the equilateral triangle shape expected of a cube corner indent. Large amounts of silica substrate pileup are associated with this ploughing, though some small areas of folded graphene are also observed around the

indent. A successful ribbon nucleation is observed in Fig. 3.3 (b) following application of hard tapping to a similar indent. Hard tapping can be applied over large scan areas covering many indents simultaneously, with all ribbon growth on this sample occurring after only 20 minutes of applied hard tapping imaging at 1.3 µN setpoint. With regular arrays of indents, many ribbons formed nucleate from either of the two longest edges of the indent's kite-like shape. With ribbon growth occurring largely perpendicular to these kite edges, many of these indents appear parallel but can grow to varying final widths. In one instance in (c), a ribbon tapers to a point with the ribbon itself then

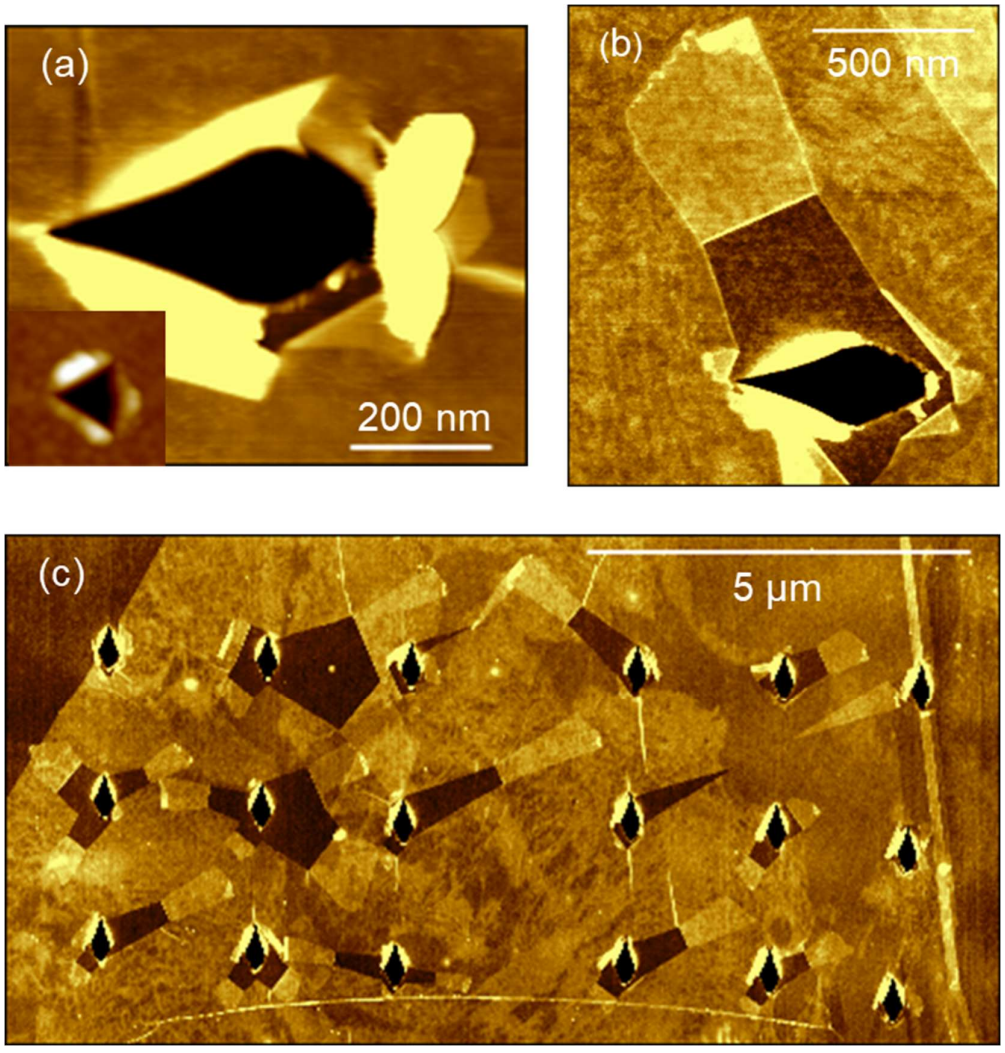

Fig. 3.3: Ribbon nucleation by AFM indentation and "hard tapping". (a) Sample elongated indent with indent from cube corner tip inset bottom left. (b) A single sample indent in single layer mechanically exfoliated graphene. (c) High yield of ribbons from AFM indentation with "hard tapping", even in the presence of extensive uncharacterised surface contaminants, indicating robustness of this method. Total linear z scale: 10 nm for (a), 4 nm for (b) and (c).

transported across the underlying graphene sheet. The presence of uncharacterised contaminants on the graphene surface in Fig. 3.3 limits determination of the crystallography of the host flake by inference of the armchair direction from the stripe orientation. Furthermore, straight flake edges at clear n × 30° intervals are also not observed to infer orientation from such edges (which would likely be either armchair or zigzag). The lower torn edge of all ribbons growing towards the top-right corner of (c) for example feature a common direction of 30.5 ± 0.8°. However, the directions of the corresponding upper torn edges of these ribbons are not aligned, with taper angles varying from 7° to 19°. Assuming that the lower edge is in fact aligned with a crystallographic direction, 4 further torn edges in (c) are measured at n × 30° from that direction, with standard deviation of all of these torn lines of only 0.8°. We will further consider the influence of the crystallography on torn edges in section 3.2.2 in instances where crystallography can be precisely derived from stripe direction. More complex tearing and peeling than the typical AK "bowtie" shape is also observed in (c), with some ribbons nucleated from the torn edges of other ribbons for example.

This combination of AFM indentation with deliberate ploughing of the sample to maximise torn graphene length and hard tapping of the resulting indents reliably results in nucleation of high yields of ribbons. We stress that all steps of this nucleation can be performed solely using standard AFM techniques, hugely increasing the potential for auto-kirigami research.

This method can also be applied to indents produced by 1D or 2D nanoindentation which previously were unsuccessful in nucleating ribbons. In Fig. 3.4 (a), 2D nanoindentation had been performed on a 7-layer mechanically exfoliated graphene sheet. In both examples, small, folded tabs are formed around the indents with lengths of up to 0.5 μm. Hard tapping imaging of the entire scan area is applied at increasing setpoint intervals of 0.5 μN from 0.5 μN to 2.0 μN with 4 scans per setpoint. No effect is observed in either instance up to 1.5 μN, while upon first application of the 2 μN setpoint ribbon growth occurs immediately (Fig. 3.4 (b)). Both edges of the ribbon are observed throughout this growth, with each AFM image requiring over 4 minutes. If ribbon growth here occurred purely by the thermodynamic, interfacial force mechanism on timescales much faster than AFM imaging, with hard tapping only

inducing initial tearing at the indent edge, we would expect to observe the final structure as in (c) immediately rather than the intermediate stages of growth seen in (b).

Furthermore, from Fig. 3.4 (b), the width of the growing folded graphene varies from 0.6 to 0.8 µm, with final maximum width of the ribbon of 0.8 µm. These are all substantially greater than the actual final fold width of 0.3 µm. This strongly indicates that in (b), we are not imaging the final ribbon but instead are only seeing the ribbon head being "dragged" along by the tip. In this instance and other applications of hard tapping, ribbon growth does not occur beyond the edges of the scan in which hard tapping is applied. However, we emphasise that this is a non-contact mode such that the ribbon is not truly dragged by the tip. Instead, we suggest two contributions of the tip to this growth. Firstly, mechanical energy is transferred from the oscillating AFM tip to the graphene. We can place an upper bound on this by considering the energy dissipation channel of PFQNM. Extracting dissipation during µN setpoint proves unreliable due to large ringing of the cantilever which prevents a reliable zero-force baseline being established. Instead, we can consider a more typical setpoint reached during PFQNM imaging with a stiff cantilever of 100 nN (as in Fig. 3.4 (c), after hard tapping) where this distortion is minimised such that a value of dissipation can be extracted, though this will underestimate energy dissipated at higher setpoints substantially. Here, an average dissipation per pixel of 0.76 keV, or 1.22×10^{-16} J is obtained. The length along either of the torn edges in Fig. 3.4 (c) is 4.65 µm, or 99 pixels.

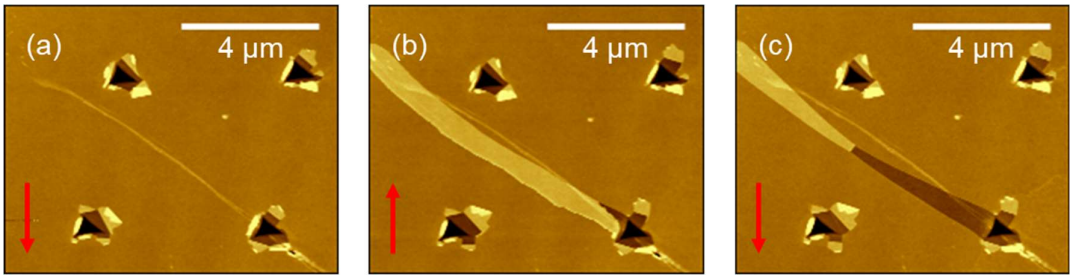

Fig. 3.4: Ribbon nucleation and growth assisted by AFM hard tapping. Red arrows indicate AFM slow scan direction. (a) Short, folded tabs and ribbons (up to 0.5 µm length) are observed on a 7-layer mechanically exfoliated graphene sheet, with no change with hard tapping setpoint up to 1 µN. Increasing the setpoint to 2 µN immediately results in ribbon tearing and folding of bottom right indent, alongside minor extensional growth of lower left and upper right indents. Final ribbon (c) extends to 5 µm length. Total linear z range: 12 nm in (a) – (c).

From this, we can calculate a maximum energy dissipated resulting in either torn edge (along that edge) of 2.57×10^{-9} J m^{-1} is derived. While all energy dissipated per oscillation cycle should not be expected to be transferred perfectly to bond breaking required for tearing graphene, this also represents an underestimate of energy dissipated due to the lower setpoint used. Nonetheless, we note the relative similarity of this value (2.57×10^{-9} J m^{-1}) and the line energy for torn graphene of 1.67×10^{-9} J m^{-1} derived by Rusanov et al[156].

Furthermore, comparing the final shape of the ribbon in (c) with intermediate structure in (b) shows that, beyond the position of the fold, the ribbon is not growing symmetrically but is in fact twisted towards the lower edge, with the intermediate upper edge accurately reproducing the final position. Ribbon growth therefore occurs asymmetrically and incrementally with each scan line. This also demonstrates that hard tapping is not simply overcoming an initial energy barrier to nucleation with the self-driven growth mechanism then taking over. Instead, it appears that the growing ribbon is being pushed along every scan line, with hard tapping apparently supplying the required energy.

We also test the effect of removing hard tapping in Fig. 3.5 (a) and (b). Initially, only a small ribbon (growing to the right) is observed, which grows upon application of hard

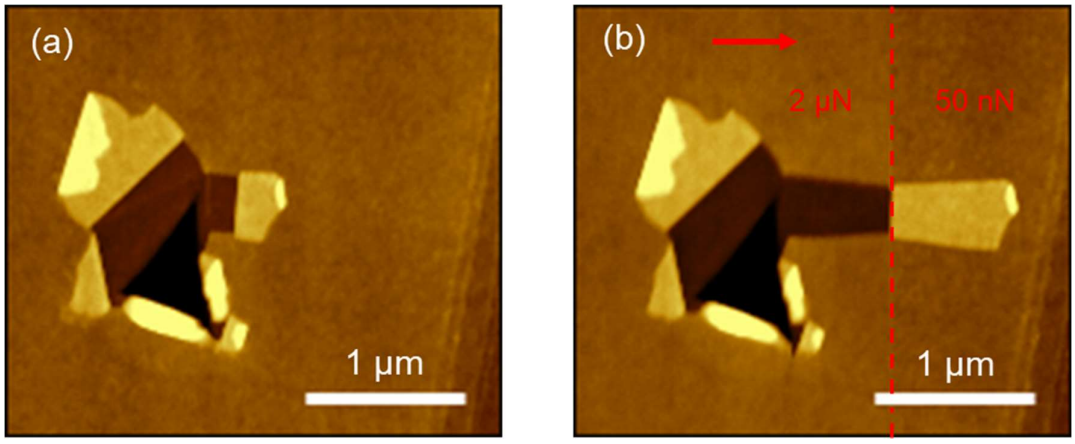

Fig. 3.5: Ribbon growth ceases in absence of hard tapping. (a) A ribbon of 0.3 µm length was nucleated by 2D indentation in 7-layer mechanically exfoliated graphene. (b) Application of hard tapping at 2 µN again results in graphene tearing and folding as in Fig. 3.4. However, upon reducing the tapping setpoint from 2 µN to 50 nN during capture of a single scan, as indicated by red dashed line, ribbon growth immediately ceases. Total linear z range: 9 nm in (a) and (b).

tapping at 2 μN in (a). The setpoint is sharply decreased from 2 μN to 50 nN at the scan line indicated by red dashed line in (b), resulting in ribbon growth immediately stopping. The resulting ribbons in Fig. 3.4 and Fig. 3.5 both show typical tapering of the ribbon, indicating that the effect of minimising fold strain leading to a reduction in width of the ribbon with growth is still applying.

We can also apply AFM indentation and hard tapping to very thick (>100 layer) graphite flakes. By Annett et al.'s model describing ribbon growth discussed in full detail in section 1.6[89], ribbon growth is thermodynamically self-driven by a net interface tension $w \cdot \Delta W = w \cdot (W_{gr\text{-}gr} - W_{gr\text{-}s})$ for ribbon width w and works of adhesion between graphene-graphene and graphene-substrate $W_{gr\text{-}gr}$ and $W_{gr\text{-}s}$ respectively. However, for increasing number of graphene layers, graphene-graphene adhesion energy becomes smaller[182] while graphene-substrate adhesion remains constant. Total graphene rupture energy $n \cdot 2\lambda c$ for n layers with rupture energy per unit length λ with tear length c will also increase with layer number, as will fold strain energy with increasing length of unadhered graphene in the fold[183]. With decreasing driving force and increasing resistance, the graphene folding required for ribbon growth becomes unfavourable on increasingly thicker graphene flakes.

However, combined with hard tapping at sufficiently high setpoints, nucleation and sustained growth can be induced nonetheless. In thick samples, rather than graphene peeling from the SiO_2 substrate, the ribbons emerge from within the graphite flake such that a thermodynamically favourable exchange of graphene-substrate for graphene-graphene adhesion is no longer present. This "graphite auto-kirigami" requires much higher tapping setpoints for nucleation to occur: 0.5 – 1.5 μN setpoints are sufficient to nucleate in few-layer graphene, while 3 μN setpoints are required on a 12 nm thick flake, 4 μN on a 24 nm thick flake and 5 μN on a 58 nm thick flake (Fig. 3.6 (a)). In the examples of ribbon nucleation on graphite demonstrated in Fig. 3.6 (a) and (b), multiple steps are observed on the ribbon and peeled areas, with maximum thicknesses of these ribbons (nucleated on separate flakes) of ≈35 nm.

In a ≈27 nm thick graphite plate pictured in Fig. 3.6 (c) and (d), ribbons of varying sizes are observed. Ribbons with the largest areas are also the thickest, with thicknesses of 14-15 nm while the smaller, narrower ribbons are thinner at 5.2 – 5.6 nm thickness

despite hard tapping being applied equally across the scan area. This suggests that an energy threshold for tearing (overcome by the energy dissipated by the probe's mechanical oscillations) which must be reached for nucleation to occur in thick samples cannot alone describe this nucleation. The crystallography of the graphite plate can also be considered. Liu et al. proposed a "stone wall" polycrystalline HOPG structure, whereby the self-retraction phenomena of their graphite mesas occurs along a slip plane[29], illustrated in Fig. 3.7. This slip plane by chance occurs where the top and/or bottom edges between the "stones" in this wall in the z direction align without locking.

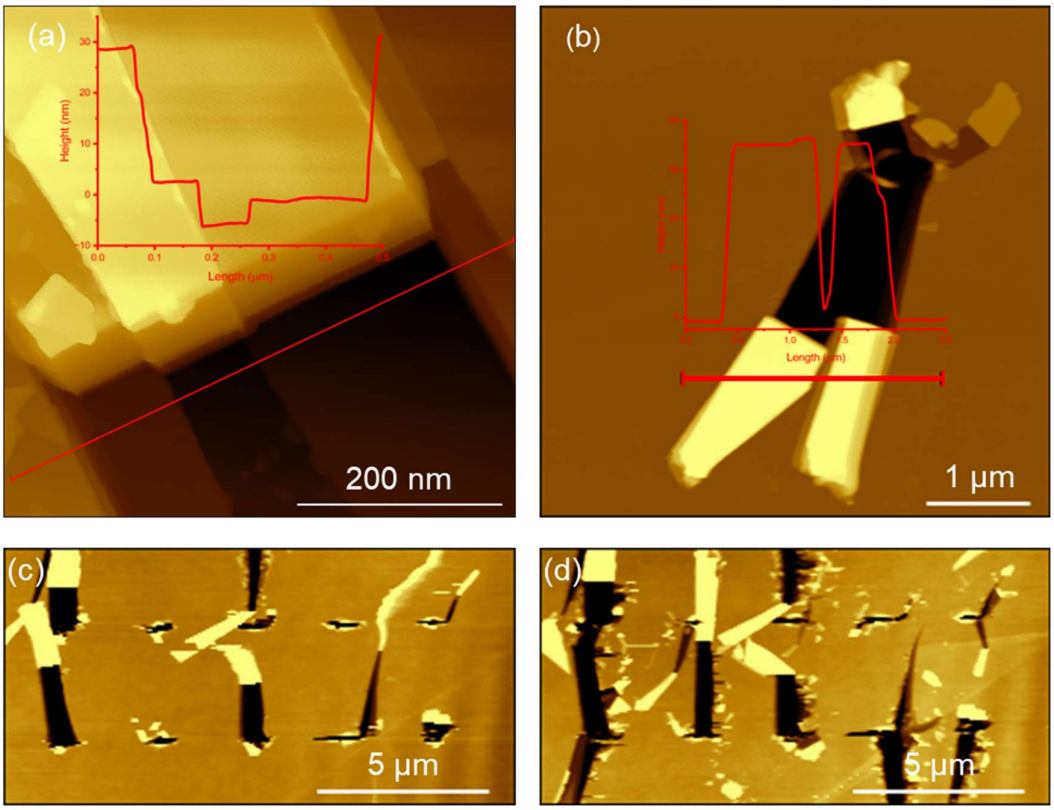

Fig. 3.6: Auto-kirigami ribbon nucleation within thick graphite without the involvement of substrate adhesion. (a) and (b): Sample ribbons nucleated in 58 and 71 nm thick graphite plates, with height profiles overlaid along marked red line one each. Ribbons thickness on each is ≈35 nm, such that ribbons peel from tens of nanometre thick graphite rather than from SiO_2 substrate. Ribbons nucleated on graphite by this method often are not uniform thickness throughout the ribbon, with multiple steps as clearly seen in height profile of (a). A minimum "hard tapping" setpoint must be reached for nucleation to occur, with all nucleation in (c) occurring during the first scan at 4 μN and none at lower setpoints. However, maintaining this setpoint for multiple scans results in widespread damage to ribbons and their edges, with damage in (d) captured after only a further 10 minutes of continuous scanning following (c). Non-linear adaptive colour scale in (a) over 100 nm, total linear z-scale of 70nm in (b) and 14 nm in (c) and (d).

The varying depth across the ribbon, with at least 8 steps present in Fig. 3.6 (a) alone within a length of less than 500 nm, may suggest that ribbon growth in graphite can occur with neighbouring "stones" of different depth contained within the ribbon. However, the size of the crystallites in this sample is unknown.

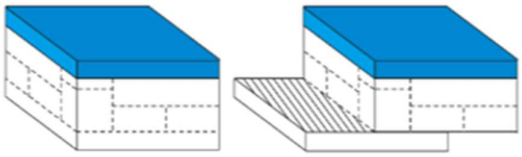

Fig. 3.7: "Stone wall" model of self-retracting motion in HOPG graphite mesas. Reproduced from 29.

We therefore suggest that an adhesion exchange remains an important aspect of this folding in graphite. Ribbons with greatest initial widths will have the largest areas and therefore largest Δ*W*, which can overcome sliding and tearing resistances.

3.2.1 Ribbon nucleation on non-graphene 2D materials

Thus far in this thesis and other published works, auto-kirigami ribbon growth has been observed only on graphene. According to our continuum energy balance model described in section 1.6, providing that 2D material self-adhesion energy is greater than 2D material to substrate adhesion energy, and that this surplus can in turn overcome tearing and sliding resistances, it should be possible for auto-kirigami ribbon growth to occur in other 2D materials as well. Here, we conduct exploratory tests to attempt to verify this conjecture. The focus in this section will be on mechanically exfoliated 2D MoS_2, while nucleation in other CVD formed 2D materials is considered in Chapter 4.

Mechanical exfoliation of MoS_2 from MoS_2 natural crystal (≈0.7 cm^2 area with purity >99%, Graphene Supermarket) proved much more challenging than graphene mechanical exfoliation. Maximum few-layer MoS_2 flake sizes of ≈100 μm^2 were obtained in very low yields. While these flake sizes are in line with other reports of mechanically exfoliated MoS_2 by this method[184–186], this severely limited our ability to perform large numbers of indents on such samples.

We note that alternative methods exist for transfer of larger areas of monolayer MoS_2, as well as other 2D materials, from bulk. Desai et al. demonstrated exfoliation of ultra-large (lateral dimensions up to ≈500 μm) monolayer MoS_2 for example by gold-mediated exfoliation[187]. In this method, they evaporate a thin layer of gold (100-150 nm) onto a target TMDC bulk crystal. Attaching and then peeling thermal tape from the gold layer results in transfer both of the evaporated gold and a strongly adhered MX_2 monolayer. The tape/gold/MX_2 is brought into contact with the target substrate, where the tape is thermally released and the gold layer etched, resulting in monolayer MX_2 on the target substrate. The thin gold layer crucially induces strain in the single topmost layer of the MX_2, weakening bonding between the topmost and underlying layer, resulting in transfer only of a monolayer[188]. Rather than directly applying thermal tape to the gold/MX_2 stack, a thick patterned photoresist which is in turn contacted with the thermal tape can allow for transfer of 100+ areas of up to 10^4 μm^2 areas in a single transfer[189]. Mechanical exfoliation of 40 2-dimensional monolayers with mm lateral dimensions has also been demonstrated onto Au (2nm)/Ti (2 nm)/SiO_2/Si substrates[190] following the same principle. While these methods were not here applied for our initial, exploratory testing of the possibility of nucleation on MoS_2, we anticipate the capability that they offer of attaining much greater statistical weight in future testing.

However, similar to graphene exfoliation, much higher yields of large area, thicker bulk-like MoS_2 are also produced. We therefore also indented on areas of thicker MoS_2 to attempt to nucleate ribbons using indentation and hard tapping as on graphite in Fig. 3.6.

With the much greater quantity of bulk-like MoS_2 compared to few-layer MoS_2, indentation experiments were performed on these samples first. 50 indents were made on two separate bulk-like MoS_2 samples (25 each on 157 nm and 176 nm thick MoS_2 samples) by AFM-based indentation. No ribbons were observed after indentation alone, so hard tapping was then applied to each array of indents in setpoint increments of 1 μN up to 5 μN with 4 scans per setpoint over a 30 μm scan size at 256 × 256 pixels, or ≈0.12 μm per pixel. Although this resulted in the removal of any pile-up material, ribbon nucleation was not observed in either case. The half-bowtie shaped peeled areas characteristic of ribbons (with depths up to ≈25 nm) were observed although ribbons

were not. These apparent peeled areas had widths of ≈ 0.2 – 0.4 μm. Tip bluntness due to the high setpoints reached reduced image quality further. We therefore suspect that ribbon nucleation may in fact have occurred successfully in these instances, but that any ribbons nucleated during hard tapping were also destroyed by the hard tapping process and could not be adequately imaged during hard tapping due to the image pixel size (only 2-4 pixels per ribbon) and tip bluntness.

Limited successful ribbon nucleation was observed on few-layer MoS_2. AFM-based indentation and hard tapping was performed on a 1-layer and a 3-layer MoS_2 sample, with areas of only ≈20 μm^2 and ≈50 μm^2 respectively. Given these small areas, only 6 indents could be positioned on the former and 10 indents on the latter. Nucleation was not observed in either case with indentation alone. With application of hard tapping as on the thicker MoS_2 samples, limited folding and ribbon nucleation was observed, as in Fig. 3.8. On the three-layer sample around a single indent in Fig. 3.8 (a)-(c), no nucleation was observed over 4 scans at 4 μN setpoint, though some tearing occurred around the indent ((a) being the last of these 4 scans). A single hard tapping scan at 5 μN immediately results in ribbon growth however as in Fig. 3.8 (b), with ribbon direction indicated by red arrows, while a further scan at this setpoint in Fig. 3.8 (c) causes the larger ribbon to fold over itself and the smaller to be apparently destroyed. We note that the jagged edges of indents in (a)-(c) is simply a digital zooming artifact, with this artifact not observed in higher resolution images featuring indents on the same sample in (e) and (f). This supports our previous suggestion that ribbons may have formed during hard tapping at 5 μN on bulk-like MoS_2 but were destroyed before they could be imaged with a higher resolution scan. The hard tapping to nucleate the ribbons in Fig. 3.8 (a) - (c) was performed with a scan size of only 8 μm, or a nearly four-fold increase decrease in pixel size compared to the bulk-like MoS_2 case, allowing these ribbons to be imaged during hard tapping. Further ribbons can be observed in Fig. 3.8 (d), with higher resolution images of the purple and blue dashed outlined areas of (d) shown in (e) and (f) respectively. The ribbons in (d)-(f) were formed following only 1 hard tapping scan at 5 μN such that damage observed in (a) – (c) did not occur.

Due to the extremely limited sample area to create ribbons in MoS_2, it is difficult to extract significant insights into auto-kirigami in this material more generally. A majority of these ribbons have very small fold widths compared to typical ribbons in graphene, ranging from ≈50 nm (Fig. 3.8 (e)) to ≈170 nm (Fig. 3.8 (b)). Over the short lengths that these ribbons grow to of ≈ 0.3 – 0.4 µm, there appears to be very little tapering of the ribbon. The exception depicted in Fig. 3.8 (d) has a fold width of ≈450 nm, though grows to only 0.25 µm in length.

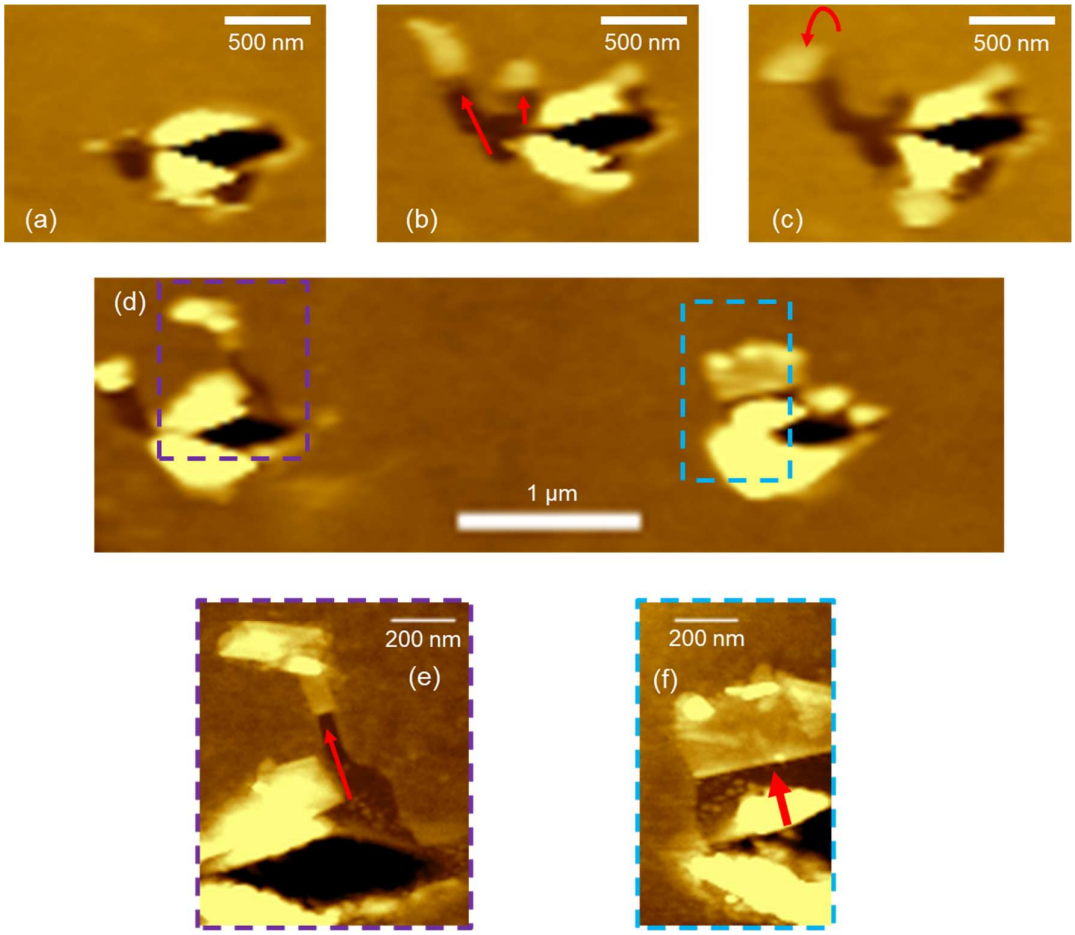

Fig. 3.8: Ribbon nucleation by AFM indentation and hard tapping on single-layer MoS_2. (a) Three-layer MoS_2 following hard tapping at 4 µN setpoint sufficient to cause some tearing but not ribbon nucleation, (b) the same indent following one scan at 5 µN setpoint at which small ribbons are immediately observed and (c) damage to and folding of ribbons in a single further hard tapping scan at 5 µN. Jagged edges of indents in (a) –(c) result from pixelation due to cropping from larger source AFM image. (d): Ribbons nucleated by a single hard tapping scan at 5 µN setpoint without severe damage from additional scanning. (e) and (f): Higher resolution images of successful, relatively intact ribbons in areas highlighted in purple and blue dashed lines in (d). Total linear z scale: 10 nm in each.

Although extensive and reliable nucleation of ribbons in MoS_2 has not yet been demonstrated, this nonetheless represents the first instance of ribbon nucleation in a non-graphene 2D material. This suggests the possibility that ribbons can be nucleated in a wider range of 2D materials, with hBN and graphene-hBN heterostructures considered in Chapter 4. With commercially available hBN crystals ranging from 0.5 – 1.5 mm in size, mechanical exfoliation could not be successfully carried out at a reasonable scale with this material following Huang et al.'s method of mechanical exfoliation incorporating an annealing step[44] used throughout this work. We note that other reports of hBN micromechanical cleavage report thinnest areas of 6-layers with lateral dimensions of those areas of less than 10 μm[191] or 1- and 2-layer with lateral dimensions less than 5 μm[31]. Tuneable, millimetre-scale exfoliation of 1-7 layer hBN has also recently been reported using metal-assisted exfoliation[192].

3.2.2 Crystallography of the torn edges of auto-kirigami ribbons

As briefly noted in section 1.2, Neubeck et al. in 2010 reported that mechanical exfoliation often produces flakes with apparently straight terminating edges at microscopic resolutions[13]. These edges are often oriented at ($n \times 30^o$) intervals to one another (for some $n \in N_0$), with Neubeck et al. determining by STM and Raman imaging that such edges predominantly follow either the armchair or zigzag direction of the graphene sheet. As discussed in section 1.6, this result was exploited by Rode et al. and Bockhorn et al. for example to determine the twist angle between graphene folds and host flakes[99,103,193]. By geometric arguments, they derive the twist angle by measurement of the angle between a straight, terminating edges of a flake (assumed to be either armchair or zigzag per above) and the fold itself.

From our observations of hundreds of mechanically exfoliated graphene flakes optically and a subset of tens of those by AFM, unambiguous straight graphene edges with regular ($n \times 30^o$) spacing are not commonly observed. Furthermore, graphene edges are very rarely perfectly armchair or zigzag, with sections of armchair on zigzag edges and vice versa[13,194], with this determination beyond the resolution of ambient AFM. Possible

lattice reorientation due to the presence of grain boundaries in a flake would also entirely obfuscate efforts to derive twist angles by this method. Requiring such unambiguous straight edges to derive only twist angle (with no insight into whether an edge is specifically armchair or zigzag, only that it is either) would impose a severe limitation on our supply of exfoliated graphene flakes. We therefore view this as an inadequate method to generally derive twist angle, and it is inherently incapable of allowing even inference of whether a crystallographic direction is armchair or zigzag. This distinction has been shown to influence for example graphene edge energy[195] and chemical reactivity[196] which in turn can result in friction at zigzag edges being two orders of magnitude greater than friction at armchair edges and reduced durability of zigzag edges[197].

Alternative methods to determine edge crystallography such as lattice-resolved AFM or Raman are available, but time-consuming. Instead, we can readily infer not only twist angle but crystallographic orientation from our observations of stripes on graphene.

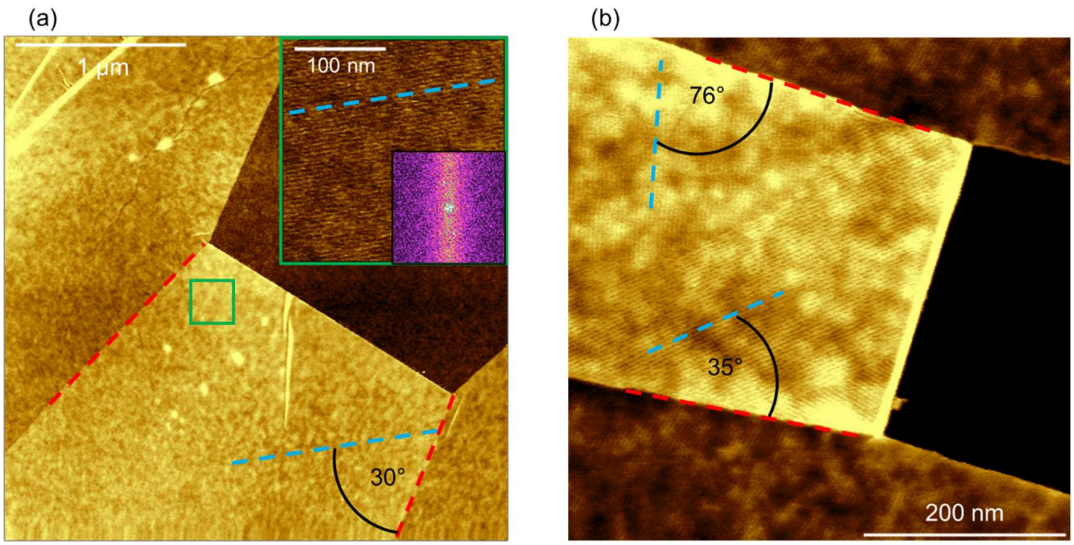

Fig. 3.9: Assessment of ribbon edge crystallography from stripe direction. Edges are indicated by red dashed lines and stripe direction by blue dashed lines. Armchair direction in (a) is inferred from the stripe direction determined from zoom-in of green highlighted area on ribbon in main of (a) inset in top right of (a). Error in stripe direction is calculated as angular radius of bright spots in 2D FFT of stripes, further inset in (a), with 9.0° ± 1.5° here. Direction of lower right ribbon edge is measured as 68°, so differs from stripe direction by n × 60° and is therefore armchair. In (b) where two stripe directions, differing by 60°, are seen on the ribbon, neither differs from a ribbon edge by n × 30° so neither are armchair or zigzag. Total z-scale: 2 nm in (a), 1.5 nm in (b).

As discussed in section 2.3, adsorbates quickly self-assemble into regular stripe patterns on freshly exposed graphitic surfaces in air, oriented along the armchair axis of the sheet. This allows for graphene crystallography to readily be determined by high-resolution PFQNM imaging in ambient conditions. Using this method, we performed a survey of ribbons nucleated on few-layer graphene to determine the alignment of torn graphene edges relative to the host sheet's crystallography as derived from stripe direction.

Our analysis is mildly complicated by the waviness seen in some stripes (see Fig. 2.1 for example). Edge direction is simplified as a straight line between ends of the folded peeled substrate area nearest the indent and the fold. Stripe direction is determined as the centre of the relevant peak in a 2D Fast Fourier Transform of the relevant area, with radius of the peak assigned as the error of this direction as in Fig. 2.2. Edges are considered armchair where these ranges of stripe and edge directions differ by specifically $n \times 60°$ and zigzag where they differ by $30° + (n \times 60°)$ for $n \in \mathbb{N}_0$. An example of this assessment for an armchair edge and for neither is shown in Fig. 3.9. This data is summarised in Fig. 3.10.

Beyond Annett et al.'s energy minimisation model[89], we may expect graphene rupture to be further influenced by the direction of lowest bond-breaking dissipation energy. Kim et al. calculated the direction-dependent work of fracture in graphene by a molecular dynamics simulation ReaxFF force field. They found that crack propagation should occur predominantly along either armchair or zigzag direction rather than intermediate directions[198]. They also observe twice as many tears aligned along the armchair direction compared to the zigzag direction by TEM in suspended monolayer graphene. However, graphene auto-kirigami ribbons also typically have a constant taper angle. In one dataset of 52 ribbons on a single mechanically exfoliated bilayer graphene for example, a range of taper angles of 4-20° is observed with mean taper angle of 13°. With all values here below 30°, even if one torn ribbon edge is aligned along the energetically preferred armchair or zigzag crack directions, the other edge cannot be as it is offset by 4-20° from the first. This could give rise to more complicated tearing behaviours to minimise rupture energy across both tears, which we examine

experimentally here. Assuming stripe adsorbate correlation to graphene sheet lattice orientation, we have surveyed the tearing edge crystallographic orientation of 31 ribbons formed in 14 distinct mechanically exfoliated graphene samples of a few layer thickness.

Ribbons in this survey were produced both by SASIN and by AFM indentation followed by hard tapping. In ribbons nucleated by SASIN, approximately equal proportions of ribbons are nucleated with one armchair edge as with one zigzag edge (and none with both edges along a crystallographic direction). Approximately half as many as either case do not have edges aligned along either crystallographic direction. However, considering only those ribbons nucleated by AFM indentation followed by hard tapping, no ribbons are observed with edges along an armchair or crystallographic direction. We speculate that a combination of the direction of the lateral shear, small angular variation in alignment of the faces of the Berkovich tip arising from slight variations in tip mounting and graphene crystallography may all contribute to the preferred tearing directions of the ensemble in Fig. 3.10.

This supports our claim that nucleation by hard tapping does not occur only due to the self-driving mechanism of adhesion energy exchange described by Annett et al. As previously observed, ribbons nucleated by hard tapping appear to grow in directions defined both by slow scan axis of the hard tapping imaging and perpendicular to the elongated indent edges. We suggest that the energy minimisation achieved by tearing along a specific crystallographic direction is negligible compared to the energy

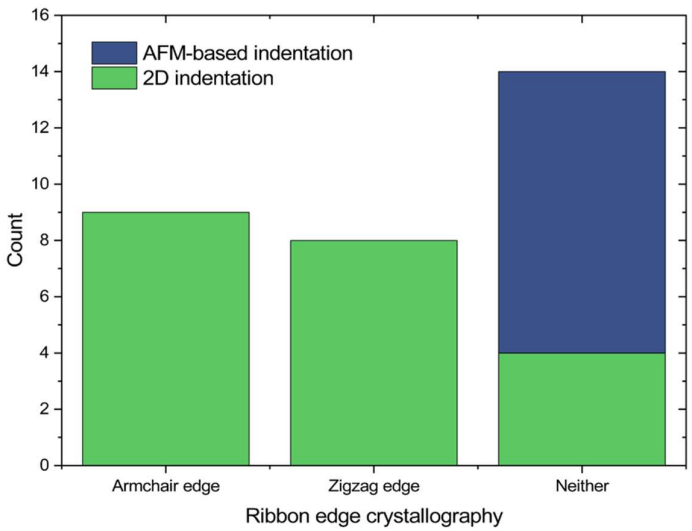

Fig. 3.10: Crystallography of ribbon edges by AFM-based indentation and by SASIN. Nearly equal proportions of ribbons are observed with one armchair or one zigzag edge, though ribbons with both edges not aligned to any crystallographic axis are most common.

transferred by the AFM tip, and hence is not observed here. This also supports our assessment of hard tapping continuously providing driving energy for growth rather than simply "unsticking" a ribbon which may have become pinned by contamination or a defect for example.

3.3 Graphene Rupture during 2D Nanoindentation

Thus far, we have discussed indentation only in the context of using this approach to rupture graphene sheets, nucleating ribbons where small amplitude, lateral oscillations are applied during nanoindentation at a high frequency compared to the indentation time. While nanoindentation was originally applied primarily for hardness testing[68,199] and then elastic modulus extraction in sub-micrometre scale volumes[77], it can also be used to test material microstructures, creep, fracture toughness, friction and wear properties among others for example. In our 2D indentation testing, we will primarily consider lateral indentation data to extract information on graphene rupture as well as ribbon nucleation. All 2D indentation is performed using the Gemini system described in section 1.5, following procedures also described there.

Firstly, we consider the influence on indentation signals when introducing a single layer thickness graphene sheet to a silicon wafer with a 300 nm SiO_2 thermal layer in Fig. 3.11. Only very minor difference is seen between load vs. sample depth penetration curves whether single layer graphene is present or not as illustrated for selected curves in Fig. 3.11 (a). The graphene sheet also does not appreciably affect vertical small amplitude contact stiffness (Fig. 3.11 (b)), or any other measured parameter measured in the vertical axis not shown here (such as damping or dynamic displacement or the raw measurement parameters of amplitude and phase[200], from which the contact stiffnesses are derived). In contrast, very different behaviour is observed in the early stages of indentation for the lateral contact stiffness signal per Fig. 3.11 (c) between the two surface conditions. In the case of bare 300 nm SiO_2/Si, a local peak in the small

amplitude (1 nm) lateral oscillatory contact stiffness is observed at 0.7 nm depth, thought to be associated with the slight rounding of the peak of the pyramidal Berkovich tip which is most pronounced at such shallow depths. The lateral stiffness then grows linearly with depth up to 100 nm. With the introduction of even a single graphene layer, a much slower increase of lateral contact stiffness with depth is seen up to a depth of 11 nm in (c), where a sudden increase occurs over a depth of only ≈0.5 nm. Following this point, the lateral contact stiffness of the SLG/SiO_2 largely follows that of bare SiO_2. The starkly lower lateral stiffness before the jump-up point is attributed to dry lubrication of the contact by the graphene sheet. The slope of lateral stiffness with penetration increases three-fold in the 10 nm after this point compared to before.

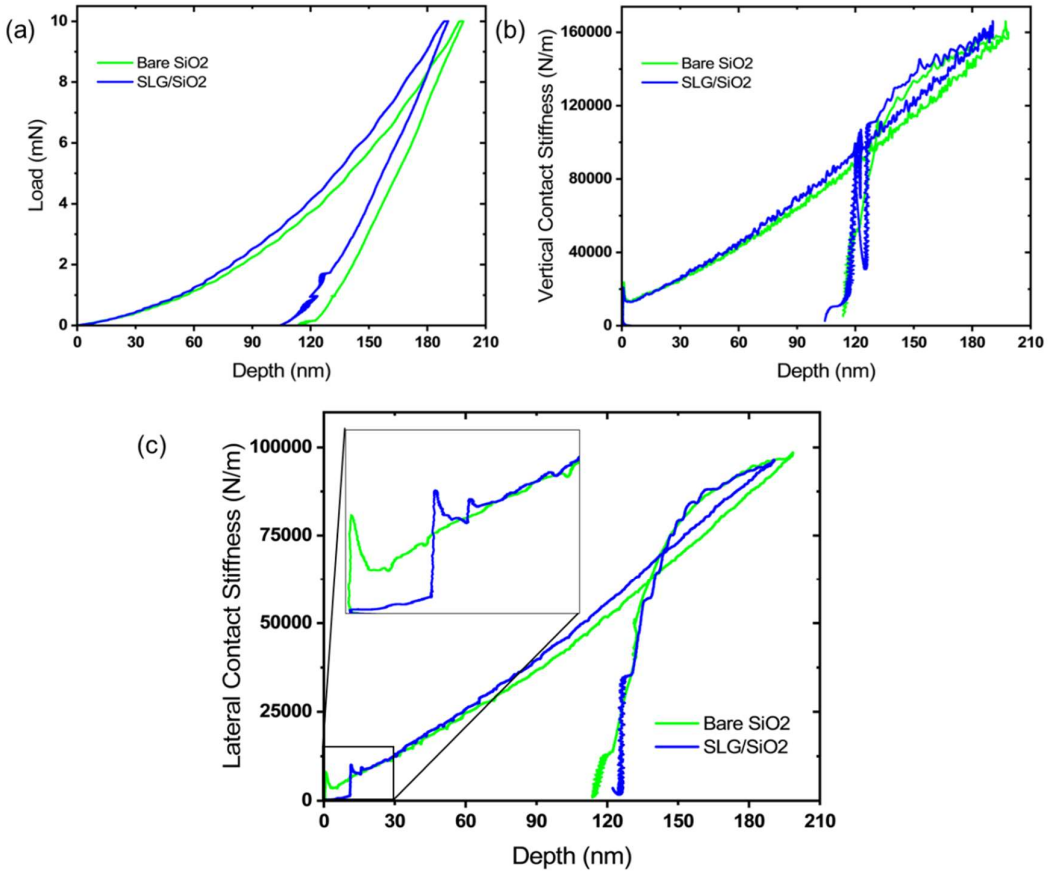

Fig. 3.11: Indentation via a 2D nanoindenter of 300 nm SiO_2/Si substrate with and without mechanically exfoliated single layer graphene on SiO_2/Si substrate. (a) Load-displacement curves for indentation on bare SiO_2 and SLG/SiO_2. Both curves are also similar for vertical contact stiffness, but a clear difference is present in lateral contact stiffness (c). Zoom to first 30 nm depth (inset top left of (c)) of SLG/SiO_2 shows very low lateral contact stiffness up to a depth of 11 nm, at which lateral contact stiffness suddenly increases.

The sudden increase in lateral contact stiffness at this point is attributed to rupture of the graphene sheet. AFM imaging of indents on graphene limited to depths below this jump point do not show tearing of the graphene sheet, while torn and punctured graphene is found in AFM images of indents following the lateral stiffness jump. We note that no feature can be seen at the critical 11 nm point in any normal direction signals that a traditional nanoindenter would measure.

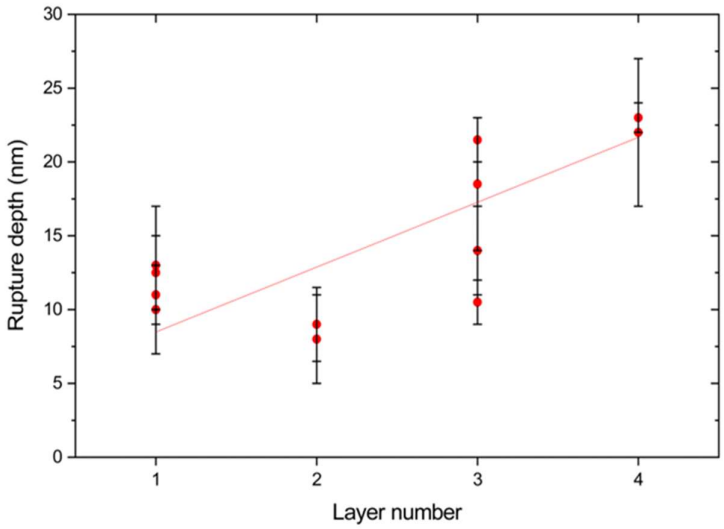

Fig. 3.12: Variation of rupture depth with graphene layer number. A general trend of increasing rupture depth with layer number is observed.

Having characterised this sudden increase in lateral contact stiffness as graphene rupture, we can use this to examine factors that influence rupture in graphene.

Fig. 3.12 summarizes the dependence of rupture depth on layer number. Here, every point represents the average rupture depth of an array of indents on different mechanically exfoliated graphene flakes. All arrays of indents are performed with identical indentation parameters, including oscillation frequencies (129 Hz in normal and 85 Hz in lateral direction) and amplitudes (3 nm in normal and 0.5 nm in lateral direction), which were rapid compared to the overall indentation strain rate of 0.02 s^{-1}. Errors bars in Fig. 3.12 are chosen to encompass the maximum and minimum rupture depth of the respective flakes represented by their mean rupture depth.

The naive assumption of a linear fit as presented in Fig. 3.12 does not model the data well with a R^2 value of only 0.58. Instead taking the average rupture depth of all indents across different graphene layer numbers and using the standard deviation as error, a much better linear fit with R^2 value of 0.83 is obtained. This is largely attributed to data

for two-layer graphene which acts as an outlier here, with an improved R^2 value of 0.994 where two-layer graphene is not considered (noting however that each data point in Fig. 3.12 represents the average rupture depth of an array of indents on a single flake, not for an individual indent). A number of factors influence the total number of indents in each category. Varying graphene flake sizes limits the number of indents that can be performed on a single flake. Some data must be discarded as an indent may be positioned in the peeled area of a ribbon nucleated by a previous indent in the same array (or on a ribbon nucleated by an indent of the same array, effectively doubling layer number). Furthermore, layer number was determined by AFM after indentation rather than before indentation. This was selected as layer number can be most reliably determined by AFM from folded areas of graphene i.e. ribbons produced by indentation rather than by surveying flakes with AFM beforehand to use substrate-flake separation as an indicator of layer number. These factors can therefore unintentionally result in an unequal distribution of indents with layer number. For 1-, 2-, 3- and 4-layer graphene in Fig. 3.12 (a), 15, 8, 22 and 23 total indents were counted for each respectively. Bilayer graphene is therefore under-represented in this dataset. Even though two samples tested were 2-layer and two 4-layer, the 4-layer flakes were of much larger area so more indents could be performed on this sample. This underrepresentation of bilayer graphene may account for this layer number acting as an outlier in this rupture data, as we do not recognise a physical basis for a non-monotonic increase of rupture depth with layer number.

Variability of the rupture depth is observed both for different flakes and within a single flake as indicated by error bars associated with each data point. Alteration of the contact stresses due to degradation of the Berkovich tip shape with extended use is not expected as all indentation data for Fig. 3.12 was taken in succession over a period of 5 days Similarly, environmental conditions such as humidity are expected to have been largely stable. We have also considered whether the location and positioning of indents may affect the rupture depth. All indents in this survey were to 10 mN peak load, resulting in a residual plastic deformation crater of ≈120 nm depth (Fig. 3.11 (a)). Indentations in this work are routinely positioned 5 µm apart, well over the recommended indent spacing of 10 times the indentation depth[82] (or 1.2 µm here)

beyond which distance the effect of plastic deformation associated with an individual indent is negligible upon neighbouring indents. It is not clear whether indent-to-indent influence might be transmitted through the graphene layer(s) (by for example tensile strain induced in the sheet by indentation) at this indent spacing. This was tested by considering rupture depths of indents specifically in 2-dimensional arrays (i.e. where indents are laid out on the surface in a rectilinear pattern with uniform spacing in both axes). Indents were grouped by their number of nearest-neighbours and next-nearest neighbours (along diagonals only) indents previously performed in an array. Using nearest neighbours as a proxy for a potential indentation-induced strain in the ribbon, no correlation was found with rupture depth. Similarly, indent location on a flake was considered in terms of a "body" or "edge" location within the host flake. Edge locations were defined as being within a variable arbitrary percentage of the flake size from the edge (e.g. choosing 10% on a square 50 μm × 50 μm flake would count any indent within 10% × 50 μm = 5 μm of a flake edge as being in an edge location) with all others being "body". This was examined as pinning sites on flake edges could affect sheet-sheet or substrate-sheet sliding at pre-rupture depths. However, again no correlation was observed with rupture depth. While we will later discuss a possibility of non-negligible variation of graphene-substrate adhesion energy across a flake, we do not currently identify any other plausible parameters which could account for the scatter in rupture depth both within and between graphene sheets of the same layer number as indicated in Fig. 3.12. Nonetheless, a general trend of increasing rupture depth with layer number is maintained over 1-to-4-layer graphene.

We also note that in mechanically exfoliated samples, the absence of secondary or further rupture points in lateral contact stiffness suggest that rupture occurs instantaneously across all layers in 2-4 layer samples. However, these additional rupture points may be hidden within the singular rupture point as fine structure in the gross signal. Here we refer specifically to the peak around the local maximum immediately following the near-vertical increase in lateral contact stiffness at the rupture point, which is examined more closely in Fig. 3.13.

Lateral contact stiffness and dynamic lateral displacement (the tip's lateral oscillation amplitude) around a representative sample rupture point are shown in Fig. 3.13 (a) and (b) respectively. The latter is a set-point signal measured by the nanoindenter capacitive displacement sensor and maintained electronically to a constant value by dynamic force feedback, while the former is a derived signal consisting of the ratio of the dynamic force to displacement amplitudes. The upward spike in lateral contact stiffness is consistently associated with a sudden decrease in lateral displacement, although the contact stiffness in fact appears to lag slightly behind lateral displacement at point A (data also highlighted in red) in Fig. 3.13 (a) and (b). The width and shape of the subsequent peaks in these signals is attributed to the electronic feedback mechanism controlling the lateral displacement. The gain of this feedback mechanism can be defined, where low gains alongside higher setpoint displacements can result in highly unstable displacements over tens of nanometres of indentation depth after rupture. Gain selected here was chosen to minimise this instability, though both set and controlled dynamic displacements measured are the root mean square values. Even with optimisation of this gain, controlled gain has returned only to 85% of the set value at point B where the turning point of lateral contact stiffness after the peak is seen. The controlled displacement returns to the set value of 3 nm (or within 1% of it) only at point C in Fig. 3.13 (b), at a further depth of 15.3 nm following rupture at point A.

Indentation on thicker graphene was not extensively performed in this work as the

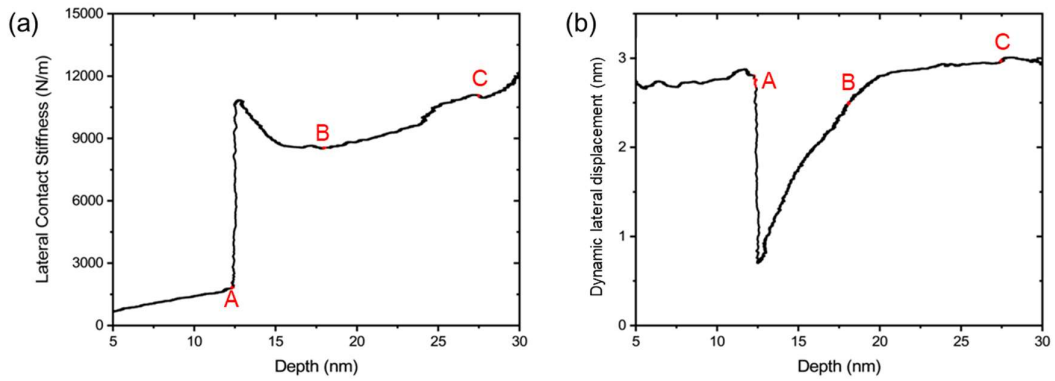

Fig. 3.13: Lateral contact stiffness and lateral displacement signals immediately before and after rupture point. Points are highlighted in both immediately before rupture A, turning point of lateral contact stiffness after rupture B and where dynamic lateral displacement returns to within 1% of its defined value of 3 nm C.

focus remained upon few-layer graphene in which 2D indentation has been demonstrated to reliably nucleate ribbons, while nucleation is not observed in flakes with layer numbers higher than about 10, perhaps due to increased strain energy of the fold at higher number of layers. Nonetheless, we can also consider selected outliers where higher graphene layer numbers are indented upon by chance.

Fig. 3.14 (a) shows an AFM image of a region of a mechanically exfoliated 3-layer graphene sheet with a smaller 13-layer area on its righthand side. An array of indents was performed on this sheet (4 of these shown in (a)), with the rightmost of these falling upon a folded area of graphene of 13-layer thickness which was apparently formed as part of the initial mechanical exfoliation. The indents on 3-layer graphene show rupture points at 20-21 nm depths, consistent with the previous sample summarized in Fig. 3.12. However, the indent on 13-layer graphene shows a rupture point at a depth of 115 nm. This is significantly higher than the value that could be extrapolated from a linear fit of Fig. 3.12 of 55 nm.

The low slope of lateral contact stiffness increase with depth previously observed up to depths of ≈10-20 nm is here maintained to this depth of 115 nm. We emphasise that this implies that the 13-layer graphene deformed without rupture with indentation to a depth of 26 times its own thickness. Assuming conformation of the graphene to the indenting tip shape during loading, a simple calculation of the projected length of graphene adhered to the indent crater forming plastically compared to the projected surface distance along a Berkovich indent vertex finds an in-plane uniaxial strain of 5.1% in the graphene layer at the rupture point. This is less than the theoretical critical strain that graphene can sustain of 32-36% along armchair and zigzag directions respectively[201,202]. Comparing the area of the graphene conformed to the tip at this depth, a biaxial strain of only 3.7% is obtained however relative to the corresponding area of graphene prior to indentation. This may suggest that highly local effects around the tip may impact rupture more than strain over the entire area of graphene in contact with both the tip and deforming substrate. Similar plastic deformation and elastic recovery is observed across all indents in this set.

However, this indent represents a special case. From comparison of folded edge and straight flake edges presumed to align with a crystallographic axis, this folded graphene should be in incommensurate contact with the main 3-layer sheet. We therefore can consider this folded graphene as a 10-layer on 3-layer twisted stack with an incommensurate interface present between the 3-layer and 10-layer rather than only A-B stacking throughout. This incommensurate interface may lead to easy sliding which could contribute to the large indentation depth achieved before graphene rupture as indicated in Fig. 3.14. However, reproduction of this result of indentation on twisted graphene stacks proves highly challenging to achieve. Although such twisted stacks can be readily produced (as in ribbons for example), only in exceptional cases are folds with areas of tens of square micrometres produced. Areas of such size are required as indent positions on the relevant area of graphene must be chosen by eye using an optical microscope, which combined with potential backlash of the stage limits fine control of indent position to within a few microns at best. However, this suggests the possibility of highly controlled studies of indentation in the presence of a known incommensurate 2n-layer interface on an otherwise n-layer commensurately stacked flake.

With this insight into the depth at which rupture occurs from lateral contact stiffness as described above, we then sought to elucidate the mechanism of graphene rupture during SASIN in conventional cases. Two general models were

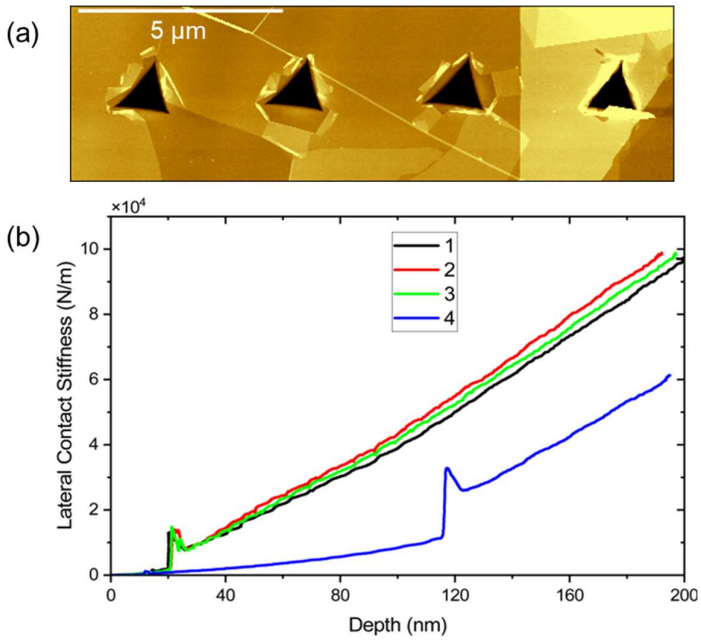

Fig. 3.14: Rupture depths in thicker graphene. (a) AFM image of 3 indents on 3-layer graphene (labelled 1-3 from left-to right in (b)) and 1 indent on 13-layer graphene (rightmost, labelled 4). Total linear z-scale of 15 nm. (b) Lateral contact stiffnesses of indents on 3-layer and 13-layer graphene. Low contact stiffness is maintained to a depth of 115 nm on 13-layer graphene.

considered: that rupture occurs at a critical stress when contact pressure of the tip exceeds a threshold, or that occurs as a result of continuous atomic attrition in a kind of wear mechanism tied to the number of oscillations experienced (which may also be a function of contact stress tied to indentation normal load and oscillatory shear amplitude). As a first look at this problem, two parameters are chosen to explore the wear mechanism: lateral oscillation frequency and normal indentation strain rate for the self-similar Berkovich tip. All tests presented in Fig. 3.15 (a) are performed on a single graphene flake (and similarly for (b) on a separate, single graphene flake).

In Fig. 3.15, mean rupture depth at each oscillation frequency (65 Hz, 129 Hz and 250 Hz) (a) and strain rate (0.02, 0.05, 0.2) (b) are represented by red circles, with standard deviation of the mean as the error bars, while black triangles represent individual indents. Large scatter is still observed in each instance. We note that lateral oscillation frequencies available are limited from 50 to 250 Hz on the 2D nanoindenter system used. With a normal oscillation frequency of 85 Hz, it is recommended to avoid both frequencies around 85 Hz and its overtones (to avoid coupling of the actuators) as well as frequencies around 100 Hz and its overtones (to avoid electrical interference).

In Fig. 3.15 (a), 8 indents are presented for 65 Hz, and 9 each at 129 Hz and 250 Hz. A mean rupture depth of 11.1 nm is observed at 65 Hz and 7.5 nm at both 129 Hz and 250 Hz. All other indentation parameters are kept constant (0.5 nm oscillation in z at 85 Hz, 3 nm lateral oscillation amplitude) and all indents were performed on the same

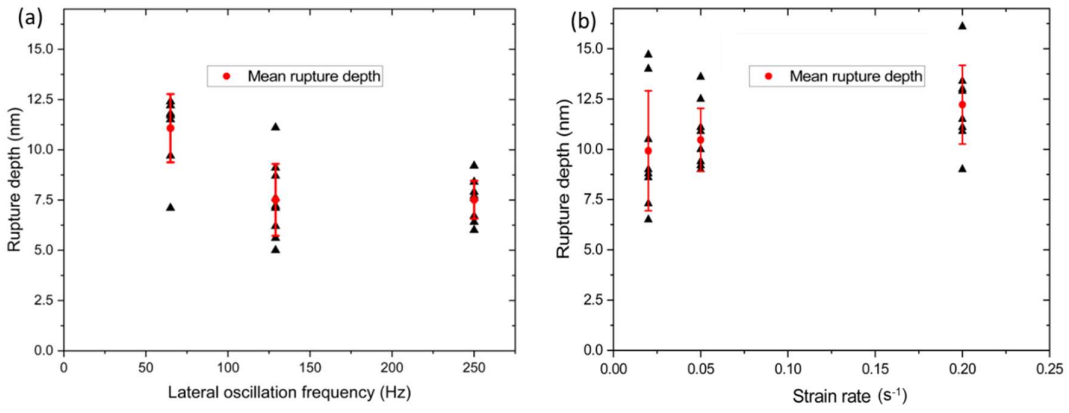

Fig. 3.15: Variation of rupture depth with lateral oscillation frequency (a) and strain rate (b). Individual data points are represented by black triangles and mean at each chosen variable in red.

graphene flake. Although this requirement limits the total number of indents that can be obtained, it was judged preferable to maintain consistency within a single flake given the scatter previously observed in rupture depths across separate graphene flakes. Here, we interpret lateral oscillation frequency as a proxy for total distance travelled by the tip laterally. Increased frequency will correspond to a greater number of cycles to a constant displacement setpoint. With a constant strain rate, this in turn corresponds to increased wear behaviour of the graphene sheet by the tip potentially leading to rupture.

Testing of rupture depth with strain rate (Fig. 3.15 (b)) was performed with 1 nm lateral oscillation amplitude at 65 Hz lateral oscillation frequency. 8 indents are represented at 0.02 s^{-1}, and 10 each at 0.05 s^{-1} and 0.2 s^{-1}, with the same considerations as above in (a).

Rupture depth increases with increasing strain rate as per Fig. 3.15 (b), from 9.93 nm at strain rate of 0.02, 10.47 nm at 0.05 and 12.22 nm at 0.2. This is fit well by a linear fit with R^2 of 0.995, albeit over only 3 set values of strain rate. Strain rate is defined as $\frac{\dot{h}}{h}$ or equivalently as $\frac{\dot{P}}{P}$. With units of s^{-1}, a higher strain rate corresponds to less time required for indentation loading. Fewer total number of oscillations can occur to a set depth at higher strain rates, such that any effect of a wear mechanism should be reduced at higher strain rates. As we see higher rupture depths with higher strain rates, this could imply rupture occurring due to depth effects (higher mean contact pressure) or that the wear mechanism cannot be applied to the same degree at these higher strain rates. A more complex convolution of both mean contact pressure or peak contact pressure and wear may in fact describe graphene rupture more accurately.

While the relationship of rupture depth with lateral oscillation amplitude was also tested, this proved more complex to decouple from other indentation parameters. As seen in Fig. 3.13 (b), a set displacement value (there 3 nm) may not be reliably reached or maintained by the force-controlled lateral actuator during the initial tens of nanometres of indentation depth. While this can be optimised with variation of feedback gains for lateral oscillation, such optimisation is also highly dependent on the set amplitude itself. As the region of most interest is often the initial 10-20 nm, applying much lower strain rates or holding the tip at a very small indentation depth pre-rupture

can result in significant distortions due to drift, either in the capacitive gauge and/or thermal drift at the tip-sample interface due to different sample material and tip temperatures. A simple method to directly study the wear mechanism would be to simply vary the maximum load hold time at sufficiently small target depths where rupture is not expected to occur. The tip would then oscillate at e.g. 5 nm depth for varying lengths of time where, by the proposed wear mechanism, rupture might occur nonetheless over longer time periods at this pre-rupture depth derived from 2D indentation to larger depths. However, drift in indentation depth of 10-20 nm over few minute hold periods prevented this method from being successfully implemented.

We can also take an AFM-based approach to gain insight into graphene rupture and post-rupture tearing during 2D nanoindentation. Ribbon area can easily be mirrored around the fold i.e. simulating ribbon reversal in a sufficiently high-resolution AFM topography image showing the entirety of the ribbon, peeled area, and indent. We can then examine whether graphene that had previously covered the indent area is accounted for within the ribbon. However, there is a common complication in typical ribbon structure that prevents more widespread application of this simple visual

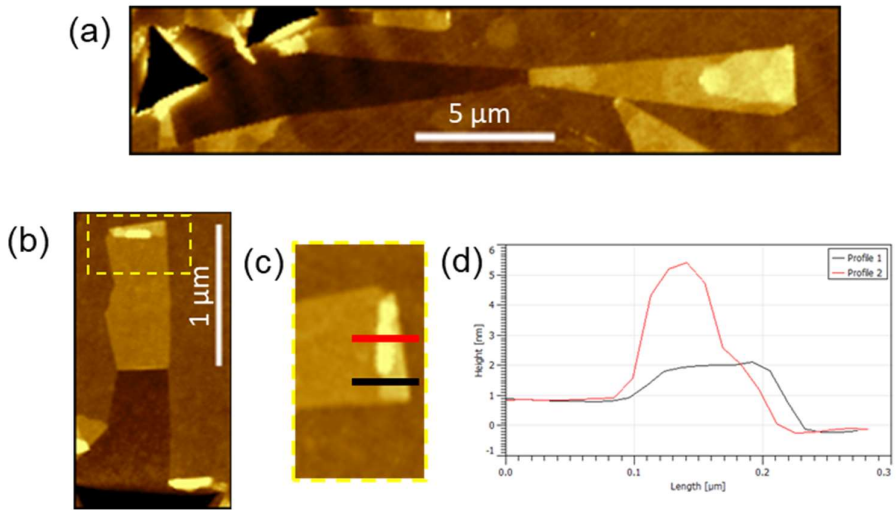

Fig. 3.16: Folding at the ribbon head. Such folding can occur over 100s nm – few µm length scales (a) or over only 100 nm at the head of a ribbon (b). Zoom in to area highlighted in yellow dashed lines in (b) shown in (c) and height profiles along black and red lines indicated in (c) show various degrees of folding. In this 3-layer graphene sheet (corresponding to height of ≈1 nm), height profile over brightest area (profile 2, red) indicates folding to 15 total layers thickness. Total linear z scale of 6.5 nm in (a) – (c).

method: the ribbon heads almost always show additional folding which cannot readily be deconvolved. This can occur to different extents, as shown in Fig. 3.16. Further folding may occur over lengths of 100s of nanometres or more, typically if a growing ribbon encounters a step barrier and folds again, reversing direction rather than growing over the barrier. Double-folding at the ribbon head over a length of 3.7 µm is observed in Fig. 3.16 (a). Such folding can also occur over lengths of only 10s of nanometres but may fold multiple times, as in Fig. 3.16 (b) and (c). The latter folds at ribbon heads appear similar to the embryonic small, folded-over tabs of adhered graphene around the indent crater described by Annett et al. as necessary for ribbon growth to occur[89]. Since folds at the ribbon head as depicted in Fig. 3.16 are very common, accurately tracing the shape of a ribbon to visually "unfold" it can prove challenging, as even 100 nm can often represent ≈5-10 % of the total ribbon length.

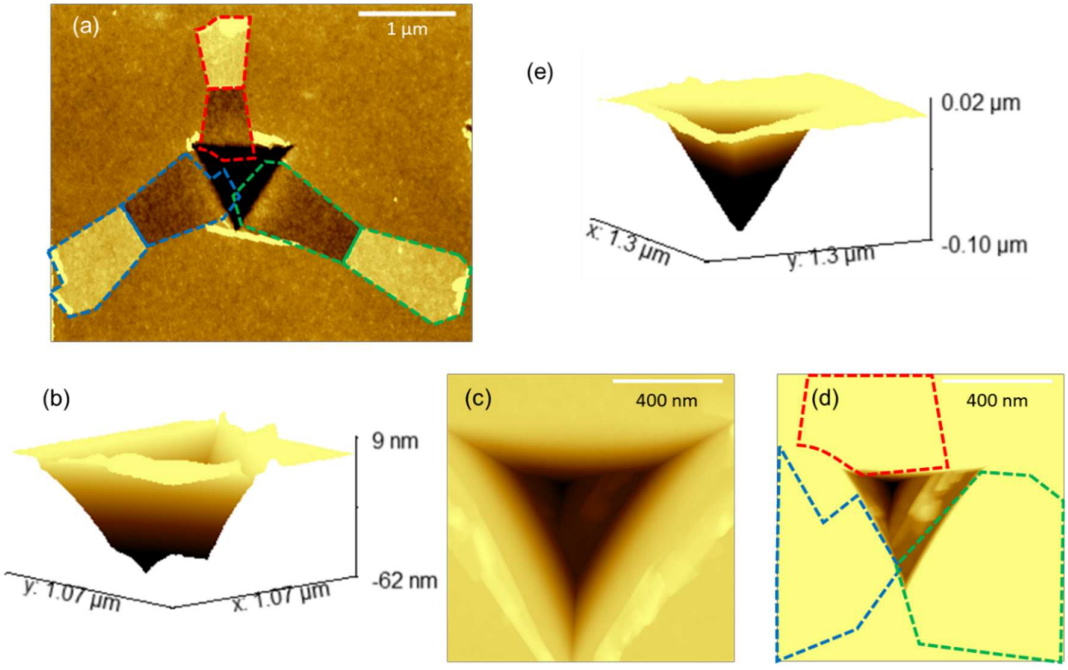

Fig. 3.17: Effect of tip shape and indent crater shape on nucleated ribbons. (a) PFQNM topography showing outlines of ribbons nucleated from an indent, with these outlines mirrored around the ribbon folds. (b): 3D view of indent in (a). The expected self-similar equilateral-triangle based pyramidal indent crater of Berkovich indentation is not observed here. (c) and (d), zoom-in to the same area around the indent in (a) with differing colour ranges, shows that this area instead appears as a plateau inside the indent with Berkovich tip shape recovered only in small area in top left corner of this plateau. Unfolded ribbon positions in (d) also indicate that folded graphene at ribbon heads originates from centre of the indent. 3D AFM topography of indent with the same tip in aluminium (e) shows that the Berkovich tip has not become damaged. Total linear z scale: 3.5 nm in (a), 50 nm in (d) and 20 nm in (e).

Nonetheless, we can apply this method to a small proportion of ribbons for which little to no additional folding is observed.

This method is applied in Fig. 3.17 (a) to a sample indent of an array for a standard strain-rate controlled indentation test. Ribbons are highlighted in red, blue and green dashed lines, with these shapes then mirrored around their respective folds to recreate the initial location of these graphene areas. These outlines extend into the indent crater but do not appear to entirely account for all of the previously present graphene. However, this indent appears irregularly shaped as indicated in a 3D view in Fig. 3.17 (b), in contrast with the shape obtained from the same tip indenting in aluminium in (e). Fig. 3.17 (c) and (d), of the same area around the ribbon but with different colour scales, indicate that a triangular plateau is present centered in the indent crater. We are confident that this is not an AFM artifact (due to the AFM tip being unable to track the indent for example) as this shape is reproduced over various scan sizes, scan rates and is also observed in contact mode. However, the Berkovich shape is recovered in the off-centre, deeper portion of the indent in the top left corner of this plateau in Fig. 3.17 (d). We attribute this to sliding of the tip during indentation. The positions of the ends of the "unfolded" ribbons as indicated by coloured dashed lines in (d) agree very well with the edges of this plateau. However, these outlines do not account for small areas of folded graphene at the ribbon heads as seen in Fig. 3.17 (a). Estimating the contribution of these folded areas suggests that rupture during indentation initially occurs at the tip vertex rather than edge for example, as edge-rupture should result specifically in triangular-shaped folded graphene areas at ribbon heads, which is not here observed.

Experiment no.		**1**	**2**	**3**	**4**
Stages					
Loading		✕	✓	✓	✓
Peak hold		✕	✕	✓	✓
Unload		✕	✕	✕	✓
Oscillation on/off: ✓/✕					

While the rupture point is observed during the loading portion of the indentation experiment, it remains unclear when folding occurs. Per Fig. 3.17 (d) however, as ribbon outlines extend into the indent crater by lengths of as much as 0.2 µm, those graphene areas should be trapped by the tip during loading and hold at peak load, and could only

nucleate to form auto-kirigami ribbons during unloading or afterwards. To test this hypothesis, a series of arrays of indents (25 indents each) were performed on few-layer mechanically exfoliated graphene. In this instance, lateral oscillation displacement could be controlled during each stage of indentation (with loading, hold at peak load, and unloading stages selected). Indentation was performed where lateral oscillations were applied selectively only during specific stages rather than during the entire indentation experiment, as indicated in the table opposite. Annett et al. had previously established that auto-kirigami occurs only in the presence of this lateral oscillation believed necessary to form initial folded tabs around the indent. However, a highly surprising result was observed. Auto-kirigami ribbon nucleation occurred in every variation of this experiment, even with purely 1D indentation without oscillations in the lateral or normal axes. Ribbon yields of 70-80% were still achieved in each instance, as in Fig. 3.18 (a). This result was reproduced in two further series of this experiment with 300 indents in total.

This unexpected result is primarily attributed to the Berkovich tip sharpness, as revealed by rupture depth across experiments. Previous (unpublished) 2D indentation results by

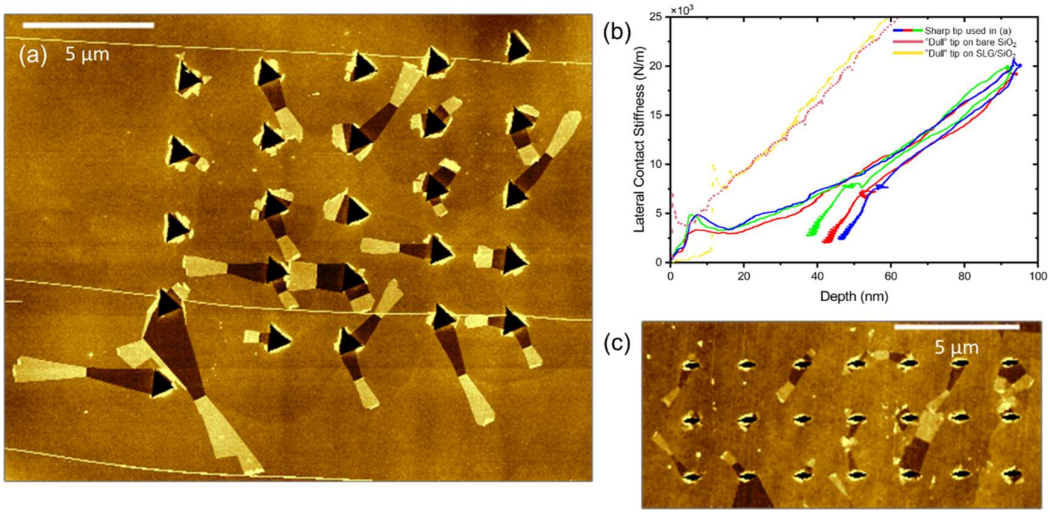

Fig. 3.18: Ribbon nucleation with no applied oscillations. (a) A high yield of ribbons is obtained using 1D indentation. (b) Different lateral contact stiffness behaviour is observed around rupture using a sharper Berkovich tip (solid lines), with no slowly rising lateral shear stiffness region before rupture and rupture at much lower depths. Representative behaviour of other, comparatively dull Berkovich tip on bare SiO_2 and single layer graphene/SiO_2 shown in dashed lines. (c) Successful nucleation has also occasionally been observed with AFM-based indentation alone i.e. with no oscillations and even without applying hard tapping.

Annett et al. using another system routinely featured rupture depths of tens to ≈100 nm for few-layer graphene, whereas we do not observe rupture depths greater than 30 nm in hundreds of indents on 1-4 layer graphene. As that system was primarily a proof-of-concept build, removal and replacement of the indenter tip proved exceedingly challenging, with the same diamond Berkovich tip used over several years. Meanwhile, nucleation with no applied oscillation was observed only where a fresh diamond Berkovich tip was installed in the Gemini 2D nanoindenter system. Previous 2D indentation work described above was performed with a previously-used diamond Berkovich tip. This tip, while it appeared suitably sharp, had a tip end radius of ≈80 nm compared to an estimated tip end radius of ≈150 nm for the older Berkovich. Curvature of the fresh Berkovich tip could not be resolved with AFM, suggesting that it may be on the order of ≈10 nm tip end radius.

This is also supported by the lateral contact stiffness behaviour of sample representative indents using this sharpest Berkovich tip (Fig. 3.18 (b)). With similar indentation parameters (strain rate, oscillation amplitudes, oscillation frequencies etc) as in experiments previously described above, rupture depths of only 1-5 nm were measured on a three-layer graphene sample. Furthermore in Fig. 3.18 (b), the characteristic low contact stiffness associated with lubrication by graphene before rupture is not observed. We propose that this lubrication behaviour is not seen due to the higher contact pressure associated with a much smaller end radius.

Annett et al. only observed ribbon nucleation where fretting by lateral oscillations formed small, folded tabs around the indent. However, such tabs are also observed here in Fig. 3.18 (a). This strongly suggests that another mechanism may exist for the formation of these embryonic folds. This is also supported by observations of AFM-based nucleation. We previously stated that AFM indentation alone is typically not sufficient to nucleate ribbons, hence the utility of hard tapping. However, on occasion successful ribbon nucleation is observed with only AFM indentation, as in Fig. 3.18 (c). Where this occurs however, yields do not exceed 30-40%, while yields of ≈70% can be obtained even where no nucleation was initially observed with application of hard tapping.

3.4 Conclusions

In this chapter, we firstly tested and reviewed methods of ribbon nucleation by AFM tip scratching. While AFM scratching can nucleate ribbons, the low yield and poor control makes this an unattractive option. We instead presented an alternative method of ribbon nucleation by AFM-based indentation followed by AFM hard tapping of the resulting indents, which can be applied in principle on almost any AFM system. Notably, this removes the requirement for lateral shear during indentation for ribbon nucleation, which previously has severely limited the applicability of this method. This has also allowed for ribbon nucleation in materials where a driving interfacial force arising from preferential adhesion of a folded structure is not present, such as in graphite and bulk MoS_2. This has also allowed for examination of buried interfaces as seen earlier in graphene in Chapter 2.

Inference of graphene crystallography by observation of stripes, aligned with the graphene armchair direction, indicates that while neither ribbon tear edge following a crystallographic direction is the most commonly observed occurrence, approximately equal proportions of ribbons feature one tear edge following either armchair or zigzag.

We also reported on a novel signature of graphene rupture observed in lateral contact stiffness signals during 2D indentation. This readily allows for extraction of data on parameters influencing graphene rupture without requirements of complex in-situ SEM for example. A number of trends are observed, including a general trend of increasing rupture depth with graphene layer number; decreasing rupture depth to a plateau with lateral oscillation frequency and increasing rupture depth with strain rate which collectively provide insight into the mechanics of graphene rupture. We also determined that rupture is highly dependent on Berkovich tip shape, as expected as this occurs at low (few nanometre) indentation depths. Auto-kirigami nucleation was also demonstrated with no applied lateral shear in contrast to previous results by Annett et al., attributed to sharpness of the Berkovich tip used, highlighting the significance of the tip geometry in this process.

While the above results provide useful insights into the mechanism of graphene rupture

under two-dimensional indentation, we acknowledge the absence of a holistic physical model to describe this more thoroughly. The limited statistics available are due largely to material limitations i.e. lacking sufficiently large areas of mechanically exfoliated graphene, despite our advances in that direction. A wide array of indentation parameters can also influence graphene rupture, including strain rate, oscillation frequencies, and the quality of Berkovich tip itself. The complexity of this mechanism also strongly motivates parallel simulations and modelling (using LAMMPS for example) of this phenomenon, though this remained outside of the scope of this experiment-oriented study. These statistical limitations strongly motivate our study of indentation in CVD 2D materials in the next chapter, with large areas of CVD samples anticipated to allow scaling of indents from tens currently practicable on an individual graphene flake up to hundreds/thousands of indents.

Chapter 4: AK formation in CVD 2D materials

4.1 Introduction

In the previous chapters, we considered only indentation of and ribbon nucleation in mechanically exfoliated graphene samples. However, such samples inherently have a number of limitations as a result of the stochastic nature of mechanical exfoliation, including for example flake sizes rarely greater than 10,000 μm^2. We therefore are motivated to increase sample size to enable improved statistical analysis of ribbon nucleation and as a precursor to large-scale application of ribbons as NEMS devices. This is here achieved by use of chemical vapour deposition (CVD) graphene and other CVD 2D materials. Furthermore, while contaminant species considered in the previous chapter were alkane hydrocarbons of atmospheric origins, here we will examine residual polymer contaminants on CVD materials and consider the impact that these residues have on the auto-kirigami process, as well as our efforts to remove them.

Although mechanically exfoliated graphene features the highest structural quality of graphene synthesis methods, limitations such as relatively small flake sizes, low throughput in production and the time-intensive efforts necessary to identify flakes by optical microscopy and to determine layer number for example restrict the application of graphene to research only[203,204]. These limitations prove extremely detrimental to efforts to scale up ribbon production from tens/hundreds at present to thousands or more. Such scaling would act as a necessary step to application-based studies and would allow greater statistical analysis of ribbon nucleation. Currently, such statistical analysis is limited by the large number of variables to be controlled even within a single flake. During indentation, oscillation frequencies and amplitudes in two axes, strain rate, hold times and indent spacing may all play a role in nucleation, yet these cannot be adequately explored in a single flake. While we may assume that layer number is the leading parameter to control of the graphene sample such that many flakes of uniform layer number could be used in such a study, this still does not account for factors such

as the atmospheric environment, crystallography and local contamination - all of which may vary between samples. Here, by crystallography we refer specifically to sample crystallographic directions relative to the faces of the Berkovich tip which largely define the torn edges from which nucleation begins. While this may be uniform within a single sample (if the sample is not rotated and crystals large enough), this cannot be adequately controlled between samples.

Therefore, to overcome such limitations, large area samples produced by chemical vapour deposition (CVD) were investigated for gr-AK formation via indentation as well. Such samples boast continuous films on square centimetre areas and advertised well-controlled thickness, quality, and coverage. Despite the polycrystallinity of such films with grains of random crystallographic orientations, and some voids, wrinkles, folds and cracks unavoidable from the transfer process, these samples were anticipated to resolve many of the above limitations.

4.2 Nucleation in CVD 2D materials

CVD samples were sourced from three commercial suppliers (Graphenea, Graphene Supermarket and 2D semiconductors) and one collaborating research group (Prof. Charlie Johnson, University of Pennsylvania). These samples included from Graphenea 1-layer, 2-layer and 3-layer CVD graphene; from Graphene Supermarket 1-layer CVD graphene, multilayer CVD graphene (patchwork of 1-7 layers with 3-10 µm patch sizes), 1-layer CVD hBN and CVD graphene-hBN heterostructure; from 2D Semiconductors 1-layer CVD graphene and 1-layer CVD MoS_2; and from the Johnson group 1-layer CVD MoS_2 as triangular islands rather than a continuous film (both as synthesised on SiO_2 and transferred to another SiO_2 substrate) and 1-layer CVD graphene transferred from copper foil onto a silicon substrate. A testing procedure was developed to test each of these samples for success of ribbon nucleation: a batch of 25 indents in a 5 × 5 array with 1.5 µm spacing to a setpoint of 0.5 mN was carried out on each sample by AFM indentation, and a batch of 10 indents in a 5 × 2 array with 5 µm spacing to a setpoint of 10 mN was carried out by 2D indentation using the Gemini system, with 0.5 nm oscillation in z at 85 Hz and 1 nm oscillation in x at 129 Hz. These parameters were

selected as they had been found to reliably produce nucleation in mechanically exfoliated samples, with frequencies away from 100 Hz chosen to prevent crosstalk and electrical noise. Indentation normal strain rate was selected as 0.02, with a data acquisition rate of 500 Hz. Hard tapping was also applied to indents produced by AFM indentation in 0.5 µN steps until nucleation is observed (up to a maximum of 4 µN) with four scans at each hard tapping setpoint. These two methods (Gemini-based SASIN and AFM indentation with later hard tapping) were selected as they represent similar total lengths of time per array of indents as defined above, to allow ready comparison of time

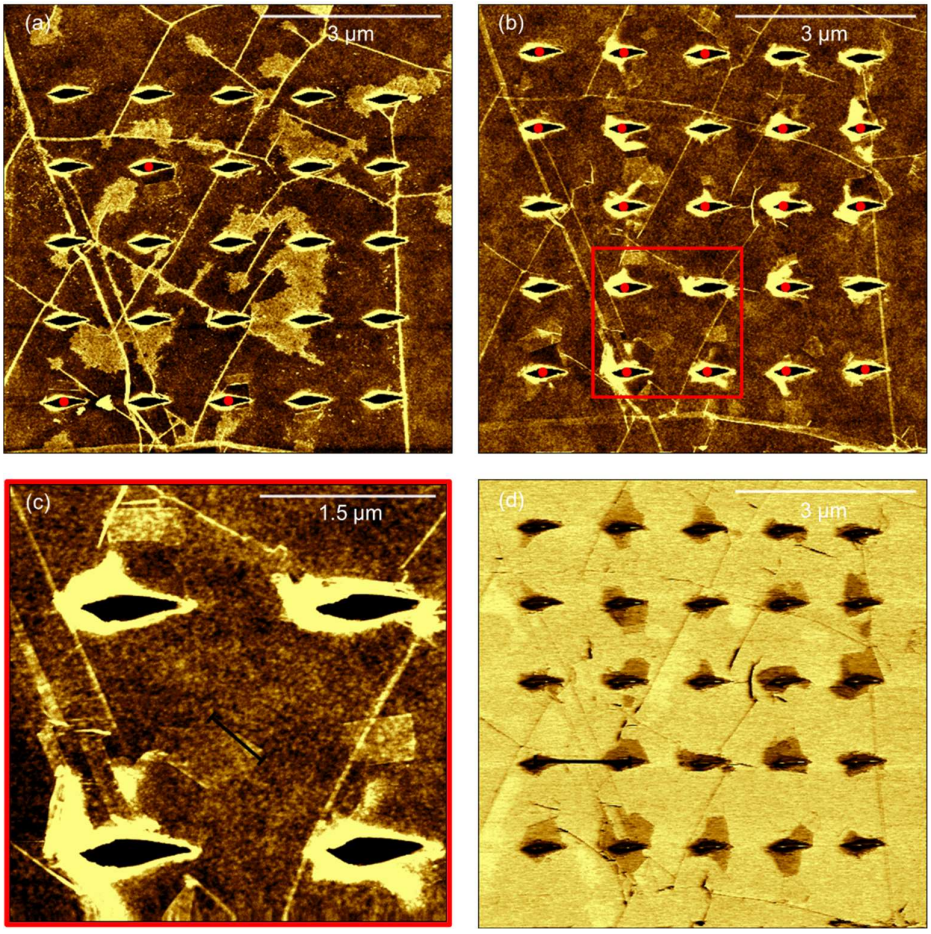

Fig. 4.1: Sample survey of AFM-based indentation by PFQNM. 3 ribbons are observed after only AFM indentation (a) and 18 after applying "hard tapping" in the same location (b). Successful indents are denoted by a red dot as a guide to the eye, with (c) zoom-in to representative ribbons in area highlighted by red in (b) showing 3 nucleated ribbons. Height differences of ≈0.3 nm are observed between CVD film and peeled area, as well as between CVD film and ribbon as expected for 1-layer graphene. Peeled areas, and associated ribbons are readily identified in dissipation and (d) adhesion channels of same area as (b). Total linear z-scale for (a) and (b): 2.5 nm, (c) 5 nN, (d) 2 nm.

required with any rates of success. These samples were then surveyed by AFM using PFQNM mode, as in Fig. 4.1 (a) and (b) before and after "hard tapping" on sample indented by AFM respectively. Ribbon growth was identified from 7.5 µm scans for the more tightly spaced ribbons produced by AFM indentation, both by examination of topography images as well as by identifying the clear contrast in adhesion and dissipation channels where graphene has peeled from the substrate during ribbon self-assembly (Fig. 4.1 (d)).

From this series of Gemini SASIN experiments on 12 samples described above, successful nucleation was observed only in one case: A single layer CVD graphene sample sourced from Graphene Supermarket. Even in this instance, rather than ribbons typically on micron length scales and with yields of ≈70% as observed in mechanically exfoliated samples, only two ribbons (from 10 indents) with lengths of 0.1 and 0.3 µm were observed.

Similarly for AFM indentation alone, ribbon nucleation was observed for only 3 of 25

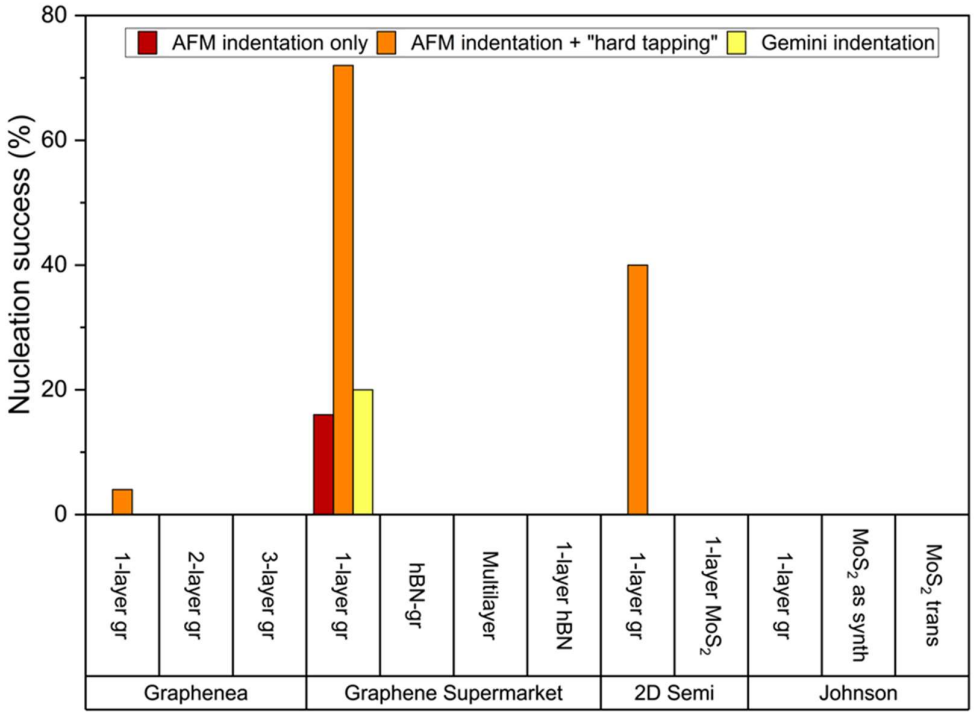

Fig. 4.2: Nucleation success rates in different CVD materials and with different nucleation methods. Graphene Supermarket's single layer CVD graphene proves to be significantly more successful in facilitating ribbon self-assembly than all other CVD samples tested.

indents, with lengths of the resulting ribbons of 0.15 – 0.25 μm. Hard tapping was however successful in inducing limited ribbon nucleation on all commercial 1-layer CVD graphene samples, with 1 ribbon for Graphenea, 18 for Graphene Supermarket and 11 2D semiconductors. Success rates for nucleation across all samples with the methods described above are summarised in Fig. 4.2. We emphasise here that for CVD materials we are focusing currently on a proof-of-concept study, such that here evidence of a peeled area of at least 0.1 μm length and folded ribbon is considered a success, although exceedingly few of these, as seen in Fig. 4.1 (c) can compare to the dimensions and relative uniformity of ribbons nucleated in mechanically exfoliated samples.

Close examination of the CVD materials themselves can also prove instructive. CVD graphene samples can appear quite uniform and clean over larger scan sizes such as Fig. 4.3 (a), with low aspect ratio wrinkles extending over widths of 0.5 – 0.6 μm and heights of only 0.5 – 1 nm. However, in smaller scan sizes at the same nominal resolution (512 samples per line and lines per sample in all of Fig. 4.3 (a)-(d)) but at higher absolute resolution with scan areas 13 and 40 times smaller respectively compared to (a), rounded "blob"-like contaminant features appear ubiquitously over the sample. As these samples were imaged shortly after delivery, such contaminants observed are expected to result from sample preparation and processing and not from environmental sources in our own laboratory.

While dimensions of the contamination vary as in Fig. 4.3 (d), they typically range from 1.7 – 5.3 nm in height and 10 – 90 nm in width. These are attributed to residual PMMA from the CVD transfer process from copper foil to silicon substrate. All CVD graphene samples studied were prepared using such a PMMA-assisted transfer from copper foils, though further details such as PMMA layer thickness, cleaning methods used on substrates and specifications of solvent washes to remove PMMA are not provided by commercial suppliers.

In smaller scan sizes, wrinkles of much higher aspect ratios with heights of 4-5 nm extending over only 35-40 nm widths are also observed in Fig. 4.3 (c). However, these heights appear to include PMMA coating the wrinkles as well as their own intrinsic heights, with heights of only 1 nm over similar widths also observed. Buildup of PMMA at wrinkles and tears has also been observed elsewhere[205].

We use the terminology introduced by Lin et al. to describe the different forms that PMMA resides can take on graphene[206]: PMMA-A for round, thick (few nanometre) residue facing the air and PMMA-G for a 2D-like monolayer residue in direct contact with graphene. PMMA-A is located on top of PMMA-G[48], though the two have the same composition with PMMA-A being higher density regions.

We note that observation of PMMA residue by AFM is often performed over larger scan sizes (at least 10 µm), and for significantly larger regions of residual PMMA as we also sometimes observe[207–210], but that analysis of the structure of PMMA as in Fig. 4.3 (c) and (d) is relatively rare in published works[211]. Critically, we also note here that the stripe formations of the previous chapter or their characteristic friction domains were not observed on any CVD samples, and to our knowledge have also not been reported on CVD samples elsewhere. We attribute this to the presence of PMMA-G on the surface preventing adsorption of stripe hydrocarbons. This PMMA contamination represents another third body present on graphene expected to influence self-assembly

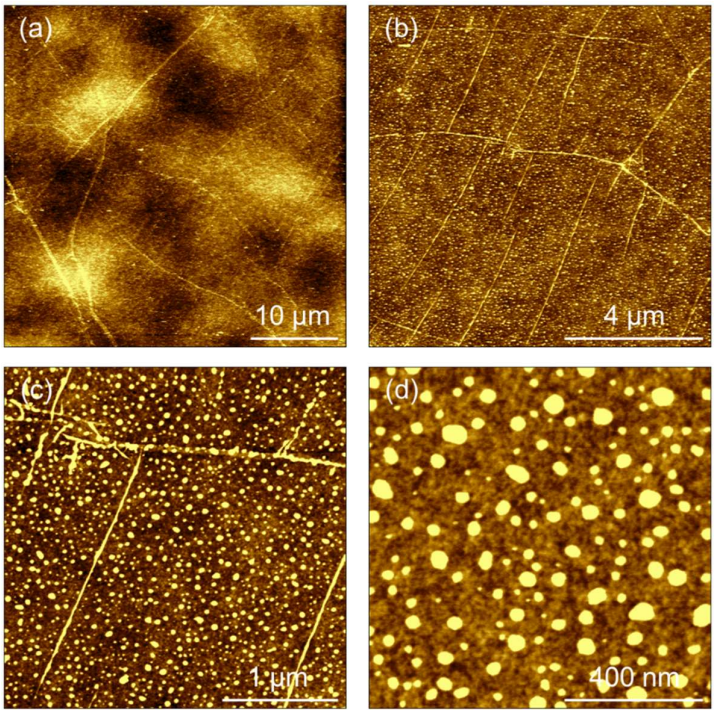

Fig. 4.3: PMMA contamination on CVD graphene samples. (a) –(d): PFQNM images of decreasing scan size (40 µm, 10 µm, 3 µm and 1 µm respectively) centred on the same point showing size scale of wrinkles, defects and PMMA "blobs". Surfaces which appear to be free of PMMA on larger size scan sizes and widely spaced wrinkles feature extensive PMMA residue and lower height wrinkles upon decreasing scan size. Total linear z scale: 3 nm for all.

by mediating graphene-graphene adhesion, while crystallinity of CVD films can influence the anisotropic graphene rupture energy critical to tearing. The presence of these contaminants may also increase the sliding friction between the host graphene sheet and growing ribbon and modify the bending energy of the fold. Adhesion energies, fracture strength, friction and fold bending energy, all of which are critical parameters in auto-kirigami nucleation, may be influenced both directly and indirectly by any third bodies present. This may be reflected in the absence of nucleation seen on the majority of CVD materials tested and relatively low yields even in the successful cases.

In many of these CVD materials where nucleation is unsuccessful, a very small initial folded tab appears to be present at the indent crater edge. This tab has however failed to propagate forward into a full AK ribbon, apparently due to the presence of contaminants or wrinkles/other surface defects as in Fig. 4.4 (a). Ribbons which grow to

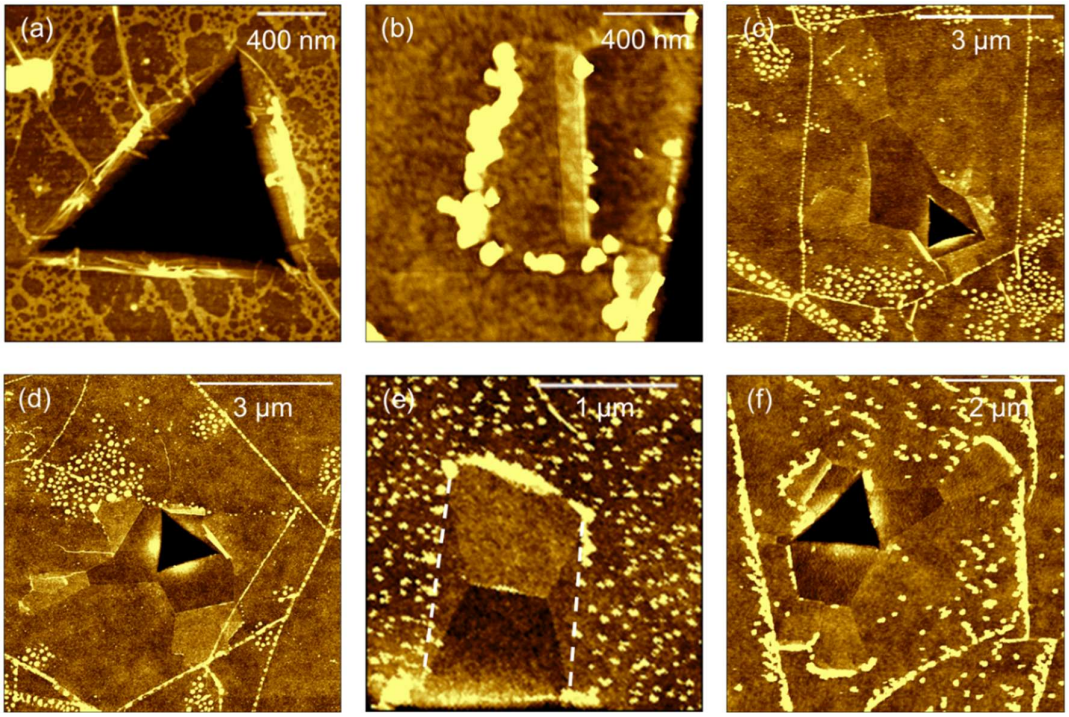

Fig. 4.4: Effect of wrinkles and surface contamination on ribbon growth in CVD materials. Wrinkles and contamination are associated with different outcomes of ribbon nucleation from SASIN alone, from none with only tightly folded tabs at the crater edge (a), very short ribbons with growth impeded by PMMA buildup at the ribbon head (b) and in rare instances, ribbons with lengths and shape comparable to those in mechanically exfoliated samples (c) – (f). Johnson CVD 1-layer graphene for (a), Graphene Supermarket for (b)-(f). Linear z scale of 10 nm for (a), 3 nm for (b)-(f).

only short lengths such as Fig. 4.4 (b) often show high densities of PMMA at the ribbon head which appear to have impeded growth. Here, although the heights of nearby "blobs" vary from 2.1 – 5.5 nm, this increases to as much as 21.0 nm and 13.4 nm for the PMMA residue at the heads of ribbons in Fig. 4.4 (b) and (e) respectively. In some instances, ribbon growth can also occur robustly even in the presence of extensive PMMA contamination as seen in Fig. 4.4 (c) – (f). Annett et al. also reported that ribbon growth can become pinned by and subsequently continue growing after displacing contaminant defects in mechanically exfoliated graphene, although this was demonstrated for single, discrete contaminant bodies with lateral dimensions of only 50-100 nm[89].

Fig. 4.4 (e) also displays another noteworthy phenomenon: mechanical self-cleaning of the PMMA by the ribbon motion. As the typical AK ribbon head starts at a maximum width and tapers, this entire width travels the length of self-assembly, sweeping PMMA residue in front of itself as indicated by the perfectly clean graphene areas within the white dashed lines indicated in Fig. 4.4 (e). Assuming a uniform distribution of PMMA across the sample, we can estimate the volume of PMMA that was on the peeled and ribbon area from a measurement of the volume of a nearby area of the same dimensions. This value (6.41×10^{-22} m^3) agrees well with the volume measured at the ribbon head of 6.11×10^{-22} m^3, and if also counting the volume either on or trapped within the center of the ribbon fold matches near perfectly at 6.40×10^{-22} m^3. This suggests that, while we do not directly observe the presence or lack thereof of PMMA residue at the interface, this self-cleaning mechanism is very thorough. The higher-than-expected ribbon height of 0.44 nm may indicate the presence of some residue at the interface however. This further suggests that accumulation of PMMA residue at the ribbon's head is the main factor limiting growth here, as the final fold width of 0.6 µm is much greater than values of 0.2 µm which are observed in Fig. 4.4 (f) for example, which is similar to the expected final ribbon widths from single layer mechanically exfoliated flakes. A bulge in the fold of Fig. 4.4 (e) may indicate that some PMMA has become trapped inside the fold itself, or that PMMA contamination at the ribbon head has resulted in non-uniform mechanical stress at the fold.

However, a different behaviour is observed between the self-cleaning ribbon in Fig. 4.4 (e) and both bottom and top left ribbons in Fig. 4.4 (f): in the latter cases, although large amounts of residue are also observed at the ribbon head, residue remains along a torn edge or a ribbon edge which should have been swept to the front if the previous interpretation holds. Previously, we have observed that uncategorised atmospheric contaminants will also accumulate on mechanically exfoliated samples which are exposed to ambient laboratory conditions over sufficiently long timescales (typically of 1+ years) as in Fig. 4.5. Such contaminants, which also appear as small "blobs" often appear to preferentially be present around ribbon edges or torn edges. We have generally attributed this build-up to potentially surface mobile contaminants migrating and becoming caught at an edge, or attraction to non-passivated bonds at these edges. However, this is not thought to be the case in Fig. 4.4 (f) for example as this imaging was performed the following day after indentation and ribbon growth, in which time any surface migration or environmental contaminants are not thought to have such an effect and the PMMA remains only at selected edges rather than all edges.

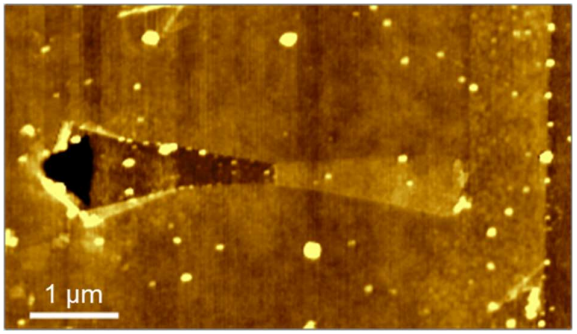

Fig. 4.5: Contaminants on samples exposed to ambient lab conditions for 1+ years. Though widely present across sufficiently old samples, such uncategorised contaminants of atmospheric origin often appear with greater density on flake and ribbon edges. Total linear z-scale: 3 nm.

However, thus far we have generally assumed that ribbon growth occurs symmetrically, in that tearing along both torn edges starts at the same time and occurs at the same rate. However, asymmetry in tearing rates of both edges, with one leading edge would result in a small angle misorientation of the growth direction from the perpendicular to the fold.

This could occur where one growing ribbon edge is actually parallel with its torn edge rather than mirrored around the fold, with the final broadly symmetric shape of the ribbon recovered where tearing at the "faster" edge crack tip has become pinned by contaminants while it continues along the "slower" tearing edge, with some rotation of

the ribbon. This could then explain how one edge becomes cleaned and the other does not. However, while we can extrapolate only a limited amount from this sample size, this may provide further insight into ribbon growth dynamics which are too rapid to be observed directly in experiment and too large to simulate in its entirety.

Graphene Supermarket's samples contain the largest areas free of wrinkles of up to ≈25 μm^2), with edges of these areas defined by wrinkles. Instances of the most successful ribbon growth as in Fig. 4.4 (c), (d) and (f) often occur where an indent by chance lands approximately central in these areas, such that any resulting ribbon growth is minimally impaired by the presence of wrinkles. Indeed, ribbon growth appears to terminate at such a wrinkle for at least one ribbon in each of these three instances.

The large variation in nucleation outcomes across CVD samples studied may also be influenced by the quality of the CVD material itself. Using conductive AFM, SEM, and cross-sectional TEM, Lanza[212] and Yuan et al.[213] studied the quality of CVD hBN samples from nine commercial suppliers. They noted significant sample-to-sample variability greater than that claimed by many commercial suppliers, ≈20 % amorphous rather than layered material by volume from the most widely cited supplier (associated with two order of magnitude more citations than the next most cited) and even samples found by TEM to be much thicker (up to ≈2 nm) than the advertised monolayer. They concluded that despite development and refinement of growth, processing and transfer processes in recent years, CVD grown 2D materials still contain many defects which hinder device performances, and that quality remains much lower than that of mechanically exfoliated samples. Although no such comparable study currently exists for CVD graphene to our knowledge (though does for liquid phase exfoliated (LPE) graphene[214], which also found massive variation in quality and classification of LPE graphene from 60 commercial suppliers), we can suspect that similar problems may plague this material too. In this work, we did not perform this verification of CVD layer thicknesses and instead we assess quality primarily by our high-resolution AFM imaging. We therefore cannot entirely correlate relative success or failure of samples to nucleate ribbons, which we here associate with greater mechanical quality and less surface contamination, with actual layer number or defect density for example. Nonetheless, that we can produce ribbons in any CVD graphene samples provides some support to

the prospect of large-scale ribbon production and that ribbon self-assembly is a sufficiently robust process.

Following our initial exploratory survey of nucleation success rates on CVD materials, only Graphene Supermarket's 1-layer CVD graphene showed successful nucleation in all methods, and with the highest rates. While Graphenea's and 2D Semiconductor's 1-layer CVD graphene film also showed some self-assembly, these were at lower rates and only following hard tapping. Despite the effectiveness of this technique, it can easily result in significant tearing to the film and any new ribbons. As we also sought to correlate statistics of end-results (i.e. ribbon shapes, sizes, yields etc) with quantitative indentation data and chosen indentation parameters, further testing with CVD materials was performed solely by Gemini 2D indentation.

A further, more comprehensive survey of nucleation success by 2D indentation compared to that shown in Fig. 4.2 was then conducted using the Gemini system, with some modified parameters (strain rate increased from 0.02 to 0.05 and x oscillation

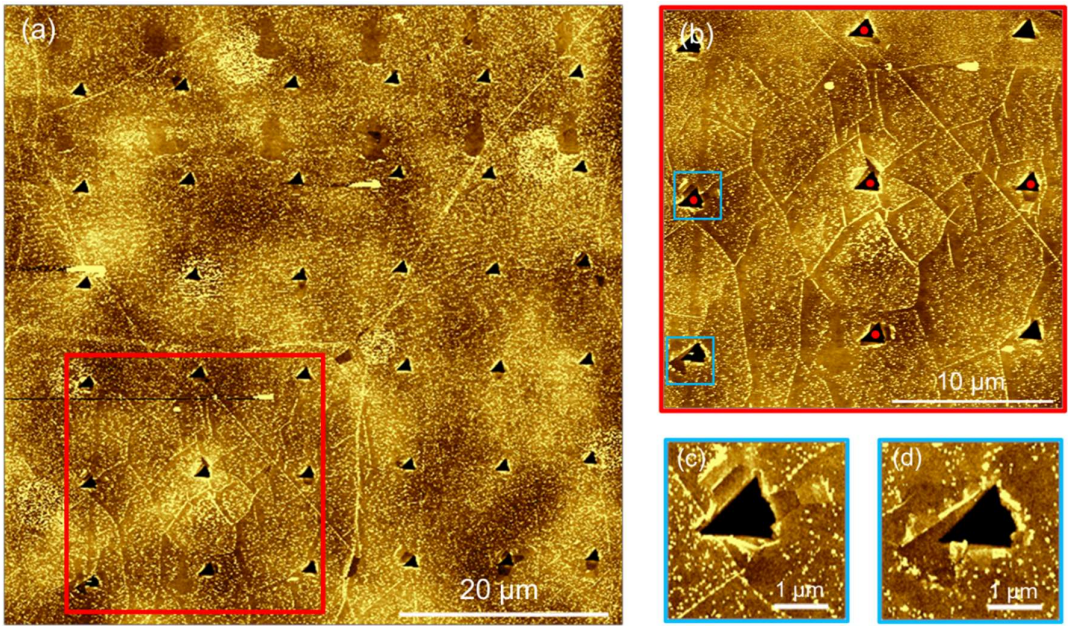

Fig. 4.6: AFM survey of many indents to assess nucleation success rates. (a) 36 of total 108 indents in this survey on Graphene Supermarket single layer CVD graphene. Arrays of 36 indents were divided into smaller batches of 9 indents as indicated in red highlighted square in (a), with zoom-in to this area shown in (b). Ribbon nucleation was primarily assessed in 25 µm scan sizes as in (b). Further imaging over smaller scan sizes of 3.5 µm was performed where nucleation was unclear, with success observed in (c) and failure in (d), where (c) and (d) are zoom-ins to middle left and bottom left blue highlights in (b). Total linear z-scale: 4 nm in each.

amplitude from 1 nm to 3 nm). This survey was conducted only on the Graphene Supermarket single-layer CVD samples. 108 indents were examined in total, applied in 3 arrays of 6 × 6 indents with 10 µm spacing between indents in x and y. Ribbon nucleation and growth was assessed by AFM per Fig. 4.6. Arrays were initially located within 60 µm scans (Fig. 4.6 (a)), which were then subdivided into 3 × 3 batches (e.g. red highlighted area in (a)) from which ribbons were primarily observed in the topography channel as indicated in Fig. 4.6 (b), as well as adhesion, dissipation and deformation channels where relevant as indicated in Fig. 4.1. Sample successful nucleation from indents is indicated in (b) by red dots within the indent crater. Further imaging was performed with higher absolute resolution in smaller scan sizes where ribbon growth could not be conclusively determined in previous steps, as indicated with blue highlighted areas in Fig. 4.6 (c) and (d) (middle left and bottom left of (c) respectively).

This survey of 108 indents yielded a 36% ribbon nucleation yield (compared to 20% from 10 indents as shown in Fig. 4.2). This remains much lower than that of mechanically exfoliated graphene, though suggests that the possibility of increased yield may lie in further optimisation of indentation parameters. However, this survey further reinforced our conclusion that the presence of PMMA hinders nucleation and ribbon growth as described above, therefore motivating study into methods to clean these residues from CVD samples.

4.3 Cleaning of CVD samples

Methods to clean residual PMMA from CVD graphene films have been the subject of extensive study, due to the contaminant's effects on mechanical properties as observed here as well as on electronic properties, contributing to unintended p-doping and reduced carrier transport for example[215–217]. A wide array of methods have been proposed to remove residual PMMA, falling broadly under the categories of thermal annealing; plasma treatment; ion beam, electron beam and light irradiation; mechanical treatment; electrolytic cleaning and current-induced cleaning[49]. In the ion beam

method, specific ions generated in plasma with a well-controlled energy distribution and direction are bombarded onto the surface to be cleaned[218]. Electron beam irradiation causes fracture of long polymer chains in PMMA, facilitating its dissolution in subsequent wet chemical treatment[219]. Removal of PMMA by light irradiation can be performed similarly to laser ablation by heating the sample locally using a visible laser, resulting in decomposition and expulsion[211], or degradation of PMMA by UV irradiation[220]. In electrolytic cleaning, graphene is used as a working electrode of an electrochemical cell, with evolved hydrogen removing PMMA residue[221]. Current-induced cleaning relies on Joule heating of graphene to high temperatures, with a similar mechanism of PMMA removal to thermal treatment[222].

However, a common trend arises that the methods which most aggressively and effectively remove PMMA also increase the number of defects in the graphene film, resulting in an expected trade-off of improved self-assembly as a result of cleaner surfaces impaired by damaged films. Considering this trade-off, how readily these methods could be applied to our samples and which methods were judged least likely to cause damage to the CVD graphene, we therefore selected of the above plasma, thermal, and mechanical cleaning.

Plasma cleaning has been reported to have a higher cleaning efficiency than thermal cleaning despite lower temperatures, with the plasma interacting with the surface in the presence of oxidising, reducing or inert gases resulting in grafting, oxidation and reduction of the surface species[49]. The mechanism for removal of PMMA by plasmas are currently unclear however (except H_2 plasmas with dissociation of -OH and H_2O and further reaction of exposed carbon atoms in PMMA to form methane). Great care must of course be taken to avoid damage to the graphene by high-energy plasma; Peltekis et al. placed samples to be cleaned 50 cm away from their plasma source to this end for example[223]. We explored variation of power and plasma exposure time using a Diener PICO Barrel Asher with 40 kHz 200 W power supply. However, using this oxygen plasma system in consultation with technical staff, we were unable to develop a method that could reliably remove PMMA residue without also removing all graphene, such that this method could not be further explored.

Thermal treatment is an attractive option for removal of PMMA residue due to its relative simplicity and ubiquity in laboratory settings. However, this method alone appears incapable of wholly removing such residue from the surface, even with a number of studies designed to optimise temperature, time and gas environment. Annealing in air environments proves most effective as this promotes oxidization and breaking of the PMMA carbon bonds[221,224], though this similarly can damage graphene carbon-carbon bonds. Reports have variously claimed that annealing at even 250 °C for 30 minutes can damage graphene[48], while increasing the temperature to 500 °C may not even wholly remove PMMA residue and can result in cracking[225]. We tested temperatures of 160 °C to 260 °C for 2 hours at few mbar pressures. Reduction in volume of PMMA-A "blobs" as measured by PFQNM of ≈20 % were observed for 160 °C (Fig. 4.7 (a)), and 40-60% for 260 °C (Fig. 4.7 (b)), comparing identical areas before and after. Applying temperatures of 260 °C caused widescale damage to the graphene film, especially around wrinkles as seen before and after in identical areas in Fig. 4.7 (d) and Fig. 4.7 (e) respectively. This is seen in the formation of two new wrinkles around which

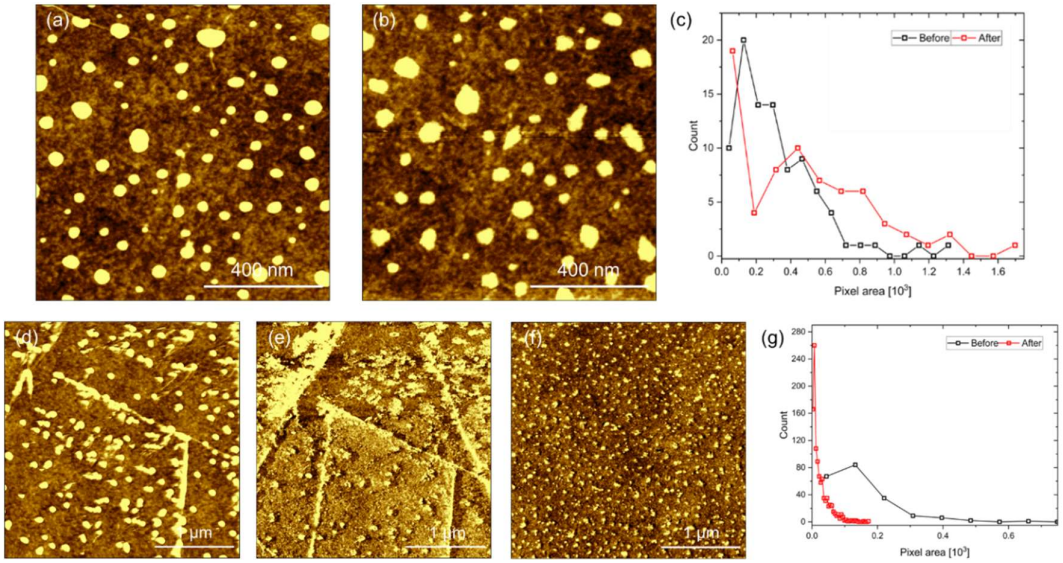

Fig. 4.7: Effect of thermal anneals on PMMA residue. Same location before (a) and after (b) thermal anneal of 160 °C for 2 hours. Measured PMMA volume reduced with "blobs" after typically being larger in area as per distribution of pixel area of each blob before and after (c) and of lower height. Similarly, same location before (d) and after (e) thermal anneal of 260 °C for 2 hours. While measured PMMA volume also reduced, the graphene was significantly damaged, especially around wrinkles. Comparison of blob pixel area before and after (g) (compared to a representative nearby location (f) rather than the damaged area shown in (e)) indicates a large change in blob size. Linear z scale of 3 nm in all.

large amounts of PMMA accumulate, lying mostly vertical in the bottom left and slanted in top right of (f), as well as in the apparent tearing and removal of graphene around wrinkles. However, we note that rather than necessarily decomposing and being removed in air as gaseous species, the PMMA-A blobs overall flattened, reducing in height but increasing in width, with smaller blobs no longer being observed. This is reflected by the distribution of pixel size of PMMA blobs shifting to the right in Fig. 4.7 (c). After annealing at 260 °C for 2 hours, PMMA is now observed as many, very small fragments (Fig. 4.7 (f)), as evident from the leftward skew of pixel dimension in Fig. 4.7 (g) whereas previously "blobs" became larger in area with annealing. We attribute this to further dispersal of the larger PMMA blobs with increased heating.

Longchamp et al. reported that the catalytic activity of platinum and palladium can complement thermal annealing to produce ultra-clean graphene[226]. After etching of the copper foil, the graphene-PMMA composite was placed on a perforated platinum coated (50 nm thickness) silicon nitride membrane, dried and annealed in air to temperatures in the range of 175 – 350 °C (Fig. 4.8 (a)). They observed complete degradation of PMMA on the platinum surface, but not on the SiO_2 surface, indicating a catalytic effect of the metal which also extended for tens of microns from the platinum edge within as little as 3 minutes for the highest temperatures in their range and 6 hours for the lowest. They propose that this occurs due to dissociation of adsorbed molecular hydrogen by the platinum, resulting in hydrogenation of the PMMA leading to cracking at these relatively low temperatures, degradation to monomers and subsequent escape into the air. As our commercially supplied CVD graphene samples are all on SiO_2 substrates for optical visibility, this exact method could not be applied. As Longchamp et al. emphasise that even proximity within tens of microns is sufficient to achieve this catalytic cleaning, we instead brought the CVD graphene directly into contact with a silicon wafer coated with a thin layer of platinum (100 nm thickness) by electron-beam evaporation, as demonstrated in Fig. 4.8 (b). However, this method proved ineffective at removing PMMA residue as demonstrated before (Fig. 4.8 (c)) and after (Fig. 4.8 (d)) annealing for 2 hours at 200 °C. Volume measurements by AFM of PMMA before and after vary by less than 1% despite the large difference in structure of the PMMA residue observed in the same location.

However, increasing the anneal time at 200 °C from 2 to 6 hours yielded apparently improved results, as seen before (Fig. 4.8 (e)) and after (Fig. 4.8 (f)) in the same area, with no PMMA directly visible after applying this cleaning.

However, despite the reduction in volume of the blobs (as also observed in Fig. 4.7), we suggest that this may in fact not indicate that the overall amount of PMMA on the surface has reduced but that it has converted from PMMA-A to PMMA-G. The former is readily identifiable by AFM but the latter appears as a smooth background, contributing to these apparent volume reductions. We can test this by applying our third cleaning method, mechanical treatment.

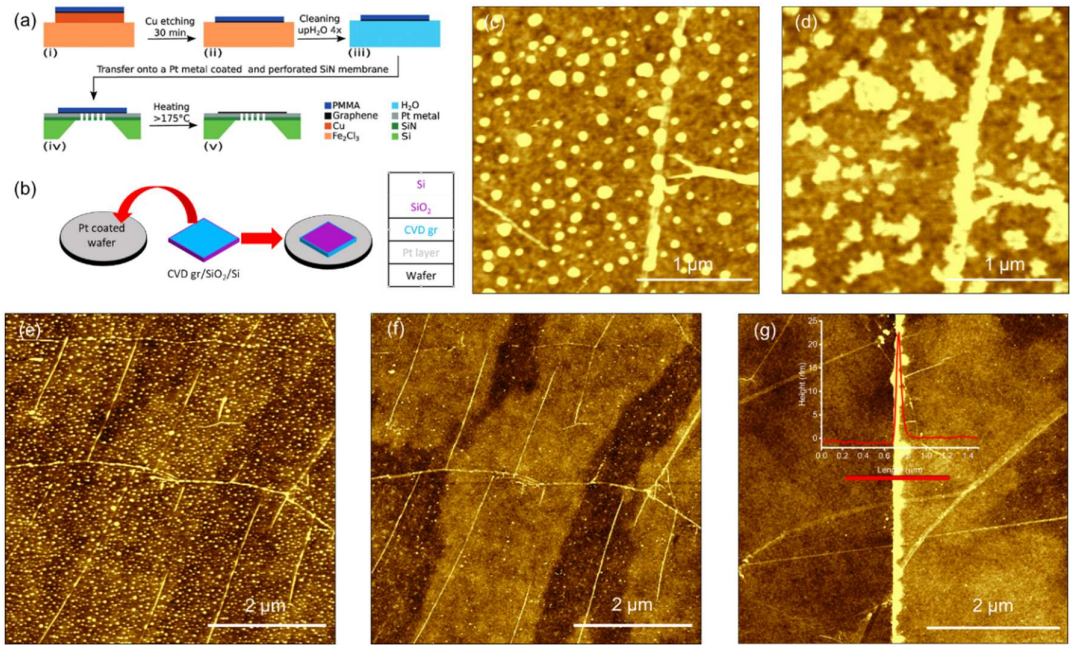

Fig. 4.8: Platinum-metal catalysed cleaning of PMMA residues. (a) Flow chart of method proposed by Longchamp et al. claimed to completely remove polymer residues, adapted from 226. (b) Sketch of our adapted method, with graphene surface with PMMA residue sandwiched between platinum layer and silicon substrate. PMMA residue on CVD graphene surface before (c) and after (d) 2 hour 200 °C thermal anneal with platinum, with significant spreading out of PMMA blobs. When the thermal anneal with platinum is applied at 200 °C for 6 hours, PMMA appears to be removed (before (e) and after (f)). However, mechanical cleaning by AFM on the now apparently cleaned CVD graphene indicates that PMMA is still present, as indicated by the 1 nm height difference between cleaned and surrounding area (left and right of (g) respectively) and large buildup at boundary of cleaning region. Inset is height profile of red line in (g). Total linear z scale: 3 nm in (c)-(g).

Unlike the other methods of CVD cleaning which rely on chemical reactions to remove PMMA residue, mechanical cleaning depends entirely on the interaction force between the residue and cleaning material. This therefore does not affect chemical integrity of the graphene, but may still result in physical damage to the film. While macro-cleaning methods are available through mechanical cleaning covering entire wafers, such as force -engineered active carbon coated lint rollers[227] and electrostatically charged fibres of a rubbing cloth[228], we focus on micro-cleaning methods here. Micro-cleaning is typically applied by AFM, where the interaction force of the tip and contaminants is greater than that between surface and contaminants, with the tip acting as a broom sweeping contaminants aside. This results in build-up of contaminants around the edge of the scanned area, such that the cleaned and surrounding areas can readily be compared. This approach was also applied by Rosenberger et al., dubbed a nano-"squeegee", capable not only of cleaning the surface but even of squeezing contaminants out from 2D material interfaces. While this micro-cleaning method has been widely used[229–231], it is severely limited by the scan range of the AFM, typically only on scales of tens of microns and requiring multiple scans for complete cleaning, decreasing throughput.

To test the effectiveness of the catalytic cleaning at chemically degrading PMMA, a 10 µm × 10 µm area was scanned in contact mode for 30 minutes at 20 nN setpoint, then surveyed in PFQNM (Fig. 4.8 (g)). PMMA residue appeared to be completely removed from the scanned areas (left hand side of Fig. 4.8 (g)), with an average height difference of 0.8 nm between cleaned and surrounding graphene areas as seen in inset height profile. An average volume of PMMA residue of 4.74×10^{-22} m^3 per 1 μm^2 area was measured pre-cleaning, with an average volume of swept PMMA per 1 µm length of the boundary of 2.51×10^{-21} m^3. Accounting for the 5 µm length from which PMMA is swept to each side, a volume per 1 µm length of the boundary is estimated at 2.37×10^{-21} m^3, in close agreement with the measured volume of 2.51×10^{-21} m^3. This suggests that as much as 95% of the PMMA residue can be removed within these 8 scans with no damage to the graphene film observed. More simply, by taking only the average height difference between cleaned and surrounding, a volume of 4.0×10^{-21} m^3 should be displaced by the scanning into the boundary. We expect that this greater discrepancy

may arise from flattening of the cleaned area, which results in overestimation of the height difference from which the 4.0×10^{-21} m^3 estimate is derived.

This application of mechanical treatment following thermal catalytic treatment indicates that while thermal methods within the ranges studied may result in apparently cleaner surfaces, they fail to truly remove PMMA from the surface and instead only appear to change its composition. This requires us to reconsider our earlier claims of reductions of PMMA volumes by as much as 40% with thermal treatment, with this instead likely representing a conversion of PMMA-A to PMMA-G which these AFM methods cannot readily directly detect with displacement of the PMMA-G layer.

As our modified version of Longchamp et al.'s setup involved graphene sandwiched between platinum and the graphene substrate, the ability of any chemically decomposed products to escape in air may have been hindered, which could coincide

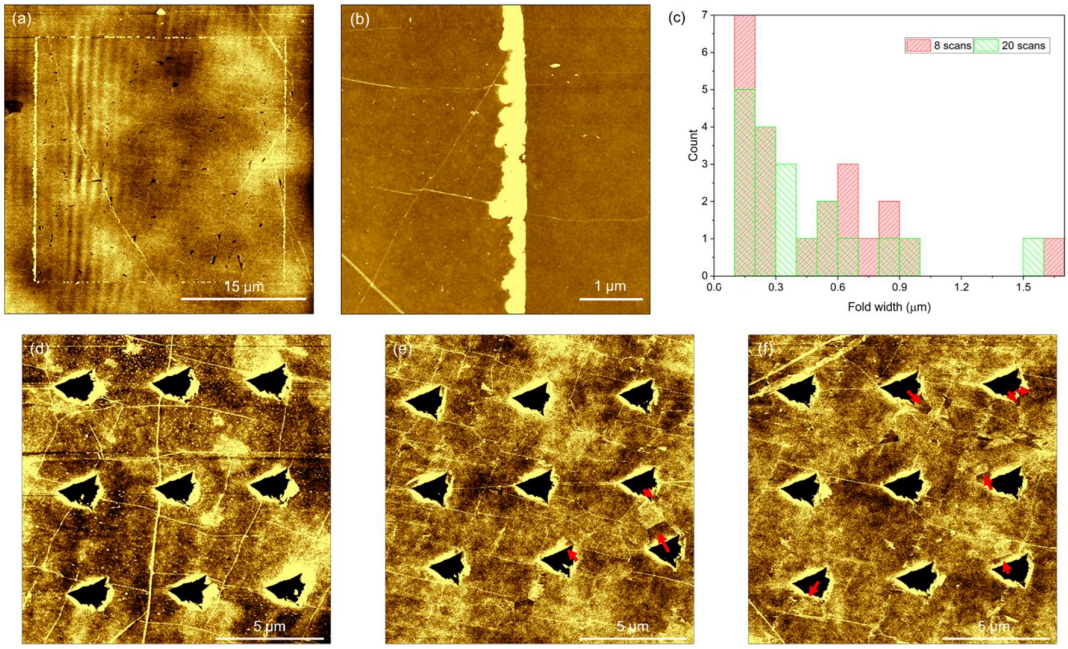

Fig. 4.9: (a) Outline of scanned area, showing PMMA swept to each side of the scan area. Total volume at left- and right-hand sides (with fast scan axis along the horizontal) is much greater than that measured along the top and bottom edges. (c) Successful nucleation is observed in both cases where AFM cleaning is applied prior, but none in this instance where AFM micro-cleaning is not observed. Representative scan areas featuring 9 of the total 25 indents in each array on CVD graphene are shown, which have undergone no AFM cleaning (d), cleaning by 8 contact mode scans (e) and cleaning by 20 contact mode scans (f). Red arrows in (e) and (f) indicate successful ribbon growth and ribbon direction. Total linear z scale: 4 nm for (a), 10 nm for (b), 1.5 nm for (d) – (f).

with another report that some surface contaminants desorbed at high temperature in vacuum annealing may reabsorb upon exposure to ambient air[40]. We do not expect that the platinum layer would have become damaged or oxidised at these temperatures, with changes in thin platinum layer morphologies elsewhere observed only at annealing to >400 °C in the presence of oxygen[232,233]. Alternatively, we note that the CVD graphene chip, as provided by the supplier, displayed large, amorphous contaminants scattered randomly over the surface. These appeared to be silicon fragments as a result of wafer dicing, with dimensions of tens of microns. Despite both host wafers being extremely flat, these asperities which could not be removed by compressed air may prevent the intimate contact between platinum and CVD graphene required.

Given the demonstrated effectiveness of mechanical cleaning, three 40 µm × 40 µm areas of a Graphene Supermarket CVD graphene sample were selected for indentation on a sample which had previously undergone thermal annealing with platinum at 200 °C for 6 hours. Of these three areas, one was cleaned by 20 scans in AFM (86 minutes of continuous scanning), one by 8 scans (30 minutes, Fig. 4.9 (a) and (b)) and one was not cleaned by AFM. In this micro-cleaning, displacement of PMMA residue is readily observed in lateral force channels during contact mode scanning as streaks oriented along the slow scan axis capture direction as residue is dragged along the sample by the tip. Change was no longer observed after 6-7 scans, with 8 scans therefore selected as one benchmark. As this may only have accounted for PMMA-A residue which is expected to be removed more readily, a further 12 scans were applied which may also remove PMMA-G from the surface.

The volume of PMMA displaced over this larger scan size (40 µm in total, or 20 µm to each side) resulted in heights of up to 131 nm of the PMMA at the left-hand side boundary (Fig. 4.9 (b)). PMMA is not distributed equally to all edges of the scan area, with nearly 85% of the total volume in the left- and right-hand side vertical edges, as expected as the fast scan axis is here along the horizontal. Deriving swept PMMA volume per square micron from the volume of PMMA at the scan boundary, a volume of 6.52×10^{-22} m^3 per 1 μm^2 is derived. This is greater than the value of 4.74×10^{-22} m^3 per 1 μm^2 derived above, but this value can be expected to account for both PMMA-A

and PMMA-G, whereas 4.74×10^{-22} m^3 per 1 μm^2 was derived considering only the volume of PMMA in "blobs" i.e. PMMA-A.

In each case, indentation was performed to 10 mN loads with a strain rate of 0.05, with 0.5 nm oscillation amplitude in z at 85 Hz frequency and 3 nm oscillation amplitude in x at 129 Hz frequency. Indentation was applied in arrays of 5 × 5 indents with 5 µm spacing in x and y for each. Resulting indents and ribbons were surveyed by PFQNM, with results summarised in Fig. 4.9 (c). No successful nucleation was observed with no cleaning, while 22 ribbons nucleated from 13 indents were observed with 8 scans and 19 ribbons nucleated from 13 indents observed with 20 scans. A similar distribution of fold widths and median fold width were observed in both latter cases (0.36 µm and 0.32 µm median fold width respectively). We can therefore conclude that even moderate application of carefully applied AFM micro-cleaning can facilitate massive increases in nucleation success rates on CVD materials.

While this micro-cleaning method has proven highly successful in this instance, it nonetheless features a number of limitations. Taking our case of 8 scans for micro-cleaning, this represents a cleaning rate of only ≈50 μm^2 per minute, which is evidently far too low to apply to wafer-scale samples. These ribbon yields remain lower than those observed in previous work (70%[89]) and in our current work on mechanically exfoliated graphene as well, suggesting a limitation introduced by film mechanical quality or adhesion of the CVD graphene to the substrate or to itself for example. This also suggest the possibility of using nucleation success as a test for graphene quality more broadly. Graphene quality in this context can encompass a number of factors, such as crystallinity, number of defects and level of contamination. Currently, these factors can be explored individually through varied techniques. Electron backscatter diffraction (EBSD) can reveal the microstructure of graphene by revealing crystal orientation, grain boundaries and hence crystallinity for example[234]. The ratio of the intensities of the D and G peaks of graphene in Raman spectroscopy is widely used to quantify defects in graphene[235]. Presence of contaminants such as PMMA or ambient hydrocarbons can be assessed by a wide range of techniques, including among others AFM[236], SEM[223], TEM[237], x-ray photoelectron spectroscopy (XPS)[238] and time-of-flight secondary ion mass spectroscopy (ToF-SIMS)[239]. Electron mobility can also be used to

probe the degree of PMMA contamination with mobilities nearly doubling with removal of PMMA residue by thermal annealing[215]. All of these factors can contribute to a more general assessment of graphene quality that any one factor cannot wholly capture. As the self-assembly process also encapsulates many properties of the graphene sheet, we suggest that nucleation success and yield can provide an overview of how many of these factors contributing to graphene quality interact.

We also highlight that the success of the micro-cleaning approach was here demonstrated only on the Graphene Supermarket 1-layer CVD graphene sample which had shown some nucleation success even without cleaning. However, we initially considered a total of 12 CVD samples as per Fig. 4.2. Of those, only 3 displayed any ribbon nucleation with the most successful chosen for further indentation studies on CVD materials, which in turn showed increased nucleation with micro-cleaning. This therefore motivates a re-examination of indentation and ribbon nucleation on the remaining 11 samples with similar application of micro-cleaning. These samples include other 2D materials of technological and mechanical interest on which nucleation has not been conclusively demonstrated before (namely MoS_2, hBN and graphene-hBN heterostructures), which could prove highly instructive. As these materials would feature varying adhesion energies and tearing resistances compared to graphene, this would allow for further testing of the existing model of thermodynamically self-driven growth, as well as potentially novel ribbon geometries and structures. Unfortunately, as this would represent at minimum several weeks of experimentation, due to time constraints this could not be performed in this work.

We can also examine the indentation data for the Graphene Supermarket 1-layer CVD graphene, especially jumps in the small amplitude lateral contact stiffness response, interpreted as the point of graphene sheet rupture as fully described in section 3.3. A sample size of 108 indents was taken on this sample with loads of 10 mN, lateral oscillation of 3 nm amplitude at 129 Hz and normal oscillation of 0.5 nm at 85 Hz. Sample lateral contact stiffness-depth curves are shown in Fig. 4.10 (a).

Variance of rupture depths in mechanically exfoliated graphene was previously noted in section 3.3, though trends of both pre-rupture and post-rupture lateral contact stiffnesses per depth were tightly grouped. Fig. 4.10 (b). This yields a mean rupture

depth of 16.6 nm with a standard deviation of 7.0 nm. In instances of rupture occurring at larger depths as indicated in Fig. 4.10 (a), pre-rupture lubrication is also inconsistent, unlike in the case of mechanically exfoliated graphene. In the red curve in (a) for example, a single, simple rupture point is not observed, though the corresponding indent crater shows a ruptured sheet as later observed by AFM. This may arise from non-uniform adhesion of the CVD graphene film to the substrate over distances of only few microns on the surface. These larger rupture depths also indicate that the CVD graphene can withstand a large degree of strain.

At a depth of 50 nm, a rupture range of 7,000 – 16,000 N/m is observed in lateral contact stiffness of separate indents on CVD materials whereas a range of 18,000 – 22,000 N/m is typically seen for mechanically exfoliated single layer graphene as in Fig. 3.11. Mechanically exfoliated and CVD transferred graphene used SiO_2/Si substrates with 290 and 285 nm oxide thicknesses respectively, a minor difference which is not expected to contribute significantly to lateral stiffness at shallow depths of indentation considered here. This discrepancy is then expected to arise from influence of CVD graphene despite the rupture depth being two orders of magnitude greater than the graphene layer thickness.

As discussed in Chapter 3 with mechanically exfoliated graphene, the shape of the

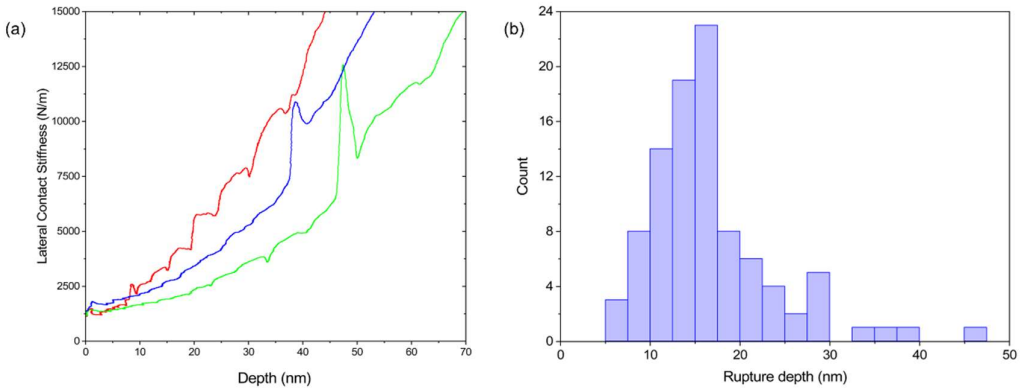

Fig. 4.10: Variance in rupture depth of CVD graphene. (a) Sample representative lateral contact stiffness vs depth curves showing very different behaviours, including early rupture (around 8 nm) with multiple later steps (red), and later ruptures (around 37 nm and 46 nm for blue and green respectively) with very different pre-rupture lubrication. (b) Histogram of rupture depths from a sample of 108 indents (13 of those not shown as rupture depth could not be conclusively determined), bin width 2.5 nm.

Berkovich tip used in nanoindentation also has a large effect on rupture depth. A series of 75 indents on Graphene Supermarket 1-layer CVD graphene was performed with another new Berkovich tip. Indentation with this sharper Berkovich tip shows rupture depths ranging from as little as 3.9 to 13.3 nm.

While rupture depth remains a useful parameter to investigate how graphene rupture occurs, a single parameter determining when rupture occurs such as mean contact pressure has not been established. Peak local contact pressure also proves difficult to extract without perfect knowledge of potential asperities on the Berkovich tip which may be central to graphene rupture at low depths. Rupture depth therefore proves difficult to directly compare across different indenter tips even with calibration of the tip area function. As the Berkovich tip inevitably suffers from some blunting during indentation with lateral oscillation due to shear forces on the tip, this may introduce variation from start to end of a particular batch as well. Determination of such a parameter remains a central goal in our understanding of graphene rupture and resulting ribbon nucleation and growth, to be informed in further indentation experiments and collaborative simulation experiments.

4.4 Conclusions

In this chapter, we crucially demonstrated the first successful nucleation of auto-kirigami ribbons on CVD graphene. A number of CVD materials procured from various suppliers were tested for their capability to undergo ribbon nucleation by AFM indentation (both with and without hard tapping) and by 2D indentation. While the highest yields were obtained with AFM indentation with hard tapping, no nucleation was observed on a majority of CVD samples, indicating a large variance in quality of available CVD materials. A major contributing factor to this variance appears to be the presence of PMMA contamination, which was extensively characterised here by AFM. While self-cleaning of this impeding PMMA contamination by growing AK ribbons was observed on occasion, it was nonetheless judged to significantly impede the auto-kirigami growth. A ribbon nucleation yield of up to 36% was observed on the most

successful CVD material, or approximately half of the yield compared to mechanically exfoliated graphene.

We therefore trialled a number of methods to clean PMMA contamination from CVD materials, including thermal annealing (both with and without a platinum catalyst), exposure to oxygen plasma, and mechanically by AFM tip. The primary effect observed of thermal annealing was in altering the distribution of PMMA on the surface rather than removal of PMMA from the surface, as also reproduced in the presence of a platinum catalyst. Mechanical micro-cleaning by an AFM tip in contact mode proved highly successful in removing PMMA contamination, but with low throughput and little ability to scale this method up. Large variance in rupture depth and rupture behaviour, derived from lateral contact stiffnesses, was observed on CVD materials, likely contributing to the high variance seen in nucleation probability and resulting ribbons.

Chapter 5: Mechanical and electrical control of gr-AK ribbons

5.1 Introduction

We have so far focused primarily on nucleation of ribbons, considering the techniques that can nucleate, parameters in these techniques, the material indented upon and contaminants on that material which are believed to strongly influence the nucleation process. While this is essential to furthering our understanding of the nucleation process and properties of the nucleated ribbons, the forward-looking application of this research is the development of ribbons as nanoelectromechanical devices, such as valves or actuators. This requires precise control of the ribbon, including reversing the spontaneous forward growth motion of the ribbon by e.g. an external stimulus. Here, we will discuss methods to manipulate existing ribbons to this end by light irradiation, mechanical manipulation by AFM tip and applied electrical signal.

5.2 Mechanical control

Thus far, growth of ribbons has fallen broadly under a few categories: growth immediately following indentation/nucleation often to micron scale lengths in extremely short timescales, further growth often on scales of tens to hundreds of nanometres over the following days, or additional growth triggered by introducing an external stimulus. The latter may either be globally by heating on a hot plate, or locally via AFM "hard tapping" or lateral force manipulation of a single ribbon, resulting in rotation or extensional growth.

We first investigated whether a means to effect the reversal of the spontaneous growth of a gr-AK could be realized – to effectively create a force opposite to the self-assembling interfacial force that "rolled-back" or unfurled the ribbon. Efforts to

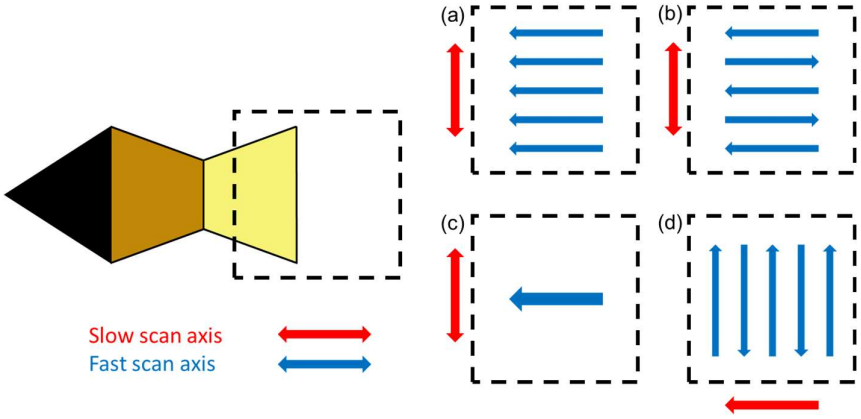

Fig. 5.1: Methods to demonstrate ribbon reversal using AFM. (a) - (d) Sketches of various scan recipes applied to attempt to induce ribbon reversal by scanning over an area around the end of a ribbon in contact-mode AFM.

demonstrate reversal by "pushing" with an AFM tip in contact mode from the end of the ribbon proved unsuccessful across a number of variations. These broadly sought to "push back the ribbon" by scanning with the fast scan axis perpendicular to the end of the fold. This included scanning in interleave, such that the tip images only along the trace direction and retracts during the retrace (or vice versa as in Fig. 5.1 (a)), as standard trace-retrace scanning over multiple scan lines covering a portion of or the entire final width of the fold (Fig. 5.1 (b)), or over only a single scan line (Fig. 5.1 (c)) or with the slow scan axis along the ribbon direction "sweeping" towards the ribbon (Fig. 5.1 (d)). Methods as depicted in Fig. 5.1 (a) – (c) broadly proved unsuccessful, with no change in ribbon position observed at low to moderate setpoints (up to ≈50 nN), while imaging at higher setpoints often caused tearing of the ribbon and underlying sheet without reversal. While methods as in Fig. 5.1 (d) could prove successful in rotating ribbons, this was not reversible with ribbons rotating into apparent commensuration.

While these contact mode AFM methods proved unsuccessful, ribbon reversal was observed successfully using the "hard tapping" method, though only on two occasions despite extensive application of "hard tapping" during this research. One of these instances is depicted in Fig. 5.2 on a 10 nm thick graphene flake, where a PF tapping setpoint of 3 µN is applied. No nucleation was observed in previous imaging at setpoints increasing from 0.5 µN in 0.5 µN steps, up to Fig. 5.2 (a). The ribbon growth in Fig. 5.2 (b) occurred on the fourth consecutive scan at this setpoint, with all images comprising

Fig. 5.2 (a) – (g) occurring sequentially with ≈4 minutes between successive images.

Ribbon growth induced by "hard tapping" at 3 µN setpoint in Fig. 5.2 (b) results in ribbon growth to 4 µm length. The ribbon, which is growing as this imaging is occurring, also rotates slightly, with a kink in the ribbon shape observed despite no such kink being present in the peeled area. With a reversal of the fast scan direction indicated by the red arrow in Fig. 5.2 (c), ribbon growth also reverses with a ribbon length of 1.6 µm now observed. With the slow scan direction again aligned from top to bottom of the image as in Fig. 5.2 (d), ribbon growth occurs again to the 4 µm length. Rotation of the ribbon near the end of growth again results in kinking, albeit at a different point. Ribbon reversal is observed in an apparently identical manner to Fig. 5.2 (c) in Fig. 5.2 (e). However, in Fig. 5.2 (f), the rotation occurs at an earlier point in the scan, resulting in the ribbon head rotating to the right such that the ribbon head is now directly opposite a neighbouring indent. In similar capture direction down scans in (b) and (d), the ribbon head must move with each scan line as dynamic rotation and motion of the ribbon is captured during both images. In (f) however, the ribbon must not have begun to grow again as the AFM scan lines came parallel to and beyond the ribbon fold as per (e), as the rotated ribbon head in (f) lies above the neighbouring indent. If the ribbon were growing from the moment of application of "hard tapping" to the fold up to the point at which rotation suddenly occurs, the ribbon head would lie further down the image in (f). In (g) and further subsequent scans not here pictured, no further reversal or growth of the ribbon is observed. Forward growth here is impaired by the barrier of the neighbouring indent, while the position of the fold at the ribbon's minimum length remains consistent across (c), (e), (f) and (g).

The direction of ribbon growth or reversal is always along the slow scan capture direction (indicated by red arrows in), indicating that this motion is primarily caused by interactions directly with the tip rather than a purely thermodynamic driving force as in ribbon nucleation by oscillatory indentation. A trace which apparently corresponds to the position of the right corner of the ribbon head during reversal (stretching in an arc approximately between the lower and middle indents imaged) is also seen in (c) and (e), suggesting tip contact inducing this motion. The position of the thinnest observed width of the healed area in (c) and (e) also corresponds exactly to the previous position of the fold before reversal in (b) and (d), confirming that this healing has occurred.

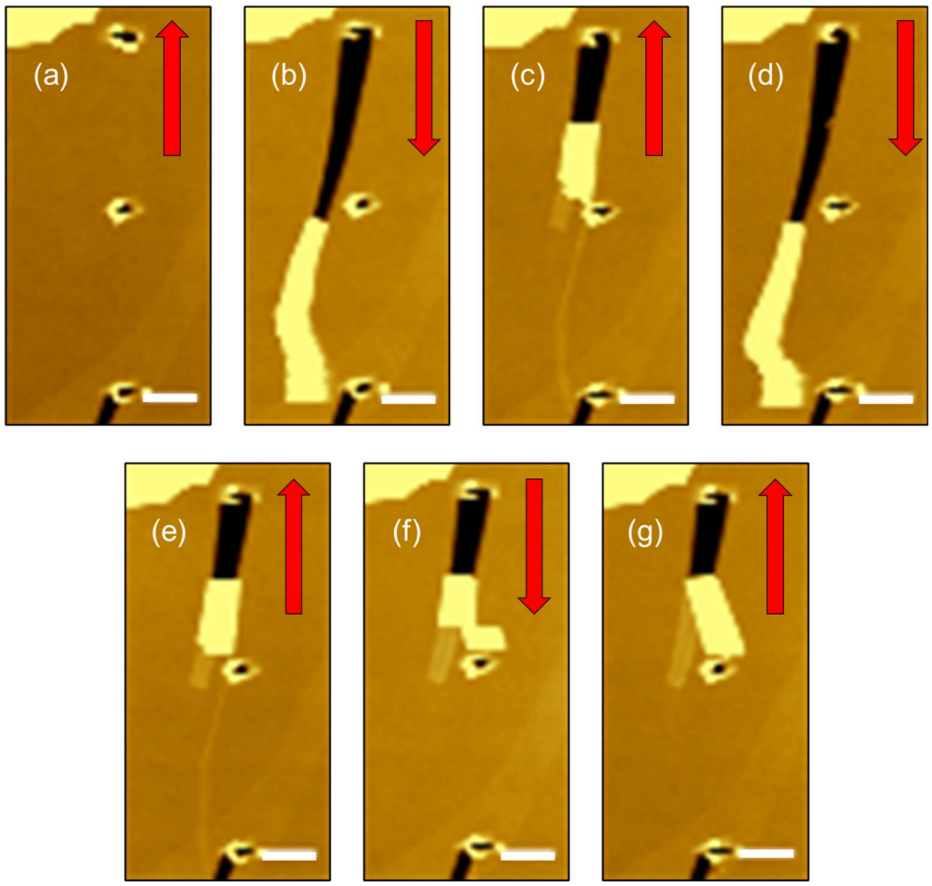

Fig. 5.2: Ribbon healing and reversal during "hard tapping" imaging. "Hard tapping" results in an indent which had not previously nucleated (a) now featuring ribbon growth (b). This ribbon reverses directly sequential reversal, growth and reversal of the ribbon in (c), (d) and (e). In (f), the ribbon rotates such that a neighbouring indent acts as a barrier to growth in subsequent scans not here shown, with final rotted ribbon position shown in (g). Red arrows indicate slow scan direction in each scan. Scale bar: 1 µm, total linear z range of 15 µm in each.

Rotation of the ribbon is also observed near the end of the ribbon in capture direction down scans as in Fig. 5.2 (b), (d) and (f), gradually over several scan lines in the former two but suddenly within a single scan line in the last. This rotation in (f) resulted in the ribbon head now being trapped by a neighbouring indent such that no further growth occurred. Although a majority of the peeled area "healed" as in (c) and (e) – (g), this healing does not seem to have occurred without scars. In a higher resolution image of this area in Fig. 5.3 (a), the healed graphene is readily distinguished from the surrounding graphene. A height profile of this ribbon in Fig. 5.3 (b) shows that this healed area is not smooth with the surrounding graphene, with a height difference of 0.8 – 7.0 nm. We note that while this cycling shown in Fig. 5.2 occurred on a relatively

thick sample, ribbon reversal and healing was also observed on a 4-layer graphene sample in another instance when applying a lower PF tapping setpoint of 1.5 µN. In that second instance depicted in Fig. 5.3 (c) and (d), a height difference of 1.1 – 2.8 nm between the host sheet and "healed" ribbon was observed, with even this lower bound comparable to the thickness of the sheet itself and the upper bound double it. However, a mismatch with the torn area, as might be indicated by the substrate being visible at either previously torn edge, is also not observed in either instance, such that the healed ribbon would be expected to lie more smoothly. In Fig. 5.3 (d), stripes can even be observed which appear to match perfectly in the host and healed areas, showing that this crumpling is not arising purely from a rotation relative to the initial position for example.

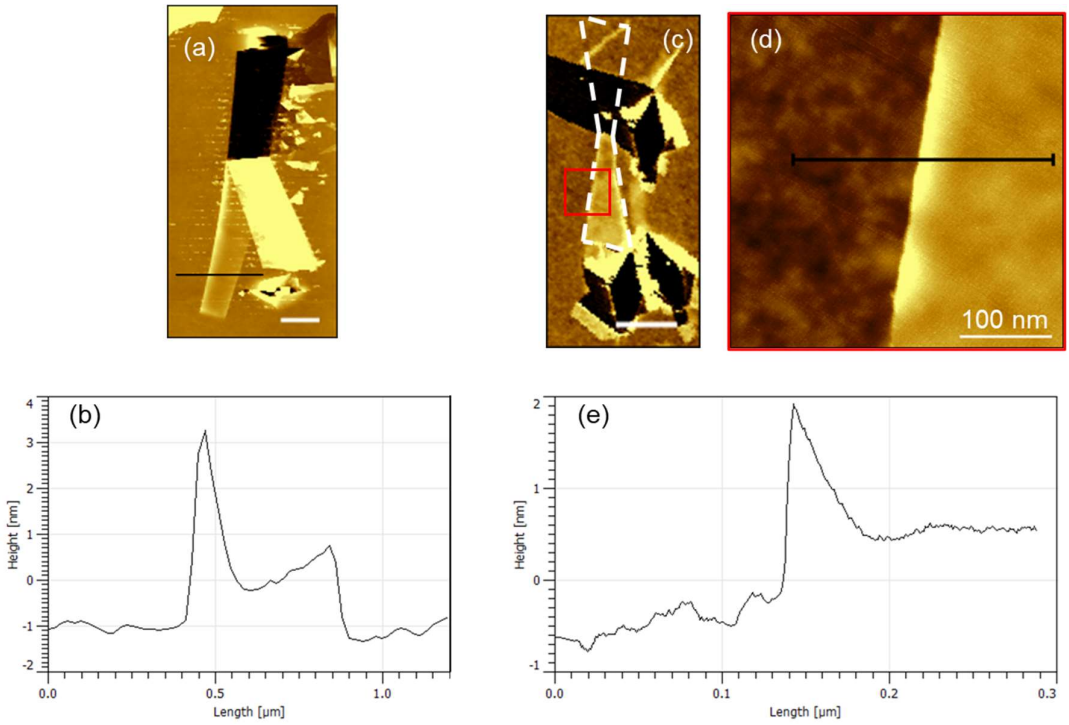

Fig. 5.3: Height discrepancies of "healed" ribbons relative to surrounding graphene sheet. (a) Higher resolution PFQNM image of healed area seen in Fig. 5.2 (b). Height profile along black line in (a), showing imperfect matching of healed and surrounding graphene. Another observed instance of ribbon healing is shown in (c) where the ribbon grew until the fold reached a peeled area of another ribbon before reversing, with previously grown and later healed areas indicated by upper and lower white dash outlines respectively. (d) PFQNM topography zoom-in with stripe resolution of area highlighted in red in (c), with height profile along the black line crossing the "healed" boundary shown in (e). Scale bar: 500 nm in (a) and (c). Total linear z scale: 15 nm in (a), 4 nm in (c), 3 nm in (d).

The setpoint necessary to induce reversal in the first instance was also sufficiently high to damage the host graphene sheet and ribbon, with debris visible in parallel horizontal lines in Fig. 5.3 (a). As the "hard tapping" was performed on a scan size of 25 μm with 256 lines per scan, this spacing of debris along lines spaced 10 nm apart exactly reproduces the spacing of the scan lines of the earlier "hard tapping". This also provides an insight into how this ribbon reversal may have occurred: rather than a continuous contact as in C-AFM, the tip interacts with the growing or reversing ribbon in a quasi-continuous manner in 10 nm steps along the slow scan direction.

While these two instances demonstrate that ribbon reversal is feasible, challenges also arise. From Annett et al.'s model described in the Introductory Chapter, this process of exchanging graphene-graphene contact with graphene-substrate contact will be thermodynamically unfavourable, which is supported by the rarity with which ribbon reversal is observed (even over many tests with mechanical manipulation). The large height difference of the healed areas indicates significant non-conformity of the ribbon with the sheet from which it tore only minutes ago in both cases shown here. Passivation of the newly torn edges may contribute to this. Nonetheless, two cycles were observed, providing a first proof-of-concept of ribbons as switchable NEMS devices.

Two methods to facilitate globally switchable control of ribbons were considered: functionalising graphene with optically sensitive spiropyran molecules to affect the adhesion balance and thus the interfacial force and direct electrical voltage control to generate a new force opposing the interfacial force through considerations of capacitance. Firstly, spiropyrans are organic compounds with photochromic properties[240]. These include switchable adhesion properties with the irradiation by UV light, whereby nonpolar spiropyrans photoisomerise to a polar merocyanine, while with visible light merocyanine reversibly switches back, which facilitates switchable adhesive strengths[241]. As the ribbon growth mechanism is driven by an exchange of adhesion energies, it was hypothesised that spiropyrans could switchably reduce graphene-graphene adhesion such that graphene-substrate contact becomes favourable and the ribbon reverses. Functionalisation of graphene by pyrene-modified spiropyrans has also been demonstrated previously[242], and growth of gr-AK ribbons on spiropyran-functionalized samples was demonstrated in the Cross lab previously. While this

method was not pursued in this work, we anticipate future experimental focus on this method.

5.3 Electrical control

Direct voltage control instead was sought to induce ribbon reversal as a lower capacitive energy state which could be achieved in principle by unfolding the ribbon. Fig. 5.4 shows a sketch of this admittedly naïve model: a voltage source charges both the conductive Si of the SiO_2/Si substrate and the graphene ribbon, while the SiO_2 acts as the dielectric with a thickness of ≈300 nm, the standard used for mechanical exfoliation as it provides maximum optical contrast of the graphene to locate it by optical microscopy. We can then write the energy of this capacitor as

$$\mathrm{U} = \mathrm{C}\,V^2 = \varepsilon \frac{w\,x}{h}\,V^2 \tag{51}$$

with capacitance *C*, voltage *V*, ribbon width and length *w* and *x* respectively, and thickness of the SiO_2 *h*. Considering an infinitesimal change in ribbon length *dx*, we can rewrite the above as

$$d\mathrm{U} = \varepsilon \frac{w\,dx}{h}\,V^2 \tag{52}$$

with permittivity *ε*. Rearranging, we can express this in terms of a force *F* acting on the fold as

$$\mathrm{F} = -\frac{dU}{dx} = -\varepsilon \frac{w}{h}\,V^2 \tag{53}$$

Substituting typical values of *w* as 350 nm, *h* as 300 nm and relative permittivity of SiO_2 of 3.9 [243], this yields F = -0.040 nN $V^{-2} \cdot (V^2)$. With the interfacial driving force during ribbon folding estimated as ≈1 nN, a voltage of as little as 5V would match this interfacial force. Unfolding specifically is predicted as this would lower the energy of the system by decreasing the separation between folded ribbon and Si, per eqn. (51).

Electrical contact was made directly with the underside of the Si chip after removal of native oxide layer by polishing. Initial tests attempted to contact with graphene flakes of suitably large dimensions (50-100 µm laterally) with silver conductive lacquer (a mixture of silver microparticles (60% w/w) in ethanol, 1-ethoxypropan-2-ol, acetone and ethyl acetate solvent)) applied to contact flake which was in turn connected to 160 µm gauge copper wire. However, while the contact could successfully be made to indented graphene flakes, concentration of silver particles is non-homogeneous near the edges of the applied droplets to lengths of up to 50 µm. This distance is comparable with the flake size, rendering application of silver paint to contact without loss of

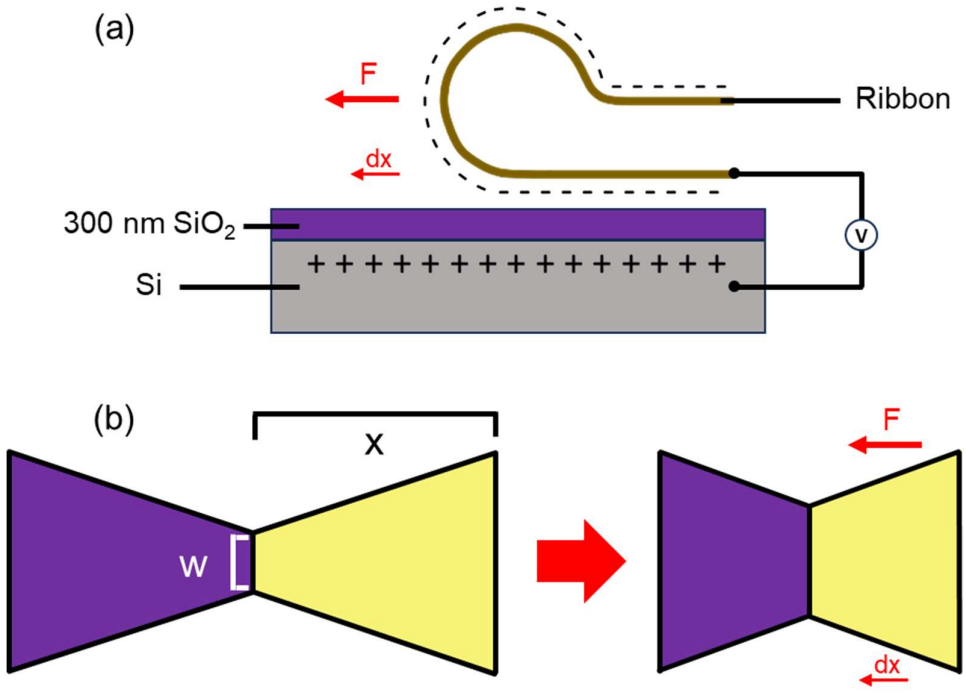

Fig. 5.4: Sketch demonstrating concept of capacitive ribbon control. (a) Sideview sketch of a capacitor, with "plates" of the Si substrate and ribbon, and SiO_2 dielectric, which is predicted to unfold with increasing voltage giving rise to a force greater than the interfacial driving force. (b) Plan view of ribbon predicted to reverse with applied voltage in capacitor setup.

conductance due to lower silver particle concentrations at or on the flake edge highly difficult. This was therefore deemed impracticable experimentally.

Instead, the SiO_2 substrates were patterned with 50 nm of gold by metal evaporation (with a 10 nm titanium layer between substrate and gold to promote adhesion and prevent delamination). Graphene was then mechanically exfoliated onto these substrates with gold patterning, with the specific aim of exfoliating flakes onto both gold and SiO_2 substrate simultaneously as flakes exfoliated entirely onto gold cannot readily be identified optically. While mechanical exfoliation is already of low yield, with coverage of the substrate by few-layer graphene often less than 0.01 %, the height difference of 60 nm between substrate and evaporated metal appeared to make exfoliation onto these areas even less favourable. As a result, only relatively thick flakes (>10 nm) were identified which had been exfoliated such that they were contacted on both the substrate and an area of evaporated gold.

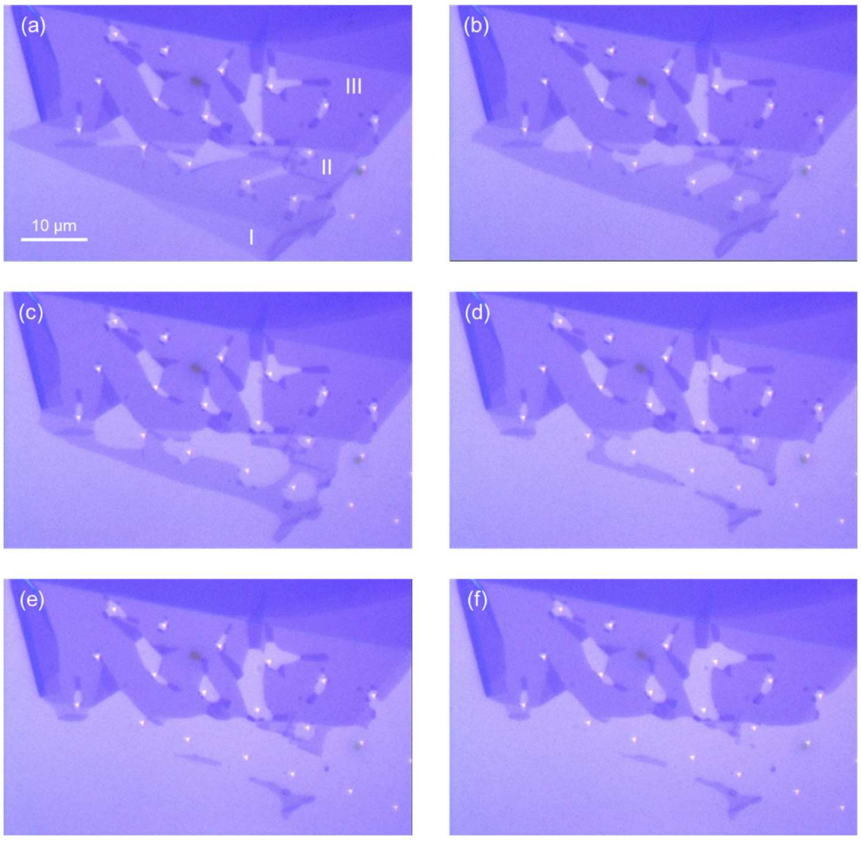

Fig. 5.5: Erosion of graphene flakes from edges with 100 V, 50 kHz sinusoidal waveform. (a)-(f): Snapshots taken at 2-minute intervals with thinner areas of graphene removed most rapidly (I and II) and thickest area more slowly (III).

However, such relatively thick flakes often are immediately adjacent to thinner areas of graphene on SiO_2, providing electrical connectivity to few-layer graphene. Indentation was performed on such few-layer areas of mechanically exfoliated graphene with ribbons nucleated as a result. Electrical signals with controlled voltage and frequency were applied using a signal generator and voltage amplifier per schematic in Fig. 5.4 (a). However, no effect was observed on ribbons for voltages up to 300 V_{ptp} in sinusoidal or square waveforms, with frequencies of 0.01 Hz to 1 kHz, in contrast with expectation from eqn. (53). While this may suggest simply that electrical contact was not continuous, a frequency-dependent erosion of graphene was observed at higher frequencies with voltages above 80 V_{ptp}, as in Fig. 5.5, disproving this suggestion. A 50 kHz sinusoidal waveform is applied, with no effect observed from 0 – ≈80 V (Fig. 5.5 (a)). This signal is maintained at 100 V_{ptp} for 10 minutes (Fig. 5.5 (a) to (f) being equally spaced over this time). The thinnest areas of graphene, denoted by their lightest blue colour, disappear rapidly, while thicker areas are only eroded slightly over the entire 10-minute interval (thinnest to thickest relevant areas are also labelled I to III in Fig. 5.5 (a)). This erosion occurs from graphene edges, both of the flake as exfoliated and from torn edges as a result of ribbon formation. This spreads in a “fire front” fashion radially from edges, as seen in the approximately oval eroded areas in thinner graphene in (c) for example. To our knowledge, this phenomenon has not been previously reported elsewhere.

While the few-layer areas of this sample were entirely removed before AFM imaging to determine layer number could be carried out, this can be estimated by colour and indirectly by the rate of erosion. As observed in Fig. 5.5, this erosion does not occur uniformly over the sample area but from graphene edges. Therefore, the change in area per time of each region was also divided by the torn length of graphene in each region from which this erosion appears to act. The calculated rate of change of area per time per torn length is double for area I relative to area II, and in turn 12 times slower in area III than area II. While this scaling for areas I and II appears to match change in layer number as estimated optically, this does not hold for II and III. This erosion process also does not occur at step edges internal to the flake. A mechanism for this erosion of graphene with applied high frequency voltage remains unclear, although we speculate that this process is selective oxidation of edges of graphene. Strong carbon-carbon

bonding can occur between active graphene edges in multilayer graphene, resulting in closed edge formation[244]. As this is expected to be more probable with greater number of layers, we speculate that this increased possibility of interlayer crosslinking at torn edges in thicker areas may make these edges more resistant to this erosion process. Ion beam irradiation can result in carbon atoms being removed from graphene sheets, generating defects and dangling bonds. The free-energies of defects and dangling bonds are minimised by cross-linking between different graphene layers[245,246], which in turn strengthens interlayer interactions. This high frequency electrical signal may have an analogous effect, with the removal of edge atoms by selective oxidation and crosslinking making erosion of remaining layers occur at a much slower rate than an expected erosion rate decreasing linearly with number of layers.

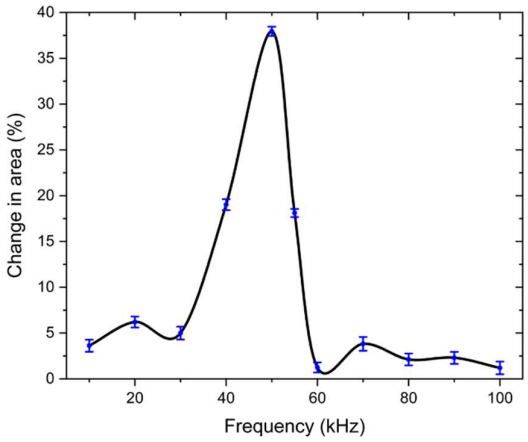

Fig. 5.6: Frequency dependence of rate of graphene erosion. A spike in area change of graphene corresponding to a higher rate of erosion is observed at frequencies around 50 kHz.

A frequency dependence of the area change of graphene was also observed over a frequency range of 1 – 100 kHz on another electrically contacted few-layer mechanically exfoliated graphene sample as in Fig. 5.6. The change in area of a few-layer graphene was recorded after applying an 80 V_{ptp} sinusoidal signal for one minute with varying frequency over 10 kHz intervals, with a peak around 50 kHz. In this test, frequencies were applied in the order of 10 kHz, 100 kHz, 20 kHz, 90 kHz … i.e. alternating between highest and lowest remaining intervals while converging on 55 kHz to minimise erosion of the limited area of graphene in earlier timesteps such that sufficient area remained to observe at central values of frequency in the range selected.

Previously, preliminary unpublished work within the group indicated that application of voltage in this capacitor model could induce ribbon growth in a similar manner to thermal treatment. Although existing samples from that period are limited, we note a variation in resistivities of such samples on orders of magnitude, which in turn are

orders of magnitude greater than the p-doped substrates (Graphene Supermarket, 0.001 – 0.005 Ω·cm) used throughout this research. As we could not replicate this result, we therefore speculate that this previous observation may instead have been a result of resistive heating of the sample.

The erosion of thinner layers soonest appears to result in ribbons becoming islands of twisted graphene of square micron scale areas, although the effect of this erosion on the fold specifically has not yet been explored. This could produce isolated, twisted areas of graphene which may be of interest in experiments surrounding superlubricity, as a much thinner version of a graphite mesa for example. Although still requiring further study, we also propose that this phenomenon could be exploited to develop a frequency dependent graphene fuse for example. While our original goal of reversible control of graphene AK-ribbons was not here realised, this novel graphene erosion process motivates further study.

5.4 Conclusions

We reported on the first known successful reversal of auto-kirigami ribbons by manipulation with an AFM tip, though incomplete healing of the graphene sheet after reversal appears to impair our ability to repeatedly cycle ribbon growth and reversal. While progress has been demonstrated, control of auto-kirigami ribbons nonetheless proves highly challenging, with alternative methods such as functionalisation of graphene by spiropyran for example still to be explored.

Efforts to induce reversal of graphene auto-kirigami by incorporating the ribbon into a capacitor with anticipated reversal as a result of minimisation of energy state capacitor model failed. This however resulted in the fortuitous observation of a novel phenomenon whereby an area of tens of square micrometres of graphene was apparently selectively eroded by oxidization from flake edges (both interior and exterior). This rate of change of area of the erosion process was shown to have a strong dependence on the electrical signal's frequency and graphene layer number.

Chapter 6: Conclusions and future work

6.1 Conclusions

In Chapter 2, we performed time-resolved studies of stripe formation on pristine mechanically exfoliated surfaces by AFM and studied how stripes and their characteristic friction domains evolve with time. The influence of surface features such as wrinkles, steps, indents and ribbons on stripe friction domains was studied to gain further insight into how stripes self-assemble on graphene surfaces. We further demonstrated that stripes are present not only on graphene surfaces but at graphene-graphene interfaces in ribbons, at buried graphene-graphene interfaces in graphitic flakes and at graphene-substrate interfaces, suggesting a stripe intercalation mechanism active at these interfaces and highlighting the ubiquity of this contaminant material.

We reviewed methods of auto-kirigami nucleation by AFM scratching in Chapter 3, which were found to be unreliable, of very low throughput and to offer little control of the resulting ribbons. In contrast, we developed a new method of auto-kirigami nucleation which can be performed using only a standard AFM, consisting of AFM based indentation and subsequent very high-setpoint tapping mode imaging (hard tapping). This method can produce yields comparable to small amplitude sheared indentation nucleation while eliminating the stringent requirement of lateral shear to induce auto-kirigami. As graphene rupture is necessary for auto-kirigami nucleation, factors affecting rupture of graphene during 2D indentation were also explored.

In Chapter 4 we expanded the applicability of auto-kirigami nucleation from only mechanically exfoliated graphene to CVD 2D materials, with successful ribbon nucleation and growth observed on CVD graphene samples. Residual PMMA was identified as a major impediment to both nucleation and growth, with methods to remove PMMA from CVD materials explored including thermal annealing, catalytic cleaning, exposure to oxygen plasma and mechanical AFM micro-cleaning.

In Chapter 5, we explored methods to control ribbons for potential application in NEMS devices, with successful ribbon reversal and growth induced. A novel phenomenon whereby graphene can become eroded by application of an electrical signal with strong frequency dependence on rate of erosion was also reported.

The above represents significant contributions to the field of graphene auto-kirigami across three broad directions: fundamentals, development and applications.

In fundamentals, we studied graphene rupture as a precursor to nucleation during 2D indentation, as well as in exploring alternative methods of nucleation; and graphene superlubricity in ribbons necessary to enable sliding and folding during auto-kirigami self-assembly.

Our first successful demonstration of auto-kirigami in 100+ layers of graphene as well as in CVD-synthesised 2D materials expands auto-kirigami from a phenomenon inherently limited by the dimensions and low yield of mechanically exfoliated graphene, the only material upon which it had previously been observed, to a much wider range of 2D materials, facilitating further developments in this field.

We also demonstrated proof-of-concept of graphene ribbons with applications as nanoelectromechanical devices by inducing cyclic reversal and growth of graphene ribbons with mechanical manipulation.

Furthermore, we demonstrated how contaminants impact in various ways upon each of these directions, with the observation of stripe adsorbates which are ubiquitously present on all graphene surfaces exposed to ambient conditions; evaluation of superlubricity in graphene ribbon growth which is not destroyed by the presence of stripes; and ribbon nucleation in CVD materials impaired by the presence of PMMA. In total, this represents the most comprehensive assessment and study of graphene auto-kirigami to date.

6.2 Future work

Firstly, we here present two curious experimental results encountered in this work which we have not included in the main text as they require further fundamental study.

Fig. 6.1 (a) shows a sample linear array of 8 indents with 4 µm spacing on monolayer graphene (with circles of different colours inset in centre of indents corresponding to individual curves in (b) and (c)). These indents were performed with the same Berkovich tip used throughout section 3.3 to loads of 10 mN with a strain rate of 0.02 s^{-1}, lateral oscillations of 3 nm amplitude at a frequency of 129 Hz. In (b), the characteristic sudden increase in lateral contact stiffness at ≈7-13 nm broadly agrees with our earlier discussion in section 3.3. However, closer examination of the rupture points in (c) (zoom-in to orange dash highlighted section in (b)) shows a "grouping" of the rupture points of certain curves. These groupings are, from left to right in terms of increasing rupture depth, of indent 4 at 6.7 nm depth; indents 1, 3 and 5 at 8.7 nm depth; indents

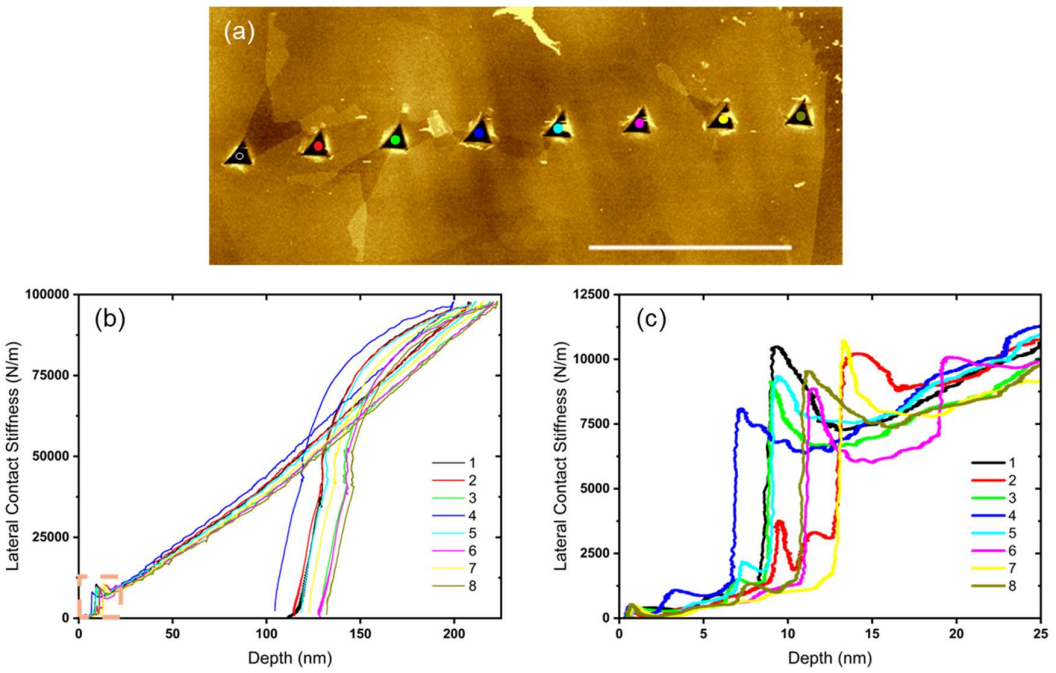

Fig. 6.1: "Grouping" of rupture points in monolayer mechanically exfoliated graphene. (a) A sample array of 8 indents to 10 mN load, with indents labelled with respect to lateral contact stiffness/depth data in (b) and (c). The characteristic graphene rupture point is observed in lateral contact stiffness data in (b). Examination of data around the rupture point in (c) (orange dashed area in (b)) shows a regular spacing of rupture points and grouping of individual curves.

6 and 8 at 10.8 nm depth and indents 2 and 7 at 12.8 nm depth. Even where lesser peaks in contact stiffness occur prior to the rupture signal as in indents 2 and 5 such that the near vertical contact stiffness increase occurs from a higher initial value of contact stiffness than other indents in their respective groups, the vertical portions of indents within a particular group nonetheless align with variation in depth of less than 0.3 nm at an arbitrary contact stiffness. We also note the highly regular 2.0-2.1 nm spacing between each group. 8 other arrays of indents (with median 7.5 indents per array) were applied over the same 3 day period as the data depicted in Fig. 6.1 on separate graphene flakes of 1-4 layer thickness (with all flakes exfoliated on the same day and stored together), this grouping effect was observed in 6 of 8, with 20-57% of indents within a particular array grouped. Grouping also does not appear to correspond to position or order of indents on the flake or within the array.

For these indents, we have also verified that regular spacing is not due to incorrect assignment of the contact point. In this load-controlled method, the contact point is primarily assigned when one of two criteria is first met: where the change in vertical dynamic phase exceeds a specified amount or where the vertical dynamic displacement becomes less than the dynamic noise level. The vertical phase and displacement data for all indents in this data set align very well in the few nanometres before contact, with no evidence of spacing arising from a systematic discrepancy in this assignment.

While this appears to strongly suggest an underlying physical phenomenon, we as of yet cannot provide a physical description of this grouping or definitively rule out the influence of an indenter-system effect rather than physical effect.

Although ribbon length and shape have varied moderately throughout the examples presented throughout this work, the ribbons presented have shown the characteristic features of straight tear edges and inward tapering to a final fold width dependent on layer thickness, but often of 200-300 nm width and to few micrometre lengths if ribbon growth is not impeded. However, in a very small proportion of ribbons (< 1%), these features are not observed as in Fig. 6.2.

Fig. 6.2 (a) shows a ribbon in which no inward tapering is observed. With a constantly increasing fold width with growth, the interfacial force scaling with ribbon area appears to readily overcome fold strain in this instance, with ribbon growth only ceasing when the ribbon head encounters the flake/substrate edge, where friction becomes too great for growth to continue. In (b) and (c), the ribbons initially taper inwards as expected, but upon reaching a width similar to the expected final width of a typical ribbon in that layer number on graphene, the ribbons then begin to widen. As in (a), growth of these ribbons ceases only when the ribbon head encounters the flake edge. In (d), the ribbon initially tapers inwards over a length of 2 µm (from indent to position I), widens gradually over ≈8 µm length (from I to II), tapers inwards again over ≈8 µm length (II to III) before both ribbon tear edges grow near parallel to one another over ≈15 µm (III to IV). These ribbons are all significantly longer than typical, with lengths of up to ≈35 µm in (d) for example.

We emphasise that these ribbons represent an extremely small proportion of all ribbons observed in this research. These anomalous ribbons do not appear randomly distributed across all graphene flakes studied, but instead multiple anomalous ribbons may be observed on a single graphene flake, and none on many other graphene flakes. Even on

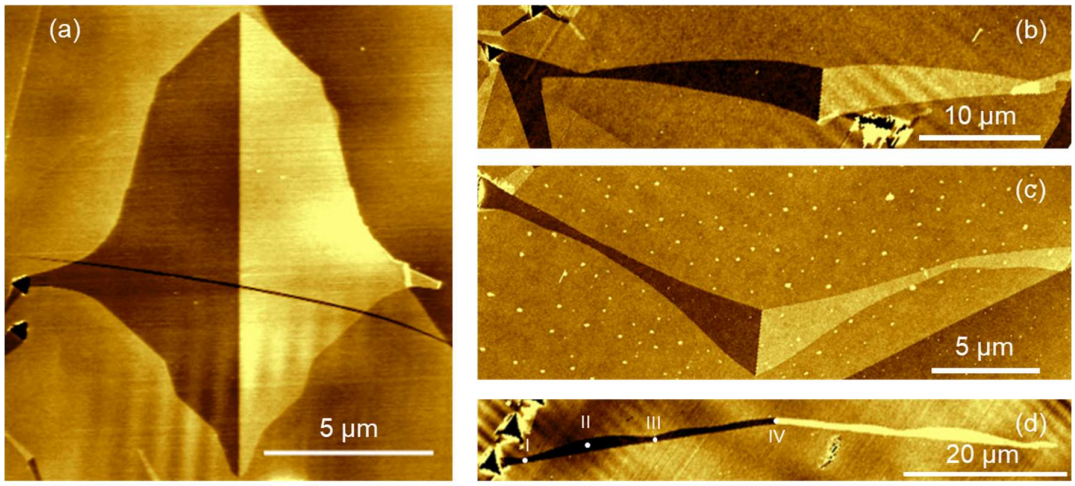

Fig. 6.2: Rare, anomalous ribbon growth in graphene. Samples of ribbon growth in which inward tapering along straight tears does not occur. In a monolayer graphene flake in (a), a ribbon widens throughout growth rather than tapering inwards. (b) and (c), on the same bilayer graphene flake, shows ribbons initially tapering inwards to typical final widths as expected, before continuing to grow and indeed widen. The ribbon in 4-layer graphene in (d) tapers inwards from its initial width to point I, widens to II, narrows again to III and grows with no apparent tapering or widening to IV. Total linear z-scale: 4 nm in (a) and (c), 3 nm in (b) and (d).

such samples, ribbons of typical shape and length are still more common than the anomalous ribbons.

Furthermore, we note that all ribbons with such anomalous growth were nucleated on especially large graphene flakes (>100 μm lateral dimensions). We speculate that such large flakes may not adhere uniformly to the substrate across their >10,000 μm^2 areas, resulting in varying graphene-substrate adhesion and therefore modifying the interfacial driving force per discussion in section 1.6. However, we have not yet obtained direct experimental evidence of this claim. Nonetheless, such ribbons are of keen interest as they may provide insight into methods of producing ribbons of much greater dimensions for example.

There are a number of further avenues to explore with respect to the research presented above. We have previously discussed planned application of AFM micro-cleaning to a wider range of CVD materials in order to increase ribbon yield in section 4.3, as well as proposed UV control of ribbons by functionalisation of the graphene surface with spiropyrans for example in section 5.2.

In Chapter 2, we clearly demonstrated that stripe adsorbate material is present not only on graphene surfaces but also within graphene-substrate and graphene-graphene interfaces, including buried graphene-graphene interfaces in 100+ layer graphite. We proposed that the hydrocarbons comprising stripes must intercalate between graphene and substrate as well as between graphene layers. AFM imaging to examine possible intermediate conditions of stripe intercalation could provide further insight into this proposed mechanism. These interfaces could be revealed by ribbon nucleation, per schematic in Fig. 6.3. At time t_0, an array of regularly spaced indents (columns here) would be performed on graphene or graphite, with some number of ribbons nucleated as a result. Similar arrays would be performed over regular time intervals (t_1, t_2 etc), with resulting ribbons imaged immediately after nucleation. Assuming that intercalation occurs as proposed, one might expect that initially no stripes would be observed on the nucleated ribbons which reveal the former substrate-graphene or graphene-graphene interface. As stripe hydrocarbons intercalate from flake edges and migrate inwards from the flake edge, stripes may be observed from ribbons nucleated from indents 1 and 5 only at t_1, at 1, 2, 4 and 5 at t_2 and at all locations 1-5 at t_3. In Fig.

6.3, we select an elongated rectangular shape to minimise migration of adsorbate material from the shorter edges of the flake to the indent locations, with migration from the long edges only to be tested here.

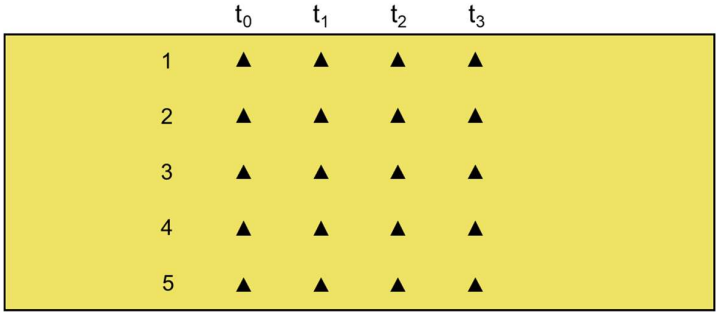

Fig. 6.3: Schematic of experiment testing intercalation of stripe adsorbates.

In Chapter 4 we implemented various methods for removal of PMMA residue from CVD materials. Catalytic cleaning with platinum as described by Longchamp et al.[226] remains highly attractive as it promises near-complete removal of PMMA with minimal damage to CVD materials as annealing can be performed at relatively moderate temperatures. We attribute the relative lack of success of this method (with a platinum layer sandwiched between CVD material and substrate) to SiO_2 residue preventing intimate contact between CVD graphene and the thin platinum layer. However, evaporating platinum onto a micropatterned surface rather than a flat silicon substrate which is then brought into contact with CVD graphene may negate this issue of substrate residue impairing contact.

All ribbon nucleation in this research was performed under ambient conditions with uncontrolled humidity and temperature. However, the edge structures produced by graphene undergoing tearing are known to be influenced by environment, with sensitivity to presence of oxygen for example[109]. Procurement is currently undergoing for acquisition of an environmental chamber which will allow for rigorous testing of the influence of gaseous species on ribbon nucleation, with capability of temperature control up to ≈60 °C, humidity control and control of gas species present at the crack tip.

References

1. Cao, Y. *et al.* Unconventional superconductivity in magic-angle graphene superlattices. *Nature* **556**, 43–50 (2018).
2. Peierls, R. Bemerkungen über Umwandlungstemperaturen. *Helvetica Physica Acta* **7**, 81 (1934).
3. Landau, L. D. On the theory of phase transitions. II. *Phys. Z. Sowjet.* **11**, 545 (1937).
4. Evans, J. W., Thiel, P. A. & Bartelt, M. C. Morphological evolution during epitaxial thin film growth: Formation of 2D islands and 3D mounds. *Surface Science Reports* **61**, 1–128 (2006).
5. Venables, J. A., Spiller, G. D. T. & Hanbucken, M. Nucleation and growth of thin films. *Reports on Progress in Physics* **47**, 399–459 (1984).
6. Meyer, J. C. *et al.* The structure of suspended graphene sheets. *Nature* **446**, 60–63 (2007).
7. Novoselov, K. S. *et al.* Electric Field Effect in Atomically Thin Carbon Films. *Science* **306**, 666–669 (2004).
8. Geim, A. K. & Novoselov, K. S. The rise of graphene. *Nature Mater* **6**, 183–191 (2007).
9. Novoselov, K. S. *et al.* Two-dimensional gas of massless Dirac fermions in graphene. *Nature* **438**, 197–200 (2005).
10. Lee, C., Wei, X., Kysar, J. W. & Hone, J. Measurement of the Elastic Properties and Intrinsic Strength of Monolayer Graphene. *Science* **321**, 385–388 (2008).

11. Balandin, A. A. Thermal properties of graphene and nanostructured carbon materials. *Nature Mater* **10**, 569–581 (2011).
12. Song, H. *et al.* Low friction and wear properties of carbon nanomaterials in high vacuum environment. *Tribology International* **143**, 106058 (2020).
13. Neubeck, S. *et al.* Direct determination of the crystallographic orientation of graphene edges by atomic resolution imaging. *Appl. Phys. Lett.* **97**, 053110 (2010).
14. Singh, A. K., Penev, E. S. & Yakobson, B. I. Armchair or Zigzag? A tool for characterizing graphene edge. *Computer Physics Communications* **182**, 804–807 (2011).
15. Hutchings, I. M. Leonardo da Vinci's studies of friction. *Wear* **360–361**, 51–66 (2016).
16. Bowden, F. P. & Tabor, D. *The Friction and Lubrication of Solids*. (Clarendon Press, 2001).
17. Prandtl, L. Ein Gedankenmodell zur kinetischen Theorie der festen Körper. *ZAMM - Journal of Applied Mathematics and Mechanics / Zeitschrift für Angewandte Mathematik und Mechanik* **8**, 85–106 (1928).
18. Tomlinson, G. a. CVI. A molecular theory of friction. *The London, Edinburgh, and Dublin Philosophical Magazine and Journal of Science* **7**, 905–939 (1929).
19. Frenkel, J. & Kontorova, T. On the theory of plastic deformation and twinning. *Izv. Akad. Nauk, Ser. Fiz.* **1**, 137–149 (1939).
20. Hirano, M. & Shinjo, K. Atomistic locking and friction. *Phys. Rev. B* **41**, 11837–11851 (1990).

21. Oo, W. H., Ashby, P. D. & Baykara, M. Z. Structural Superlubricity at High Sliding Speeds under Ambient Conditions. Preprint at https://doi.org/10.48550/arXiv.2407.06971 (2024).

22. Hölscher, H., Schirmeisen, A. & Schwarz, U. D. Principles of atomic friction: from sticking atoms to superlubric sliding. *Philosophical Transactions of the Royal Society A: Mathematical, Physical and Engineering Sciences* **366**, 1383–1404 (2007).

23. Dienwiebel, M. *et al.* Superlubricity of Graphite. *Phys. Rev. Lett.* **92**, 126101 (2004).

24. Dietzel, D., Feldmann, M., Schwarz, U. D., Fuchs, H. & Schirmeisen, A. Scaling Laws of Structural Lubricity. *Phys. Rev. Lett.* **111**, 235502 (2013).

25. Cihan, E., İpek, S., Durgun, E. & Baykara, M. Z. Structural lubricity under ambient conditions. *Nat Commun* **7**, 12055 (2016).

26. Özoğul, A., İpek, S., Durgun, E. & Baykara, M. Z. Structural superlubricity of platinum on graphite under ambient conditions: The effects of chemistry and geometry. *Applied Physics Letters* **111**, 211602 (2017).

27. Deng, H., Ma, M., Song, Y., He, Q. & Zheng, Q. Structural superlubricity in graphite flakes assembled under ambient conditions. *Nanoscale* **10**, 14314–14320 (2018).

28. Wang, K. *et al.* Structural superlubricity with a contaminant-rich interface. *Journal of the Mechanics and Physics of Solids* **169**, 105063 (2022).

29. Liu, Z. *et al.* Observation of Microscale Superlubricity in Graphite. *Physical Review Letters* **108**, (2012).

30. Li, Q., Lee, C., Carpick, R. W. & Hone, J. Substrate effect on thickness-dependent friction on graphene. *physica status solidi (b)* **247**, 2909–2914 (2010).

31. Lee, C. *et al.* Frictional Characteristics of Atomically Thin Sheets.

32. Chen, X., Yi, C. & Ke, C. Bending stiffness and interlayer shear modulus of few-layer graphene. *Applied Physics Letters* **106**, 101907 (2015).

33. Zeng, X., Peng, Y., Liu, L., Lang, H. & Cao, X. Dependence of the friction strengthening of graphene on velocity. *Nanoscale* **10**, 1855–1864 (2018).

34. Li, S. *et al.* The evolving quality of frictional contact with graphene. *Nature* **539**, 541–545 (2016).

35. Hernandez, Y. *et al.* High-yield production of graphene by liquid-phase exfoliation of graphite. *Nature Nanotech* **3**, 563–568 (2008).

36. Su, C.-Y. *et al.* High-Quality Thin Graphene Films from Fast Electrochemical Exfoliation. *ACS Nano* **5**, 2332–2339 (2011).

37. Lang, B. A LEED study of the deposition of carbon on platinum crystal surfaces. *Surface Science* **53**, 317–329 (1975).

38. Somani, P. R., Somani, S. P. & Umeno, M. Planer nano-graphenes from camphor by CVD. *Chemical Physics Letters* **430**, 56–59 (2006).

39. Wang, J., Manga, K. K., Bao, Q. & Loh, K. P. High-Yield Synthesis of Few-Layer Graphene Flakes through Electrochemical Expansion of Graphite in Propylene Carbonate Electrolyte. *J. Am. Chem. Soc.* **133**, 8888–8891 (2011).

40. Achee, T. C. *et al.* High-yield scalable graphene nanosheet production from compressed graphite using electrochemical exfoliation. *Sci Rep* **8**, 14525 (2018).

41. Emtsev, K. V. *et al.* Towards wafer-size graphene layers by atmospheric pressure graphitization of silicon carbide. *Nature Mater* **8**, 203–207 (2009).

42. Nair, R. R. *et al.* Fine Structure Constant Defines Visual Transparency of Graphene. *Science* **320**, 1308–1308 (2008).

43. Blake, P. *et al.* Making graphene visible. *Applied Physics Letters* **91**, 063124 (2007).

44. Huang, Y. *et al.* Reliable Exfoliation of Large-Area High-Quality Flakes of Graphene and Other Two-Dimensional Materials. *ACS Nano* **9**, 10612–10620 (2015).

45. Bunch, J. S. *et al.* Impermeable Atomic Membranes from Graphene Sheets. *Nano Lett.* **8**, 2458–2462 (2008).

46. Li, X. *et al.* Large-Area Synthesis of High-Quality and Uniform Graphene Films on Copper Foils. *Science* **324**, 1312–1314 (2009).

47. Huang, P. Y. *et al.* Grains and grain boundaries in single-layer graphene atomic patchwork quilts. *Nature* **469**, 389–392 (2011).

48. Lin, Y.-C. *et al.* Graphene Annealing: How Clean Can It Be? *Nano Lett.* **12**, 414–419 (2012).

49. Zhuang, B., Li, S., Li, S. & Yin, J. Ways to eliminate PMMA residues on graphene — — superclean graphene. *Carbon* **173**, 609–636 (2021).

50. Binnig, G., Quate, C. F. & Gerber, Ch. Atomic Force Microscope. *Phys. Rev. Lett.* **56**, 930–933 (1986).

51. Lal, R. & John, S. A. Biological applications of atomic force microscopy. *https://doi.org/10.1152/ajpcell.1994.266.1.C1* (1994) doi:10.1152/ajpcell.1994.266.1.C1.

52. Kaemmer, S. B. Introduction to Bruker's ScanAsyst and PeakForce Tapping AFM Technology. in vol. 133 1–12 (Bruker Appl. Notes, 2011).

53. Ogletree, D. F., Carpick, R. W. & Salmeron, M. Calibration of frictional forces in atomic force microscopy. *Review of Scientific Instruments* **67**, 3298–3306 (1996).

54. Pittenger, B., Erina, N. & Su, C. Quantitative Mechanical Property Mapping at the Nanoscale with PeakForce QNM. *Bruker Application Note AN128* (2010).

55. Su, C., Shi, J., Hu, Y., Hu, S. & Ma, J. Method and apparatus of using peak force tapping mode to measure physical properties of a sample. (2016).

56. Yablon, D. & Pittenger, B. Nanomechanical Characterization with AFM. *Application Note 160*.

57. Kittel, C. *Introduction to Solid State Physics*. (Wiley, Hoboken, NJ, 20).

58. Sader, J. E., Chon, J. W. M. & Mulvaney, P. Calibration of rectangular atomic force microscope cantilevers. *Review of Scientific Instruments* **70**, 3967–3969 (1999).

59. Sader, J. E. Frequency response of cantilever beams immersed in viscous fluids with applications to the atomic force microscope. *Journal of Applied Physics* **84**, 64–76 (1998).

60. Sader, J. E. *et al.* Spring constant calibration of atomic force microscope cantilevers of arbitrary shape. *Review of Scientific Instruments* **83**, 103705 (2012).

61. Hertz, H. Ueber die Berührung fester elastischer Körper. **1882**, 156–171 (1882).

62. Johnson, K. L. One Hundred Years of Hertz Contact. *Proceedings of the Institution of Mechanical Engineers* **196**, 363–378 (1982).

63. Boussinesq, J. (1842-1929) A. du texte. *Application Des Potentiels à l'étude de l'équilibre et Du Mouvement Des Solides Élastiques, Principalement Au Calcul Des Déformations et Des Pressions Que Produisent, Dans Les Solides, Des Efforts Quelquonques Exercés Sur Une Petite Partie de Leur Surface Ou de Leur Intérieur :*

Mémoire Suivi de Notes Étendues Sur Divers Points de Physique Mathématique et d'analyse / Par J. Boussinesq,... (1885).

64. Cappella, B. & Dietler, G. Force-distance curves by atomic force microscopy. *Surface Science Reports* **34**, 1–104 (1999).

65. Sneddon, I. N. Boussinesq's problem for a rigid cone. *Proceedings of the Cambridge Philosophical Society* **44**, 492 (1948).

66. Derjaguin, B. V., Muller, V. M. & Toporov, Yu. P. Effect of contact deformations on the adhesion of particles. *Journal of Colloid and Interface Science* **53**, 314–326 (1975).

67. Johnson, K. L., Kendall, K. & Roberts, A. D. Surface energy and the contact of elastic solids. *Proc. R. Soc. Lond. A* **324**, 301–313 (1971).

68. Bulychev, S. I., Alekhin, V. P., Shorshorov, M. K., Ternovskij, A. P. & Shynrev, G. D. Determination of Young modulus by the hardness indentation diagram. *Zavodskaya Laboratoriya* **41**, 1137–1140.

69. Sneddon, I. N. The relation between load and penetration in the axisymmetric boussinesq problem for a punch of arbitrary profile. *International Journal of Engineering Science* **3**, 47–57 (1965).

70. Bhushan, B. & Palacio, M. L. B. Nanoindentation. in *Encyclopedia of Nanotechnology* (ed. Bhushan, B.) 1576–1596 (Springer Netherlands, Dordrecht, 2012). doi:10.1007/978-90-481-9751-4_41.

71. Pharr, G. M. & Bolshakov, A. Understanding nanoindentation unloading curves. *Journal of Materials Research* **17**, 2660–2671 (2002).

72. Doerner, M. F. & Nix, W. D. A method for interpreting the data from depth-sensing indentation instruments. *Journal of Materials Research* **1**, 601–609 (1986).

73. Oliver, W. C. & Pethica, J. B. Method for continuous determination of the elastic stiffness of contact between two bodies. (1989).

74. Oliver, W. C. & Pharr, G. M. Measurement of hardness and elastic modulus by instrumented indentation: Advances in understanding and refinements to methodology. *Journal of Materials Research* **19**, 3–20 (2004).

75. Sen, I. & Kumar S, S. Characterizing Stress-Strain Behavior of Materials through Nanoindentation. in (2021). doi:10.5772/intechopen.98495.

76. Hay, J., Agee, P. & Herbert, E. Continuous Stiffness Measurement During Instrumented Indentation Testing. *Experimental Techniques* **34**, 86–94 (2010).

77. Oliver, W. C. & Pharr, G. M. An improved technique for determining hardness and elastic modulus using load and displacement sensing indentation experiments. *J. Mater. Res.* **7**, 1564–1583 (1992).

78. McElhaney, K. W., Nix, W. D. & Vlassak, J. J. Determination of indenter tip geometry and indentation contact area for depth-sensing indentation experiments. *Journal of Materials Research* **13**, 1300–1306 (1998).

79. Badt, N., Goldsby, D., Pharr, G. & Walker, C. Frictional Aging of Single-Asperity Nanoindentation Contacts in Quartz and Calcite. *Geophysical Research Letters* **51**, (2024).

80. Brazil, O., Pethica, J. B. & Pharr, G. M. The contribution of plastic sink-in to the static friction of single asperity microscopic contacts. *Proceedings of the Royal*

Society A: Mathematical, Physical and Engineering Sciences **477**, 20210502 (2021).

81. Samuels, L. E. & Mulhearn, T. O. An experimental investigation of the deformed zone associated with indentation hardness impressions. *Journal of the Mechanics and Physics of Solids* **5**, 125–134 (1957).
82. Sudharshan Phani, P. & Oliver, W. C. A critical assessment of the effect of indentation spacing on the measurement of hardness and modulus using instrumented indentation testing. *Materials & Design* **164**, 107563 (2019).
83. Pethica, J. B. Nanoindentation in more than one dimension – Experimental challenges and opportunities. *Current Opinion in Solid State and Materials Science* **27**, 101100 (2023).
84. Sirghi, L., Ponti, J., Broggi, F. & Rossi, F. Probing elasticity and adhesion of live cells by atomic force microscopy indentation. *Eur Biophys J* **37**, 935–945 (2008).
85. Hua, Y. PeakForce QNM Advanced Applications Training. (2014).
86. Lawn, B. *Fracture of Brittle Solids*. (Cambridge University Press, Cambridge, 1993). doi:10.1017/CBO9780511623127.
87. Szlufarska, I., Chandross, M. & Carpick, R. W. Recent advances in single-asperity nanotribology. *J. Phys. D: Appl. Phys.* **41**, 123001 (2008).
88. Carpick, R. W. & Salmeron, M. Scratching the Surface: Fundamental Investigations of Tribology with Atomic Force Microscopy. *Chem. Rev.* **97**, 1163–1194 (1997).
89. Annett, J. & Cross, G. L. W. Self-assembly of graphene ribbons by spontaneous self-tearing and peeling from a substrate. *Nature* **535**, 271–275 (2016).

90. Pereira Junior, M. L. & Ribeiro Junior, L. A. Self-folding and self-scrolling mechanisms of edge-deformed graphene sheets: a molecular dynamics study. *Phys. Chem. Chem. Phys.* **23**, 15313–15318 (2021).

91. Quintana, M. *et al.* A Simple Road for the Transformation of Few-Layer Graphene into MWNTs. *J. Am. Chem. Soc.* **134**, 13310–13315 (2012).

92. Shin, Y.-E. *et al.* An ice-templated, pH-tunable self-assembly route to hierarchically porous graphene nanoscroll networks. *Nanoscale* **6**, 9734–9741 (2014).

93. Xie, X. *et al.* Controlled fabrication of high-quality carbon nanoscrolls from monolayer graphene. *Nano Lett* **9**, 2565–2570 (2009).

94. Viculis, L. M., Mack, J. J. & Kaner, R. B. A Chemical Route to Carbon Nanoscrolls. *Science* **299**, 1361–1361 (2003).

95. Zhang, Z. & Li, T. Carbon Nanotube Initiated Formation of Carbon Nanoscrolls. *Applied Physics Letters* **97**, 081909 (2010).

96. Bryk, P. *et al.* What Is the Value of Water Contact Angle on Silicon? *Materials* **13**, 1554 (2020).

97. Li, Z. *et al.* Effect of airborne contaminants on the wettability of supported graphene and graphite. *Nature Mater* **12**, 925–931 (2013).

98. Tilmann, R. *et al.* Identification of Ubiquitously Present Polymeric Adlayers on 2D Transition Metal Dichalcogenides. *ACS Nano* **17**, 10617–10627 (2023).

99. Rode, J. C., Smirnov, D., Belke, C., Schmidt, H. & Haug, R. J. Twisted Bilayer Graphene: Interlayer Configuration and Magnetotransport Signatures. *Annalen der Physik* **529**, 1700025 (2017).

100. Nemes-Incze, P., Osváth, Z., Kamarás, K. & Biró, L. P. Anomalies in thickness measurements of graphene and few layer graphite crystals by tapping mode atomic force microscopy. *Carbon* **46**, 1435–1442 (2008).

101. Yankowitz, M. *et al.* Emergence of superlattice Dirac points in graphene on hexagonal boron nitride. *Nature Phys* **8**, 382–386 (2012).

102. Rode, J. C., Belke, C., Schmidt, H. & Haug, R. J. Interlayer Configurations in Twisted Bilayers of Folded Graphene. Preprint at http://arxiv.org/abs/1608.08133 (2016).

103. Rode, J. C. *et al.* Linking interlayer twist angle to geometrical parameters of self-assembled folded graphene structures. *2D Mater.* **6**, 015021 (2018).

104. He, Z.-Z., Zhu, Y.-B. & Wu, H.-A. Self-folding mechanics of graphene tearing and peeling from a substrate. *Front. Phys.* **13**, 138111 (2018).

105. Fonseca, A. F. & Galvão, D. S. Self-Driven Graphene Tearing and Peeling: A Fully Atomistic Molecular Dynamics Investigation. *MRS Advances* **3**, 463–468 (2018).

106. Fonseca, A. F. & Galvão, D. S. Self-tearing and self-peeling of folded graphene nanoribbons. *Carbon* **143**, 230–239 (2019).

107. Van Duin, A. C. T., Dasgupta, S., Lorant, F. & Goddard, W. A. ReaxFF: A Reactive Force Field for Hydrocarbons. *J. Phys. Chem. A* **105**, 9396–9409 (2001).

108. Rawlins, C. M. & Tribello, G. A. Measuring friction from simulations of folded graphene sheets. Preprint at http://arxiv.org/abs/2402.07768 (2024).

109. Huang, X., Yang, H., Van Duin, A. C. T., Hsia, K. J. & Zhang, S. Chemomechanics control of tearing paths in graphene. *Phys. Rev. B* **85**, 195453 (2012).

110. Yang, F. *et al.* Effect of Environmental Contaminants on the Interfacial Properties of Two-Dimensional Materials. *Acc. Mater. Res.* **3**, 1022–1032 (2022).

111. VACUUM TECHNOLOGY. in *Building Scientific Apparatus* (eds. Davis, C. C., Moore, J. H. & Coplan, M. A.) 93–146 (Cambridge University Press, Cambridge, 2009). doi:10.1017/CBO9780511609794.004.

112. Chapter 1.8 - Surface Physics and Its Relation to Vacuum Science. in *Handbook of Vacuum Science and Technology* (eds. Hoffman, D. M., Singh, B., Thomas, J. H. & Thomas, J. H.) 40–55 (Academic Press, San Diego, 1998). doi:10.1016/B978-012352065-4/50050-X.

113. Schedin, F. *et al.* Detection of individual gas molecules adsorbed on graphene. *Nature Mater* **6**, 652–655 (2007).

114. Wehling, T. O. *et al.* Molecular Doping of Graphene. *Nano Lett.* **8**, 173–177 (2008).

115. Romero, H. E. *et al.* n-Type Behavior of Graphene Supported on Si/SiO2 Substrates. *ACS Nano* **2**, 2037–2044 (2008).

116. Lu, Y.-H., Yang, C.-W. & Hwang, I.-S. Molecular Layer of Gaslike Domains at a Hydrophobic–Water Interface Observed by Frequency-Modulation Atomic Force Microscopy. *Langmuir* **28**, 12691–12695 (2012).

117. Wastl, D. S. *et al.* Observation of 4 nm Pitch Stripe Domains Formed by Exposing Graphene to Ambient Air. *ACS Nano* **7**, 10032–10037 (2013).

118. Wastl, D. S., Weymouth, A. J. & Giessibl, F. J. Atomically Resolved Graphitic Surfaces in Air by Atomic Force Microscopy. *ACS Nano* **8**, 5233–5239 (2014).

119. Choi, J. S. *et al.* Friction Anisotropy–Driven Domain Imaging on Exfoliated Monolayer Graphene. *Science* **333**, 607–610 (2011).

120. Choi, J. S. *et al.* Facile characterization of ripple domains on exfoliated graphene. *Review of Scientific Instruments* **83**, 073905 (2012).

121. Choi, J. S. *et al.* Correlation between micrometer-scale ripple alignment and atomic-scale crystallographic orientation of monolayer graphene. *Sci Rep* **4**, 7263 (2015).

122. Tang, S. *et al.* Precisely aligned graphene grown on hexagonal boron nitride by catalyst free chemical vapor deposition. *Sci Rep* **3**, 2666 (2013).

123. Gallagher, P. *et al.* Optical Imaging and Spectroscopic Characterization of Self-Assembled Environmental Adsorbates on Graphene. *Nano Lett.* **18**, 2603–2608 (2018).

124. Park, Y. *et al.* Configuration of ripple domains and their topological defects formed under local mechanical stress on hexagonal monolayer graphene. *Sci Rep* **5**, 9390 (2015).

125. Gallagher, P. *et al.* Switchable friction enabled by nanoscale self-assembly on graphene. *Nat Commun* **7**, 10745 (2016).

126. Rastei, M. V., Heinrich, B. & Gallani, J. L. Puckering Stick-Slip Friction Induced by a Sliding Nanoscale Contact. *Phys. Rev. Lett.* **111**, 084301 (2013).

127. Rastei, M. V., Guzmán, P. & Gallani, J. L. Sliding speed-induced nanoscale friction mosaicity at the graphite surface. *Phys. Rev. B* **90**, 041409 (2014).

128. Boland, M. J., Nasseri, M., Hunley, D. P., Ansary, A. & Strachan, D. R. Striped nanoscale friction and edge rigidity of MoS_2 layers. *RSC Adv.* **5**, 92165–92173 (2015).

129. Singh, S. K., Neek-Amal, M., Costamagna, S. & Peeters, F. M. Thermomechanical properties of a single hexagonal boron nitride sheet. *Phys. Rev. B* **87**, 184106 (2013).

130. Temiryazev, A., Frolov, A. & Temiryazeva, M. Atomic-force microscopy study of self-assembled atmospheric contamination on graphene and graphite surfaces. *Carbon* **143**, 30–37 (2019).

131. Seibert, S., Klassen, S., Latus, A., Bechstein, R. & Kühnle, A. Origin of Ubiquitous Stripes at the Graphite–Water Interface. *Langmuir* **36**, 7789–7794 (2020).

132. Pálinkás, A. *et al.* The composition and structure of the ubiquitous hydrocarbon contamination on van der Waals materials. *Nat Commun* **13**, 6770 (2022).

133. Cholakova, D. & Denkov, N. Rotator phases in alkane systems: In bulk, surface layers and micro/nano-confinements. *Advances in Colloid and Interface Science* **269**, 7–42 (2019).

134. Caumo, S., Bruns, R. E. & Vasconcellos, P. C. Variation of the Distribution of Atmospheric n-Alkanes Emitted by Different Fuels' Combustion. *Atmosphere* **11**, 643 (2020).

135. Filippov, A. E., Dienwiebel, M., Frenken, J. W. M., Klafter, J. & Urbakh, M. Torque and Twist against Superlubricity. *Phys. Rev. Lett.* **100**, 046102 (2008).

136. Koren, E., Lörtscher, E., Rawlings, C., Knoll, A. W. & Duerig, U. Adhesion and friction in mesoscopic graphite contacts. *Science* **348**, 679–683 (2015).

137. Feng, X., Kwon, S., Park, J. Y. & Salmeron, M. Superlubric Sliding of Graphene Nanoflakes on Graphene. *ACS Nano* **7**, 1718–1724 (2013).

138. Lu, X., Yu, M., Huang, H. & Ruoff, R. S. Tailoring graphite with the goal of achieving single sheets. *Nanotechnology* **10**, 269 (1999).

139. Zheng, Q. *et al.* Self-Retracting Motion of Graphite Microflakes. *Phys. Rev. Lett.* **100**, 067205 (2008).

140. Geim, A. K. & Grigorieva, I. V. Van der Waals heterostructures. *Nature* **499**, 419–425 (2013).

141. Haigh, S. J. *et al.* Cross-sectional imaging of individual layers and buried interfaces of graphene-based heterostructures and superlattices. *Nature Mater* **11**, 764–767 (2012).

142. Georgiou, T. *et al.* Vertical field-effect transistor based on graphene–WS2 heterostructures for flexible and transparent electronics. *Nature Nanotech* **8**, 100–103 (2013).

143. Lui, C. H., Liu, L., Mak, K. F., Flynn, G. W. & Heinz, T. F. Ultraflat graphene. *Nature* **462**, 339–341 (2009).

144. Wang, L. *et al.* One-Dimensional Electrical Contact to a Two-Dimensional Material. *Science* **342**, 614–617 (2013).

145. Chen, S. *et al.* Tip-Based Cleaning and Smoothing Improves Performance in Monolayer MoS_2 Devices. *ACS Omega* **6**, 4013–4021 (2021).

146. Wang, W. *et al.* Clean assembly of van der Waals heterostructures using silicon nitride membranes. *Nat Electron* **6**, 981–990 (2023).

147. Mayorov, A. S. *et al.* Micrometer-Scale Ballistic Transport in Encapsulated Graphene at Room Temperature. *Nano Lett.* **11**, 2396–2399 (2011).

148. Frisenda, R. *et al.* Recent progress in the assembly of nanodevices and van der Waals heterostructures by deterministic placement of 2D materials. *Chem. Soc. Rev.* **47**, 53–68 (2018).

149. Cao, Y. *et al.* Quality heterostructures from two dimensional crystals unstable in air by their assembly in inert atmosphere. Preprint at http://arxiv.org/abs/1502.03755 (2015).

150. Late, D. J., Liu, B., Matte, H. S. S. R., Dravid, V. P. & Rao, C. N. R. Hysteresis in Single-Layer MoS $_2$ Field Effect Transistors. *ACS Nano* **6**, 5635–5641 (2012).

151. Peyrard, M. & Aubry, S. Critical behaviour at the transition by breaking of analyticity in the discrete Frenkel-Kontorova model. *J. Phys. C: Solid State Phys.* **16**, 1593 (1983).

152. He, G., Müser, M. H. & Robbins, M. O. Adsorbed Layers and the Origin of Static Friction. *Science* **284**, 1650–1652 (1999).

153. Kawai, S. *et al.* Superlubricity of graphene nanoribbons on gold surfaces. *Science* **351**, 957–961 (2016).

154. Li, H. *et al.* Superlubricity between MoS2 Monolayers. *Advanced Materials* **29**, 1701474 (2017).

155. Ma, M. *et al.* Diffusion through Bifurcations in Oscillating Nano- and Microscale Contacts: Fundamentals and Applications. *Phys. Rev. X* **5**, 031020 (2015).

156. Rusanov, A. I. Cohesive energy and line energy of graphene. *Nanoscale* **6**, 8130–8133 (2014).

157. Li, P., You, Z. & Cui, T. Adhesion energy of few layer graphene characterized by atomic force microscope. *Sensors and Actuators A: Physical* **217**, 56–61 (2014).

158. Yang, J. *et al.* Observation of High-Speed Microscale Superlubricity in Graphite. *Phys. Rev. Lett.* **110**, 255504 (2013).

159. Allers, W., Schwarz, A., Schwarz, U. D. & Wiesendanger, R. A scanning force microscope with atomic resolution in ultrahigh vacuum and at low temperatures. *Review of Scientific Instruments* **69**, 221–225 (1998).

160. McGonigal, G. C., Bernhardt, R. H. & Thomson, D. J. Imaging alkane layers at the liquid/graphite interface with the scanning tunneling microscope. *Applied Physics Letters* **57**, 28–30 (1990).

161. Groszek, A. Selective Adsorption at Graphite/Hydrocarbon Interfaces. *PROCEEDINGS OF THE ROYAL SOCIETY OF LONDON SERIES A-MATHEMATICAL AND PHYSICAL SCIENCES* **314**, 473- (1970).

162. Nemes-Incze, P. *et al.* Preparing local strain patterns in graphene by atomic force microscope based indentation. *Sci Rep* **7**, 3035 (2017).

163. Woods, C. R. *et al.* Macroscopic self-reorientation of interacting two-dimensional crystals. *Nat Commun* **7**, 10800 (2016).

164. Ishigami, M., Chen, J. H., Cullen, W. G., Fuhrer, M. S. & Williams, E. D. Atomic Structure of Graphene on SiO_2. *Nano Lett.* **7**, 1643–1648 (2007).

165. Chen, L. *et al.* Friction at single-layer graphene step edges due to chemical and topographic interactions. *Carbon* **154**, 67–73 (2019).

166. Bacon, G. E. The interlayer spacing of graphite. *Acta Cryst* **4**, 558–561 (1951).

167. Bondi, A. van der Waals Volumes and Radii. *J. Phys. Chem.* **68**, 441–451 (1964).

168. Casiraghi, C. *et al.* Rayleigh Imaging of Graphene and Graphene Layers. *Nano Lett.* **7**, 2711–2717 (2007).

169. Gupta, A., Chen, G., Joshi, P., Tadigadapa, S., & Eklund. Raman Scattering from High-Frequency Phonons in Supported n-Graphene Layer Films. *Nano Lett.* **6**, 2667–2673 (2006).

170. Chen, Z., Lin, Y.-M., Rooks, M. J. & Avouris, P. Graphene nano-ribbon electronics. *Physica E: Low-dimensional Systems and Nanostructures* **40**, 228–232 (2007).

171. Xu, K., Cao, P. & Heath, J. R. Graphene Visualizes the First Water Adlayers on Mica at Ambient Conditions. *Science* **329**, 1188–1191 (2010).

172. Tallon, B., Lipton-Duffin, J. & MacLeod, J. Exfoliation of Graphene onto Si(111)-7 × 7 under Ultrahigh Vacuum Provides Some Protection against Exposure to Air. *Langmuir* **40**, 25692–25697 (2024).

173. Shearer, C. J., Slattery, A. D., Stapleton, A. J., Shapter, J. G. & Gibson, C. T. Accurate thickness measurement of graphene. *Nanotechnology* **27**, 125704 (2016).

174. Yao, Y., Ren, L., Gao, S. & Li, S. Histogram method for reliable thickness measurements of graphene films using atomic force microscopy (AFM). *Journal of Materials Science & Technology* **33**, 815–820 (2017).

175. Sidorov, A. N. *et al.* Electrostatic deposition of graphene. *Nanotechnology* **18**, 135301 (2007).

176. Annett, J. Atomic scale influences on the tribology of nano to meso-scale systems. (Trinity College (Dublin, Ireland). School of Physics, 2015).

177. Qu, C. *et al.* Origin of Friction in Superlubric Graphite Contacts. *Phys. Rev. Lett.* **125**, 126102 (2020).

178. de Wijn, A. S. (In)commensurability, scaling, and multiplicity of friction in nanocrystals and application to gold nanocrystals on graphite. *Phys. Rev. B* **86**, 085429 (2012).

179. Hartmuth, F., Dietzel, D., de Wijn, A. S. & Schirmeisen, A. Friction vs. Area Scaling of Superlubric NaCl-Particles on Graphite. *Lubricants* **7**, 66 (2019).

180. Sen, D., Novoselov, K. S., Reis, P. M. & Buehler, M. J. Tearing graphene sheets from adhesive substrates produces tapered nanoribbons. *Small* **6**, 1108–1116 (2010).

181. Yi, C. L., Zhang, L. Y., Chen, X. M., Wang, X. Q. & Ke, C. H. Nanomechanical Unfolding of Self-Folded Graphene on Flat Substrate. *Exp Mech* **59**, 381–386 (2019).

182. Zhang, Q., Ma, X. & Zhao, Y. Adhesion Behavior between Multilayer Graphene and Semiconductor Substrates. *Applied Sciences* **8**, 2107 (2018).

183. Chen, X., Zhang, L., Zhao, Y., Wang, X. & Ke, C. Graphene folding on flat substrates. *Journal of Applied Physics* **116**, 164301 (2014).

184. Li, H. *et al.* Fabrication of Single- and Multilayer MoS_2 Film-Based Field-Effect Transistors for Sensing NO at Room Temperature. *Small* **8**, 63–67 (2012).

185. Li, H., Wu, J., Yin, Z. & Zhang, H. Preparation and Applications of Mechanically Exfoliated Single-Layer and Multilayer MoS2 and WSe2 Nanosheets. *Acc. Chem. Res.* **47**, 1067–1075 (2014).

186. Ottaviano, L. *et al.* Mechanical exfoliation and layer number identification of MoS_2 revisited. *2D Mater.* **4**, 045013 (2017).

187. Desai, S. B. *et al.* Gold-Mediated Exfoliation of Ultralarge Optoelectronically-Perfect Monolayers. *Advanced Materials* **28**, 4053–4058 (2016).

188. Sun, H. *et al.* Theory of thin-film-mediated exfoliation of van der Waals bonded layered materials. *Phys. Rev. Materials* **2**, 094004 (2018).

189. Gramling, H. M. *et al.* Spatially Precise Transfer of Patterned Monolayer WS_2 and MoS_2 with Features Larger than 10^4 μm^2 Directly from Multilayer Sources. *ACS Appl. Electron. Mater.* **1**, 407–416 (2019).

190. Huang, Y. *et al.* Universal mechanical exfoliation of large-area 2D crystals. *Nat Commun* **11**, 2453 (2020).

191. Pacilé, D., Meyer, J. C., Girit, Ç. Ö. & Zettl, A. The two-dimensional phase of boron nitride: Few-atomic-layer sheets and suspended membranes. *Applied Physics Letters* **92**, 133107 (2008).

192. McKeown-Green, A. S. *et al.* Millimeter-Scale Exfoliation of hBN with Tunable Flake Thickness for Scalable Encapsulation. *ACS Appl. Nano Mater.* **7**, 6574–6582 (2024).

193. Bockhorn, L. *et al.* Interlayer configurations of self-assembled folded graphene. *Appl. Phys. Lett.* **118**, 173101 (2021).

194. Liu, Z., Suenaga, K., Harris, P. J. F. & Iijima, S. Open and Closed Edges of Graphene Layers. *Phys. Rev. Lett.* **102**, 015501 (2009).

195. Liu, Y., Dobrinsky, A. & Yakobson, B. Graphene Edge from Armchair to Zigzag: The Origins of Nanotube Chirality? *Physical review letters* **105**, 235502 (2010).

196. Kim, J., Yamada, Y., Fujita, R. & Sato, S. Bromination of graphene with pentagonal, hexagonal zigzag and armchair, and heptagonal edges. *J Mater Sci* **50**, 5183–5190 (2015).

197. Yan, W. *et al.* Understanding and Preventing Lubrication Failure at the Carbon Atomic Steps. *Small* **19**, 2301515 (2023).

198. Kim, K. *et al.* Ripping Graphene: Preferred Directions. *Nano Lett.* **12**, 293–297 (2012).

199. Pethica, J. B., Hutchings, R. & Oliver, W. C. Hardness measurement at penetration depths as small as 20 nm. *Philosophical Magazine A* **48**, 593–606 (1983).

200. Pethica, J. B. & Oliver, W. C. Tip Surface Interactions in STM and AFM. *Phys. Scr.* **1987**, 61 (1987).

201. Peng, Z., Chen, X., Fan, Y., Srolovitz, D. J. & Lei, D. Strain engineering of 2D semiconductors and graphene: from strain fields to band-structure tuning and photonic applications. *Light Sci Appl* **9**, 190 (2020).

202. Akinwande, D. *et al.* A review on mechanics and mechanical properties of 2D materials—Graphene and beyond. *Extreme Mechanics Letters* **13**, 42–77 (2017).

203. Novoselov, K. S. *et al.* A roadmap for graphene. *Nature* **490**, 192–200 (2012).

204. Mbayachi, V. B. *et al.* Graphene synthesis, characterization and its applications: A review. *Results in Chemistry* **3**, 100163 (2021).

205. Liang, X. *et al.* Toward Clean and Crackless Transfer of Graphene. *ACS Nano* **5**, 9144–9153 (2011).

206. van der Lee, A., Hamon, L., Holl, Y. & Grohens, Y. Density Profiles in Thin PMMA Supported Films Investigated by X-ray Reflectometry. *Langmuir* **17**, 7664–7669 (2001).

207. Borin Barin, G. *et al.* Optimized graphene transfer: Influence of polymethylmethacrylate (PMMA) layer concentration and baking time on graphene final performance. *Carbon* **84**, 82–90 (2015).

208. Kim, S. *et al.* Robust graphene wet transfer process through low molecular weight polymethylmethacrylate. *Carbon* **98**, 352–357 (2016).

209. Choi, W., Arslan Shehzad, M., Park, S. & Seo, Y. Influence of removing PMMA residues on surface of CVD graphene using a contact-mode atomic force microscope. *RSC Advances* **7**, 6943–6949 (2017).

210. Abdelaal, A. F. *et al.* Polymethylmethacrylate (PMMA) deposition and removal optimization in CVD-grown graphene transfer: A Taguchi technique study. *Diamond and Related Materials* **149**, 111660 (2024).

211. Jia, Y. *et al.* Toward High Carrier Mobility and Low Contact Resistance: Laser Cleaning of PMMA Residues on Graphene Surfaces. *Nano-Micro Lett.* **8**, 336–346 (2016).

212. Lanza, M. AFM-Based Characterization of the Properties of 2D Materials and Heterostructures. (2024).

213. Yuan, Y. *et al.* On the quality of commercial chemical vapour deposited hexagonal boron nitride. *Nat Commun* **15**, 4518 (2024).

214. Kauling, A. P. *et al.* The Worldwide Graphene Flake Production. *Advanced Materials* **30**, 1803784 (2018).

215. Pirkle, A. *et al.* The effect of chemical residues on the physical and electrical properties of chemical vapor deposited graphene transferred to SiO2. *Applied Physics Letters* **99**, 122108 (2011).

216. Kang, J., Shin, D., Bae, S. & Hong, B. H. Graphene transfer: key for applications. *Nanoscale* **4**, 5527–5537 (2012).

217. Ahn, Y., Kim, H., Kim, Y.-H., Yi, Y. & Kim, S.-I. Procedure of removing polymer residues and its influences on electronic and structural characteristics of graphene. *Applied Physics Letters* **102**, 091602 (2013).

218. Tyler, B. J. *et al.* Removal of Organic Contamination from Graphene with a Controllable Mass-Selected Argon Gas Cluster Ion Beam. *J. Phys. Chem. C* **119**, 17836–17841 (2015).

219. Son, B. H. *et al.* Electron beam induced removal of PMMA layer used for graphene transfer. *Sci Rep* **7**, 18058 (2017).

220. Jeong, H. J. *et al.* Improved transfer of chemical-vapor-deposited graphene through modification of intermolecular interactions and solubility of poly(methylmethacrylate) layers. *Carbon* **66**, 612–618 (2014).

221. Sun, J., Finklea, H. O. & Liu, Y. Characterization and electrolytic cleaning of poly(methyl methacrylate) residues on transferred chemical vapor deposited graphene. *Nanotechnology* **28**, 125703 (2017).

222. Moser, J., Barreiro, A. & Bachtold, A. Current-induced cleaning of graphene. *Applied Physics Letters* **91**, 163513 (2007).

223. Peltekis, N. *et al.* The effect of downstream plasma treatments on graphene surfaces. *Carbon* **50**, 395–403 (2012).

224. Gong, C. *et al.* Rapid Selective Etching of PMMA Residues from Transferred Graphene by Carbon Dioxide. *J. Phys. Chem. C* **117**, 23000–23008 (2013).

225. Tripathi, M. *et al.* Cleaning graphene: comparing heat treatments in air and in vacuum. *Physica Rapid Research Ltrs* **11**, 1700124 (2017).

226. Longchamp, J.-N., Escher, C. & Fink, H.-W. Ultraclean freestanding graphene by platinum-metal catalysis. *Journal of Vacuum Science & Technology B, Nanotechnology and Microelectronics: Materials, Processing, Measurement, and Phenomena* **31**, 020605 (2013).

227. Sun, L. *et al.* A Force-Engineered Lint Roller for Superclean Graphene. *Advanced Materials* **31**, 1902978 (2019).

228. Choi, W. J. *et al.* A Simple Method for Cleaning Graphene Surfaces with an Electrostatic Force. *Advanced Materials* **26**, 637–644 (2014).

229. Jalilian, R. *et al.* Scanning gate microscopy on graphene: charge inhomogeneity and extrinsic doping. *Nanotechnology* **22**, 295705 (2011).

230. Goossens, A. M. *et al.* Mechanical cleaning of graphene. *Applied Physics Letters* **100**, 073110 (2012).

231. Lindvall, N., Kalabukhov, A. & Yurgens, A. Cleaning graphene using atomic force microscope. *Journal of Applied Physics* **111**, 064904 (2012).

232. Golosov, D. A. *et al.* Stability of the platinum electrode during high temperature annealing. *Thin Solid Films* **661**, 53–59 (2018).

233. Xiao, L., Zhao, Z., Du, L., Wu, S. & Liu, Q. Annealing effect on the stability of platinum thin films covered by SiO2 or SiNx layer. in *The 8th Annual IEEE International Conference on Nano/Micro Engineered and Molecular Systems* 352–355 (IEEE, Suzhou, China, 2013). doi:10.1109/NEMS.2013.6559749.

234. Reed, B. W. & Schuh, C. A. Grain Boundary Networks. in *Electron Backscatter Diffraction in Materials Science* (eds. Schwartz, A. J., Kumar, M., Adams, B. L. & Field, D. P.) 201–214 (Springer US, Boston, MA, 2009). doi:10.1007/978-0-387-88136-2_15.

235. Cançado, L. G. *et al.* Quantifying Defects in Graphene via Raman Spectroscopy at Different Excitation Energies. *Nano Lett.* **11**, 3190–3196 (2011).

236. Tyagi, A. *et al.* Ultra-clean high-mobility graphene on technologically relevant substrates. *Nanoscale* **14**, 2167–2176 (2022).

237. Ferrah, D. *et al.* XPS investigations of graphene surface cleaning using H 2 - and Cl 2 -based inductively coupled plasma. *Surface and Interface Analysis* **48**, 451 (2016).

238. Cunge, G. *et al.* Dry efficient cleaning of poly-methyl-methacrylate residues from graphene with high-density H2 and H2-N2 plasmas. *Journal of Applied Physics* **118**, 123302 (2015).

239. Xie, W., Weng, L.-T., Ng, K. M., Chan, C. K. & Chan, C.-M. Clean graphene surface through high temperature annealing. *Carbon* **94**, 740–748 (2015).

240. Berkovic, G., Krongauz, V. & Weiss, V. Spiropyrans and Spirooxazines for Memories and Switches. *Chem. Rev.* **100**, 1741–1754 (2000).

241. Gately, T. J., Li, W., Mostafavi, S. H. & Bardeen, C. J. Reversible Adhesion Switching Using Spiropyran Photoisomerization in a High Glass Transition Temperature Polymer. *Macromolecules* **54**, 9319–9326 (2021).

242. Jang, A.-R. *et al.* Reversibly Light-Modulated Dirac Point of Graphene Functionalized with Spiropyran. *ACS Nano* **6**, 9207–9213 (2012).

243. Zukowski, P., Koltunowicz, T. N., Czarnacka, K., Fedotov, A. K. & Tyschenko, I. E. Carrier transport and dielectric permittivity of SiO2 films containing ion-beam synthesized InSb nanocrystals. *Journal of Alloys and Compounds* **846**, 156482 (2020).

244. Zhang, X., Xin, J. & Ding, F. The edges of graphene. *Nanoscale* **5**, 2556 (2013).

245. Wu, X., Zhao, H., Zhong, M., Murakawa, H. & Tsukamoto, M. Molecular dynamics simulation of graphene sheets joining under ion beam irradiation. *Carbon* **66**, 31–38 (2014).

246. Wu, X., Zhao, H. & Pei, J. Fabrication of nanopore in graphene by electron and ion beam irradiation: Influence of graphene thickness and substrate. *Computational Materials Science* **102**, 258–266 (2015).